## *Perturbative predictions for 4 jet production at LEP and prompt photon emission at the tevatron*

Cullen, M. A.

# Perturbative Predictions for 4 Jet Production at LEP and Prompt Photon Emission at the Tevatron

A thesis submitted for the degree of
Doctor of Philosophy
by

**M.A.Cullen**



University of Durham
Department of Physics
September 1999

# Declaration

I declare that no material presented in this thesis has previously been submitted for a degree at this or any other university.

The research described in this thesis has been carried out in collaboration with Dr.E.W.N.Glover and Dr.J.M.Campbell and has been published as follows

- Four jet event shapes in electron-positron annihilation
  J.M.Campbell, M.A.Cullen and E.W.N.Glover, Eur.Phys.J.**C9**, 245-265
- Photon production at the Tevatron using the ALEPH measurement of the photon fragmenatation function
  M.A.Cullen and E.W.N.Glover (in preparation)

# Acknowledgements

First and foremost I would like to thank Nigel Glover for his enjoyable supervision. Thank you for taking a young physicist and teaching him the wonders of QCD àla FORTRAN. Also the numerous discussions on who should play for England. Thank you for getting me through three years.

Although the whole of the CPT group have been a great team to work with (both staff and students alike) a special thanks must go to my surrogate big brother and friend, John Campbell. I am very grateful for the many hours you have spent as a teacher, a collaborator and a fellow Norwich City football club fan. I'll miss those rare headed goals and your generous nature. I wish you luck with whatever you do. Also, I would like to thank those saintly people who put up with my singing in the office and were ever ready for a good distraction from work. Thank you Pete, Ania and John. May you enjoy office cricket wherever you go.

I am grateful to Norwich City football club for having had three awful seasons and thus proving no distraction to work at all.

Many thanks to my parents and brother and sister for listening to my moans and groans. I promise to tell you all what I've been doing for the last three years in English sometime.

Finally I would like to thank the person who bore the real brunt, my fiancée Wendy. Thank you for all your support and love. I could not have done it without you. Thank you for being patient, caring and someone to talk to, but most of all a friend.

# Abstract

Many contemporary experimental QCD results achieve greater accuracy in measurement than equivalent theoretical predictions calculated at leading order. Therefore it is necessary to consider next to leading order (NLO) predictions for many processes in order to compare experiment with theory. Accurate theoretical predictions are also important in order to reduce the uncertainty in QCD parameters such as the coupling constant $\alpha_s$ and to test whether QCD is in fact the correct theory to describe the strong interaction. With NLO results it is also possible to separate different clustering algorithms and test non-perturbative effects.

This thesis concentrates on the techniques necessary for the calculation of NLO observables from the processes $e^+e^- \to 4$ jets and $p\overline{p} \to \gamma + X$. We formulate a new version of the hybrid subtraction scheme based on the colour antenna structure of the final state to evaluate the necessary phase space integrals for the 4 jet process. The scheme is universal and can be applied to any QCD processes. The general purpose Monte Carlo `EERAD2` which incorporates this new technique is compared with both experimental data gathered by the DELPHI collaboration and other groups which have reported similar calculations.

A Monte Carlo written for the process $p\overline{p} \to \gamma + X$ requires a knowledge of the non-perturbative photon fragmentation function, $D_\gamma$, and the second half of this thesis concentrates on a calculation of this process using the ALEPH measurement of $D_\gamma$ based on a democratic algorithm. The Monte Carlo `DPRAD` incorporates these techniques and results from it are compared with data from the Tevatron.

# Contents


**1 Introduction** **1**

1.1 In the beginning... . . . . 1

1.2 The QCD Langrangian . . . . . 7

1.3 The renormalisation of QCD . . . . . 14

1.4 Theoretical uncertainty . . . . . 20

1.5 Summary . . . . . 23

**2 Experiments, Next-to-Leading Order and Motivation** **25**

2.1 Introduction . . . . . 25

2.2 Jets and higher orders . . . . . 26

2.2.1 Jet-finding algorithms . . . . . 27

2.2.2 Recombination schemes . . . . . 33

2.3 Next-to-Leading order techniques . . . . . 33

2.3.1 Introduction . . . . . 33

2.3.2 KLN theorem . . . . . 34

2.3.3 $e^+e^- \to 2$ jets . . . . . 35

2.3.4 Divergences and Dimensional regularisation - "to infinity and beyond" 36

2.3.5 Colour in QCD calculations and colour algebra . . . . . 39
2.3.6 The colour factors of SU(3) . . . . . 39
2.3.7 $q\overline{q} \to gg$ . . . . . 43
2.3.8 Matrix element and Subamplitude factorisation . . . . . 50
2.4 Phase space . . . . . 58
2.5 Motivation . . . . . 61
2.6 Summary . . . . . 63

**3 NLO Numerical Techniques** **66**

3.1 Introduction . . . . . 66
3.2 Subtraction, Slicing and Hybrid subtraction . . . . . 67
3.2.1 Slicing[42] . . . . . 67
3.2.2 Subtraction[44] . . . . . 69
3.2.3 Hybrid subtraction . . . . . 70
3.3 Antenna factorisation . . . . . 71
3.3.1 Momentum mapping . . . . . 72
3.3.2 The universal subtraction terms . . . . . 75
3.3.3 Quark-Antiquark antenna . . . . . 77
3.3.4 Quark-Gluon antenna . . . . . 78
3.3.5 Gluon-Gluon antenna . . . . . 80
3.3.6 Antenna where a quark-antiquark pair merge . . . . . 81
3.4 Summary . . . . . 82

**4 Matrix elements/subtraction terms for the calculation of $e^+e^- \to$ 4 jets 84**

4.1 Introduction . . . . . 84

4.2 The virtual loop matrix elements . . . . . 85

4.2.1 $e^+e^- \to q\bar{q}gg$ . . . . . 85

4.2.2 $e^+e^- \to q\bar{q}Q\overline{Q}$ . . . . . 88

4.3 The unresolved parton matrix elements . . . . . 96

4.3.1 $e^+e^- \to q\bar{q}ggg$ . . . . . 96

4.3.2 $e^+e^- \to q\bar{q}Q\overline{Q}g$ . . . . . 98

4.4 Symmetries and negligible contributions . . . . . 100

4.4.1 Negligible contributions . . . . . 101

4.4.2 Symmetry factors . . . . . 101

4.5 Using hybrid subtraction for the NLO calculation of $e^+e^- \to 4$ jets . . . . . 105

4.6 Summary . . . . . 114

**5 Data results for NLO 4 jet observables 115**

5.1 Introduction . . . . . 115

5.2 Four jet event shapes . . . . . 116

5.2.1 Definition of Variables . . . . . 116

5.2.2 Structure of Perturbative Prediction . . . . . 118

5.2.3 Scale choice, theoretical uncertainty and resummations . . . . . 118

5.3 Comparison with existing results . . . . . 119

5.3.1 Four jet rates . . . . . 119

5.3.2 Shape variables . . . . . 119

5.4 New results . . . . . 121

5.4.1 Light Hemisphere Mass . . . . . 122

5.4.2 Narrow Hemisphere Broadening . . . . . 123

5.4.3 Jet transition variables . . . . . 123

5.5 Comparison with experimental data . . . . . 124

5.6 Summary . . . . . 129

**6 A new calculation: $p\bar{p} \to \gamma +$ jets at $O(\alpha\alpha_s^2)$** **133**

6.1 Introduction . . . . . 133

6.2 Photon emission and fragmentation functions . . . . . 134

6.3 Construction of the $q \to \gamma$ fragmentation function . . . . . 137

6.4 Initial state radiation and crossing functions . . . . . 144

6.5 The full result and structure of DPRAD . . . . . 154

6.5.1 LO contributions to 1 jet final states . . . . . 154

6.5.2 LO contributions to 2 jet final states . . . . . 156

6.5.3 Extra unresolved parton contribution to 1 jet final states . . . . . 159

6.5.4 Virtual corrections . . . . . 160

6.5.5 Crossing terms and fragmentation contributions . . . . . 162

6.5.6 Final result . . . . . 165

6.5.7 $s_{\min}$ independence . . . . . 166

6.6 Summary . . . . . 166

**7 Results and comparisons with prompt photon data** **169**

7.1 Introduction . . . . . 169

7.1.1 Initial parton contributions . . . . . 169

7.2 Uncertainty in the theoretical prediction . . . . . 170

7.2.1 Differences between the fragmentation functions . . . . . 171

7.2.2 Renormalisation and factorisation scale dependence . . . . . 174

7.2.3 Dependence on the photon isolation criteria . . . . . 175

7.2.4 Dependence on the parton density functions . . . . . 179

7.2.5 Predictions using the resummed fragmentation function . . . . . 179

7.3 Comparison with the data . . . . . 181

7.4 Intrinsic $k_T$ broadening and initial state soft gluon resummation . . . . . 182

7.5 Summary . . . . . 184

**8 Conclusions** **186**

8.1 Review . . . . . 186

**A** **191**

**B** **194**

**C** **200**

C.0.1 2 body final states . . . . . 200

C.0.2 3 body final states . . . . . 201

C.0.3 Two to two body scattering . . . . . 203

# Chapter 1

# Introduction

## 1.1 In the beginning...

At the start of the 1930's, it was recognised that the strong nuclear force between nucleons did not depend on the identity of the nucleons involved. This meant that the strong interaction between a proton and another proton is seen to be identical to the interaction between a neutron and a proton and similarly between two neutrons. Consider the three nuclei $^6He$,$^6Li$ and $^6Be$. These can be thought of as two neutrons, a proton and a neutron and two protons attached to a $^4He$ nucleus respectively. After allowing for differing electromagnetic effects, the masses of these three nuclei are found to be very similar.[1] From these observations particle physicists considered that the proton and neutron might be two different states of the same particle, the *nucleon*. Thus the proton and neutron were thought to be much akin to the up and down spin states of the electron. Therefore these two particles were grouped together in a SU(2) *baryon isospin doublet* where isospin is a mathematical construct analogous to electron spin and SU(2) is the two dimensional representation of the rotation group $J = 1/2$. The group $J = 1/2$ defines the compositions that are formed by combining particles that can exist in either of two states i.e. an "up" state and a "down" state. Combinations are either symmetric or antisymmetric, so when two particles combine according to the $J = 1/2$ group, the following states can be created.

[1] The ground state energy of the lithium nucleus is actually 2 MeV lower than the other two nuclei and it is the excited state with isospin equal to 1 that has the equivalent mass of the other two nuclei.

$$\left(\begin{array}{lll} S=1 & M_s=1 & \uparrow\uparrow \\ S=1 & M_s=0 & \sqrt{\left(\frac{1}{2}\right)}\left(\uparrow\downarrow+\downarrow\uparrow\right) \\ S=1 & M_s=-1 & \downarrow\downarrow \end{array}\right) \tag{1.1.1}$$

$$S=0, M_s=0,, \quad \sqrt{\left(\tfrac{1}{2}\right)}\left(\uparrow\downarrow-\downarrow\uparrow\right)$$

where $S$ is the total spin of the pair and $M_s$ is the $z$ component of this spin. The top three configurations of "up" and "down" form the symmetric triplet of two $J = 1/2$ particles. The remaining state is the antisymetric singlet. SU(2) is a representation of this group, making use of the Pauli spin matrices in its fundamental representation.

The requirement that the strong nuclear force be invariant under isospin transformations demanded that all particles that are affected by the strong nuclear force fill such isospin multiplets and that isospin be a conserved quantity or a conserved *quantum number*. In 1948 the discovery of the three pions, which also have similar masses, forced particle physicists to create a new multiplet and by the 1960's a whole proliferation of baryons and mesons had been found and similarly grouped. The light baryons of spin 1/2 (from here onwards spin refers to the intrinsic angular momentum of a particle and not isospin) formed a octet and the light mesons of spin 0 also formed another octet (with a ninth at considerably higher mass). Also, the existence of another quantum number, that of *strangeness*, had been postulated by Gell-Mann [1] and, independently, by Nishijima [2]. This new conserved quantity was proposed in order to explain the long lifetimes of some of the newly observed particles (such as the $\Sigma^-$). With such large multiplets and two independently conserved numbers, the natural consequence was to arrange the particles into a larger, all embracing group which would link strange and non-strange particles. With two conserved quantum numbers, a group would need to contain two mutually commuting generators that could give quantum numbers to each particle (i.e. a group of rank 2) and in 1961 the group $SU(3)_{\text{flavour}}$ was proposed. The fundamental representation of $SU(3)_{\text{flavour}}$ is a triplet composed of the three different flavours, 'up','down' and 'strange'. All other multiplets can be built up from this and its conjugate. This fundamental representation is the basis of what is known today as the *Quark Model* proposed independently by Gell-Mann [3] and Zweig[4].

By considering the fundamental triplet and the corresponding anti-triplet i.e. an identical triplet except that the quantum numbers are reversed in sign, the lightest meson multiplet

can be formed. Let the elements of the fundamental triplet/anti-triplet be,

$$\begin{pmatrix} u \\ d \\ s \end{pmatrix}, \begin{pmatrix} \overline{u} \\ \overline{d} \\ \overline{s} \end{pmatrix}. \tag{1.1.2}$$

Then, by considering the group operation $\mathbf{3} \otimes \overline{\mathbf{3}} = \mathbf{8} \oplus \mathbf{1}$, the meson octet and singlet are formed. In terms of quark content they are

$$u\bar{d}, u\bar{s}, d\bar{u}, d\bar{s}, s\bar{u}, s\bar{d} \tag{1.1.3}$$

and also the three linear combinations of $u\bar{u}, d\bar{d}$ and $s\bar{s}$,

$$\sqrt{\frac{1}{3}}(u\bar{u} + d\bar{d} + s\bar{s}), \quad \sqrt{\frac{1}{2}}(u\bar{u} - d\bar{d}), \quad \sqrt{\frac{1}{6}}(u\bar{u} + d\bar{d} - 2s\bar{s}). \tag{1.1.4}$$

where the first combination forms the symmetric singlet, the second completes the non-strange antisymmetric triplet and we are forced into the form of the last combination by demanding orthogonality between states. Other more massive mesons are also combinations of these nine states with varying discrete amounts of angular and intrinsic spin between the quark/antiquark pair.

Similarly we can form the various baryons multiplets by considering the $\mathrm{SU}(3)_{\text{flavour}}$ group operation $\mathbf{3} \otimes \mathbf{3} \otimes \mathbf{3} = \mathbf{10} \oplus \mathbf{8} \oplus \mathbf{8} \oplus \mathbf{1}$ which are the multiplets formed by combining three fundamental triplets. The baryon octet that contains the proton and neutron form one of the above octets. The quark model successfully predicts the quantum numbers for hundreds of baryons which are excitations of this basic $\mathbf{10}, \mathbf{8}, \mathbf{8}, \mathbf{1}$ form. Akin to the Periodic Table of Chemistry, the quark model also successfully predicts the existence (and mass) of hitherto unseen particles such as the $\Omega^-$. However the symmetry of $\mathrm{SU}(3)_{\text{flavour}}$ is not a perfect one. For this to be true would require that all the masses of particles in the same multiplet be *exactly* the same.

But the idea of quarks other than mathematical constructs to explain the $SU(3)_{\text{flavour}}$ group properties of the hadrons did not gain full support until 1968 when direct evidence for the existence of point-like objects in nucleons was first seen at the deep inelastic scattering experiments of SLAC-MIT [5].

However, there still remained some difficulties. How can a fermion such as the $\Delta^{++}$ which has spin of 3/2 exist with both symmetrical quark content ($uuu$) and symmetrical spin orientation of the quarks? The answer is to introduce a new quantum number which is referred to as *colour* and to make the $\Delta^{++}$ antisymmetric in this new quantity. Colour comes in three varieties, red, green and blue (R,G and B) together with their antipartners ($\overline{R}, \overline{G}$ and $\overline{B}$). The combination of all three colours is regarded as a colour singlet (or *colourless*) as is the mixture of a colour and its antipartner. It was proposed that all hadrons are colourless, but the quarks that make up the particles are coloured and thus the $\Delta^{++}$ retains its Fermi-Dirac statistics by having a linear combination of a red up quark, a blue up quark and a green up quark which is antisymmetric under $SU(3)_{colour}$ rotation. This new quantum number also explains the apparent short-fall in the R ratio by a factor of 3. The R factor is the ratio

$$R = \frac{\sigma(e^+e^- \rightarrow \text{ hadrons})}{\sigma(e^+e^- \rightarrow \mu^+\mu^-)} \tag{1.1.5}$$

and as such is only dependent on the number of energetically available quarks and the square of their charge. See Figure 1.1. The observed experimental value was seen to be a factor of 3 too large compared to the theoretical prediction if only one quark of each flavour is considered, but with colour there now exist three independent quarks of each flavour e.g. $u_R$ , $u_B$ and $u_G$ which accounts for the discrepancy. Another consequence of colour and the demand that all observed particles are colourless is that we can never see an isolated quark. Nor can we ever remove a single quark from a hadron. This limitation is known as *confinement* and is still not well understood.

Colour is another example of an SU(3) group, but not to be confused with the flavour SU(3) group previously mentioned. The number of quark flavours is now known to be equal to six and so $SU(3)_{\text{flavour}}$ is only used when considering the light quarks. $SU(3)_{\text{colour}}$ however, is the group that exactly describes colour and as such the triplet R,G,B makes up

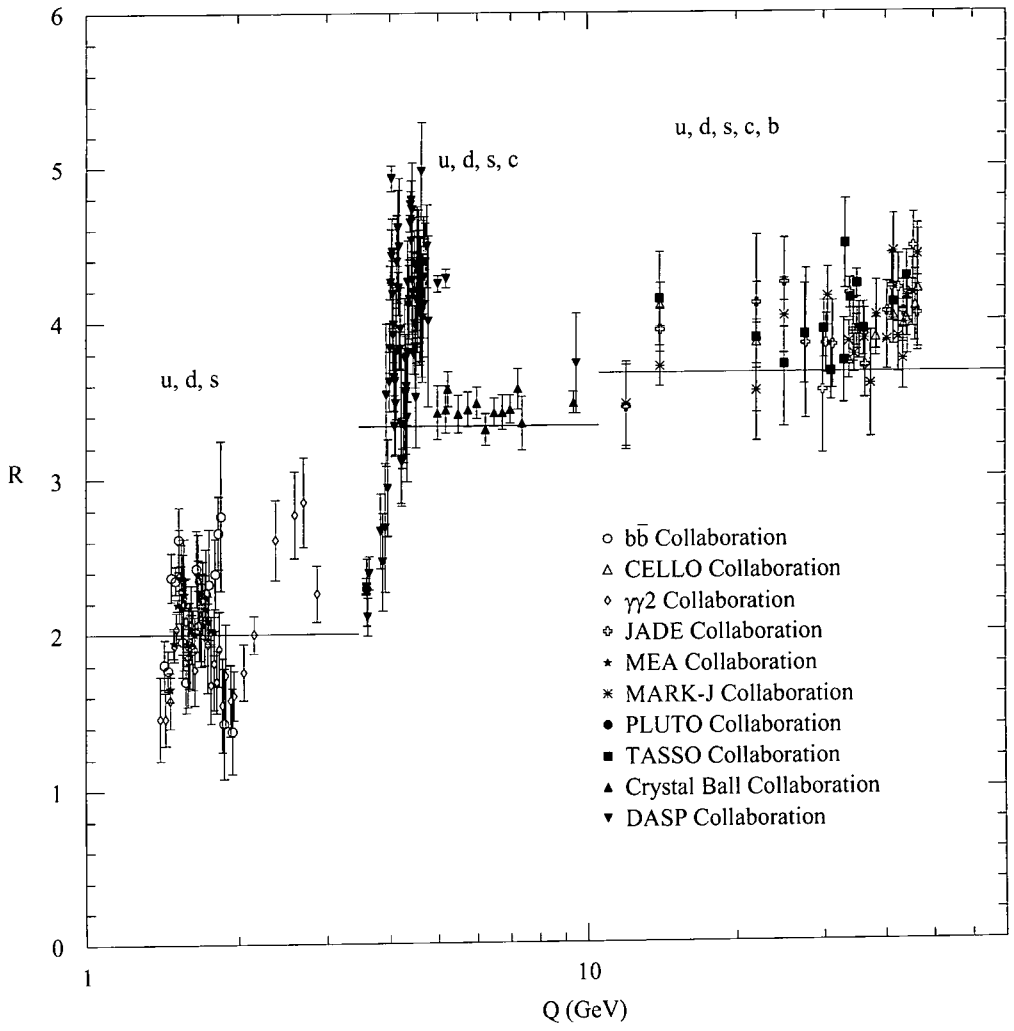


Figure 1.1: The R ratio of Equation 1.1.5 as a function of $Q$. The horizontal lines indicate the expected values of R with 3 colours and with 3, 4 and 5 active quark flavours. As we can clearly see, without the colour factor, theoretical predictions could not predict the overall normalisation of the ratio. The peaks at approximately 4 GeV are the $J/\psi$ and $\chi$ resonances. This diagram is taken from a collection of data over many papers.[7]

its fundamental representation. As we shall see later, it is also the group that we use to describe the theory of quark interactions.

With any unitary group, we need to consider the generators of the symmetry and for SU(3) there are 8 Gell-Mann matrices that make up these generators. Just as the fundamental representation corresponds to the basic building blocks of the group (and the basic field for the Lagrangian), the *adjoint* representation of SU(3) contains the generators of the group and these represent the mediators of the strong force that bind all coloured particles. They are known as *gluons*. As we shall see later, these eight additional fields are necessary for the Lagrangian of the strong force to remain locally gauge invariant (i.e. the Lagrangian does not change if the definition of colour depends on position) and the adjoint representation is the source of these gluon fields. For the electromagnetic force (a U(1) symmetry) the photon ensures that a position dependent definition of charge does not affect the QED Lagrangian (the theory of electromagnetic interactions). The only difference between the two sorts of gauge bosons is that the gluon is colour-charged whereas the photon carries no electrical charge. If the gluons did not carry colour charge then we could bind together three red quarks to form a coloured hadron violating our earlier postulate of colourless physical particles. In fact the gluon must carry colour and anticolour to ensure no coloured hadrons are seen. Since we have 3 colours this gives us nine gluons, but one is a colourless singlet and so decouples, having no interaction with either quarks or other gluons. It can be shown that the gluon must have spin 1, like the photon, in order to mediate the interactions of spin 1/2 quarks. Also, as the gluons are coloured they can interact with each other as well as the quarks. We shall see this more clearly when we consider the Langrangian of the strong interactions.

In this thesis we shall concern ourselves with a quantitative description of quarks and the colour forces that bind them. This construction is known as *Quantum Chromodynamics* (QCD) and is an example of a quantum field theory. These are highly successful theories that link all of particle physics. The Standard Model of particle physics consists of three such theories which are all described mathematically with reference to unitary groups. But in this thesis we concern ourselves with that group and theory that describes the strong interactions of the constituents of the nucleus. In Section 1.2 we shall see how we proceed from the QCD Langrangian to a point where we can calculate experimental variables using the *Feynman rules* of QCD. However the theory at this stage still contains hidden infinities and these need

to be removed using a prescription known as *renormalisation*. We shall consider this and its influence on QCD in Section 1.3. Finally we shall study the error involved in using a truncated perturbation theory (the technique used for all quantum field theory calculations in this thesis) and how this can be reconciled with the full theoretical result. This we present in Section 1.4

## 1.2 The QCD Langrangian

In this section we shall consider the structure of an SU(3) gauge theory and how we can relate the Langrangian of this theory to a more perturbative, diagrammatically orientated prescription. From this we can derive rules for the calculation of physical parameters such as the cross-section and event shape variables.

We begin by considering the Langrangian of QCD, the theory of strong interactions. From the same deep inelastic scattering experiments that suggested a point-like structure to the nucleon, it was shown that these *partons* also have intrinsic spin 1/2 and so they are fermions. From this we can write down an expression for a single flavour massless coloured quark

$$\mathcal{L}_{\text{quark+gluon}} = i\overline{\psi_i}\gamma_\mu\partial^\mu\psi_i \quad \text{where} \quad \psi = \begin{pmatrix} \psi_R^\nu \\ \psi_G^\nu \\ \psi_B^\nu \end{pmatrix} \tag{1.2.6}$$

where $\psi_i$ is a member of the SU(3) triplet of 4 component Dirac spinors, $i = R, G, B$, $\nu = 0, 1, 2, 3$ and $\gamma_\mu$ are the 4 by 4 matrices that satisfy the Clifford algebra $\{\gamma_\mu, \gamma_\nu\} = 2g_{\mu\nu}$. We also have an implied summation over the index $i$.

However, if we wish to enforce local colour invariance i.e. changing the colours in different ways at different points in space-time without changing the Lagrangian we are led to the following form of $\mathcal{L}_{\text{quark+gluon}}$

$$\mathcal{L}_{\text{quark+gluon}} = i\overline{\psi_i}\gamma_\mu\mathcal{D}_{ij}^\mu\psi_j \tag{1.2.7}$$

We define the covariant derivative, $\mathcal{D}_{ij}^{\mu}$ as

$$\mathcal{D}_{ij}^{\mu} = \partial^{\mu}\delta_{ij} + igt_{ij\,a}A_a^{\mu}, \tag{1.2.8}$$

where $A_a^{\mu}$ is the gluon field in the adjoint representation labelled with colour index $a$ and couples to quarks of colour $i, j$ via the 8 Gell-Mann matrices $t_{ij\,a}$ and with strength $g$. These colour matrices do not commute as do the U(1) charge matrices present in QED. Instead they obey the commutation relation $[t_a, t_b] = if_{abc}t_c$ where $f_{abc}$ are the structure constants of SU(3). Having constructed the matter content of the QCD Lagrangian, we now consider the dynamics of the gauge particles. We include a kinetic term by incorporating the field strength tensor of the gluon field, $F_a^{\mu\nu}$ such that

$$\mathcal{L}_{\text{quark+gluon}} = i\overline{\psi}_i\gamma_{\mu}\mathcal{D}_{ij}^{\mu}\psi_j - \frac{1}{4}F_a^{\mu\nu}F_{\mu\nu\,a} \tag{1.2.9}$$

where there is an implied summation over $a = 1..8$. The field strength tensor is defined so as to ensure local colour invariance under SU(3) rotations. It is given by,

$$F_a^{\mu\nu} = \partial^{\mu}A_a^{\nu} - \partial^{\nu}A_a^{\mu} - gf_{abc}A_b^{\mu}A_c^{\nu}. \tag{1.2.10}$$

We can clearly see that the gluonic kinetic energy term in the Lagrangian will generate terms which have three and four gluon fields and therefore produce self-interactions of the gluon. It is these terms that will be crucial to the renormalisation of the theory (See Section 1.3).

Let us now see how the local invariance of the proposed Lagrangian works. We can describe an SU(3) transformation by rotating the fundamental triplet using $V_{ij}(x)$ where

$$V_{ij}(x) = e^{i\theta_a(x)t_{ij\,a}}, \tag{1.2.11}$$

and $\theta_a(x)$ is an arbitrary function that depends on the four vector $x$ so that,

$$\psi_i \rightarrow V_{ij}(x)\psi_j \tag{1.2.12}$$

As $V_{ij}(x)$ is a unitary transformation this ensures any mass term incorporated into the Langrangian will remain unaffected under rotation. (Any mass must have the form $m\overline{\psi_i}\psi_i$). When we apply $V_{ij}(x)$ to Equation. 1.2.9 we see that if $\mathcal{L}$ is to be unaffected this implies that,

$$\mathcal{D}^{\mu}{}_{ij}\psi_j \rightarrow V_{ij}(x)\mathcal{D}^{\mu}{}_{jk}\psi_k. \tag{1.2.13}$$

which then forces a transformation rule on the gluon field $A$. The invariance of the quark field term in the Lagrangian can be seen when the transformations of Equations 1.2.12 and 1.2.13 are applied to Equation 1.2.8. (See Appendix A)

Thus the first term of equation 1.2.9 is invariant under an SU(3) gauge transformation. In a similar manner it can be shown that the gluon kinetic energy term is also invariant with respect to the transformations of equation 1.2.12 and the gluon field transformation (see Appendix A).

However, there is still some ambiguity to our Lagrangian. The gluon field is not uniquely defined as we can transform it without affecting any measureable quantity. In fact the propagator cannot exist unless we remove some of these extra degrees of freedom. This is done by adding a *gauge-fixing* term of the form

$$\mathcal{L}_{\text{gauge}} = -\frac{1}{2\xi}(\partial_\mu A^\mu_a)^2 \tag{1.2.14}$$

where $\xi$ is the arbitrary gauge parameter and defines the covariant propagator to be used. We associate the Lorentz condition $\partial_\mu A^\mu_a = 0$ with the covariant propagator and for this

thesis $\xi$ will be taken to be 1 which is usually known as the Feynman gauge. (It is not necessary to impose the Lorentz condition to derive a set of Feynman rules. Axial gauges define an axial vector $n^\mu$ that can be used). This process is necessary to uniquely define the photon propagator in QED as well.

The final term in the QCD Lagrangian is required to keep the number of polarization states of external gluons equal to two. We have associated with the covariant gluon propagator four degrees of freedom. In QED the photon has a similar problem, however the longitudinal and scalar components cancel with each other to leave the physically-seen two transverse degrees of freedom. In QCD this does not happen due to the gluon self-interaction. So an additional term is added to the Lagrangian to ensure that longitudinal gluons do not propagate. This term is given by

$$\mathcal{L}_{\text{ghost}} = \partial_\mu \eta_a^\dagger (\mathcal{D}_{ac}^\mu \eta_c) \tag{1.2.15}$$

where $\eta$ is a scalar field in the adjoint representation which obeys Fermi statistics. This term is known as the *ghost* term and is important when considering gluon loop diagrams.

Therefore the full QCD Lagrangian can be written as

$$\mathcal{L}_{\text{QCD}} = \mathcal{L}_{\text{quark+gluon}} + \mathcal{L}_{\text{ghost}} + \mathcal{L}_{\text{gauge}} \tag{1.2.16}$$

The full QCD Lagrangian can now be used to write the action, $\mathcal{S}$ of the theory which consists of a free theory term $\mathcal{S}_0$ and an interaction term $\mathcal{S}_I$. If the coupling of quarks and gluons is assumed to be small then the interaction term can be treated as a perturbation and a series can be calculated using Feynman's *path integral* formalism. A detailed account of Feynman's path integral formalism can be found in [6]. One way of visualizing this is by using *Feynman diagrams.* These diagrams, together with the *Feynman rules* derived from the Lagrangian via the path integral formalisms can be used to calculate experimental transition probabilities. All viable, topologically different diagrams of a given order are summed to give an amplitude $i\mathcal{M}$ which when squared gives the transition probability of a final state

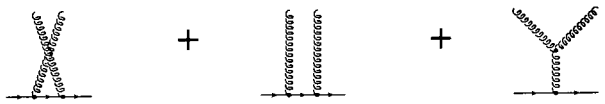

Figure 1.2: The three diagrams that form the process $q\bar{q} \to gg$ in QCD. Note the additional diagram with the triple gluon vertex. In QED, the U(1) charges commute so that the first two diagrams are all that is required for gauge invariance. However, the SU(3) colour charges of QCD require the additional diagram to conserve gauge invariance and thus using this process, the form of the triple gluon vertex can be deduced

being produced from any given initial state. By integrating the product of this and certain phase space and intial flux factors over relevant momentum variables an experimental value can be calculated such as the cross-section or any jet observable.

The Feynman rules for QCD in the Feynman gauge (a covariant gauge with $\xi = 1$) can be seen in Figure 1.3. Another convenient method of obtaining the Feynman rules for the triple gluon self-interaction is by considering the reaction $q\bar{q} \to gg$. Without the triple gluon vertex, there would be two diagrams that contribute to this process (see the first two diagrams of Figure 1.2). In the analogous QED process these two diagrams would be invariant under the gauge transformation $\varepsilon_\mu \to \varepsilon_\mu + ap_\mu$ where $\varepsilon_\mu$ is the polarisation state of one of the photons and $p_\mu$ is its four momentum. This is because the U(1) charge matrices present in the matrix elements commute. This gauge invariance leads to the formulation of the *Ward Identity* which states that

$$p_\mu \mathcal{M}^\mu = 0 \tag{1.2.17}$$

where $\mathcal{M}^\mu$ is the matrix element of the process. However, with the non-Abelian nature of QCD, the SU(3) colour matrices present do not commute and if we consider the same two diagrams we are left with a gauge dependent answer. By introducing the triple gluon diagram and demanding that the sum of these is gauge invariant, the form of the triple gluon vertex can be derived. A similar argument can be used to derive the form of the four gluon vertex by considering the gauge invariance of the the process $gg \to gg$. Other Feynman rules that are used to calculate squared matrix elements include

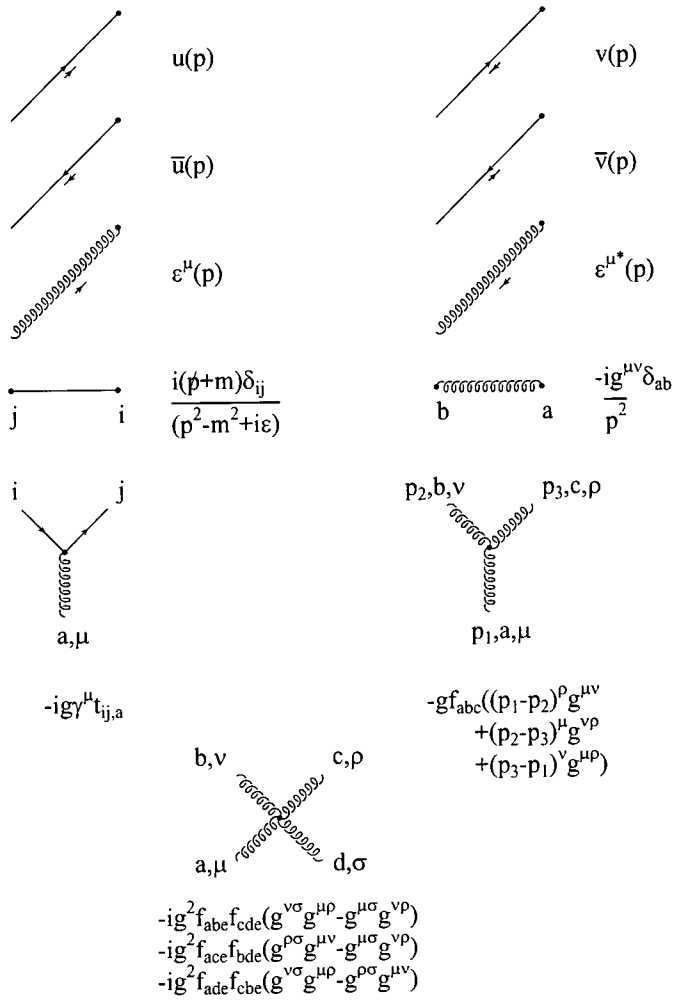


Figure 1.3: Feynman rules for covariant gauge QCD with $\xi = 1$. The straight lines correspond to quark tracks and the springs correspond to gluon tracks. The rules for external and virtual particles are almost identical to those for QED, the only differences being the coupling strength and the presence of an SU(3) Gell-Mann matrix as opposed to the U(1) charge matrix. As can be seen in the QCD Lagrangian there exist triple and quadruple gluon self-interactions and the rules for these can be calculated by considering the processes $q\bar{q} \to gg$ and $gg \to gg$ and demanding local gauge invariance

- The completeness relations of any fermion, derived from the Dirac equation.

$$\begin{aligned} \sum_{s=1,2} u^{(s)}(p)\bar{u}^{(s)}(p) &= \not{p} + m \\ \sum_{s=1,2} v^{(s)}(p)\bar{v}^{(s)}(p) &= \not{p} - m \end{aligned} \tag{1.2.18}$$

  where $s$ is the spin of the fermion.

- The completeness relation for the vector bosons

$$\sum_{s=1,2} \epsilon_\mu^s \epsilon_\nu^{s\star} = -g_{\mu\nu} + \frac{p_\mu p_\nu}{p^2}(1-\xi) \tag{1.2.19}$$

  where $s$ is the spin of the boson.

- Spin-summing final states and averaging over initial state spins of a matrix element. This is performed only for unpolarized physical observables meaning that no information about the spins of the initial state particles is passed through the calculation.

- multiplying by a factor -1 for every fermion loop (and ghost loop although this will not concern us).

- multiplying by a factor $1/n!$ for $n$ identical final state particles.

- integration over any loop momenta e.g. $\int d^4l/(2\pi)^4$.

Throughout this thesis we shall work with the masses of all the quarks set to zero which will simplify the calculation of matrix elements containing a large number of external particles. This may be seen as working without any reference to physical quarks, but because the centre-of-mass energies we will be using are far greater than the masses of the light quarks any mass effects can usually be neglected. (For an example of QCD calculations involving mass effects and the techniques involved the reader is referred to [8]).

Another parameter important to any QCD calculation is $\alpha_s$ which is defined as $g^2/(4\pi)$ where $g$ is the coupling strength of QCD. The value of $\alpha_s$ is a subject of huge diversity and

interest to anyone working in QCD. However, this parameter is not uniquely defined until we consider the renormalisation of QCD. The succeeding two sections will concentrate on the theory and application of renormalisation and the different methods that are used.

## 1.3 The renormalisation of QCD

When the Feynman rules described in the last section are applied to leading order (LO) diagrams (i.e. those diagrams corresponding to the first term in the perturbation series), they are seen to work reasonably well for high energies (energies of the order of the Z mass). Within theoretical confines which we shall look at later, LO QCD results give a good general description for many distributions. However, if we were to consider Feynman diagrams corresponding to higher terms in the series such as diagrams that contain loops, the current Feynman rules give infinite answers. For example, consider the 1-loop correction to the quark propagator. The matrix element describing this graph contains the integral

$$\int_0^\infty \frac{d^4l}{l^2(k-l)^2} \tag{1.3.20}$$

where $k$ is the external momentum. In the limit $l \to \infty$ the integral can be seen to become logarithmically divergent; this is known as an ultraviolet divergence. This is true for both QED and QCD.

The remedy for ultraviolet poles is to absorb these divergences into the definition of quark masses and fields, the couplings and the gluon fields. Thus the Langrangian we introduced in Equation 1.2.16 can be thought of as the *bare* QCD Lagrangian which depends solely on the bare charges, masses and fields which are all infinite. Once the divergences of the loop contributions are absorbed by the infinite bare parameters the physical or *dressed* parameters are rendered finite.

Bare and dressed parameters can be related using infinite counter terms. The diagrams of Figure 1.4 show the graphs which contribute to the counter terms at the 1-loop level for the quark and gluon fields and the coupling of quarks to gluons. The loop integrals have to be regularized so that the divergences can be made explicit. This can be done by either applying

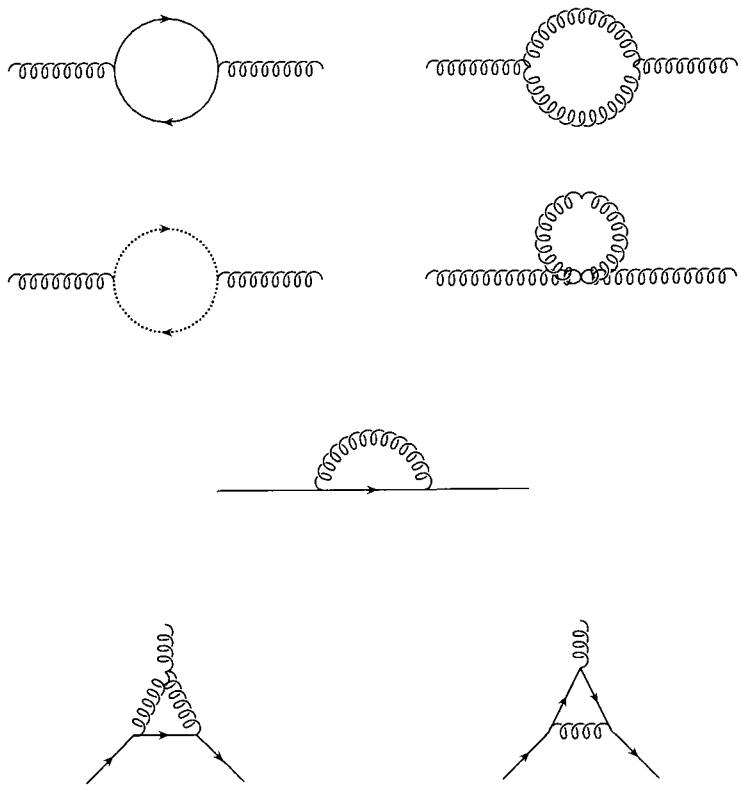

Figure 1.4: The 1-loop contributions to the counterterms for the gluon self energy (top 4 diagrams), the quark self-energy (the middle diagram) and the quark charge (bottom 2 diagrams)

an upper bound to the loop momentum or by continuing the number of dimensions of space-time to $d$ where $d = 4-2\epsilon$. This latter technique is known as dimensional regularization. We shall consider the implications of this in the next chapter. Using either method introduces a scale $\mu$ to the calculation such that the coupling constant is rendered dimensionless. This scale is referred to as the *renormalisation scale* and as such all truncated observables depend upon it. When calculating quantities such as the gluonic self-energy in perturbative QCD (pQCD) the ultraviolet divergences can be made explicit in terms of $1/\epsilon$ poles which must be subtracted to make the answer finite. If only the poles are removed this procedure is known as the *Minimial Subtraction* scheme ($MS$). However, with the poles there are also finite terms of the form $\log 4\pi - \gamma_E$ where $\gamma_E$ is the Euler constant. If these terms are also removed then the new renormalisation procedure is known as the $\overline{MS}$ scheme. For a more detailed calculation of the gluonic self energy the reader is referred to [9].

Having introduced a renormalisation procedure we can now see how this affects the results of a fixed order calculation. As we have seen, the removal of the ultraviolet poles from the loop diagrams has required us to redefine the coupling constant of QCD. Whereas before we had $\alpha_s$ which was a constant, we now have $\alpha_s(\mu)$ which is referred to as a *running coupling constant.* To show the effect this has on our calculations consider a dimensionless quantity $R$ which depends on a single energy scale $Q$ (let this be the centre of mass energy of the experiment e.g. $M_Z$ for LEP1 experiments) which is large enough to make other scales such as the quark masses negligible. If we renormalize the perturbation series for $R$ we introduce a second scale $\mu$ (this can be thought of as the energy at which the subtractions take place). Now $R$ depends in general on the ratio $Q/\mu$. Also $\alpha_s$ will depend on $\mu$ i.e. $\alpha_s \to \alpha_s(\mu)$. However, the renormalisation scale $\mu$ is an arbitrary parameter and $R$ cannot depend on the value of this scale as it is not present in the QCD Lagrangian. This independence can be expressed as

$$\frac{d}{d\mu}R\left(\frac{Q}{\mu}, \alpha_s(\mu)\right) = \left[\frac{\partial}{\partial\mu} + \frac{\partial\alpha_s}{\partial\mu}\frac{\partial}{\partial\alpha_s}\right] R\left(\frac{Q}{\mu}, \alpha_s(\mu)\right) = 0 \tag{1.3.21}$$

which we can rewrite by making the substitution, $\beta(\alpha_s) = \mu\frac{\partial\alpha_s}{\partial\mu}$ and using the chain rule to rewrite the derivative with respect to $Q$,

$$\left[-Q\frac{\partial}{\partial Q} + \beta(\alpha_s)\frac{\partial}{\partial\alpha_s}\right] R = 0. \tag{1.3.22}$$

We introduce the new variable $t$ where

$$\frac{Q}{\mu} = e^t \tag{1.3.23}$$

Therefore we can rewrite Equation 1.3.22 as

$$\left[-\frac{\partial}{\partial t} + \beta(\alpha_s)\frac{\partial}{\partial\alpha_s}\right] R(e^t, \alpha_s(\mu)) = 0 \tag{1.3.24}$$

We can solve this partial differential equation by introducing a new function, $\alpha_s(Q)$ such that

$$t = \int_{\alpha_s(\mu)}^{\alpha_s(Q)} \frac{dx}{\beta(x)} \tag{1.3.25}$$

Differentiating Equation 1.3.25 using the identity

$$t = \int_{x_1}^{x_2} dy\, f(y) \;\Rightarrow\; \frac{\partial x_2}{\partial t} = \frac{1}{f(x_2)} \tag{1.3.26}$$

gives

$$\frac{\partial \alpha_s(Q)}{\partial t} \doteq \beta(\alpha_s(Q)), \quad \frac{\partial \alpha_s(Q)}{\partial \alpha_s(\mu)} = \frac{\beta(\alpha_s(Q))}{\beta(\alpha_s(\mu))} \tag{1.3.27}$$

Therefore $R(1, \alpha_s(Q))$ is a solution of Equation 1.3.24. We can see from this that all the scale dependence in $R$ is due to the running of the coupling constant $\alpha_s(Q)$ and if $R(1, \alpha_s(\mu))$ is known at one scale we can predict its variation with $Q$ by solving Equation 1.3.25 which can be performed by using perturbation theory for sufficiently high values of $Q$. This is due to the asymptotically free nature of QCD i.e. $\alpha_s(Q)$ decreases as $Q$ increases.

To solve Equation 1.3.25 we must know the form of the $\beta$ function in QCD which can be calculated using the counter term graphs we saw in Figure 1.4. It has a perturbative expansion of the form

$$\beta(\alpha_s) = -b\alpha_s^2(1 + b'\alpha_s + O(\alpha_s^2)) \tag{1.3.28}$$

with the one loop graphs from Figure 1.4 determining $b$, the coefficient

$$b = \frac{(11N - 2n_f)}{12\pi} \tag{1.3.29}$$

where $N$ is the number of colours and $n_f$ is the number of light flavours of quark that could form quark loops in the gluon propagator. The value of $b'$ is also known from 2-loop graphs. However, even higher order coefficients are dependent on the renormalisation scheme employed. As can be seen from Equation 1.3.29, QCD with $n_f < 17$ gives a negative value for $\beta(\alpha_s)$ and therefore according to Equation 1.3.22 $\alpha_s$ decreases as the scale increases making QCD an asymptotically free theory. This is the exact opposite behaviour to QED where the $\beta$ function is given as

$$\beta_{QED}(\alpha) = \frac{1}{3\pi}\alpha^2 \tag{1.3.30}$$

at the 1-loop level which is clearly positive.

Having written a perturbative form for the $\beta$ function we can now write an expression for the variation of $\alpha_s$. Starting from the definition of $\beta$ we may write,

$$Q\frac{\partial \alpha_s(Q)}{\partial Q} = -b\alpha_s^2(Q)[1 + b'\alpha_s(Q) + O(\alpha_s^2(Q))]. \tag{1.3.31}$$

If both $\alpha_s(\mu)$ and $\alpha_s(Q)$ are sufficiently small to lie in the perturbative region we can truncate the $\beta$ function series and solve the remaining differential equation. If we only include the first term of the series then,

$$\alpha_s(Q) = \frac{\alpha_s(\mu)}{1 + \alpha_s(\mu)b\ln\frac{Q}{\mu}}. \tag{1.3.32}$$

Thus we can see that, given a value of $\alpha_s$ at some scale $\mu$ its value at other perturbative scales can be calculated. Using this technique, experiments at very different energies can

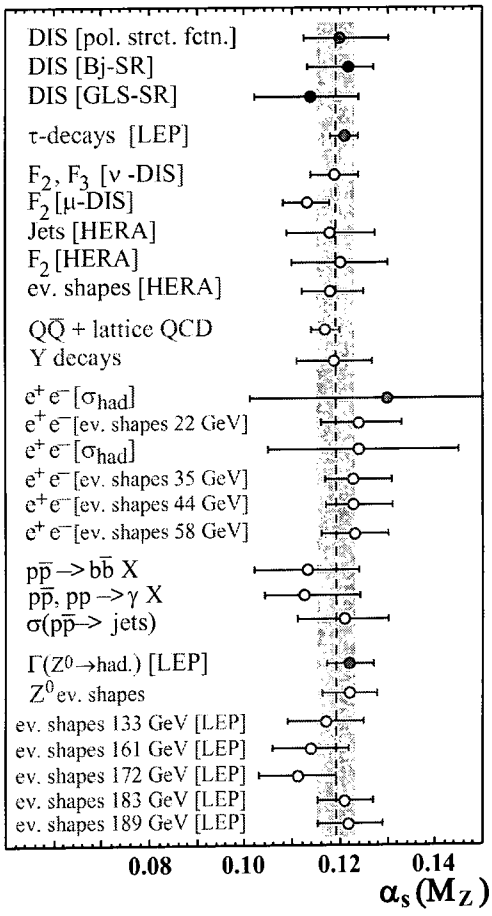


Figure 1.5: The current world average for $\alpha_s(M_Z^2) = 0.119 \pm 0.004$ in the $\overline{MS}$ scheme taken from a variety of experiments with energy ranges 1.6 GeV up to 189 GeV.[10]

compare values of $\alpha_s$ at a given scale. Physicists calculate $\alpha_s$ at the experimental energy scale of the process (this is known as the *physical scale*). This is to avoid large logarithms of the form $\log(\mu/Q)$ which occur in next to leading order and higher terms. As $\mu$ is arbitrary, we could do the calculations for $\alpha_s$ at any scale and if we included all the terms of the perturbative expansion the $\mu$ dependence would fall out. However, with our truncated series, to remove these large logarithms we choose the physical scale and later allow the coupling to run to compare $\alpha_s$ at different energies by using Equation 1.3.32. Due to the large number of experiments at LEP1 and that it lies far from any quark thresholds well within the perturbative region the most common scale at which to compare experimental values of $\alpha_s$ is taken to be $M_Z$. The results of 'running' the coupling to this scale can be seen in Figure 1.5.

Alternatively, we can introduce another dimensionless parameter into the definition of $\alpha_s(Q^2)$. This is known as $\Lambda_{QCD}$ which is defined as,

$$\ln \frac{Q^2}{\Lambda^2_{\rm QCD}} = -\int_{\alpha_s(Q^2)}^{\infty} \frac{dx}{\beta(x)}. \tag{1.3.33}$$

$\Lambda_{QCD}$ can be thought of as the scale at which the coupling becomes too large for perturbation theory. At present, its value is thought to be around 200MeV and thus QCD is thought to break down at the scale of the masses of the light hadrons. With $\Lambda_{QCD}$ we can rewrite $\alpha_s(Q^2)$ in terms of the beta function coefficients and $Q^2$, removing the dependence on the renormalization scale. For the equivalent equation to Equation 1.3.32 we get,

$$\alpha_s(Q^2) = \frac{1}{b \ln(Q^2/\Lambda^2_{\rm QCD})}. \tag{1.3.34}$$

However this technique is not favoured as $\Lambda_{QCD}$ changes as more terms are included in the perturbative expansion and it also takes different values as more quarks are introduced. Thus it is more common in the literature to convert all couplings to $\alpha_s(M_Z^2)$ and for the rest of this thesis we shall adopt this approach.

## 1.4 Theoretical uncertainty

The largest uncertainty in any theoretical prediction for physical observables comes from the uncertainty in the renormalisation scale and its relation to the inclusion of higher order terms. It is clear that to achieve the same experimental results, a truncation after the first coefficient would require a larger value of $\alpha_s(Q^2)$ than one which retained the next term (assuming that the coefficient of the second term was positive). To allow for this uncertainty in the coupling, the scale is often allowed to vary, usually between $Q/2$ and $2Q$. As each term is included in the calculation, this scale dependence cancels between terms and if all the terms are used it is obvious that the result is independent of $\mu$. This can be seen in the example of the average Thrust distribution. Thrust is a 3-jet like observables describing the

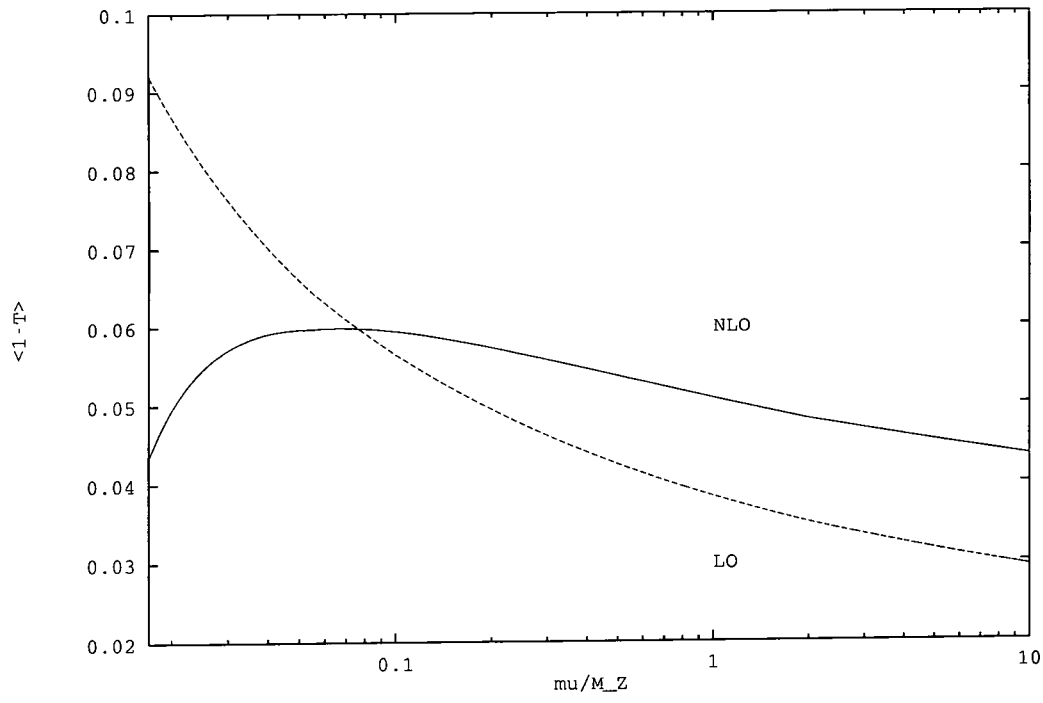


Figure 1.6: The leading order and next to leading order calculation of $< 1 - T >$ according to Equation 1.4.35 and the respective dependence on the renormalisation scale $\mu$. Not shown on this graph is that the NLO calculation becomes negative divergent as $\mu \to 0$. This is due to the additional logarithm in $\mu$ in the calculation.

spatial distribution of the event. For back to back events $T = 1$ and for completely spherical ones $T = 1/2$. Let us consider the perturbative expansion of this event shape variable [11].

$$< 1 - T >= 2.10 \left(\frac{\alpha_s(\mu^2)}{2\pi}\right) + \left(40.74 + 4.2\pi b \ln\left(\frac{\mu^2}{M_Z^2}\right)\right)\left(\frac{\alpha_s(\mu^2)}{2\pi}\right)^2 \qquad (1.4.35)$$

where 2.1 and 40.74 are the first and second coefficient of the perturbative series calculated with five active quark flavours. As with all variables the only scheme independent coefficients in the expansion are the first two. Higher order terms are not known. The dependence of $< 1 - T >$ on the renormalisation scale at each level of truncation is shown in Figure 1.6. As can be seen from the diagram the leading order calculation is highly scale dependent, being positive divergent as $\mu/Q \to 0$ and slowly tending to zero as $\mu/Q \to \infty$. This is expected as $< 1 - T >$ at leading order is simply a scaled $\alpha_s(Q^2)$ distribution. At NLO, the

presence of an additional $\log(\mu/M_Z)$ dominates at small $\mu$ and forces the distribution to 'roll over' and become negative divergent as $\mu \to 0$. However, it can be seen that there exists a relatively flat period of the distribution between $\mu/Q = 0.05$ and $\mu/Q = 10$. It is here that the calculation is fairly insensitive to the value of $\mu$ and thus theoretical calculations of $< 1 - T >$ have smaller errors than those calculated at scales (or orders) where the calculation is more dependent on the scale. Also, using the expansion of Equation 1.4.35, the value for $\alpha_s$ deduced from experiment at the physical scale will contain smaller errors.

However, the physical scale is not the only choice we can make of $\mu$ that reduces theoretical error. If we can model the rest of the perturbative series at each order by our choice of $\mu$ then we exchange our uncertainty in higher perturbative coefficients for an uncertainty in $\mu$. This is the main idea used for *The Principle of Minimal Sensitivity* proposed by Stevenson [12]. For this we assume that the value of $\mu$ that best models the rest of the perturbative series is the value at the local maximum where the dependence on it is smallest. So we differentiate $< 1 - T >$ with respect to $\log(\mu)$ using the two loop expansion for $\alpha_s(\mu)$ and set the answer to zero. At NLO (ignoring all term of order $\alpha_s^3$ and higher) we find

$$Ab' + \frac{1}{\pi}\left(B + 2\pi Ab \log\left(\frac{\mu^{PMS}}{M_Z}\right)\right) = 0 \tag{1.4.36}$$

which defines the scale $\mu_{PMS}$.

There also exists another scale choice which attempts to allow for higher order corrections. The *Fastest Apparent Convergence* method or FAC scale[13] assumes that all higher order corrections are zero. This scale is first estimated at NLO and occurs when the LO result and NLO result coincide such that the NLO contribution is zero.

As can be seen from Figure 1.6 the PMS scale and FAC scale are relatively close and it can be shown that this occurs at next-to-next-to-leading order [14] as well. In general, the scales only differ by approximately 15%. However, as we shall see later in this thesis, the physical scale and the FAC/PMS scale can be widely separated as in this example.

## 1.5 Summary

This first chapter has introduced the main ideas and motivations behind modern particle physics such as how the vast array of 'fundamental' particles can be explained by the quark model and how the proposal of a colour charge was able to prevent the violation of the Pauli exclusion principle and describe the R ratio. The justification of these theories was finally proven by the discovery of the parton in the SLAC-MIT experiments.

From this basis it is possible to build a Lagrangian of a SU(3) group that describes the quark model. It is subtly different from QED in that QCD is a non-Abelian theory and contains interactions not found in QED such as the gauge boson self-interactions. From this Lagrangian the Feynman rules are derived and it is the covariant Feynman gauge set of rules that are used throughout the rest of this thesis.

Having calculated the necessary rules, it is then possible to show that although these rules work at leading order, when loop diagrams are considered such as the quark self energy, the rules derived from the bare Lagrangian give divergent answers (ultraviolet divergences).These ultraviolet divergences introduce the concept of renormalisation

Renormalisation involves cancelling the infinite bare parameters found in the Lagrangian (such as mass and coupling constants) with the divergent loop diagrams to give finite dressed parameters. These parameters are related to the bare ones via counter terms which can be calculated using a momentum cut-off in the integral or dimensional regularization. Both prescriptions introduce an additional scale known as the renormalisation scale $\mu$ which is arbitrary and on which any truncated theory is dependent. (For an all orders result, any observable must be independent of $\mu$ as it does not appear in the QCD Lagrangian.) However, when using truncated theories, the observable does depend on the scale. This dependence can be placed into the coupling and as such introduces the idea of a running coupling constant where the coupling depends on the scale used. Couplings at different energy scales can be related using the beta function and the value of $\alpha_s(M_Z)$ can be calculated from very different experiments. The usual scale at which $\alpha_s$ is calculated before running it up to $M_Z$ is the experimental process energy and is known as the physical scale. However, there exist prescriptions which try to reproduce the entire perturbative series by the choice of scale.

The rest of this thesis will concentrate on the calculation of physical observables using the Feynman rules derived and on comparing the theoretical results to current experimental data.

# Chapter 2

# Experiments, Next-to-Leading Order and Motivation

## 2.1 Introduction

In the previous chapter we outlined the formulation of QCD, a quantum field theory that can be used to describe strong processes in terms of quarks, gluons and their interactions. This led to the description of any physical quantity (such as the cross section) in terms of a perturbative series in the coupling constant which converges for high energies (such as $M_Z$). Each term in the expansion can be represented diagramatically as a set of Feynman diagrams, all of which have indistinguishable initial and final states from each other [1] and the same power in the coupling constant, $g$.

This chapter will be primarily concerned with the background theory necessary for the calculation of higher order corrections and specifically next-to-leading order (NLO) calculations. Section 2.2 will briefly review how we can reconcile the theoretical Feynman picture with that of observed experimental jets. We shall concentrate on the techniques used for identifying resolvable jets, both at leading order and for higher orders. In section 2.3 we will consider two simple QCD processes, $e^+e^- \to 2$ jets and $q\bar{q} \to gg$ in order to demonstrate some of the techniques used for evaluating higher order corrections. These included colour algebra, colour decompostion, matrix element factorisation and dimensional regularisation.

[1] Typically, theoretical calculations of higher order corrections for a given process consist of diagrams which have more initial and/or final state partons than the leading order diagram. These extra partons are experimentally unresolvable and therefore we consider the series to consist of diagrams which have indistinguishable initial and final states at all orders in the series.

Section 2.5 will look at the motivations for performing NLO calculations in general, but specifically the NLO calculation for the process $e^+e^- \to 4$ jets.

## 2.2 Jets and higher orders

In $e^+e^-$ annihilation experiments, the measured particles seen in detectors are hadrons which form in a nonperturbative manner. But the general distribution of these hadrons is governed by the short distance creation of quark/antiquark pairs and subsequent gluon emissions. The uncertainty principle states that the fluctuation of a virtual $Z/\gamma$ into a quark/antiquark pair occurs in a space-time interval of $1/Q$ where $Q$ is the centre of mass energy of the experiment. If $Q$ is large enough then we lie in a regime where perturbation theory and the Feynman rules can be used to calculate physical quantities. Quarks and gluons will bind into hadrons in a time scale of $1/\Lambda_{QCD}$ where the coupling becomes large. Typical values of $\Lambda_{QCD}$ range from about 100 MeV to about 400 MeV and as such these effects take place long after the original partons have been produced. Therefore the final state distribution of kinematics between the hadrons is governed by the non-perturbative *hadronization* effect, but the likelihood of a given process occuring is dictated by the short distance interactions of the partons which can be calculated using perturbation theory.

In hadronization, "jets" of hadrons are created which, as a first approximation, can be associated directly with the original partons which govern the short distance dynamics of the process. If the hadrons created from a high energy quark have a limited transverse energy compared to the original quark, (*collinear fragmentation*) then the quark can be interpreted as a *jet* at leading order. For example, in the experiments performed at LEP1, $e^+e^-$ can annihilate to form quark/antiquark pairs and any number of gluons. Naively we might expect that for every parton emitted at this short distance a corresponding jet can be expected in the detector. At leading order it is true that each final state parton *can* be identified with one of the final state jets. However, if we consider the process $e^+e^- \to q\bar{q}g$ there are final state configurations that are experimentally indistingusihable from two jet final states due to the finite resolution of the detector (see Figure 2.1). In terms of the original partons these states are when the gluon either becomes too soft to form a jet that will register in the detector or when the gluon's momentum is collinear to one of the other final state partons, producing two jets that merge into a single one. The precise definition

of soft and collinear partons is dependent on the prescription of the jet-finding algorithm and as such we defer this until Section 2.3. Therefore to calculate the next to leading order contribution to $e^+e^- \to 2$ jets we are naturally led to consider graphs with more than two final state partons.

### 2.2.1 Jet-finding algorithms

The number of jets present in a final state is now complicated. Just when is a parton resolvable or not? To formalize this we introduce the idea of the *jet measure*. This is a procedure which attempts to clarify the number of jets in a final state of hadrons (or the number of resolvable quarks and gluons for theoretical calculations) and facilitate the exclusive calculation of $n$ jets in the final state. By considering some quantity formed from jet (or parton) momenta and comparing this to our jet measure we can cluster jets/partons into clearly distinguishable jets. To be useful this measure should give cross-sections which are insensitive to the presence of additional collinear and soft partons when calculating higher order corrections in perturbation theory and also be insensitive to hadronization effects. One technique suggested to make jet cross-sections calculable was one presented by Sterman and Weinberg [17]. Their prescription describes a final state as two jet-like if all but a fraction $\varepsilon$ of the total energy is present in a pair of cones of half-angle $\delta$. The two jet cross section is then obtained by integrating over the phase space region described by $\varepsilon$ and $\delta$. Consider again the example of $e^+e^- \to 2$ jets. At leading order this corresponds to the production of $\mathrm{e^+e^-} \to q\bar{q}$ and thus we should integrate over the whole of the phase space. However at $\mathcal{O}(\alpha_s)$ the process to consider is $e^+e^- \to q\bar{q}g$ and this only requires integrating over specific values of the quark and antiquark energy fractions $x_1$ and $x_2$ as defined by $\varepsilon$ and $\delta$. This is shown in Figure 2.2. The two jet region is that between the edges of the entire phase space triangle and the boundaries formed by the limits on $\varepsilon$ and $\delta$. Inside the $\varepsilon - \delta$ region we have three jet-like events. By introducing this jet measure, we also introduce logarithms into the result of the order $\alpha_s \log(\delta) \log(\varepsilon)$ and if $\delta$ is set to be small these logarithms need to be resummed to all orders in perturbation theory. However, at higher orders, the Sterman-Weinberg measure is not well-suited to calculating multijet final states.

Another technique to measure the topology of final state systems is the JADE jet finding algorithm [18]. This prescription uses a measurable quantity known as the scaled invariant

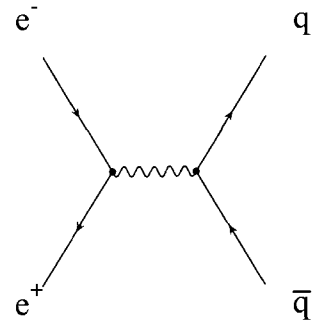


Figure a

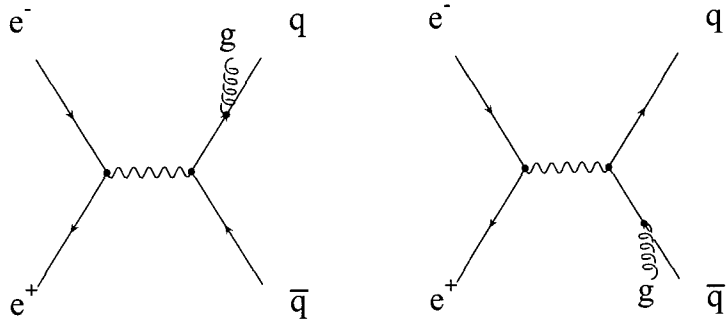


Figure b

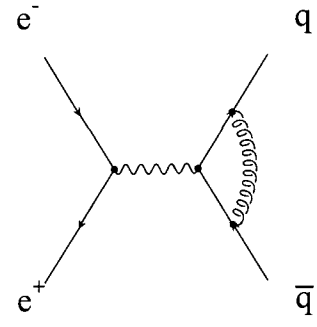


Figure c

Figure 2.1: Figure (a) shows a leading order Feynman diagram for the process $e^+e^- \rightarrow 2$ jets. Here each parton in the final state is associated with a jet in the detector. Figures (b) and (c) show next to leading order Feynman diagrams for the same process. Although there are three partons in the final state of Figure (b), the gluon is unresolvable either by being too soft to register or too collinear to the quark or antiquark thereby forming one large jet. Therefore only two jets are counted experimentally. Figure (c) shows the virtual correction that also contributes to the NLO calculation of any jet observsable.

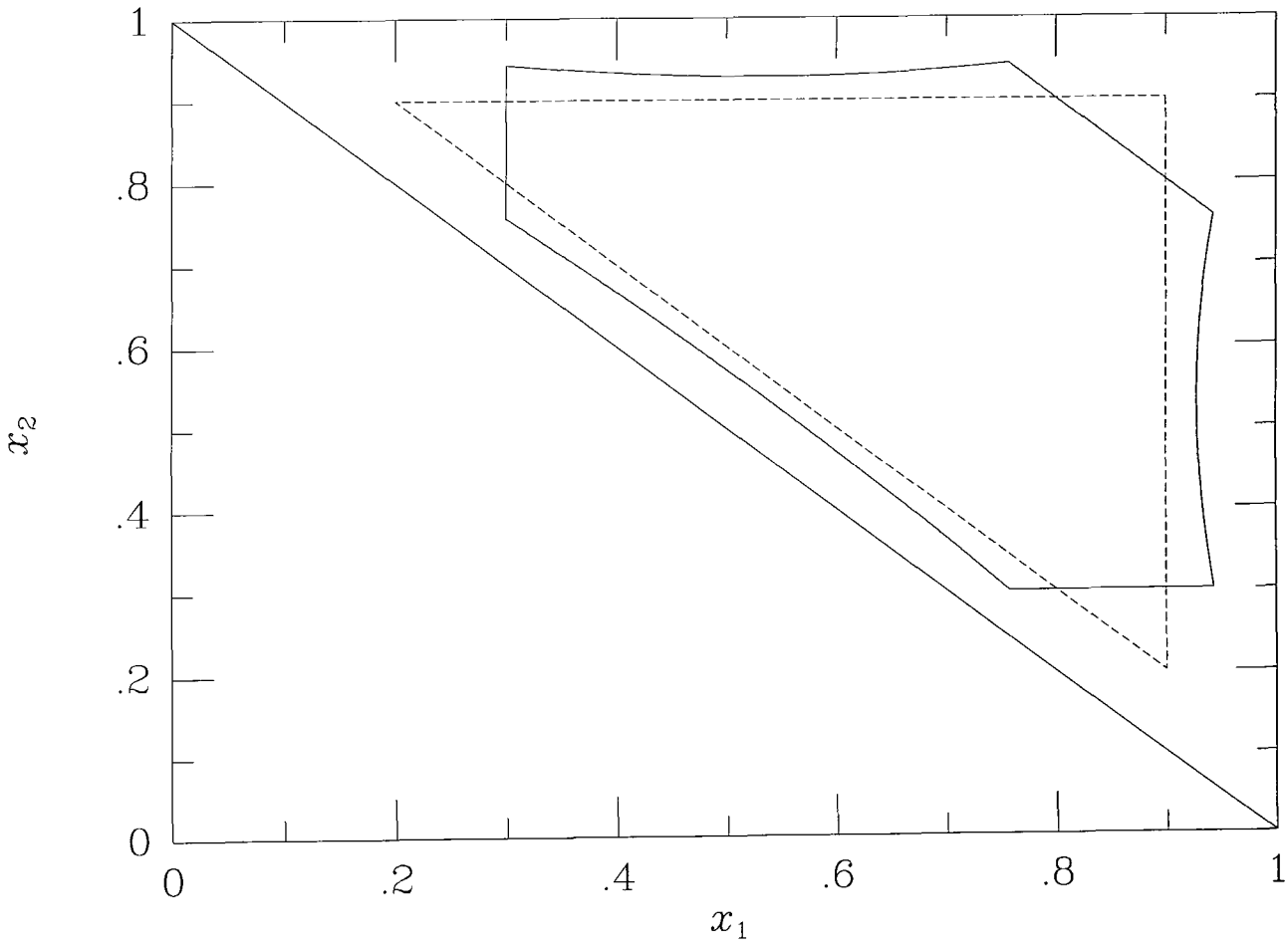


Figure 2.2: Area of phase space defined to be two jet like is bounded by the physical phase space triangle and the Sterman-Weinberg jet scaled measure (solid line) with $\varepsilon = 0.3$ and $\delta = 30°$ or the JADE scaled measure with $y_{\text{cut}}=0.1$ (dotted line)depending on the measure used. $x_1$ and $x_2$ are the energy fractions of the quark and antiquark respectfully. This diagram is taken from [20]

mass. This is defined as

$$y_{ij} = (p_i + p_j)^2/Q^2 = \frac{s_{ij}}{Q^2} \tag{2.2.1}$$

where $Q^2$ is the total energy in the final state. For the JADE algorithm the measure we use is such that

$$d_{ij} = \frac{s_{ij}}{E_{\text{vis}}^2} \tag{2.2.2}$$

where $E_{\text{vis}}$ is the total visible energy in the final state. This quantity is calculated for all possible pairs of the final state partons. For example, between the three partons $q\bar{q}g$ there are three invariant masses that need to be considered, $d_{qg}, d_{g\bar{q}}$ and $d_{q\bar{q}}$. If the minimum invariant mass is larger than the preset measure cut $y_{\text{cut}}$ then the process has as many resolvable jets as it has final state partons. Thus

$$d_{ij} = \frac{(p_i + p_j)^2}{E_{\text{vis}}^2} = \frac{2E_iE_j(1 - \cos\theta_{ij})}{E_{\text{vis}}^2} > y_{\text{cut}} \qquad i, j = q, \bar{q}, g \tag{2.2.3}$$

assuming that the final state partons are all massless. This corresponds to a boundary in the phase space which is also shown in Figure 2.2 for the process $e^+e^- \to q\bar{q}g$. Again, the region in which two of the partons are clustered together to give a 2 jet final state lies between the edge of the physical phase space triangle and the boundary as defined by the measure. The 3 jet-like region lies within the shape defined by the measure. Whereas before we generated terms of the order $\alpha_s \log(\delta) \log(\varepsilon)$ for the Sterman-Weinberg model, we now form $\alpha_s \log^2(y_{\text{cut}})$ terms. This prescription is easily extended to multijet final states. Let us assume that there are $n$ partons in the final state. Firstly, we calculate the minimum invariant mass. If this is greater than $y_{\text{cut}}$ then there are $n$ jets in the final state. If it is less than the cut then the partons are combined into a single pseudo-parton (the method used for combining the partons also has several schemes, see Section 2.2.2) and the next minimum is

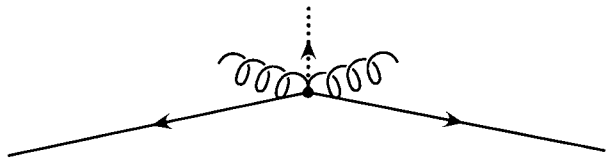

Figure 2.3: A possible configuration of the final state $q\bar{q}gg$ where the minimum invariant mass lies between the two gluons. Even though the angle between the two gluons is large, if their invariant mass is smaller than $y_{\text{cut}}$ a jet will be formed in the direction of the dotted line and the process will be identified as a three jet event, despite the original orientation of the partons towards a two jet-like event.

calculated. If this too is less than $y_{\text{cut}}$ (including all new invariants formed using the pseudo parton) then this clustering continues until the minimum invariant mass is greater than the cut. The remaining number of clusters at this point is the number of final state jets. This way, any number of jets from $n$ to 2 can be found. The above procedure is that taken for a theoretical calculation. For experimental purposes, the clustering is over the final-state hadrons. This technique is sensitive to hadronization effects for some recombination schemes [21] but at high energies these are found to be small.

The JADE algorithm, as all algorithms must, needs to have the large logarithms at small $y_{\text{cut}}$ resummed. However, for the JADE algorithm, there is no simple formula which allows this sum to be explicitly calculated [19]. Also the JADE algorithm has a tendency to produce pseudojets which are combinations of partons which have a net momentum in a direction that is not an obvious choice for a final state jet. Consider the configuration of a quark and antiquark which emit two soft gluons in Figure 2.3. When the invariant masses are calculated, the mass between the two soft gluons will be the minimum despite their large separation. If this mass is less than the cut, a cluster will be formed in the direction of the dotted line. This is obviously not the direction of a jet as it is not remotely close to the direction of any of the original partons. If all the rest of the invariant masses exceed $y_{\text{cut}}$ then a spurious jet has been created and the event is labeled three jet-like.

There have been several algorithms suggested to overcome these problems such as the DURHAM or $k_T$ algorithm [21] and the Geneva algorithm [22]. All of these are variations of the original JADE algorithm.

The Durham algorithm attempts to better model the arrangement of jets by making

use of a quantity related to the transverse momenta of the parton pair. We notice that in the example above, the relative transverse momenta of the two gluons is larger than that of the gluon with the quark. Therefore if we choose to cluster according to the minimum relative transverse momentum of the pair, the pseudo jet will not appear and a more sensible 2 jet event will be recorded. However, we cannot use the relative transverse momenta directly as for back to back events the invariant also vanishes leading to a false clusterings. Instead we make use of a related quantity that for small angles gives identical results where $\sin^2\theta \approx 2(1-\cos\theta)$. This measure is given by

$$d_{ij} = \frac{2\min(E_i^2, E_j^2)(1-\cos\theta_{ij})}{E_{\text{vis}}^2}. \tag{2.2.4}$$

The Durham jet finding algorithm has become the standard method due to three reasons. Firstly, it has smaller hadronisation corrections compared to the JADE algorithm at higher orders such as the $q\bar{q}g$ contribution to the two jet cross section. Secondly the large logarithms present at small $y_{\text{cut}}$ can be resummed in the Durham algorithm. And finally the variation of variables with respect to the renormalisation scale close to the physical scale is less than that seen using the JADE algorithm [21].

The Geneva algorithm again attempts to avoid the clustering of soft partons together and ensures that soft gluons are only grouped together if the angle between them is much smaller than those considered in the JADE algorithm. The Geneva dimensionless measure is defined to be

$$d_{ij} = \frac{8E_iE_j(1-\cos\theta_{ij})}{9(E_i+E_j)^2} \tag{2.2.5}$$

where the factor 8/9 is to ensure that the maximum value of $y_{\text{cut}}$ that reconstructs three jets from three partons is 1/3 as it is in the other two algorithms. The energy factor $E_iE_j/(E_i+E_j)^2 \approx \min(E_i,E_j)/\max(E_i,E_j)$ again favours soft partons clustering to hard ones as opposed to other soft ones. The Geneva algorithm is claimed to suffer less from perturbative corrections due to soft gluon emissions at the physical scale as compared to

the Durham algorithm which means that the variation with the renormalisation scale, $\mu$ is less for $\mu \approx Q$ [22]. Another advantage of the Geneva algorithm is that it is expected to be sensitive to the number of light flavours[23] thus making it a good algorithm to use in searches for new physics. However, the Geneva algorithm is sensitive to experimental measurement error as it depends purely on the energies of the partons involved and not on the better known total energy. It may also be more sensitive to hadronization effects as modelled by parton shower programs[22]. For more information on jet-finding algorithms the reader is referred to [24]

### 2.2.2 Recombination schemes

Having chosen a jet-finding algorithm there still remains some ambiguity over how the clustering of partons should be performed. To study this and the problems inherent with each scheme, let us consider the clustering of two partons $i, j$ to another parton $k$ such that $i + j \to k$. The simplest technique (known as the E-scheme) is to retain all the momentum and energy of each parton and sum them to form the energy and momentum of the final state parton. However, in doing this, it is assumed that all final state particles are massless and as such $p_k^2 = 0$. But we can see from summing over the two partons that $p_k^2 = (p_i + p_j)^2 = 2p_i.p_j \neq 0$. Thus we have problems combining this technique with matrix elements calculated assuming all final state particles are massless. Another technique which retains massless final state particles (the P scheme) does so by defining the energy with regards to the momentum such that $p_k = p_i + p_j$ and $E_k = |p_k|$. But now we have preserved masslessness at the cost of energy conservation. A third scheme chooses instead to violate momentum conservation and conserve energy instead (the E0 scheme) such that $E_k = E_i + E_j$ and $p_k = E_k(p_i + p_j)/|p_i + p_j|$.

## 2.3 Next-to-Leading order techniques

### 2.3.1 Introduction

In considering the details of higher order calculations it is valuable to consider two simple examples. For this reason we will review the NLO calculation of the process, $e^+e^- \to 2$ jets

and the LO calculation of the process $q\overline{q} \to gg$. Using the $e^+e^- \to 2$ jets process, we can study the different methods used for analytically cancelling divergent contributions inherent in both the virtual loop diagram and the extra, unresolved parton processes. These are known as infra red divergences and occur when the loop momenta is allowed to become zero. The $q\overline{q} \to gg$ process will be useful in demonstrating how techniques such as colour algebra, colour decomposition and matrix element factorisation can be utilised to simplify difficult QCD calculations.

### 2.3.2 KLN theorem

Infrared poles are inherent in all NLO QCD calculations and are due to integrals of the form

$$\int_0^\infty \frac{d^4k}{k^2(k-p)^2(q-k)^2} \tag{2.3.6}$$

when the limit $k \to 0$ is taken. These integrals are found in vertex loop integrals leading to divergent results. However, another source of infrared divergences can be shown to cancel the loop divergences exactly. When calculating a NLO quantity not only must loop corrections be considered, but we must also include extra unresolved partons in real emission processes such as in Section 2.2. These contributions have integrals of the form

$$\int_0^1 dy_{qg} \int_0^{1-y_{qg}} dy_{g\overline{q}} \frac{y_{qg}^2 + y_{g\overline{q}}^2 + 2y_{q\overline{q}}}{y_{qg}y_{g\overline{q}}} \tag{2.3.7}$$

where the scaled invariant, $y_{ij}$, is defined in the same way as for Equation 2.2.1. (The equation shown above is that for the process $e^+e^- \to 2$ jets.) The divergences are due to the integration over the lower bounds of $y_{qg} = 0, y_{g\overline{q}} = 0$. It can be shown that for all processes these infrared poles can be cancelled at each order for infrared safe observables such as Thrust. By infrared safe observables we mean observables that are not sensitive to soft or collinear gluon emission (which we define later) and are dominated by short distance physics i.e. perturbative physics. All the divergences created by the loop diagrams of a $n$ parton final state process are cancelled when we consider the tree level diagrams of an $n+1$

parton final state process where one or more is unresolvable. By unresolved, we mean that the scaled invariant mass of the unresolved parton with its colour-connected neighbour (see Section 2.3.7 for a definition of colour connections) is less than some cut, $y_{\min}$. Therefore, if the invariant mass of a parton and its colour-connected neighbour is less than $y_{\min}$ and the invariant mass of the parton with its other colour connected neighbour is less than $y_{\min}$ then both integrals will give large values, the matrix element will be large and the parton is said to be *soft*. If only one of the scaled invariant masses is less than $y_{\min}$ then only one integral blows up, the matrix element is still large and the pair of partons are said to be *collinear*. In both these limits we shall find that the matrix elements can be factorised. We shall study these definitions and what they mean in terms of matrix elements in Section 2.3.5 and Appendix C. That such cancellations occur at all orders was first proved for QED by Kinoshita [15] and later developed for QCD by Nauenberg and Lee [16]. Divergences are made explicit by regularising the integral. This can be done in a number of ways, but for this thesis we shall concentrate on the technique of extending the number of space-time dimensions the integral is performed under. For more details on this prescription and how the poles are made explicit see Section 2.3.4 and Appendix B. We shall study examples of this cancellation in the proceeding sections.

### 2.3.3 $e^+e^- \to 2$ jets

We begin by considering the simple NLO calculation for the process $e^+e^- \to 2$ jets. We have already seen (in general terms) that this consists of two separate contributions, the extra unresolved parton and the virtual loop (See Figure 2.1). Also we have stated that each of these contributions is separately infra-red divergent, but that the sum of the two is finite with the poles cancelling exactly according to the Kinoshita-Lee-Nauenberg (KLN) theorem. To introduce the different techniques used in making these poles explicit we consider the squared matrix element for the real emission process,

$$\left|\overline{\mathcal{M}}\right|^2_{3 \text{ partons}} = 8C_F e_q^2 g^2 \left[\frac{y_{qg}}{y_{\bar{q}g}} + \frac{y_{\bar{q}g}}{y_{qg}} + \frac{2y_{q\bar{q}}}{y_{qg}y_{\bar{q}g}}\right]. \tag{2.3.8}$$

As we have shown previously the loop contribution introduces a divergence due to integrating over the virtual loop momentum. In Equation 2.3.8 we see indications of the divergences that

will cancel the infra-red pole from the loop diagram. (The actual pole in Equation 2.3.8 is not explicit until we incorporate the phase space integration over the scaled invariant masses present in the denominator which run from 0 to a finite phase space boundary limit.) As the loop momentum from the virtual term tends to zero, the divergence is exactly cancelled by the above squared matrix element in the phase space regions in which the unresolved gluon becomes soft ($y_{qg}$ and $y_{\bar{q}g} \to 0$) or where it becomes collinear to either the quark or antiquark ($\theta_{qg}$ or $\theta_{g\bar{q}} \to 0$ which forces either $y_{qg}$ or $y_{\bar{q}g} \to 0$).

Normally the integration of the matrix elements over the allowed phase space region is too difficult to analytically perform and the only method of calculating NLO observables is to evaluate the integrals numerically. However numerical integration cannot give sensible results when we have divergent contributions. Therefore we need to find a technique which allows us to analytically isolate and cancel the separate poles. Then the resultant sum can be integrated numerically with safety.

### 2.3.4 Divergences and Dimensional regularisation - "to infinity and beyond"

To explicitly demonstrate the divergences present in NLO calculations and specifically show that the cancellations of the KLN theorem work, we need a method to isolate and regularize the infinite parts of the integrals. There are a number of prescriptions that have been suggested and we outline three of these below.

- By applying a cut-off on the loop momentum such that the integral runs between 0 and the cut-off $\Lambda$. For example, we may have an integral of the form

$$\int_0^\infty \frac{x^2 dx}{2(x+\Delta)^3} \tag{2.3.9}$$

  By applying the cut-off we regulate the pole and introduce logarithms of the cut-off into the result.

$$\int_0^\Lambda \frac{x^2 dx}{2(x+\Delta)^3} = \int_0^\Lambda \frac{dx(x+\Delta)^2 - 2\Delta(x+\Delta) + \Delta^2}{2(x+\Delta)^3} \approx \int_0^\Delta \frac{dx}{(x+\Delta)} + O\left(\frac{\Delta}{\Lambda}\right) \approx \log\left(\frac{\Lambda+\Delta}{\Delta}\right) + O\left(\frac{\Delta}{\Lambda}\right) \tag{2.3.10}$$

However, this prescription is only applicable to ultraviolet divergences and violates both Lorentz and gauge invariance.

- By introducing a large fictitious mass into the boson propagator (Pauli-Villars regularisation [30]). Therefore we make the replacement

$$\frac{1}{k^2} \to \frac{1}{k^2} - \frac{1}{k^2 - M^2} \tag{2.3.11}$$

where $M$ is the mass of the boson. When $k^2 << M^2$ we return the usual propagator and when $k^2 >> M^2$ we find terms cancel and a smooth cut-off is achieved. Thus the original integral in Equation 2.3.9 becomes

$$\int_0^\infty x^2 dx \left[\frac{1}{2(x+\Delta)^3} - \frac{1}{2(x+\Delta_M)^3}\right] = \frac{1}{2}\log\left(\frac{\Delta_M}{\Delta}\right) + O\left(\frac{1}{M^2}\right) \tag{2.3.12}$$

where $\Delta_M = \Delta + xM^2$. This regularisation technique is problematic if we consider massive QCD calculations where it violates gauge invariance

- By analytically continuing the number of space-time dimensions that the integral is calculated in to $4-2\varepsilon$ where $\varepsilon$ is small and positive to regularise ultra-violet poles and small and negative to regularise infra-red poles (Dimensional regularisation [31])

For the rest of this thesis we shall use dimensional regularisation as it preserves both Lorentz and gauge invariance. Divergences present in the integral are made explicit in terms of $1/\varepsilon$ and $1/\varepsilon^2$ poles. These poles can then be manipulated until it is clear that they cancel between diagrams. Once these poles are removed the limit $\varepsilon \to 0$ can be safely taken and the finite answer returned to the usual 4 space-time dimensions.

However, within dimensional regularisation, there are a number of schemes. These are dependent on how many dimensions particles' momenta and polarisations are taken in, both for internal and external particles. The 'tHooft-Veltman scheme retains four dimensions for external particles' momenta and polarisation. Only the internal gluon polarisations and momenta are taken in $d$ dimensions. Compare this with the conventional dimensional regularisation where all the momenta and polarisations are in $d$ dimensions. For use in supersymmetric calculations it is essential that the number of dimensions used be the same both for the polarisations of the quarks and the gluons in order to preserve the SUSY Ward identities. This scheme is referred to as dimensional reduction and uses 4 dimensions for the number of polarisations. For the rest of this thesis we shall use the conventional scheme and occasionally refer to the 'tHooft-Veltmann scheme.

$d$ dimensional integration is a non-trivial problem and as such needs to be defined. For a detailed introduction to non-integer dimensional integration the reader is referred to [32]. We begin by considering the 3 body phase space integral needed for the 2 jet NLO calculation considered above.

$$\int \frac{d^{d-1}p_q}{2E_q}\frac{d^{d-1}p_{\overline{q}}}{2E_{\overline{q}}}\frac{d^{d-1}p_g}{2E_g}\frac{\delta^d(p_\gamma - p_q - p_{\overline{q}} - p_g)}{(2\pi)^{3-2d}} \tag{2.3.13}$$

where $p_\gamma$ is the centre of mass four momentum. By redefining a $d-1$ dimensional integral in terms of a one dimensional radial integral and a $d-2$ angular integral (c.f. $d^3r = r^2 dr d\Omega_2 = r^2\sin(\theta)drd\theta d\phi$) we find

$$\frac{1}{(2)^{d+1}}\int Q^{2-d} ds_{12}ds_{13}ds_{23}d\Omega_{d-2}d\Omega_{d-3}(s_{12}s_{13}s_{23})^{\frac{d-4}{2}}\delta(s_{12}+s_{13}+s_{23}-Q^2)(2\pi)^{3-2d} \tag{2.3.14}$$

where we have subtituted the energies of each individual parton for the invariant masses between them. See Appendix C for more details.

For the 2 jet 1-loop correction we must consider an integral of the form (after Feynman parameterisation and Wick rotation. See Appendix B).

$$\int \frac{l^2 d^d l}{(l^2+\Delta)^3} = \int d\Omega_d \int \frac{l^2 (l^2)^{d-1} dl}{(l^2+\Delta)^3} \tag{2.3.15}$$

where $d\Omega_d$ is a $d$ dimensional solid angle such that

$$\int d\Omega_d = \frac{2(\pi)^{d/2}}{\Gamma(d/2)}. \tag{2.3.16}$$

Other consequences of changing the number of space-time dimensions include

- The contraction of metrics $g_{\mu\nu}g^{\mu\nu} = d$. However we keep the metric $g_{\mu\nu}$ and the gamma matrices,$\gamma^\mu$ as $4 \times 4$ matrices as well as retaining the Clifford algebra $\{\gamma^\mu, \gamma^\nu\} = 2g^{\mu\nu}$.
- The Lagrangian now must have dimension $d$ with the coupling constant redefined as $\alpha_s = g^2\mu^{-2\varepsilon}/4\pi$

### 2.3.5 Colour in QCD calculations and colour algebra

Now that we have a prescription that will isolate and cancel the divergences we can study the details for the NLO calculation of $e^+e^- \to 2$ jets. One aspect we have neglected to date is that of the colour structure of the matrix elements. In QCD, the Feynman rules describing the interaction of quarks and gluons are governed by the SU(3) colour representation. Instead of the one dimensional charges found in QED, we have a more complicated formalism. Each vertex is the source of a $3 \times 3$ colour matrix. The prescription that determines the colour structure of the final squared quantity is that of *colour algebra.* But before we can study this algebra we shall familiarise ourselves with some of the properties of the SU(3) colour group.

### 2.3.6 The colour factors of SU(3)

The colour factors of QCD are derived by considering the generator matrices of SU(3) in the adjoint representation which are defined by the commutation relations show in Equation 2.3.17. (For this section we use a different notation for colour labelling as compared to

Section1 and the Appendix A simply for aesthic reassons. The mathematical formulae are unaffected by placing the colour index in superscript or the subscript.)

$$[t^a, t^b] = if^{abc}t^c \tag{2.3.17}$$

and for which we adopt the normalisation procedure such that

$$tr[t^a t^b] = T_R \delta^{ab} \tag{2.3.18}$$

where $a, b = 1..8$ and the trace runs over the $3 \times 3$ matrices. By convention the normalisation constant $T_R$ is taken to be equal to $1/2$.

In QCD calculations we are often faced with quantities such as $(t^a t^a)_{ij}$, $f^{acd}f^{bcd}$ and $(t^a t^b t^a)_{ij}$ with implicit sums over repeated indices. Here $i, j$ represents the colour of the external quarks the gluons are attacted to. The SU(3) generators are traceless and making use of this property we can derive a very useful relation known as *Fierz' identity*. Using this, we will then be in a position to derive all possible combinations of colour structure such as the three examples above.

Consider an arbitrary $3 \times 3$ matrix $M$. It can, in general, be decomposed into two parts

$$M = \zeta_0 \mathbf{I} + \sum_a \zeta_a t^a \tag{2.3.19}$$

where $t^a$ are the SU(3) generators in the fundemental representation. By taking the trace of $M$ we can find expressions for the coefficients, $\zeta_0$ and $\zeta_a$ (recalling that the trace of a single SU(3) generator is zero).Thus, $\zeta_0$ is given by

$$\zeta_0 = \frac{tr(M)}{N} \tag{2.3.20}$$

as the unit matrix gives a trace of $N = 3$ in the fundamental representation. If we multiply $M$ by $t^b$ and take the trace we find

$$\zeta_a = 2tr(t^a M) \tag{2.3.21}$$

using Equation 2.3.18 with the usual normalisation constant. Therefore we write $M$ as

$$M = \frac{tr(M)}{N}\mathbf{I} + \sum_a 2tr(t^a M)t^a. \tag{2.3.22}$$

If we now show the indices contracted over, $M$ has the form

$$M_{ij} = \frac{M_{kk}}{N}\delta_{ij} + \sum_a 2t^a_{lk} M_{kl} t^a_{ij}. \tag{2.3.23}$$

However, as this form is true for all $M$, we can write

$$M_{kl}\left(\delta_{ik}\delta_{jl} - \frac{\delta_{kl}\delta_{ij}}{N} - \sum_a 2t^a_{lk}t^a_{ij}\right) = 0. \tag{2.3.24}$$

Therefore

$$\sum_a 2t^a_{lk}t^a_{ij} = \delta_{ik}\delta_{jl} - \frac{\delta_{kl}\delta_{ij}}{N}. \tag{2.3.25}$$

This relationship is known as the Fierz identity and diagrammatically can be thought of as the decomposition of a gluon attached between two quark lines in terms of the two separate colour lines. (See Figure 2.4)

Immediate consequences of this identity are that we can write the form of two of the colour structures mentioned earlier (see Figure 2.5).

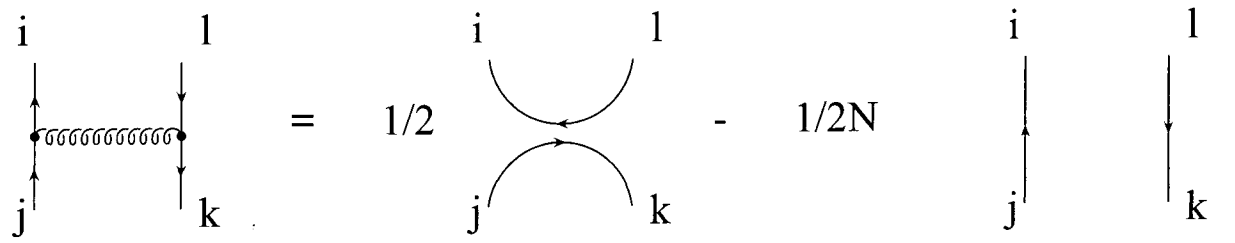


Figure 2.4: A diagramatic representation of Fierz's identity. The colour structure of a gluon line between two quark lines in terms of colour flow along the quark lines and the colour factors. If the first term on the right hand side was zero then we would have a QED like process

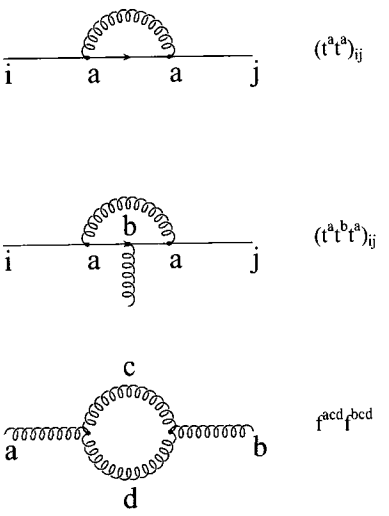


Figure 2.5: The diagramatic representations of the three colour structures used in the text as examples. Using the Fierz identity, the form of structure constants can be written in terms of the number of colours, N.

$$(t^a t^a)_{ij} = \frac{N^2-1}{2N}\delta_{ij} = C_F\delta_{ij} \ , (t^a t^b t^a)_{ij} = \frac{-1}{2N}t^b_{ij} \tag{2.3.26}$$

The final colour structure can be derived by making use of Equations 2.3.17 and 2.3.18

$$\begin{aligned} f^{acd}f^{bcd} &= -2tr([t^a,t^c][t^b,t^c]) \\ &= -2tr(2t^a t^c t^b t^c - (t^a t^b + t^b t^a)t^c t^c) \end{aligned} \tag{2.3.27}$$

Applying the first two colour structures to this we find

$$\begin{aligned} f^{acd}f^{bcd} &= -2tr(2t^a_{ji}(t^c t^b t^c)_{ij} - (t^a t^b + t^b t^a)_{ji}(t^c t^c)_{ij}) \\ &= -2tr(2t^a_{ji}\frac{-1}{2N}t^b_{ij} - (t^a t^b + t^b t^a)_{ji}\frac{N^2-1}{2N}\delta_{ij}) \\ &= -2(\frac{-1}{2N}\delta^{ab} - \frac{N^2-1}{2N}\delta^{ab}) \\ &= N\delta^{ab} \\ &= C_A\delta^{ab} \end{aligned} \tag{2.3.28}$$

The three colour structures we have considered ($(t^a t^a)_{ij}$, $(f^{acd}f^{bcd})_{ij}$ and $(t^a t^b)_{ii}$) form what are known as the quadratic Casimir operators. These Casimirs commute with all SU(3) operators and as such are fundamental quantities of the gauge group. The quadratic Casimir factors ($C_F, C_A$ and $T_R$ respectively) can be thought of as colour charges analogous to the electric charge of QED. When the diagrams shown in Figure 2.6 are present in a QCD calculation then the constants are factored into the squared matrix element as the electric charge is factored into any QED process. We now have all the elements necessary to perform leading order QCD calculations.

### 2.3.7 $q\overline{q} \to gg$

We can see how colour factors greatly simplify more difficult QCD calculations when we consider the leading order calculation of the process $q\overline{q} \to gg$. We can decompose the

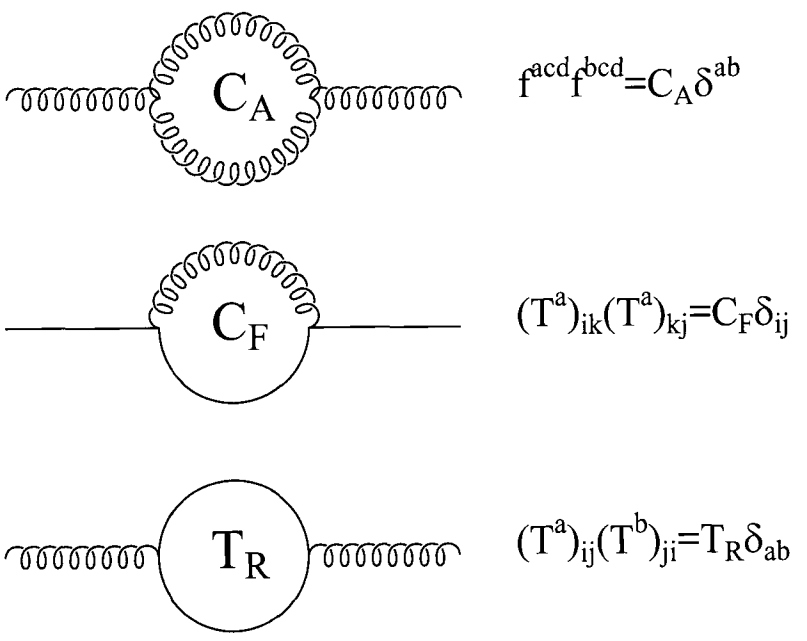


Figure 2.6: The three Casimir factors of SU(N) can be associated with colour charges that are utilized in QCD calculations. Repeated indices are summed over, $1..N^2-1$ for the gluon colour indices $a, b, c$ and over $1..N$ for the quark colour indices $i, j, k$

relevant matrix elements into colourless kinematic subamplitudes (which we shall see later have their own factorisation properties) and the colour structures we have studied above.

Unlike the related QED process $q\overline{q} \to \gamma\gamma$, there are three Feynman diagrams to consider (due to the self-coupling of gluons in QCD). These are shown in Figure 2.7. The sum of these three form the total matrix element.

$$\mathcal{M} = (t^a t^b)_{ij}\mathcal{M}_1 + (t^b t^a)_{ij}\mathcal{M}_2 + (if^{abc}t^c)_{ij}\mathcal{M}_3 \tag{2.3.29}$$

where $\mathcal{M}_i$ are the kinematical terms from each diagram. However because the three diagrams have different colour structures we will have several different colour factors multiplying each separate kinematic term when the matrix element is squared e.g. squaring the first term gives $C_F^2 N\mathcal{M}_1^2$ whereas the interference between the first and second term is $-C_F/2\mathcal{M}_1\mathcal{M}_2^\dagger$. We can simplify the number of structures by using the identity $[t^a, t^b] = if^{abc}t^c$. By applying this identity to the third term we can write it as $(t^a t^b)_{ij}\mathcal{M}_3 - (t^b t^a)_{ij}\mathcal{M}_3$ and therefore

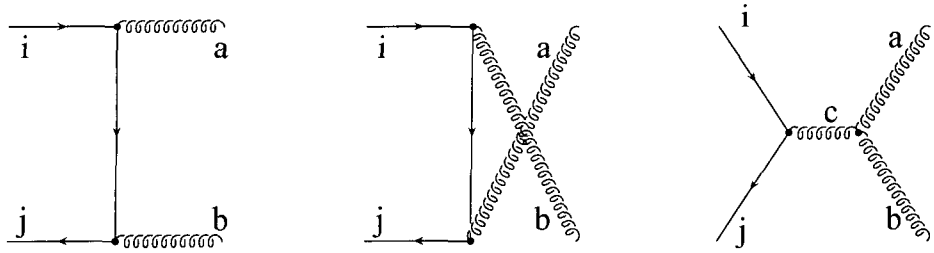


$(t^a t^b)_{ij}$ $(t^b t^a)_{ij}$ $(if^{abc}t^c)_{ij}$

Figure 2.7: The three Feynman diagrams that are needed to evaluate the leading order calculation $q\bar{q} \to gg$. Below we show the different colour structures for each amplititude. From this we can see that there are nine possible colour structures that can be formed in the squared matrix element.

$$\mathcal{M} = (t^a t^b)_{ij}(\mathcal{M}_1 + \mathcal{M}_3) + (t^b t^a)_{ij}(\mathcal{M}_2 - \mathcal{M}_3). \tag{2.3.30}$$

Now we have only two colour structures to consider. The squared terms give colour structure $tr(t^a t^b t^b t^a) = C_F^2 N$ and the interference gives $tr(t^a t^b t^a t^b)$ which, using the two identities in Equation 2.3.26, gives $-C_F/2$. Therefore

$$|\mathcal{M}|^2 = NC_F^2[|\mathcal{M}_1+\mathcal{M}_3|^2+|\mathcal{M}_2-\mathcal{M}_3|^2]-\frac{C_F}{2}[|\mathcal{M}_1+\mathcal{M}_3||\mathcal{M}_2-\mathcal{M}_3|^\dagger+|\mathcal{M}_2-\mathcal{M}_3||\mathcal{M}_1+\mathcal{M}_3|^\dagger]. \tag{2.3.31}$$

This colour structure is true even under rearrangement of the partons between the final and initial states. It is also true under addition of any colour neutral particles (such as photons). Therefore, this simple mechanism for computing the colour structure of one process has become a powerful tool which can be used to describe the colour structure of many more processes such as $qg \to qg$, $\gamma^* \to q\bar{q}gg$ and $q\bar{q} \to gg\gamma$. The only terms that change between these processes are the kinematic colourless subamplitudes. The primary function of this division into colour structure and kinematical terms is to allow the factorisation of the

colourless subamplitudes when one parton becomes unresolvable, such as is necessary for NLO calculations.

We recall from our simple example that the colourless subamplitudes actually describe the kinematic part of a specific ordered gluon emission i.e. $|\mathcal{M}_1+\mathcal{M}_3|$ describes the kinematical factor related to the emission of gluon $a$ before gluon $b$. To represent this we redefine the subamplitude to be $g^4\mathcal{S}(Q;a,b;\overline{Q})$ where $g$ is the coupling constant that we now make explicit. Similarly for the other subamplitude we write $g^4\mathcal{S}(Q;b,a;\overline{Q})$. This idea of grouping parts of diagrams into ordered gluon amplitudes is the basis behind *colour decomposition*. Firstly, after decompostion we find that the subamplitudes now display factorisation properties when a parton becomes unresolvable. Secondly, the singular terms from unresolved partons are found to be due only to soft gluons and colour connected collinear partons. Colour connected partons are those that are colour neighbours and at leading order in colour these are simply those partons next to each in the ordering e.g. for a $qg_ag_b\overline{q}$ ordered final state, the colour connected neighbours of gluon $a$ are the quark $q$ and gluon $b$ while for gluon $b$ they are gluon $a$ and the antiquark $\overline{q}$. Note that the quark and gluon $b$ are not colour connected in this ordering. By leading colour we refer to those contributions that have the largest colour factor. For example, in considering the $q\overline{q}\to gg$ case we had two colour factors. Rewriting the squared matrix element we see

$$\begin{aligned}|\mathcal{M}|^2 &= \frac{N^2C_F}{2}\left[|\mathcal{M}_1+\mathcal{M}_3|^2+|\mathcal{M}_2-\mathcal{M}_3|^2-\frac{1}{N^2}|\mathcal{M}_1+\mathcal{M}_3+\mathcal{M}_2-\mathcal{M}_3|^2\right]\\ &= \frac{N^2C_Fg^4}{2}\left[|\mathcal{S}(Q;a,b;\overline{Q})|^2+|\mathcal{S}(Q;b,a;\overline{Q})|^2-\frac{1}{N^2}|\mathcal{M}_1+\mathcal{M}_2|^2\right] \qquad (2.3.32)\end{aligned}$$

Thus the squared colour ordered subamplitudes were both leading and sub-leading in colour whereas the interference terms were only sub-leading. However this leads to the cancellation of the gluon splitting diagram in the sub-leading colour term and the result is a QED-type, ordering independent term. The gluons have become colour detacted (photon-like) from each other and thus are no longer colour connected neighbours. To represent this we write the sub-leading colour term as

$$\begin{aligned}\mathcal{M}_1 + \mathcal{M}_2 &= \mathcal{S}(Q;\tilde{a},\tilde{b};\overline{Q}) \\ &= \mathcal{S}(Q;a,b;\overline{Q}) + \mathcal{S}(Q;b,a;\overline{Q}) \end{aligned} \tag{2.3.33}$$

where the accents indicate that there is no colour ordering. We also note that for the sub-leading colour terms, the only colour connection the gluons can make is with the quark line. Thus the only singular contributions from the sub-leading colour term are soft gluons and gluons collinear to the quark or antiquark. The size of contributions from collinear partons that are not colour connected is typically of the order of the invariant mass cut $y_{\min}$ whereas the colour connected contributions (after cancellation of the poles) give terms such as $\log(y_{\min})$.

When more than two gluons are present in the process, we can have several different degrees of colour factor and related subamplitudes. Let us consider the process $e^+e^- \to q\overline{q}g_1g_2g_3$ which for the phase space region of one unresolved parton is a NLO contribution to any 4 jet calculation. The full matrix element is given by

$$\mathcal{M} = g^3 \sum_{P(123)} t^{a_1}t^{a_2}t^{a_3}\mathcal{S}_\mu(Q;1,2,3;\overline{Q})V^\mu \tag{2.3.34}$$

where $V^\mu$ is the well known lepton current. Six permutations of gluons are needed to include all the colour orderings. For the squared matrix element there exists a leading colour term in which the colour ordering of the subamplitude is maintained and all the partons are colour connected to their ordered neighbours written as $|S_\mu(Q;1,2,3;\overline{Q})V^\mu|^2$. Here it is interesting to note that the middle gluon only gives a singular contribution when it is collinear to one of the other gluons and not when it becomes collinear with the quark line. There is also a most sub leading colour term where none of the gluons are colour connected and all behave like colour neutral particles e.g. only giving a singular contribution to the calculation when they become collinear with the quark line. This is written as $|\mathcal{S}_\mu(Q;\tilde{1},\tilde{2},\tilde{3};\overline{Q})V^\mu|^2$ which is given by

$$\begin{aligned}\mathcal{S}(Q;\tilde{1},\tilde{2},\tilde{3};\overline{Q})V^{\mu} &= |\mathcal{S}_{\mu}(Q;1,2,3;\overline{Q})V^{\mu}+\mathcal{S}_{\mu}(Q;1,3,2;\overline{Q})V^{\mu}+\mathcal{S}_{\mu}(Q;2,3,1;\overline{Q})V^{\mu} \\ &+ \mathcal{S}_{\mu}(Q;2,1,3;\overline{Q})V^{\mu}+\mathcal{S}_{\mu}(Q;3,2,1;\overline{Q})V^{\mu}+\mathcal{S}_{\mu}(Q;3,1,2;\overline{Q})V^{\mu}\end{aligned} \tag{2.3.35}$$

Finally, there is another term which has a colour structure that lies between the other two. This is where two of the gluons are still colour connected and thus ordered, leaving one detacted. Here, the ordered gluons give a singular contribution when they are collinear to each other or the respective quark/antiquark (whichever is their colour connected neighbour) but not with the colour detacted gluon which only contributes as in the most sub leading term. This term is written as $|\mathcal{S}_{\mu}(Q;1,2,\tilde{3};\overline{Q})V^{\mu}|^2$ with the ordering permutated. This is given by

$$\mathcal{S}_{\mu}(Q;1,2,\tilde{3};\overline{Q})V^{\mu}=\mathcal{S}_{\mu}(Q;1,2,3;\overline{Q})V^{\mu}+\mathcal{S}_{\mu}(Q;1,3,2;\overline{Q})V^{\mu}+\mathcal{S}_{\mu}(Q;3,1,2;\overline{Q})V^{\mu} \tag{2.3.36}$$

Therefore the total squared matrix element is given by

$$\begin{aligned}|\mathcal{M}|^2 &= \frac{N^3C_F}{4}\left[\left(\sum_{P(123)}|\mathcal{S}_{\mu}(Q;1,2,3;\overline{Q})V^{\mu}|^2-\frac{1}{N^2}|\mathcal{S}_{\mu}(Q;1,2,\tilde{3};\overline{Q})V^{\mu}|^2\right)\right. \\ &+ \left.\frac{N^2+1}{N^4}|\mathcal{S}_{\mu}(Q;\tilde{1},\tilde{2},\tilde{3};\overline{Q})V^{\mu}|^2\right]\end{aligned} \tag{2.3.37}$$

From these two examples we see the form that all QCD final states of the form $q\overline{q}+ng$ take at leading order in colour. We write

$$|\mathcal{M}|^2=\left(\frac{g^2N}{2}\right)^n\frac{N^2-1}{N}\sum_{P(1,2...n)}|\mathcal{S}(Q;1,2,..,n;\overline{Q})|^2 \tag{2.3.38}$$

For a rigourous derivation of this formula the reader is refered to [34] which derives this equation from the gluon recursion relation.

We also colour decompose diagrams which have two quark lines such as final states like $q\bar{q}Q\overline{Q}$ (where $q$ and $Q$ may or may not of the same flavour). The matrix element of the process $e^+e^- \to q\bar{q}Q\overline{Q}$ is given by

$$\begin{aligned}\mathcal{M} &= i\frac{eg^2}{2}\left[\delta_{c_1\,c_4}\delta_{c_3\,c_2}\left(\mathcal{A}_\mu(Q_1;\overline{Q_2})V^\mu + \mathcal{A}_\mu(Q_3;\overline{Q_4})V^\mu + \frac{\delta_{qQ}}{N}\left(\mathcal{A}_\mu(Q_1;\overline{Q_4})V^\mu + \mathcal{A}_\mu(Q_3;\overline{Q_2})V^\mu\right)\right)\right. \\ &- \left.\delta_{c_1\,c_2}\delta_{c_3\,c_4}\left(\frac{1}{N}\left(\mathcal{A}_\mu(Q_1,\overline{Q_2})V^\mu + \mathcal{A}_\mu(Q_3,\overline{Q_4})V^\mu\right) + \delta_{qQ}\left(\mathcal{A}_\mu(Q_1,\overline{Q_4})\,V^\mu + \mathcal{A}_\mu(Q_3,\overline{Q_2})V^\mu\right)\right)\right.\end{aligned} \tag{2.3.39}$$

The subamplitude $\mathcal{A}$ has two possible directions of colour flow, which we represent with the delta functions of the quark colour indices e.g. $\delta_{c_1\,c_4}\delta_{c_3\,c_2}$ indicates that quark 1 and antiquark 4 are colour connected. There also exists the supressed configuration where quark 1 and antiquark 2 are colour connected. The arguments of the functions indicate which quark line the colour neutral $Z/\gamma^\star$ attacts to. With crossing symmetry we include all the other diagrams for both like and unlike pairs of quarks.

Using the same rules as before we find the squared matrix element of the above four quark final state (produced by a colour neutral particle such as a virtual photon) is given by

$$\begin{aligned}|\mathcal{M}|^2 &= e^2\left(\frac{g^2N}{2}\right)^2\left(\frac{N^2-1}{N^2}\right)\left[|\mathcal{T}_\mu(Q_1,\overline{Q_2};Q_1,\overline{Q_2})V^\mu|^2 + |\mathcal{T}_\mu(Q_1,\overline{Q_2};Q_3,\overline{Q_4})V^\mu|^2\right. \\ &+ \frac{\delta_{qQ}}{N}(|\mathcal{T}_\mu(Q_1,\overline{Q_2};Q_1,\overline{Q_4})V^\mu|^2 + |\mathcal{T}_\mu(Q_1,\overline{Q_2};Q_3,\overline{Q_2})V^\mu|^2) \\ &+ \left.(Q_1 \leftrightarrow Q_3,\overline{Q_2} \leftrightarrow \overline{Q_4}) + \delta_{qQ}(Q_1 \leftrightarrow Q_3) + \delta_{qQ}(\overline{Q_2} \leftrightarrow \overline{Q_4})\right]\end{aligned} \tag{2.3.40}$$

where we define the $\mathcal{T}$ functions as

$$|\mathcal{T}_\mu(i,j;k,l)V^\mu|^2 = |(\mathcal{A}_\mu(i,j)V^\mu)^\dagger\mathcal{A}_\mu(k,l)V^\mu| \tag{2.3.41}$$

This corresponds to $|\mathcal{T}(Q_1, \overline{Q_2}; Q_1, \overline{Q_2})|^2$ being the squared subamplitude where quark 1 and antiquark 2 are attacted to the virtual photon (this attactment defines the initial quark line) and $|\mathcal{T}(Q_1, \overline{Q_2}; Q_3, \overline{Q_4})|^2$ being the interference between quark 1 and antiquark 2 forming the initial quark line and quark 3 and antiquark 4 coupling to the virtual photon in the conjugate. See Figure 2.8. Again, for a detailed derivation of this formula the reader is referred to [33]

### 2.3.8 Matrix element and Subamplitude factorisation

In this section we shall consider the singular behaviour of the squared matrix elements for the NLO calculation of the process $e^+e^- \to n+2$ jets considering both extra unresolved partonic final states $q\overline{q}+(n+1)g$ and $q\overline{q}Q\overline{Q}+(n-1)g$. For the moment we shall only consider terms leading in colour as this will simplify the calculation. This can be done utilizing the Fierz identity we derived earlier. The calculation is easily extended to include sub-leading colour terms [33] and we will use results from this reference for the full NLO 4 jet calculation later.

The factorisation of the matrix element when one of the final state partons is soft is very similar to that of QED and the eikonal factors seen there [37]. This eikonal factor multiplies the remaining hard process when an external photon becomes soft (see Figure 2.9). If we consider a single photon final state QED process in which the photon is soft (momentum $K$ and polarisation vector $\epsilon$) coupled to a quark/antiquark fermion line (with momentum $Q$ and $P$ respectively), the matrix element factorises such that

$$\mathcal{M}(Q;K;P) \to e_q \;\; e(Q;K;P)\mathcal{M}(Q;P) \tag{2.3.42}$$

where

$$e(Q;K;P) = \epsilon^\mu \left( \frac{Q_\mu}{Q\cdot K} - \frac{P_\mu}{K\cdot P} \right) \tag{2.3.43}$$

In QCD, as the gluons carry colour, the usual matrix element cannot be factorised in this manner for soft gluons. However, with the colour decomposition shown earlier, the soft

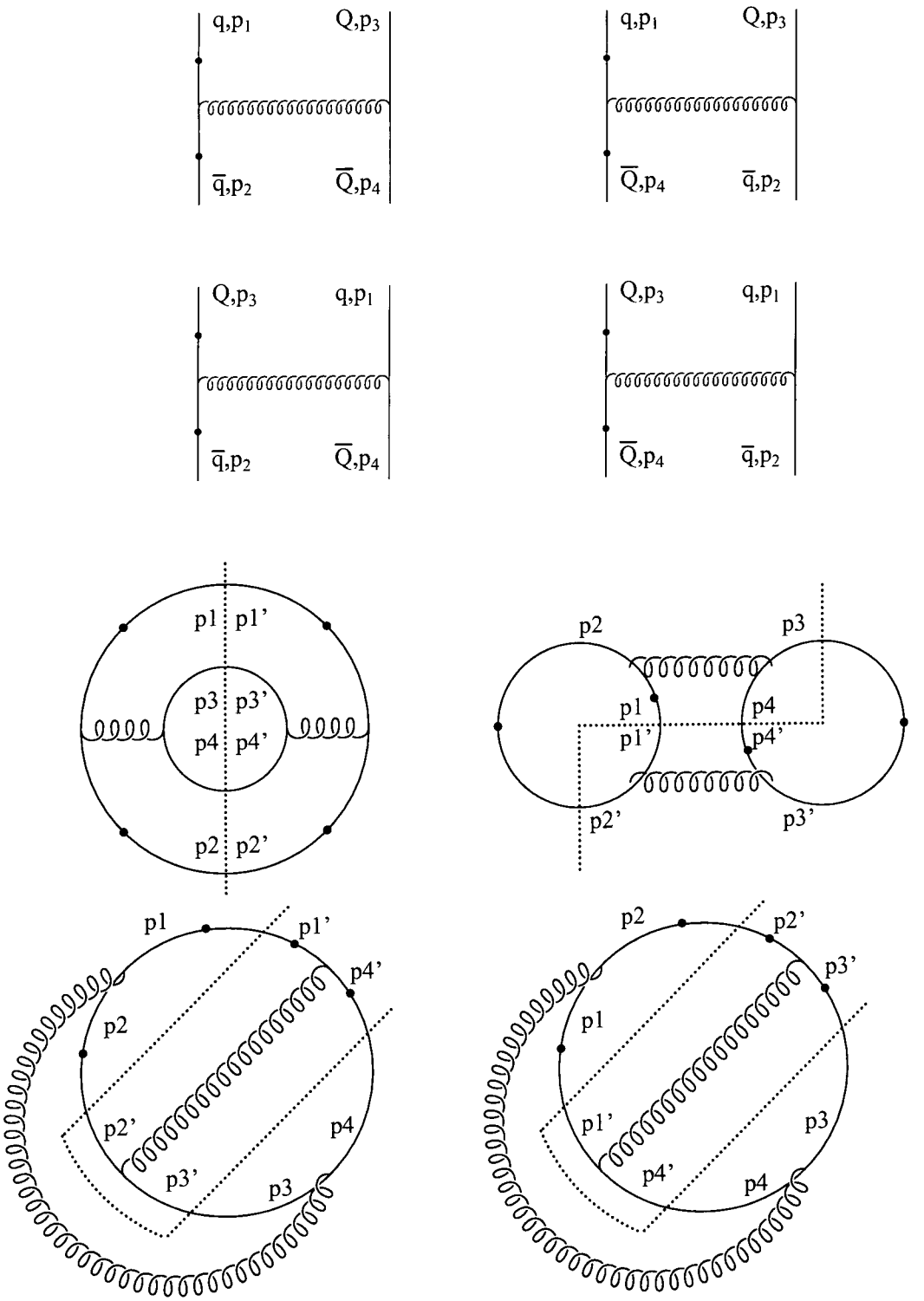


Figure 2.8: The Feynman diagrams for the process $\gamma^* \to q\bar{q}Q\overline{Q}$. The solid circle indicates the location of the $Z/\gamma^*$ vertex. Below these are diagrams to indicate the colour structure of the squared matrix elements. The dotted line indicates the boundary between the matrix element and the conjugate. Thus we have at leading order in colour $|\mathcal{T}_\mu(Q_1, \overline{Q_2}; Q_1, \overline{Q_2})V^\mu|^2, |\mathcal{T}_\mu(Q_1, \overline{Q_2}; Q_3, \overline{Q_4})V^\mu|^2$ and subleading we have $|\mathcal{T}_\mu(Q_1, \overline{Q_2}; Q_1, \overline{Q_4})V^\mu|^2, |\mathcal{T}_\mu(Q_1, \overline{Q_2}; Q_3, \overline{Q_2})V^\mu|^2$ respectively

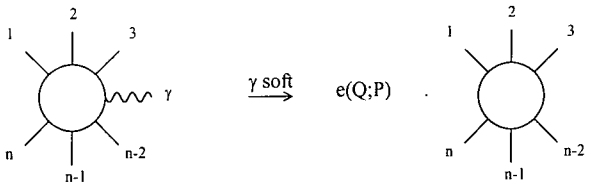


Figure 2.9: The eikonal factor multiplying the remaining hard process in the presence of a soft photon. This QED process is exactly analogous to the colour ordered QCD process present in all NLO calculations.

factorisation of the colourless subamplitudes is now possible [35]. This is due to the ordering of the partons which form well-defined lines of colour which the gluon can couple to. Thus we can retrieve an eikonal factor from the soft gluon factorisation of the colour ordered subamplitudes. It is precisely these eikonal factors that contain the divergent terms that will cancel the $1/\varepsilon^2$ poles coming from the virtual 1-loop correction (see Appendix B). The eikonal factor is only dependent on the momentum of its colour ordered neighbours, regardless of their identity. Examining the form of the eikonal factor for our $e^+e^- \to q\bar{q} + (n+1)g$ process letting gluon $s$ be our soft unresolved parton, we find,

$$\begin{aligned}
\mathcal{S}_\mu(Q_1;1,...,n,s;\overline{Q_2})V^\mu &\to g\,e(n;s;\overline{Q_2})\mathcal{S}_\mu(Q_1;1,...,n;\overline{Q_2})V^\mu \\
\mathcal{S}_\mu(Q_1;1,..,m,s,m+1,..,n;\overline{Q_2})V^\mu &\to g\,e(m;s;m+1)\mathcal{S}_\mu(Q_1;1,...,n;\overline{Q_2})V^\mu \\
\mathcal{S}_\mu(Q_1;s,1,..,n;\overline{Q_2})V^\mu &\to g\,e(Q_1;s;1)\mathcal{S}_\mu(Q_1;1,...,n;\overline{Q_2})V^\mu \qquad (2.3.44)
\end{aligned}$$

where $V^\mu$ describes the lepton current and is well defined. This, when extended to squared matrix elements, becomes

$$\left|\widehat{\mathcal{S}_\mu}V^\mu\right|^2 \to e^2\left(\frac{g^2N}{2}\right)^n\left(\frac{N^2-1}{N}\right)\sum_{P(1,...,n)}\left[s_F(Q_1;1,...,n;\overline{Q_2})|\mathcal{S}_\mu(Q_1;1,...,n;\overline{Q_2})V^\mu|^2\right] \qquad (2.3.45)$$

where $\left|\widehat{\mathcal{S}_\mu}V^\mu\right|^2$ is the full squared matrix element. We find

$$s_F(Q_1;1,...,n:\overline{Q_2}) = \left(\frac{g^2N}{2}\right)[f_{Q_11}(s) + f_{12}(s) + ... + f_{n\overline{Q_2}}(s)] \tag{2.3.46}$$

which is related to the eikonal factors such that

$$f_{ab}(s) = |e(a;s;b)|^2 = \frac{4s_{ab}}{s_{as}s_{sb}} \tag{2.3.47}$$

Therefore the full squared matrix element has been decomposed into a sum of squared colour ordered subamplitudes multiplied by similarly ordered divergent eikonal factors which are dependent on the permutation of the gluons.

For the process $e^+e^- \to q\overline{q}Q\overline{Q} + (n-1)g$ with one soft gluon at leading order in colour we find a similar decomposition which follows the same pattern as for the $n+1$ gluon final state.

$$\begin{aligned}\left|\widehat{\mathcal{T}_\mu}V^\mu\right|^2 \;\to\; & e^2\left(\frac{g^2N}{2}\right)^n\left(\frac{N^2-1}{N^2}\right)\sum_{P(1,...,n-2)}\sum_{i=0}^{n-2}\Big[\, s_F(Q_1;1,...,i;\overline{Q_4}|Q_3,i+1,...,n-2;\overline{Q_2}) \\ \times\; & \left(|\mathcal{T}^i_\mu(Q_1,\overline{Q_2};Q_1,\overline{Q_2};1,...,n-2)V^\mu|^2 + |\mathcal{T}^i_\mu(Q_1,\overline{Q_2};Q_3,\overline{Q_4};1,...,n-2)V^\mu|^2\right) \\ +\; & (Q_1 \leftrightarrow Q_3, \overline{Q_2} \leftrightarrow \overline{Q_4}) + \delta_{qQ}(\overline{Q_2} \leftrightarrow \overline{Q_4}) + \delta_{qQ}(Q_1 \leftrightarrow Q_3)\Big]\end{aligned} \tag{2.3.48}$$

where $\left|\widehat{\mathcal{T}_\mu}V^\mu\right|^2$ represents the full squared matrix element and $|\mathcal{T}^i_\mu(Q_1,\overline{Q_2};Q_3,\overline{Q_4};1,...,n-2)V^\mu|^2$ corresponds to the colourless subamplitudes we saw in Equation 2.3.41 except here there are $i$ gluons attacted to the initial quark line and the rest are attacted to the other quark line. This is summed over to include all possible diagrams. The soft factor is given by

$$\begin{aligned}&s_F(Q_1;1,...,i;\overline{Q_4}|Q_3;i+1,...,n-2;\overline{Q_2}) = \\ &\left(\frac{g^2N}{2}\right)\left[f_{Q_11}(s) + f_{12}(s) + ... + f_{i\overline{Q_4}}(s) + f_{Q_3i+1}(s) + ... + f_{n-2\overline{Q_2}}(s)\right]\end{aligned} \tag{2.3.49}$$

Therefore, as we found for the $n+1$ gluon final state, the four quark soft gluon limit becomes the sum of the tree level process multiplied by a divergent factor that depends on the ordered emission of gluons along the quark lines.

Now we have shown that using colour decomposition it is possible to factorise soft matrix elements, we consider final state collinear partons. As we saw earlier, these divergent terms come from the integral over the matrix element when one of the invariant masses between two colour-connected neighbours tends to zero. If both masses tend to zero the parton is said to be soft, but if one is greater than the invariant cut, it is the angle between the other two that tends to zero, thus making the partons unresolvable. Let the sum of the partons momenta form the four momenta of a new parton. Thus,

$$P_a + P_b = P_c. \tag{2.3.50}$$

There are several methods of dividing the momenta of the new parton between the old ones. For the moment we shall consider one based on the Altarelli-Parisi splitting functions [38] which simply split the momenta thus.

$$P_a = zP_c, \quad P_b = (1-z)P_c \tag{2.3.51}$$

This method however does have a problem. If we are working with matrix elements that assume all final state partons are massless, this implies that $(P_a+P_b)^2 = P_c^2 = 0$ for all areas where we are applying this division of momentum. But $(P_a + P_b)^2 = 2P_a.P_b$ which is only equal to zero on the divergent edge of phase space. We are applying this combination in regions of phase space where $s_{ab} < s_{\min}$ and so throughout this region (except on the divergent edge) we are using contradictory ideas of the mass of $P_c$. Other methods of dividing the momentum have been considered and will be studied in greater depth in following chapters. But for the moment we will use this technique to show how the matrix elements factorise when two partons become collinear.

Unlike the soft gluon case, the entire squared matrix element does factorise in the case of a collinear pair of partons. The divergent factor relating the sqaured matrix element of

$n+1$ partons to the squared matrix element of $n$ partons does depend on the identity of the partons becoming collinear and so,

$$|\mathcal{M}(...,a,b,...)|^2 = c_F^{ab\to c}|\mathcal{M}(...,c,...)|^2 \tag{2.3.52}$$

where

$$\begin{aligned} c_F^{gg\to g} &= \left(\frac{g^2N}{2}\right)\frac{P_{gg\to g}(z)}{s_{gg}} \\ c_F^{qg\to q} &= \left(\frac{g^2N}{2}\right)\left(1-\frac{1}{N^2}\right)\frac{P_{qg\to q}(z)}{s_{qg}} \\ c_F^{q\bar{q}\to g} &= \left(\frac{g^2n_f}{2}\right)\frac{P_{q\bar{q}\to g}(z)}{s_{q\bar{q}}} \end{aligned} \tag{2.3.53}$$

and where the $P_{ab\to c}$ are the Altarelli-Parisi splitting functions given by

$$\begin{aligned} P_{gg\to g}(z) &= 2\left(\frac{1+z^4+(1-z)^4}{z(1-z)}\right) \\ P_{qg\to q}(z) &= 2\left(\frac{1+z^2-\varepsilon(1-z)^2}{1-z}\right) \\ P_{q\bar{q}\to g} &= 2\left(\frac{z^2+(1-z)^2-\varepsilon}{1-\varepsilon}\right) \end{aligned} \tag{2.3.54}$$

These splitting functions are symmetric in $z$ and $(1-z)$ such that $z \leftrightarrow (1-z)$ implies $P_{qg\to q} \leftrightarrow P_{gq\to q}$ and they are also symmetric under charge conjugation. However, depending on whether the final state combined parton is treated in 4 or $d$ dimensions, a different scheme can be used. The splitting functions in Equation 2.3.54 are defined in the conventional dimensional regularisation scheme where the combined parton is calculated in $d$ dimensions. The 't Hooft-Veltman[39] scheme uses 4 dimensions instead and differs in terms proportional to $\varepsilon$ which will then give different finite terms between schemes.

It should be noted that singular terms only come from collinear colour-connected partons. If the partons are not joined by a colour line, then the result is a term proportional to the

invariant cut. The singular term from two gluons becoming collinear and forming another gluon for the process $e^+e^- \to q\overline{q} + (n+1)g$ is given by

$$|\widehat{\mathcal{S}_\mu}(Q_1;1,...,m-1,g_1,g_2,m+1,...,n;\overline{Q_2})V^\mu|^2 \to \left(\frac{g^2N}{2}\right)\frac{P_{gg\to g}(z)}{s_{g_1g_2}}|\mathcal{S}_\mu(Q_1;1,...,m-1,g_3,m+1,...,n;\overline{Q_2})V^\mu|^2 \tag{2.3.55}$$

and the factorisation when a gluon becomes collinear with either a quark or an antiquark is

$$\begin{aligned}|\widehat{\mathcal{S}_\mu}(q;g,1,...,n;\overline{Q_2})V^\mu|^2 &\to \left(\frac{g^2N}{2}\right)\left(1-\frac{1}{N^2}\right)\frac{P_{qg\to Q_1}(z)}{s_{qg}}|\mathcal{S}_\mu(Q_1;1,...,n;\overline{Q_2})V^\mu|^2 \\ |\widehat{\mathcal{S}_\mu}(Q_1;1,...n,g;\overline{q})V^\mu|^2 &\to \left(\frac{g^2N}{2}\right)\left(1-\frac{1}{N^2}\right)\frac{P_{g\overline{q}\to\overline{Q_2}}(z)}{s_{g\overline{q}}}|\mathcal{S}_\mu(Q_1;1,...,n;\overline{Q_2})V^\mu|^2\end{aligned} \tag{2.3.56}$$

The only time a quark and antiquark can become collinear in the final state is when they have been created from the decay of gluon which was emitted from another quark line. Thus the four quark contribution also contributes in a unique way to the cancellation of the 1-loop correction. The singular terms from this process when $Q_3$ and $\overline{Q_4}$ are collinear are

$$\begin{aligned}|\widehat{\mathcal{T}_\mu}(Q_1,\overline{Q_2};Q_3,\overline{Q_4})V^\mu|^2 &\to \left(\frac{g^2n_f}{2}\right)\frac{P_{q\overline{q}\to g}(z)}{s_{Q_3\overline{Q_4}}}|\mathcal{S}_\mu(Q_1;g;\overline{Q_2})V^\mu|^2 \\ |\widehat{\mathcal{T}_\mu}(Q_1,\overline{Q_4};Q_3,\overline{Q_2})V^\mu|^2 &\to 0\end{aligned} \tag{2.3.57}$$

where we have a factor $n_f$ for the number of quarks flavours that could be produced. Therefore the four quark squared matrix element factorises to a divergent term multiplied by the two quark matrix element squared, but with one less power of $N$. So the quark/antiquark collinear configuration of the four quark squared matrix element factorises to a sub-leading colour contribution of the two quark final state. Thus for the process $e^+e^- \to q\overline{q}Q\overline{Q}+(n-1)g$ we have

$$|\widehat{\mathcal{T}}_\mu V^\mu|^2 \to e^2 \left(\frac{g^2 N}{2}\right)^n \left(\frac{N^2-1}{N}\right) \sum_{P(1,\ldots,n)} \left[\left(\frac{g^2 n_f}{2}\right) \frac{P_{q\bar{q}}(z)}{s_{Q_3\overline{Q_4}}} |\mathcal{S}_\mu(Q_1;1,\ldots,n;\overline{Q_2})V^\mu|^2 + O\left(\frac{1}{N}\right)\right] \tag{2.3.58}$$

giving a final form for the full squared matrix element of the two quark final state where two partons become collinear

$$|\widehat{\mathcal{S}}_\mu V^\mu|^2 + |\widehat{\mathcal{T}}_\mu V^\mu|^2 \to e^2 \left(\frac{g^2 N}{2}\right)^n \left(\frac{N^2-1}{N}\right) \sum_{P(1,\ldots,n)} [c_F(Q_1;1,\ldots,n;\overline{Q_2}) |\mathcal{S}_\mu(Q_1;1,\ldots,n;\overline{Q_2})V^\mu|^2] \tag{2.3.59}$$

where

$$c_F(Q_1;1,\ldots,n;\overline{Q_2}) = \left(\frac{g^2 N}{2}\right) \left[\frac{P_{qg\to q}(z)}{s_{qg_1}} + \frac{P_{gg\to g}(z)}{s_{g_1g_2}} + .. + \frac{P_{g\bar{q}\to\bar{q}}(z)}{s_{g_n\bar{q}}} + \frac{n_f n}{N}\frac{P_{q\bar{q}\to g}(z)}{s_{q\bar{q}}}\right]. \tag{2.3.60}$$

We have a similar structure to that of the soft parton where ordered divergent factors are multiplied to the colourless subamplitudes and the result is summed over the permutation of the gluons to include all graphs. The four quark structure is also of the same form as its soft counterpart. Its factorisation for the process $e^+e^- \to q\bar{q}Q\overline{Q} + (n-1)g$ is given by

$$\begin{aligned} |\widehat{\mathcal{T}}_\mu V^\mu|^2 \;\to\; & e^2 \left(\frac{g^2 N}{2}\right)^n \left(\frac{N^2-1}{N^2}\right) \sum_{P(1,\ldots,n-2)} \sum_{i=0}^{n-2} \Big[ c_F(Q_1;1,\ldots,i;\overline{Q_4}|Q_3;i+1,\ldots,n-2;\overline{Q_2}) \\ & \times \; |\mathcal{T}^i_\mu(Q_1,\overline{Q_2};Q_1,\overline{Q_2};1,\ldots,n-2)V^\mu|^2 + |\mathcal{T}^i_\mu(Q_1,\overline{Q_2};Q_3,\overline{Q_4};1,\ldots,n-2)V^\mu|^2 \Big] \\ & + \; (Q_1 \leftrightarrow Q_3, \overline{Q_2} \leftrightarrow \overline{Q_4}) + \delta_{qQ}(Q_1 \leftrightarrow Q_3) + \delta_{qQ}(\overline{Q_2} \leftrightarrow \overline{Q_4}) \end{aligned} \tag{2.3.61}$$

where we define the $c_F$ function to be

$$c_F(Q_1;1,\ldots,i;\overline{Q_4}|Q_3;i+1,\ldots,n-2;\overline{Q_2}) = \frac{g^2 N}{2}\left[\frac{P_{qg\to q}(z)}{s_{q_1g_1}} + \frac{P_{gg\to g}(z)}{s_{g_1g_2}} + \ldots + \frac{P_{g\bar{q}}(z)}{s_{g_{n-1}\overline{q_4}}}\right] \tag{2.3.62}$$

Recall that these terms are only those at leading order in colour.

## 2.4 Phase space

Now we have factorised the squared matrix elements in their singular limits, we wish to repeat the procedure with phase space. With a factorised phase space, we can write the divergent $n+1$ partonic physical quantity, $\sigma_{n+1}$, as the finite $\sigma_n$ multiplied by a divergent factor such that for the soft limit

$$\begin{aligned} d\sigma_{n+1} &= |\mathcal{M}_{n+1}|^2 d^d P_{n+1} \\ &\to |\mathcal{M}_n|^2 d^d P_n \int ds_{au} ds_{bu} F(s_{au}^{-1-\varepsilon}, s_{ub}^{-1-\varepsilon}) \\ &\to d\sigma_n \int ds_{au} ds_{bu} F(s_{au}^{-1-\varepsilon}, s_{ub}^{-1-\varepsilon}) \end{aligned} \tag{2.4.63}$$

where $F(s_{au}^{-1-\varepsilon}, s_{ub}^{-1-\varepsilon})$ is the divergent term from the matrix element factorisation and the integral is due to the extra phase space necessary to integrate over.

There are several techniques for performing this factorisation. We shall briefly review the technique employed by [36] and see that this prescription needs to be improved. Another technique we shall consider in the next chapter is the Seymour and Catani dipole formalism. Also in the next chapter we shall present a new procedure for the phase space factorisation of NLO QCD calculations which tackles the problems of massless partons and phase space approximations in a wholly symmetric and universal manner.

One way of performing this factorisation is to approximate the phase space factor using the same limits as we did for the matrix elements e.g. neglecting all terms in the phase space factor not singular when the soft/collinear limits are taken. This was the technique used by [36]. For example, consider 3 final state partons with momentum $P_i$ and energy $E_i$ all derived from the decay of a colourless neutral boson with centre of mass energy equal to $Q$. Then the phase space factor derived from the final state kinematics of the system is given by

$$
\begin{aligned}
dP^d(Q;P_1,P_2,P_3) &= \left[\prod_{i=1}^{3}\frac{d^{d-1}P_i}{(2\pi)^{d-1}2E_i}\right](2\pi)^d\delta^d(Q-P_1-P_2-P_3) \\
&= (2\pi)^{3-2d}\frac{\pi^{\frac{d-2}{2}}}{2\Gamma(\frac{d-2}{2})}(Q^2)^{\frac{2-d}{2}}[s_{12}s_{13}s_{23}]^{\frac{d-4}{2}}\frac{d\Omega_{d-1}}{2^{d-1}}ds_{12}ds_{13}ds_{23}\times \\
&\quad \delta(s_{12}+s_{13}+s_{23}-Q^2) \qquad (2.4.64)
\end{aligned}
$$

where we have changed the measures to be over final state invariant masses and a solid angle and have averaged over the azimuthal angle.

Let us assume that parton 3 becomes soft. Then $s_{13} < s_{\min}$ and $s_{23} < s_{\min}$. Therefore we assume all terms with $s_{13}$ and $s_{23}$ in the numerator are negligible and ignore them. This gives

$$
\begin{aligned}
d^dP(Q;P_1,P_2,P_3) &\to (2\pi)^{3-2d}\frac{\pi^{\frac{d-2}{2}}}{2\Gamma(\frac{d-2}{2})}s_{12}^{\frac{2-d}{2}}ds_{13}ds_{23}[s_{13}s_{23}]^{\frac{d-4}{2}}\Theta(s_{\min}-s_{13})\Theta(s_{\min}-s_{23})\times \\
&\quad s_{12}^{\frac{d-4}{2}}\frac{d\Omega_{d-1}}{2^{d-1}}ds_{12}\delta(s_{12}-Q^2) \\
&\to (2\pi)^{1-d}\frac{\pi^{\frac{d-2}{2}}}{2\Gamma(\frac{d-2}{2})}s_{12}^{\frac{2-d}{2}}ds_{13}ds_{23}[s_{13}s_{23}]^{\frac{d-4}{2}}\Theta(s_{\min}-s_{13})\Theta(s_{\min}-s_{23}) \\
&\quad \times\ dP^d(Q;P_1,P_2) \qquad (2.4.65)
\end{aligned}
$$

Therefore we see that in the soft limit, we can perform the desired factorisation of the 3 parton phase space factor to the 2 parton phase space multiplied by a soft term which will regulate the divergent term from the matrix element factorisation. However, we have used the assumption that $s_{13} = s_{23} = 0$ for the whole region $s_{13} < s_{\min}$, $s_{23} < s_{\min}$ which is clearly false.

For the collinear regime we use the Altarelli-Parisi splitting functions. We again take the 3 parton phase space factor (after azimuthal averaging) and apply the splitting of the two collinear momenta. Let us assume that partons 2 and 3 are collinear and that we assign a fraction $z$ of the total momenta to parton 2 such that

$$
\begin{aligned}
s_{1a} &= s_{12} + s_{13} \\
s_{12} &= z s_{1a}, \;\; s_{13} = (1-z) s_{1a}.
\end{aligned} \tag{2.4.66}
$$

Applying these transformations to our phase space factor we find

$$
\begin{aligned}
d^d PS(Q; P_1, P_2, P_3) \;\; \rightarrow \;\; & (2\pi)^{3-2d} \frac{\pi^{\frac{d-2}{2}}}{2\Gamma(\frac{d-2}{2})} ds_{23} dz [s_{23} z(1-z)]^{\frac{d-4}{2}} \Theta((s_{\min} - s_{23}) \times \\
& s_{1a}^{\frac{d-4}{2}} \frac{d\Omega_{d-1}}{2^{d-1}} ds_{1a} \delta(s_{1a} - Q^2) \\
\rightarrow \;\; & (2\pi)^{1-d} \frac{\pi^{\frac{d-2}{2}}}{2\Gamma(\frac{d-2}{2})} ds_{23} dz [s_{23} z(1-z)]^{\frac{d-4}{2}} \Theta((s_{\min} - s_{23}) \\
\times \;\; & d^d P(Q; P_1, P_a)
\end{aligned} \tag{2.4.67}
$$

Again, we find the desired factorisation of the 3 parton phase space into the 2 parton phase space factor multiplied by the collinear term. Here we make the same mistake as before by assuming that the factorisation is exact throughout the collinear region whereas it is only strictly true at the edges of the 3 parton phase space.

Any multiparton phase space can be approximated in the soft and collinear limits using this 3 parton procedure. By dividing out the unresolved parton with its colour connected neighbours to form a separate 3 parton subspace, we can make these approximations and then the remaining 2 parton subspace is integrated back into the whole phase space factor. This technique is independent of the partons used.

This method of phase space factorisation is problematic because the assumption that terms can be neglected throughout a region in which they are not necessarily zero is false and as the number of particles increases these terms begin to contribute. Also, the mapping of momenta from $n+1$ partons to $n$ partons is inconsistent with the massless nature of the matrix elements. Finally, the mapping of momenta from one set of partons to another is not symmetrical and may lead to problems between regions where the momenta are mapped differently. The technique we present in the next chapter manages all these problems and produces a factorisation technique that is free from these errors.

## 2.5 Motivation

In Section 2.2 we saw how experimental observables such as jets and theoretical constructions such as partons are related both at and beyond leading order. We also compared the different techniques employed in studying the final state of any interaction. But we have not yet addressed the question of why it is so important to consider processes beyond leading order. In this section we shall consider the motivation and background leading to the main calculation of this thesis, namely the phenomenological calculation of the process $e^+e^- \to 4$ jets at next to leading order (NLO).

It is important to consider the four jet process at NLO both from a physical and mathematical perspective. We note that four jet production is sensitive both to the Casimir structure of QCD (thus making it an excellent test bed for QCD) and also the possible presence of light gluinos which are present in many supersymmetry models (see for example [27]). These hypothetical particles would have an effect similar to that of increasing the number of active quarks from $n_f$ to $n_f + 3$. Thus the process $e^+e^- \to 4$ jets is a superb process to test well-established theories such as QCD and also a good source of possible new physics. Other physical motivations include

1. Another method for deriving the strong coupling constant $\alpha_s$ either directly from the event shape distributions or the energy dependence of their average value[29].

2. Better detailed predictions for distributions of event shape variables akin to Thrust. This is due to the uncertainty in the renormalisation scale and at LO the only motivated choice of scale we can make is the physical scale argument. At NLO other scale choices can be calculated.

3. A test for non-perturbative effects such as power corrections which can be hidden by the uncertainty in higher order perturbation calculations.

4. By calculating higher order terms the theoretical uncertainty can be reduced by reducing the renormalisation scale dependence. Thus higher order theoretical calculations are necessary to maintain parity with experimental errors.

5. Only at NLO can a discernible difference between jet-finding algorithms be seen.

Higher order calculations are necessary to model the hadronic jets seen in detectors where there are typically 20 or more hadrons.

6. Direct production of 4 jets is a large source of background at the new LEP2 energies and as such needs to be well known so that it can be removed from new physics searches.

The NLO $e^+e^- \to 4$ jets has also proven to be very mathematically insightful. For a NLO calculation it is necessary to perform 1-loop integrals and those integrals were for many years a bottle neck to the NLO calculation. Many improved techniques and methods were required to solve them. Also, when we consider integrating the matrix elements over the available phase space it was necessary to develop techniques that could handle two separately divergent answers, but when combined give a finite answer. We shall consider these problems in more detail when we look in-depth at the NLO $e^+e^- \to 4$ jets calculation in the following chapters. For present however, we shall concentrate on the tests of QCD that the calculation provides and the background theory necessary for these calculations.

A reliable test of the SU(3) nature of QCD is to measure the colour factors present in any QCD calculation. This test can be made at the 2 and 3 jet level[26], but the non-Abelian nature of QCD only becomes present in multijet final states greater or equal to 4 as one of the colour factors, $C_A$, is only present in the calculation for the triple gluon vertex. Thus 4 jet final states are the first place we can study this colour structure at leading order. Having calculated the Casimirs for SU(3) we can compare these values to what is actually seen in experiment. For any suitable 4 jet observable, the tree level calculation can be written as

$$\frac{1}{\sigma_0} d\sigma_{4\,\text{jet}} = \left(\frac{\alpha_s C_F}{2\pi}\right)^2 \left(A(O) + \frac{C_A}{C_F} B(O) + \frac{T_R}{C_F} C(O)\right) dO \tag{2.5.68}$$

where $\sigma_0$ is the 2 jet cross-section and $A, B$ and $C$ are the coefficients calculated from the three relevant processes, namely $q\bar{q}gg, q\bar{q}q\bar{q}$ and $q\bar{q}Q\overline{Q}$. $O$ is any 4 jet like observable. Thus by fitting the theoretical calculation to the data, one can extract the colour ratios, $C_A/C_F$ and $T_R/C_F$. Results from [25] give a value

$$\frac{C_A}{C_F} = 2.11 \pm 0.32, \quad \frac{T_R}{C_F} = 0.40 \pm 0.17 \tag{2.5.69}$$

compared with the SU(3) values of $C_A/C_F = 2.25$ and $T_R/C_F = 0.375$. Figure 2.10 shows how the experimental values compare with those colour factors from different types of gauge group. As we can see, the current experimental values do not rule out other gauge groups such as SU(4) or Sp(4), but by performing the same fit at NLO the errors can be drastically reduced[28].

## 2.6 Summary

In this chapter we have attempted a review of the techniques and ideas used when considering higher order calculations. As partons are not directly seen in experiment it is essential to have a prescription that catagorises the event such that theoretical calculations can be directly compared with data. The development of jet finding algorithms has gone a long way to reconciling theoretical and experimental perspectives and is now a necessary tool in all QCD calculations. Here we have outlined some of the more common variants and later we shall use them in calculating the NLO term for the cross-section and other 4 jet observables. We shall see how different algorithms, although consistent at leading order, now differ and the magnitude of these deviations.

We have also seen the different techniques used to regularise the infra red pole structure of higher order diagrams such as the vertex corrections necessary for the NLO calculation of the cross section for the process $e^+e^- \to 2\,\text{jets}$. Using dimensional regularisation solves the problem of cancelling divergences analytically at this level without introducing Lorentz or gauge invariance violation. However, for process of more complexity it becomes impossible to deal with the integration by hand and we are forced to consider numerical methods. These prescriptions will constitute the main part of the next chapter.

Colour algebra enables us to visualise QCD calculations as we would QED ones by introducing colour factors akin to the simpler QED electric charge factor. Thus we are able to write complicated matrix elements as colourless subamplitudes multiplied by colour terms. This leads on to the idea of colour decompostion where the various Feynman diagrams can be split into colour ordered subamplitudes such as in the $q\bar{q} \to gg$ case where the three diagrams can be shown to divide into subamplitudes where the gluons are ordered and one where the gluons are colour detacted. This then simplifies NLO calculations for unresolved

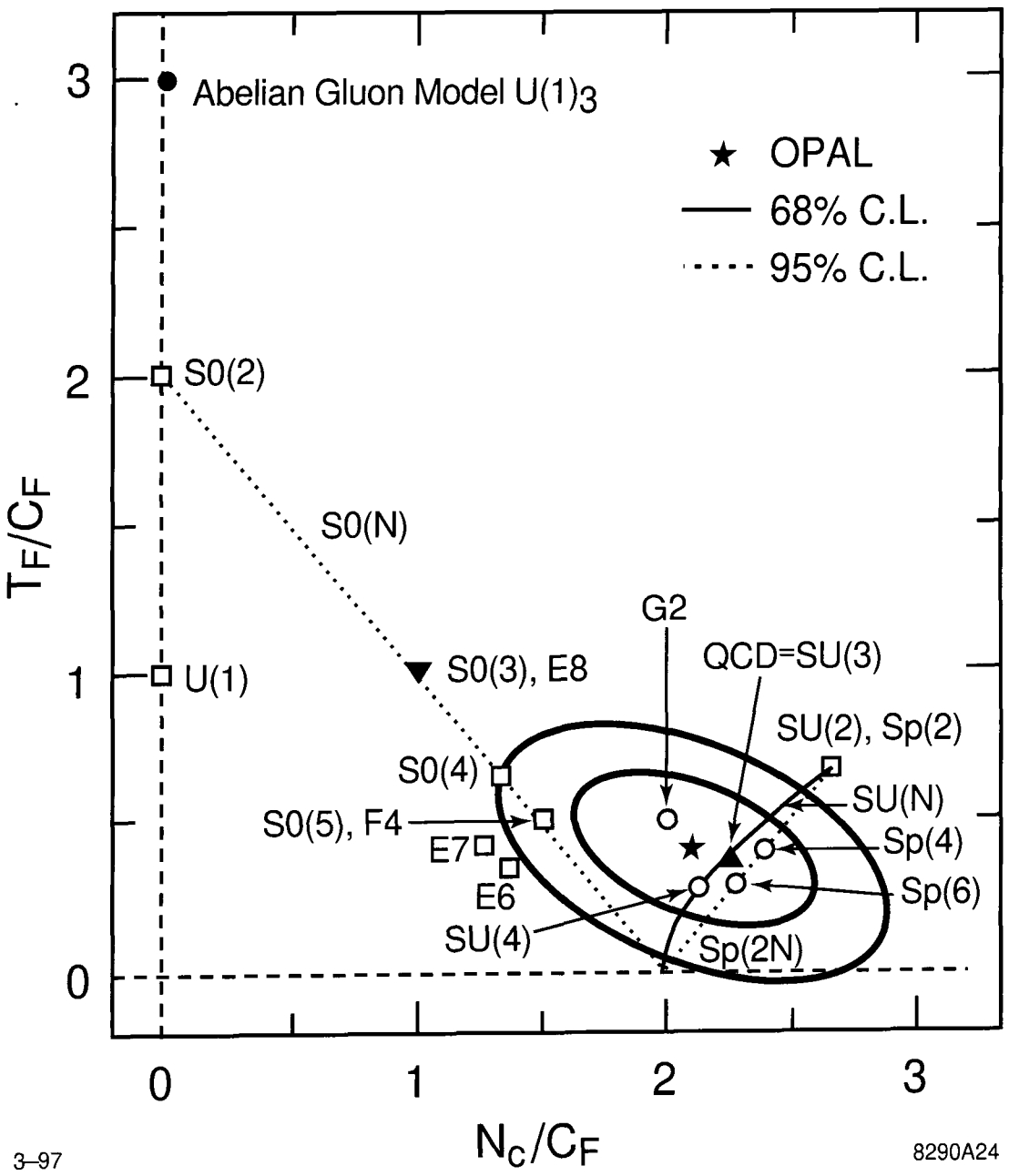


Figure 2.10: The colour factors as measured by the OPAL collaboration. The circles around the central star show confidence limits,the inner being the 68% level and the outer one the 95% level. This diagram is taken from reference [25].

partons where the only singular collinear contributions are those between colour connected neighbours. For those ordered amplitudes this just means their neighbour in the ordering whereas for the colour detacted gluons, their only singular terms come from being collinear to the quark or antiquark. The final NLO technique we studied was that of the factorisation properties of the subamplitudes and phase space factors under unresolved partons. This property is only true for the subamplitudes in the soft partons limit and is not seen for the full matrix element. However, in the collinear limit both the $n$ parton subamplitude and full matrix element factorises into a divergent term proportional to the Altarelli-Parisi splitting functions (if we divide the momenta of the newly formed parton between the collinear pair linearly) and the hard $n-1$ subamplitude or full matrix element.

Finally we looked at the motivation for considering NLO calculations. We see that not only is it a good test for Standard Model physics and beyond, but that the calculations have produced new techniques in solving loop integrals and numerically calculating the finite sum of two divergent contributions. NLO calculations are also useful for calculating $\alpha_s$, comparing jet-finding algorithms and reducing scale dependence in the final answer.

# Chapter 3

# NLO Numerical Techniques

## 3.1 Introduction

In the previous chapters we outlined some of the standard techniques used in QCD calculations both for leading order and higher order corrections. However there is a very important issue that has not yet been fully addressed. Performing the integrations required for these calculations is in general beyond analytic methods. For example the NLO term for the cross section for the process $e^+e^- \to 4$jets involves an eleven dimensional integral over all the 5 particle phase space. Therefore we are required to utilise numerical methods. But these techniques remain unstable until we have analytically removed the divergences present in the virtual and unresolved contributions. Section 3.2 will review some of the different prescriptions used to remove the pole structure analytically before numerical integration and Section 3.3 will detail one, namely that of hybrid subtraction which is used for the calculation of the process $e^+e^- \to 4$jets. This method is general to any QCD process and is well behaved throughout phase space. We present and calculate new universal subtraction terms which utilise a symmetric momentum transformation which preserves the massless nature of the partons involved. These subtraction terms have been implemented into a new Monte Carlo routine for the NLO calculation of the process $e^+e^- \to 4$ jets.

## 3.2 Subtraction, Slicing and Hybrid subtraction

At present there are three main methods used for removing the pole structure of NLO contributions. These are best described by considering a simple toy example of a NLO calculation combining both the unresolved parton contribution and the virtual loop term [41]. Consider the integral equation for the calculation of any jet observable, $\mathcal{I}$, such as the $n$ jet cross section.

$$\mathcal{I} = \lim_{\varepsilon \to 0} \left( \int_0^1 \frac{\mathcal{M}(x)}{x} x^{\varepsilon} dx - \frac{1}{\varepsilon} \mathcal{M}(0) \right) \tag{3.2.1}$$

where the first term is the unresolved parton contribution and the second term is the virtual loop. Here, the integral over the extra phase space (due to the unresolved parton) is represented by an integral over $x$ which can be thought of as any physical quantity that tends to zero in the unresolved limit such as the angle between two partons or the energy of a gluon. The function $\frac{\mathcal{M}(x)}{x}$ represents the $n+1$ parton matrix element which is singular as $x \to 0$. In this limit $\mathcal{M}(x) \to \mathcal{M}(0)$ where $\mathcal{M}(0)$ is the $n$ parton tree level matrix element. The factor $x^{\varepsilon} dx$ is due to the extra phase space of the unresolved parton. In performing this integral it is assumed that $0^{\varepsilon} = 0$. The second term represents the virtual contribution which is proportional to tree level with the explicit $1/\varepsilon$ pole coming from the the evalution of the loop integral itself. As $x \to 0$ we see that the unresolved parton term is regularised by the phase space factor although the integral is still divergent for $\varepsilon \to 0$. This divergence is cancelled by the explicit $\varepsilon$ pole in the second term. Therefore the total integral is finite and the limit $\varepsilon \to 0$ can be taken. Using this example we can outline the current methods used to deal with this cancellation.

### 3.2.1 Slicing[42]

Slicing or phase space slicing solves the problem of analytically handling the pole structure of complicated integrals by using soft and collinear approximations to the full matrix element within well defined areas of the available phase space. The phase space is divided into two areas $0 < x < \delta$ and $\delta < x < 1$ and it is within the first of these that the approxi-

mation $\mathcal{M}(x) \approx \mathcal{M}(0)$ applies assuming that the cut-off $\delta$ is small. (Errors made by the approximation are due to neglected terms of the order $\delta$.) This then gives

$$\begin{aligned}
\mathcal{I} &\approx \lim_{\varepsilon\to 0}\left(\int_\delta^1 \frac{dx}{x}x^\varepsilon \mathcal{M}(x) + \mathcal{M}(0)\int_0^\delta \frac{dx}{x}x^\varepsilon - \frac{1}{\varepsilon}\mathcal{M}(0)\right) \\
&\approx \lim_{\varepsilon\to 0}\left(\int_\delta^1 \frac{dx}{x}x^\varepsilon \mathcal{M}(x) + \mathcal{M}(0)\frac{\delta^\varepsilon}{\varepsilon} - \frac{1}{\varepsilon}\mathcal{M}(0)\right) \\
&\approx \int_\delta^1 \frac{dx}{x}\mathcal{M}(x) + \mathcal{M}(0)\log(\delta) + \mathcal{O}(\varepsilon) \qquad (3.2.2)
\end{aligned}$$

The pole structure of the observable has been removed by expanding $\delta^\epsilon = e^{\varepsilon\log(\delta)} = 1 + \varepsilon\log(\delta) + ...$

The benefits of slicing are that the approximations used are the same as those derived in the previous chapter and are therefore universal to all QCD processes. However, this method does introduce a theoretical parameter into the calculation of a physical quantity. Obviously $\mathcal{I}$ cannot depend on $\delta$ and therefore the $\delta$ dependence of the lower limit of the first term (which is now finite and can be calculated numerically) should cancel with the second term leaving a finite, $\delta$ independent answer. As we stated above the approximations are valid only for small values of $\delta$. But if we choose a very small value (where the approximation is almost exact) we introduce the cancellation of large logarithms which leads to numerical instability (see Figure 9.3 of [43]). Therefore the results produced using this technique vary with $\delta$ where at small $\delta$ we have a correct answer but with large errors, but at large $\delta$ we have an erroneous result with small errors. A good example of this is Figure 1 of [36] where the factor $\frac{\sigma^{NLO}}{\sigma^{LO}}$ for the process $e^+e^- \to 2$ jets is calculated making use of the slicing prescription. For this calculation the integrals are actually simple enough to do analytically thus the value is known exactly. For $\delta > 0.1$ the numerical answer over estimates by about 2% but with error bars too small to show on the plot. For $0.01 < \delta < 0.1$ the slicing method gives the correct value with error bars giving an uncertainty of about 0.5%. However, for $\delta < 0.01$ the error bars have become of the order of 1% with the value lying on the correct answer. Therefore the choice of $\delta$ is critical for accurate, precise measurements.

### 3.2.2 Subtraction[44]

Another method developed originally for the evaluation of $O(\alpha_s^2)$ observables in electron-positron annihilation experiments by Ellis, Ross and Terrano is the subtraction prescription. The basic idea behind this technique is to add and subtract a divergent subtraction term. This term is an integral over $n+1$ partonic phase space with the same pointlike structure as the extra unresolved contribution and can therefore be included in the extra integration, leaving a finite $n+1$ phase space integral. But it is also analytically integrable over the single parton subspaces leading to the explicit soft/collinear $\varepsilon$ poles. The result can then be combined with the virtual contribution leaving a finite $n$ partonic phase space integral. Subtracting this term from the first term in Equation 3.2.1 and adding it to the second gives

$$\begin{aligned} \mathcal{I} &= \lim_{\varepsilon\to 0}\left(\int_0^1 \frac{dx}{x}x^\varepsilon(\mathcal{M}(x)-\mathcal{M}(0)) + \mathcal{M}(0)\int_0^1 \frac{dx}{x}x^\varepsilon - \frac{1}{\varepsilon}\mathcal{M}(0)\right) \\ &= \int_0^1 \frac{dx}{x}(\mathcal{M}(x)-\mathcal{M}(0)) \end{aligned} \tag{3.2.3}$$

where the virtual pole is cancelled by evaluating the second term and letting $\varepsilon \to 0$ after setting $x = 0$ so that $0^\varepsilon = 0$. The combined first term can now be performed numerically in the usual 4 dimensions (so that the $x^\varepsilon$ term becomes equal to 1). The difficulty of this technique is the analytic evaluation of the full $\int_0^1 \frac{dx}{x}x^\varepsilon$ term for real processes. Originally, it was necessary to recalculate this quantity for every process. However, a variant of the subtraction method using a new factorisation formula called the dipole formula has generalised these subtraction terms so that they are universal [45]. This uses a dipole structure where the factorisation depends solely on the momentum and colour of three partons where two of these partons are set to become soft and/or collinear. These three partons are then mapped into two partons in a momentum conserving manner. However, this mapping is not symmetric over the whole of phase space and is dependent on which half of the 3 parton subspace the mapping is being done in. Unlike the slicing method, the subtraction prescription makes no assumptions about the phase space or the matrix elements and it does not introduce any new theoretical parameter into the calculation.[1]

[1] In practice it is impossible to integrate numerically from 0 and so a small cut-off is applied to the lower bound of the final integral

### 3.2.3 Hybrid subtraction

Finally, we consider the numerical method known as hybrid subtraction. This technique uses elements of both prescriptions described above to preserve the universality of the procedure whilst removing the dependence of the answer (and its precision) on $\delta$.

This is achieved by introducing a second cut-off or scale $\Delta$. Phase space is again divided up into regions where

- between $0 < x < \delta$, the slicing procedure (using universal approximations to the matrix element and phase space) is applied.
- between $\delta < x < \Delta$, an analytically integrable set of universal subtraction terms, $E(x)$, are added and subtracted from the two terms in an identical fashion to the subtraction method.
- between $\Delta < x < 1$ the integrals are numerically calculated

This then gives

$$\begin{aligned}
\mathcal{I} &\approx \lim_{\varepsilon\to 0}\left(\int_\delta^1 \frac{dx}{x}\mathcal{M}(x) + \int_0^\delta \frac{dx}{x}x^\varepsilon \mathcal{M}(0) - \frac{1}{\varepsilon}\mathcal{M}(0) + \int_\delta^\Delta E(x)\frac{dx}{x} - \int_\delta^\Delta E(x)\frac{dx}{x}\right) \\
&\approx \left(\int_\delta^1 \frac{dx}{x}\mathcal{M}(x) + \mathcal{M}(0)\log(\delta) + \int_\delta^\Delta E(x)\frac{dx}{x} - \int_\delta^\Delta E(x)\frac{dx}{x}\right) \\
&\approx \left(\int_\delta^1 \frac{dx}{x}(\mathcal{M}(x) - E(x)\Theta(\Delta - x)) + \int_\delta^\Delta E(x)\frac{dx}{x} + \mathcal{M}(0)\log(\delta)\right) \qquad (3.2.4)
\end{aligned}$$

There are a number of requirements that $E(x)$ must fulfill for it to be consider a valid subtraction term. Firstly, we require the $\int_\delta^\Delta E(x)\frac{dx}{x}$ term to integrate analytically without any approximations to the phase space, giving a term $-M(0)\log(\delta)$ from the lower bound, cancelling all $\delta$ dependence arising from the slicing procedure. Therefore $\delta$ can be driven as low as is necessary (and practical) for the slicing approximations to hold. Secondly, $E(x)$ must approximate smoothly to $M(x)$ as $x \to 0$, making certain that no $\delta$ dependence comes from the lower bound of the first term and that no discontinuities exist at phase space boundaries. This makes the integral safe to numerically integrate. Ideally, $E(x)$ should

be smooth and close to $M(x)$ over the entire phase space region $x < \Delta$. As we add and subtract the same term any $\Delta$ dependence vanishes and we allow this cut-off to be big so as to reduce errors from cancelling logarithms. This is the method that we shall use for all the $e^+e^- \to 4$ jets calculations in this thesis. In the next section we shall outline the derivation of the universal subtraction terms that can be used in hybrid subtraction and how they are employed in calculations

## 3.3 Antenna factorisation

As we have already seen the factorisation of an $n+1$ parton matrix element in the singular limit of an unresolved parton is solely dependent on the momentum and identity of the colour connected neighbours to the unresolved parton, $u$. In these limits the matrix element factorises into a divergent term dependent on the invariants of the unresolved parton with its colour connected neighbours and the hard $n$ parton tree level matrix element with the unresolved parton removed. Therefore we can divide these three partons from the rest of the $n+1$ parton matrix element and treat this *antenna* separately. From the singular behaviour of this antenna we can predict the singular behaviour of the entire matrix element with respect to that particular unresolved parton. And then by adding together all possible antenna, we can calculate any singular behaviour the $n+1$ parton matrix element might portray.

Think of the antenna as three partons $a, b$ and $u$ where one of these partons, $u$ will be unresolved. In the completely unresolved limit we are left with two hard partons, $A$ and $B$. Alternatively we can think the reverse process of two hard partons $A$ and $B$ emitting a third unresolved parton, $u$. See Figure 3.1. The singular limits of the antenna function now depends solely on terms such as $\frac{1}{s_{au}}$, $\frac{1}{s_{bu}}$ and $\frac{1}{s_{au}s_{bu}}$ and the squared matrix elements factorise as

$$|\mathcal{M}(...,a,u,b,...)|^2 \to A_{aub}|\mathcal{M}(...,A,B,...)|^2 \tag{3.3.5}$$

where $A_{aub}$ is the antenna function and has the correct behaviour in each of the unresolved limits. With only three partons in the antenna we see that there is only a small number of

potential antennae e.g $ggg$, $qgg$ and $qg\bar{q}$. If we calculate the singular limits for each of these potential antennae we can use them in an universal manner that would describe the singular limits of any QCD process with an unresolved parton. We postpone the detail of calculating the antenna functions until we have considered the division of the phase space under this antenna factorisation.

### 3.3.1 Momentum mapping

In collapsing the hard partons down into three separate partons, the momenta will obviously change and we need to use a momentum mapping of three partons to two that will respect the masslessness nature of the partons before and after the mapping. Also, this mapping should be smooth across the phase space of the antenna. We would like to factorise the $n+1$ parton phase space into an $n$ parton phase space and an antenna phase space term. We can write the full phase space factor as the product of the 3 parton antenna phase space attached to the $n-2$ parton phase space integrating over the total invariant mass of the antenna, $s_{aub}$.

$$dPS(Q^2; p_1, ..., p_n) = dPS(Q^2; p_1, ..., p_{aub}, ...p_n)\frac{ds_{aub}}{2\pi}dPS(s_{aub}; p_a, p_u, p_b) \tag{3.3.6}$$

Here $p_{aub} = p_a + p_u + p_b$ and $s_{aub} = p_{aub}^2$. To get Equation 3.3.6 in the desired form we multiply the right hand side of the equation by

$$\frac{dPS(s_{AB}; p_A, p_B)}{\int dPS(s_{AB}; p_A, p_B)} \tag{3.3.7}$$

where particles $A$ and $B$ have momenta $p_A$ and $p_B$ such that, $p_{aub} = p_{AB} = p_A + p_B$, $p_A^2 = p_B^2 = 0$ and $s_{aub} = s_{AB}$. In other words,

$$\begin{aligned} dPS(Q^2; p_1, ..., p_n) &= dPS(Q^2; p_1, ..., p_{AB}, ..., p_n)\frac{ds_{AB}}{2\pi}dPS(s_{AB}; p_A, p_B) \times dPS^{\text{sing}} \\ &= dPS(Q^2; p_1, ..., p_A, p_B, ..., p_n) \times dPS^{\text{sing}}. \end{aligned} \tag{3.3.8}$$

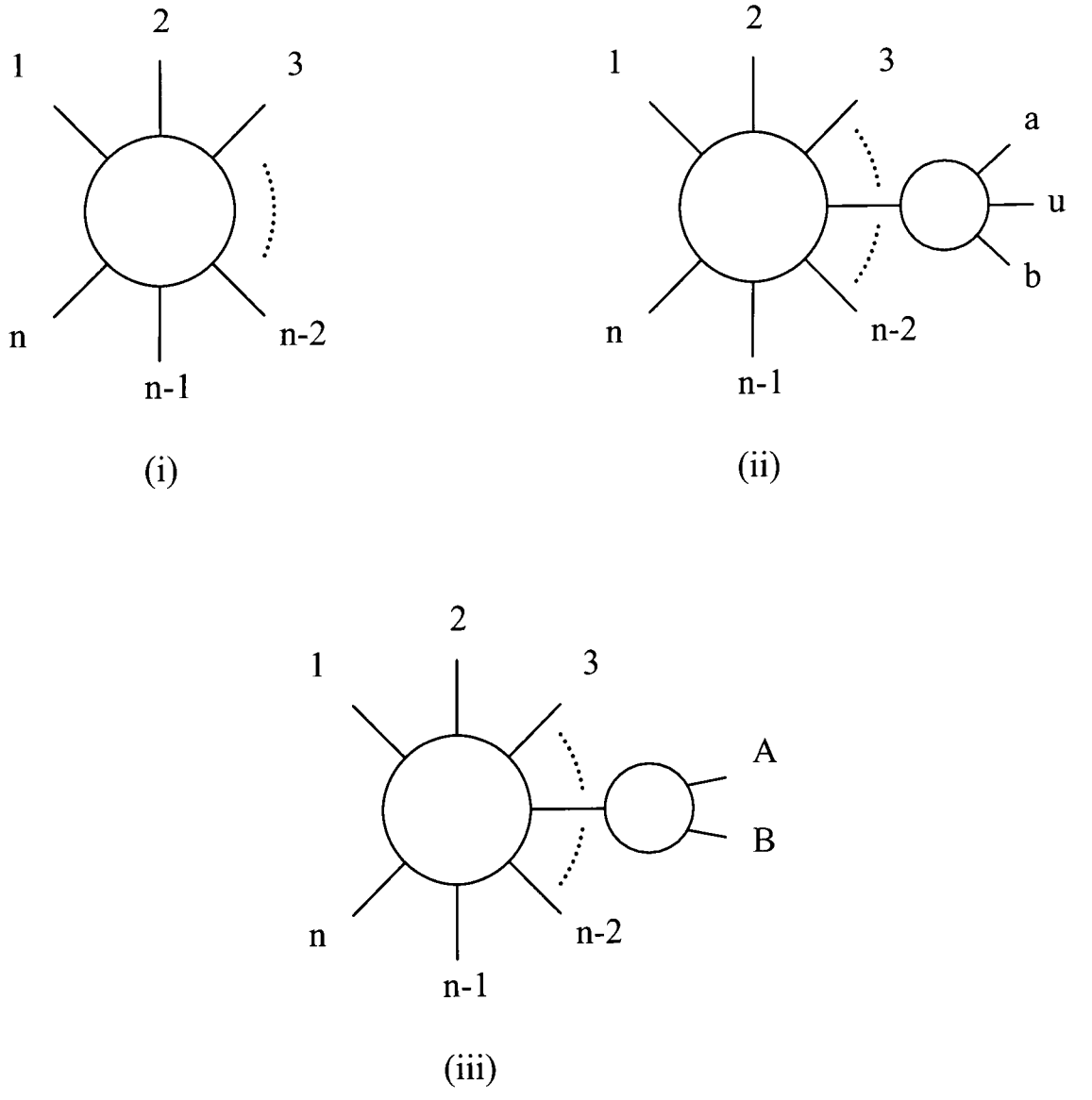


Figure 3.1: The singular limit of a $n+1$ parton matrix element (i) can be calculated by dividing it into a 3 parton antenna attached to the $n-2$ hard partons. By dividing out the three body antenna that contains the soft/collinear partons (ii) the antenna's singular limits can be found once and for all. These limits will be the same as for the entire $n+1$ parton matrix element when the parton in the antenna becomes unresolved as the limits only depend on the invariants of the parton with its coloue connected neighbours and not on any of the other $n-2$ partons. Therefore the 3 parton antenna can be collapsed down to a 2 parton antenna multiplied by the divergent singular terms using a symmetric momentum mapping that preserves the massless condition. The two body antenna (iii) can then be reconstructed with the rest of the matrix element to give a $n$ parton matrix element in the singluar limit of a specific unresolved parton. By summing over all possible antenna the singualr limits that can ever exist are then calculated.

As desired, we have the phase space for an final state containing $n$ lightlike particles multiplied by $dPS^{\text{sing}}$. Working in four-dimensions and after integration over the Euler angles,

$$\begin{aligned} dPS^{\text{sing}} &= \frac{dPS(s_{aub}; p_a, p_u, p_b)}{\int dPS(s_{AB}; p_A, p_B)} \\ &= \frac{1}{16\pi^2} s_{aub} dx_{au} dx_{ub} dx_{ab} \delta(1 - x_{au} - x_{ub} - x_{ab}), \end{aligned} \tag{3.3.9}$$

where $x_{ij} = s_{ij}/s_{aub}$. For this to work, a mapping must exist that determines $p_A$ and $p_B$ for a given set of momenta $p_a$, $p_b$ and $p_u$. Many choices are possible [45, 46] and we choose the symmetric mapping of [46],

$$\begin{aligned} p_A &= \frac{1}{2}\left[1 + \rho + \frac{s_{ub}(1 + \rho - 2r_1)}{s_{ab} + s_{au}}\right] p_a + r_1 p_u + \frac{1}{2}\left[1 - \rho + \frac{s_{au}(1 - \rho - 2r_1)}{s_{ab} + s_{ub}}\right] p_b, \\ p_B &= \frac{1}{2}\left[1 - \rho - \frac{s_{ub}(1 + \rho - 2r_1)}{s_{ab} + s_{au}}\right] p_a + (1 - r_1) p_u + \frac{1}{2}\left[1 + \rho - \frac{s_{au}(1 - \rho - 2r_1)}{s_{ab} + s_{ub}}\right] p_b, \end{aligned} \tag{3.3.10}$$

where,

$$r_1 = \frac{s_{ub}}{s_{au} + s_{ub}}, \tag{3.3.11}$$

and,

$$\rho = \sqrt{\frac{s_{ab}^2 + (s_{au} + s_{ub}) s_{ab} + 4 r_1 (1 - r_1) s_{au} s_{ub}}{s_{ab} s_{aub}}}. \tag{3.3.12}$$

Note that this transformation approaches the singular limits smoothly. For example, as $s_{au} \to 0$, then $r_1 \to 1$, $\rho \to 1$ and $p_A \to p_a + p_u$, $p_B \to p_b$. Also note that this mapping produces massless partons at all points in phase space and not just along the singular boundary where $p_i . p_j = 0$.

### 3.3.2 The universal subtraction terms

Having factorised the phase space, we now wish to find the analogues of the subtraction functions $E(x)$ discussed in Section 3.2. These functions should ideally be valid over the whole of the antenna phase space $dPS^{\text{sing}}$ and, in the soft and collinear regions must match onto the singular limits of the full $n+1$ matrix elements. In other words, for a given $(n+1)$ particle amplitude, in the limit where particle $u$ is unresolved,

$$|S_\mu(...,a,u,b,...)V^\mu|^2 \to A_{aub}|S_\mu(...,A,B,...)V^\mu|^2, \tag{3.3.13}$$

where we have replaced the antenna comprising $a,u,b$ by the hard partons $A$ and $B$ to obtain an $n$ particle amplitude. The antenna function $A_{aub}$ depends on the momenta of the radiated particles $a$, $b$ and $u$, but the $n$ particle amplitude $|S_\mu(...,A,B,...)V^\mu|^2$ does not.

The leading colour contribution to an observable cross section from an $(n+1)$ particle final state with a particular colour ordering is proportional to,

$$\left(\frac{g^2N}{2}\right)^{n+1}|S_\mu(...,a,u,b,...)V^\mu|^2 J_{(n+1)}dPS(Q^2;...,p_a,p_u,p_b,...), \tag{3.3.14}$$

where the observable function $J_{(n+1)}$ represents the cuts applied to the $(n+1)$ particle phase space to define the observable. Using the factorisation of the matrix elements defined in Equation 3.3.13, when particle $u$ is unresolved we should subtract,

$$\left(\frac{g^2N}{2}\right)^{n+1}A_{aub}|S_\mu(...,A,B,...)V^\mu|^2 J_{(n)}dPS(Q^2;...,p_a,p_u,p_b,...), \tag{3.3.15}$$

from the $(n+1)$ particle contribution and, using the phase space factorisation of Equation 3.3.8, add,

$$\left(\frac{g^2N}{2}\right)^{n+1}A_{aub}dPS^{\text{sing}}|S_\mu(...,A,B,...)V^\mu|^2 J_{(n)}dPS(Q^2;...,p_A,p_B,...), \tag{3.3.16}$$

to the $n$ particle contribution where both the observable function $J$ and matrix elements $|S_\mu V^\mu|^2$ depend only on the momenta of the $n$ remaining hard partons. Note that for any infrared safe observable, in the limit that one particle is unresolved, $J_{(n+1)} \to J_{(n)}$. In the subtraction term Equation 3.3.15, we use the transformations of Equation 3.3.10 to map the momenta $p_a$, $p_u$ and $p_b$ defined in the $(n+1)$ particle phase space onto the momenta $p_A$ and $p_B$ used in the $n$-particle matrix elements and observable functions. In Equation 3.3.16, all dependence on the momenta of particles $a$, $b$ and $u$ may be integrated out to give the antenna factor, $F$,

$$F_{AB}(s_{AB}) = \left(\frac{g^2 N}{2}\right) \int A_{aub} dPS^{\text{sing}}, \tag{3.3.17}$$

multiplying the $n$ particle cross section (for a given colour ordered amplitude),

$$\left(\frac{g^2 N}{2}\right) |S_\mu(..., A, B, ...)V^\mu|^2 J_{(n)} dPS(Q^2; ..., p_A, p_B, ...). \tag{3.3.18}$$

The full set of subtraction terms is obtained by summing over all possible antennae.

The Dalitz plot for the $(AB) \to aub$ phase space is shown in Figure 3.2. In the hybrid scheme we are implementing, we use the slicing method of [36] in the region $\min(s_{au}, s_{ub}) < \delta$, and the subtraction scheme in the region, $\delta < \min(s_{au}, s_{ub}) < \Delta$. In the slicing region, the phase space and soft and collinear approximations to the matrix elements are kept in $d = 4 - 2\varepsilon$ dimensions to regularise the singularities present when either invariant vanishes. Using the approach of [36], there are three separate contributions (a) soft gluon when $\max(s_{au}, s_{ub}) < \delta$, (b) $a$ and $u$ collinear when $s_{au} < \delta$ but $s_{ub} > \delta$ and (c) $b$ and $u$ collinear when $s_{ub} < \delta$ but $s_{au} > \delta$.

Before turning to the explicit forms for the antenna subtraction terms, we note that while quarks are only directly colour connected to one particle - a gluon or antiquark, gluons are directly connected to two particles - the gluon (or quark) on either side. Therefore,while the quark (or antiquark) appear in a single antenna, gluons appear in two. This gives an ambiguity in how to assign the collinear singularities of a pair of gluons to each antenna.

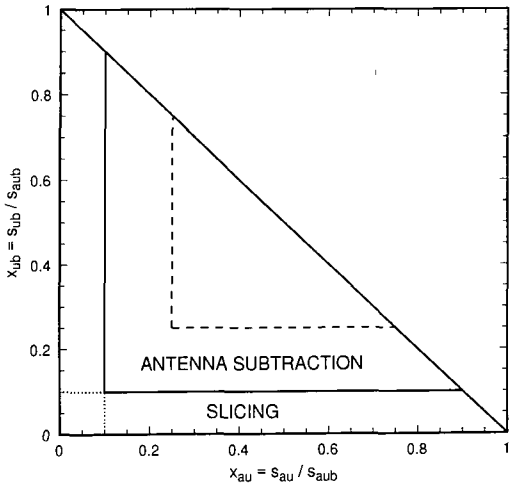


Figure 3.2: The phase space for the decay $(AB) \to aub$. The cut $\min(s_{au}, s_{ub}) = \delta$ with $\delta = 0.1\ s_{aub}$ is shown as a solid line while $\min(s_{au}, s_{ub}) = \Delta$ is shown as a dashed line for $\Delta = 0.25\ s_{aub}$. The region $\min(s_{au}, s_{ub}) < \delta$ defines where the slicing approach is utilised, with the soft and collinear regions demarked by dotted lines. Antenna subtraction is applied when $\delta < \min(s_{au}, s_{ub}) < \Delta$.

Later we will exploit this ambiguity to make the antenna functions $A_{aub}$ for different pairs of hard partons finite simpler.

### 3.3.3 Quark-Antiquark antenna

Let us first consider a system containing a quark, antiquark and a gluon. This is produced by an antenna comprising of a hard quark and antiquark pair that decays by radiating a gluon. Any function that has the correct soft gluon and collinear quark/gluon singularities in the appropriate limit is satisfactory. Here the hard particles in the antenna are $Q$ and $\overline{Q}$ which radiate to form $q$, $\overline{q}$ and the gluon $g$. A suitable choice for the antenna function is,

$$\begin{aligned} A_{qg\overline{q}} &= \frac{|S_\mu(q;g;\overline{q})V^\mu|^2}{|S_\mu(Q;\overline{Q})V^\mu|^2} \\ &= \frac{2}{s_{aub}}\left(\frac{x_{au}}{x_{ub}} + \frac{x_{ub}}{x_{au}} + \frac{2x_{ab}x_{aub}}{x_{au}x_{ub}}\right). \end{aligned} \tag{3.3.19}$$

Because this is proportional to the three parton matrix elements, $|S_\mu(q;g;\overline{q})V^\mu|^2$, it automatically contains the correct soft and collinear limits. Furthermore, it is smooth over the whole three particle phase space and singularities only appear in the $s_{au} \to 0$ and $s_{ub} \to 0$ limits.

Explicitly integrating over the antenna phase space for $\delta < \min(s_{au}, s_{ub}) < \Delta$ we find,

$$\begin{aligned} F_{Q\overline{Q}}(s_{Q\overline{Q}}) &= \left(\frac{g^2 N}{2}\right) \int A_{qg\overline{q}} dPS^{\text{sing}} \\ &= \left(\frac{\alpha_s N}{2\pi}\right) \left(\ln^2\left(\frac{\delta}{s_{Q\overline{Q}}}\right) + \frac{3}{2}\ln\left(\frac{\delta}{s_{Q\overline{Q}}}\right)\right) + F^{\Delta}_{Q\overline{Q}}\left(\frac{\Delta}{s_{Q\overline{Q}}}\right) + O(\delta). \end{aligned} \quad (3.3.20)$$

Since we intend to take the $\delta \to 0$ limit, the terms of $O(\delta)$ may be safely neglected. The $\delta$ independent function $F^{\Delta}_{Q\overline{Q}}$ is given by,

$$F^{\Delta}_{Q\overline{Q}}(x) = \left(\frac{\alpha_s N}{2\pi}\right) \left(-\ln^2(x) + \frac{5x}{2} - 2\text{Li}_2(x) + \left(\frac{3}{2} - 2x + \frac{x^2}{2}\right)\ln\left(\frac{1-x}{x}\right)\right). \quad (3.3.21)$$

### 3.3.4 Quark-Gluon antenna

For antenna made of a quark $Q$ and gluon $G$, there are two possible ways of radiating. Either a gluon can be radiated so that a quark-gluon-gluon system is formed, or the gluon may split into a antiquark-quark pair. This latter possibility is subleading in the number of colours and the discussion of situations like this is deferred to Section 3.3.6.

For a quark-gluon-gluon system there is a less obvious choice of antenna function, particularly since the singularity that is produced when the gluon splits sits in more than one antenna. If, in the collinear limit, the gluon splits into an unresolved gluon $u$ which carries momentum fraction $z$ and a hard gluon $b$ with momentum fraction $1-z$, the antenna function should naively be proportional to $P_{gg\to g}$ which is singular as $z \to 0$ and $z \to 1$. This corresponds to singularities as both $s_{au} \to 0$ and $s_{ab} \to 0$ where $a$ is the quark, $Q$. However, because the collinear singularity sits in more than one antenna - the two gluons also occur

in a second antenna where the role of the two gluons is reversed - we can make use of the $N = 1$ supersymmetric identity to rewrite $P_{gg\to g}$ as,

$$P_{gg\to g} = P_{qg\to q} + P_{gq\to q} - P_{q\bar{q}\to g}. \tag{3.3.22}$$

The soft singularities as $z \to 0$ are contained in $P_{gq\to q}$ while those as $z \to 1$ are in $P_{qg\to q}$. We therefore divide $P_{gg\to g}$ amongst the two antennae such that $P_{gq\to q}$ sits in the antenna where gluon $u$ is unresolved. The $z \to 1$ singularities are placed in the antenna where the role of the two gluons is reversed. The remaining $P_{q\bar{q}\to g}$ may be divided between the two antennae according to choice. With a slight modification due to the $P_{q\bar{q}\to g}$ term, the antenna function used for the $Q\overline{Q}$ antenna has the correct limits, so that,

$$A_{qgg} = A_{qg\bar{q}} - \frac{2}{s_{aub}}\left(\frac{x_{au}^2}{x_{ub}x_{aub}}\right). \tag{3.3.23}$$

This is again smooth over the whole three particle phase space with singularities only appearing in the $s_{au} \to 0$ and $s_{ub} \to 0$ limits. In particular, as $z \to 0$, the collinear limit matches onto the soft limit which would not have been the case if we had divided the soft/collinear singularities equally between the two antenna.

After integrating over the antenna phase space for $\delta < \min(s_{au}, s_{ub}) < \Delta$ we find,

$$\begin{aligned} F_{QG}(s_{QG}) &= \left(\frac{g^2 N}{2}\right)\int A_{qgg}\, dPS^{\text{sing}} \\ &= \left(\frac{\alpha_s N}{2\pi}\right)\left(\ln^2\left(\frac{\delta}{s_{QG}}\right) + \frac{10}{6}\ln\left(\frac{\delta}{s_{QG}}\right)\right) + F_{QG}^{\Delta}\left(\frac{\Delta}{s_{QG}}\right) \end{aligned} \tag{3.3.24}$$

with the $\delta$ independent function $F_{QG}^{\Delta}$ given by,

$$\begin{aligned} F_{QG}^{\Delta}(x) &= \left(\frac{\alpha_s N}{2\pi}\right)\left(-\ln^2(x) + \frac{19x}{6} - \frac{x^2}{6} + \frac{x^3}{9} - 2\mathrm{Li}_2(x)\right. \\ &\quad \left. + \left(\frac{10}{6} - 2x + \frac{x^2}{2} - \frac{x^3}{6}\right)\ln\left(\frac{1-x}{x}\right)\right). \end{aligned} \tag{3.3.25}$$

Antennae containing a gluon and an antiquark are described by,

$$A_{gg\bar{q}} = A_{qgg}(a \leftrightarrow b), \tag{3.3.26}$$

and,

$$F_{G\bar{Q}}(s_{G\bar{Q}}) = F_{QG}(s_{G\bar{Q}}). \tag{3.3.27}$$

### 3.3.5 Gluon-Gluon antenna

For antenna comprising only gluons, we repeat this SUSY inspired trick for each of the resolved gluons so that,

$$A_{ggg} = A_{qg\bar{q}} - \frac{2}{s_{aub}}\left(\frac{x_{au}^2}{x_{ub}x_{aub}} + \frac{x_{ub}^2}{x_{au}x_{aub}}\right). \tag{3.3.28}$$

It is noted in passing that Kosower [46] has proposed an antenna factorisation for gluonic processes,

$$A_{ggg}^{\text{Kosower}} = \frac{4}{s_{aub}}\left(\frac{(x_{aub}(x_{aub} - x_{ab}) + x_{ab}^2)^2}{x_{au}x_{ub}x_{ab}x_{sub}}\right), \tag{3.3.29}$$

which, in the $u/b$ collinear limit regenerates the full $P_{gg\to g}$ splitting function, as well as the soft limits.

Integration of the antenna function $A_{ggg}$ over the whole of the subtraction region yields,

$$\begin{aligned} F_{GG}(s_{GG}) &= \left(\frac{g^2N}{2}\right)\int A_{ggg}dPS^{\text{sing}} \\ &= \left(\frac{\alpha_s N}{2\pi}\right)\left(\ln^2\left(\frac{\delta}{s_{GG}}\right) + \frac{11}{6}\ln\left(\frac{\delta}{s_{GG}}\right)\right) + F_{GG}^{\Delta}\left(\frac{\Delta}{s_{GG}}\right) \end{aligned} \tag{3.3.30}$$

with the $\delta$ independent function $F^{\Delta}_{GG}$ given by,

$$F^{\Delta}_{GG}(x) = \left(\frac{\alpha_s N}{2\pi}\right)\left(-\ln^2(x) + \frac{23x}{6} - \frac{2x^2}{6} + \frac{2x^3}{9} - 2\mathrm{Li}_2(x) + \left(\frac{11}{6} - 2x + \frac{x^2}{2} - \frac{x^3}{3}\right)\ln\left(\frac{1-x}{x}\right)\right). \tag{3.3.31}$$

### 3.3.6 Antenna where a quark-antiquark pair merge

There are also configurations when two (or more) colour lines are present. Here the matrix elements have the form,

$$|S_\mu(..., a, \overline{q}|q, b, ...)V^\mu|^2. \tag{3.3.32}$$

In the collinear limit, the quark-antiquark pinch the two colour lines together to form a single colour line,

$$|S_\mu(..., a, \overline{q}|q, b, ...)V^\mu|^2 \to P_{\overline{q}q\to g}(z, s_{\overline{q}q})|S_\mu(..., a, G, b, ...)V^\mu|^2, \tag{3.3.33}$$

with $P_{\overline{q}q\to G}(z, s)$ given by Equation 2.3.54. There is no soft singularity, nor is there any dependence on the type of adjacent parton, $a$ or $b$. Clearly, the quark-antiquark pair can sit in two antennae, $(a, \overline{q}, q)$ and $(\overline{q}, q, b)$ and we have some freedom of how to assign the singularities to the antennae. There are two obvious choices. Either we divide the singular contribution equally over the two antennae, or, we place the $z^2$ part of $P_{\overline{q}q\to g}(z)$ in one antenna and the $(1-z)^2$ part in the other (as we did with the three gluon antenna before). While there appears to be no preference, we follow this latter route so that the antenna function vanishes as the unresolved particle becomes soft,

$$A_{a\overline{q}q} = \frac{2}{s_{a\overline{q}q}}\left(\frac{x^2_{a\overline{q}}}{x_{\overline{q}q}x_{a\overline{q}q}}\right), \tag{3.3.34}$$

and,

$$A_{\bar{q}qb} = A_{a\bar{q}q}(x_{a\bar{q}} \to x_{qb}, x_{a\bar{q}q} \leftrightarrow x_{\bar{q}qb}). \tag{3.3.35}$$

Following this procedure and integrating over the whole of the subtraction region yields,

$$\begin{aligned} F_{aG}^{N_F}(s_{aG}) &= \left(\frac{g^2 N_F}{2}\right) \int A_{a\bar{q}q} dPS^{\text{sing}} \\ &= \left(\frac{\alpha_s N_F}{2\pi}\right) \left(-\frac{1}{6} \ln\left(\frac{\delta}{s_{aG}}\right)\right) + F_{aG}^{N_F \Delta}\left(\frac{\Delta}{s_{aG}}\right), \end{aligned} \tag{3.3.36}$$

and,

$$F_{Gb}^{N_F}(s_{Gb}) = F_{aG}^{N_F}(s_{Gb}). \tag{3.3.37}$$

The factor of $N_F$ arises because each of the $N_F$ quark flavours may contribute. The $\delta$ independent function is,

$$\begin{aligned} F_{aG}^{N_F \Delta}(x) &= F_{Gb}^{N_F \Delta}(x) \\ &= \left(\frac{\alpha_s N_F}{2\pi}\right) \left(-\frac{2x}{3} + \frac{x^2}{6} - \frac{x^3}{9} - \left(\frac{1}{6} - \frac{x^3}{6}\right) \ln\left(\frac{1-x}{x}\right)\right). \end{aligned} \tag{3.3.38}$$

## 3.4 Summary

In this chapter we have attempted to detail the problems inherent in calculating NLO observables due to the complex, divergent integrals that need to be numerically evaluated. We have outlined three techniques that have been used in the literature and seen the benefits and failings of these prescriptions. We have choosen to use hybrid subtraction for the main

calculations of the thesis. We have seen earlier that some phase space mappings lead to ambiguities in the massless nature of the final combined partons and so we have choosen to use a phase space mapping procedure proposed by Kosower which is smooth and symmetric over the entire range of phase space and produces massless final combined partons.

In this chapter we have also introduced the concept of the antenna, as two hard partons that are colour connected and from which a third irresolvable parton is emitted. This leads to the prescription of evaluating subtraction functions for each antenna so that we have universal functions that can be used for any QCD process. For the simplest antenna, that of a quark and an antiquark emitting a gluon, we use the scaled squared matrix element for the process $e^+e^- \to q\bar{q}g$. This has the right singular behaviour and is smooth over the entire phase space region. For the more complex quark-gluon-gluon and three gluon antennae, we can make use of the $N = 1$ supersymmetric identity that relates the Altarelli-Paresi splitting functions. The problem for these antennae is the ambiguity of which antenna contains which divergences. By splitting the two singluar regions of the $P_{gg\to g}$ between the two antennae (and including a term from the $P_{q\bar{q}\to g}$ splitting function), we arrive at expressions that have the correct singular behaviour and that smoothly link the soft and collinear regions. By combining all the antennae functions for a squared matrix element, the whole of the gluon splitting function is recovered.

# Chapter 4

# Matrix elements/subtraction terms for the calculation of $e^+ e^- \to 4$ jets

## 4.1 Introduction

We now collect together all of the ideas covered in the preceding chapters in order to calculate the cross section of the process $e^+e^- \to 4$ jets. Once this has been formulated the calculation (and associated numerical routines) can be adapted to evaluate any infra-red safe, four jet-like observable. (We define a small group of such observables which have been implemented into the Monte Carlo already and which we compare with experimental data in Chapter 5.)

As we have seen, NLO calculations consist of virtual loop corrections and extra, unresolved parton contributions. However, at the four jet level, there are two different underlying processes. For the virtual loop corrections we must consider the loops that modify the tree level process $e^+e^- \to q\bar{q}gg$ and also the tree level processes $e^+e^- \to q\bar{q}Q\overline{Q}$ where the flavour of $q$ and $Q$ are not necessarily the same. Similarly, the extra unresolved parton contributions have terms derived from the processes $e^+e^- \to q\bar{q}ggg$ and $e^+e^- \to q\bar{q}Q\overline{Q}g$. Section 4.2 will briefly consider the relevant diagrams and squared matrix elements for the virtual terms, while Section 4.3 will repeat the process for the unresolved parton contribution. Section 4.4 will look at the symmetries of the sub processes and justify neglecting some of the terms, making the final calculation more compact. Finally Section 4.5 will make use of the antenna functions and phase space mapping derived in the last chapter to outline the finite terms multiplying the tree level processes after the analytic removal of the infra-red poles.

## 4.2 The virtual loop matrix elements

### 4.2.1 $e^+e^- \to q\bar{q}gg$

We begin by considering the relevant diagrams and related squared matrix elements for the tree level and 1 loop contribution to the sub process $e^+e^- \to q\bar{q}gg$. We outline the colour structure and show how the entire contribution can be written in terms of five independent colourless subamplitudes. The full squared matrix element for this process was first calculated by [66] and [63] independently using different methods (the basics of which we describe later). For more details on the loop integrals and pole structure necessary for this calculation the reader is referred to [66],[63],[64] and [65]. For the purpose of all these calculations we will concentrate on the QCD current, neglecting the well known leptonic current, $V^\mu$. It is easily replaced and we drop it solely to keep the notation compact.

As we have already shown in Section 2.3.7 the tree level matrix element for the process $Z/\gamma^\star \to q\bar{q}gg$ has a structure directly related to the process $q\bar{q} \to gg$. The virtual matrix element is also similar in form. Therefore we write the matrix element of each as

$$\mathcal{M}^n = \epsilon^\mu \epsilon^\nu \epsilon^\rho \mathcal{M}^n_{\mu\nu\rho} = eg^2 \left(\frac{g}{4\pi}\right)^{2n} \left[(t^{a_3}t^{a_4})\mathcal{M}^n_a(3,4) + (t^{a_4}t^{a_3})\mathcal{M}^n_a(4,3) + \frac{1}{2}\delta_{a_3a_4}\mathcal{M}^n_b(3,4)\right] \tag{4.2.1}$$

where $n = 0$ describes the tree level matrix element and $n = 1$ the 1 loop correction. The different gluon colours are given by $a_3$ and $a_4$ and the arguments of the functions, $\mathcal{M}$, indicate the ordering of the gluon emission e.g. $\mathcal{M}(3,4)$ has the gluon with momentum $p_3$ emitted before the gluon with momentum $p_4$. See Figure 4.1. For all the two gluon processes we fix the quark to have momentum $p_1$ and the antiquark momentum $p_2$. At tree level $\mathcal{M}^0_b(3,4) = 0$. The functions $\mathcal{M}^n_a(3,4)$, $\mathcal{M}^n_a(4,3)$ and $\mathcal{M}^n_b(3,4)$ can themselves be colour decomposed and at the 1 loop level are given by

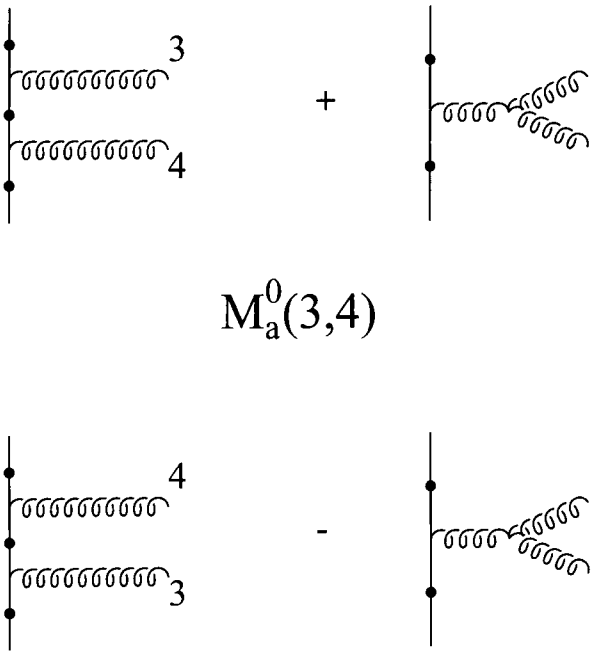


Figure 4.1: The relevant tree level Feynman diagrams for the process $Z/\gamma^\star \to q\bar{q}gg$. The top two diagrams have the gluon with momentum $p_3$ emitted before the gluon with momentum $p_4$ whereas in the bottom two diagrams the roles are reversed and the gluon with momentum $p_4$ is emitted before the gluon with momentum $p_3$. The solid black circles indicates the possible positions for the $Z/\gamma^\star$ vertex.

$$
\begin{aligned}
\mathcal{M}^1_a(3,4) &= N\,\mathcal{M}^1_A(3,4) - \frac{1}{N}\mathcal{M}^1_B(3,4) \\
\mathcal{M}^1_a(4,3) &= N\,\mathcal{M}^1_A(4,3) - \frac{1}{N}\mathcal{M}^1_B(4,3) \\
\mathcal{M}^1_b(3,4) &= \mathcal{M}^1_C(3,4) = \mathcal{M}^1_C(4,3)
\end{aligned}
\tag{4.2.2}
$$

where the colourless amplitudes $\mathcal{M}^1_A(i,j)$, $\mathcal{M}^1_B(i,j)$ and $\mathcal{M}^1_C(3,4)$ represent the combination of diagrams that give the same colour structure. Figures 4.2, 4.3 and 4.4 demonstrate the relevant diagrams for each of these amplitudes. This gives the following form for the tree level and 1-loop squared matrix elements. The tree level is expressed as

$$
\sum_{\text{spins}} |\mathcal{M}^0|^2 = \frac{e^2 g^4}{4}(N^2-1)N\left[\mathcal{S}(3,4) + \mathcal{S}(4,3) - \frac{1}{N^2}\mathcal{S}\right] \tag{4.2.3}
$$

where

$$
\begin{aligned}
\mathcal{S}(3,4) &= \sum_{\text{spins}} |(\mathcal{M}^0_a(3,4))^\dagger \mathcal{M}^0_a(3,4)| \\
\mathcal{S} &= \sum_{\text{spins}} |((\mathcal{M}^0_a(3,4))^\dagger + (\mathcal{M}^0_a(4,3))^\dagger)(\mathcal{M}^0_a(3,4) + \mathcal{M}^0_a(4,3))|
\end{aligned}
\tag{4.2.4}
$$

where $\mathcal{S}$ has no contribution from the triple gluon diagram as seen previously. For the 1 loop level we find

$$
\begin{aligned}
\sum_{\text{spins}} 2|(\mathcal{M}^0)^\dagger \mathcal{M}^1| &= \frac{e^2 g^4}{4}\left(\frac{\alpha_s N}{2\pi}\right)(N^2-1)N \\
&\quad \times \left[\mathcal{L}_A(3,4) + \mathcal{L}_A(4,3) - \frac{1}{N^2}(\mathcal{L}_A + \mathcal{L}_B(3,4) + \mathcal{L}_B(4,3) - \mathcal{L}_C) + \frac{1}{N^4}\mathcal{L}_B\right]
\end{aligned}
\tag{4.2.5}
$$

where we define the ordered structures and QED like contributions as

$$\begin{aligned}\mathcal{L}_i(3,4) &= \sum_{\text{spins}} \text{Re}[(\mathcal{M}_i^1(3,4))^\dagger \mathcal{M}_a^0(3,4)] \\ \mathcal{L}_i &= \sum_{\text{spins}} \text{Re}[((\mathcal{M}_i^1(3,4))^\dagger + (\mathcal{M}_i^1(4,3))^\dagger)(\mathcal{M}_a^0(3,4) + \mathcal{M}_a^0(4,3))] \qquad (4.2.6)\end{aligned}$$

Therefore we see that the 1 loop squared matrix element is composed of five independent functions which obey the following symmetry properties : $\mathcal{L}_i(3,4)$ remains unaltered after the exchange $p_1 \leftrightarrow p_2$ and $p_3 \leftrightarrow p_4$ whereas $\mathcal{L}_i$ is symmetric after the rearrangement $p_1 \leftrightarrow p_2$ or $p_3 \leftrightarrow p_4$.

### 4.2.2 $e^+e^- \to q\bar{q}Q\overline{Q}$

The second part of the virtual contribution derives from the 1 loop correction to the process $e^+e^- \to q\bar{q}Q\overline{Q}$. Again, for a detailed account of the calculation the reader is referred to [67],[63],[64] and [65]. Here we shall detail the colour decompostion of the relevant diagrams, leaving the full result until it is implemented in a Monte Carlo program. We write the matrix elements of the tree level process ($n = 0$) and the one loop correction ($n = 1$) as

$$\begin{aligned}\mathcal{M}^n &= \frac{eg^2}{2}\left(\frac{g}{4\pi}\right)^{2n} \\ &\Bigg[\delta_{c_1\,c_4}\delta_{c_3\,c_2}\left(\mathcal{A}_1^n(Q_1;\overline{Q_2}) + \mathcal{A}_1^n(Q_3;\overline{Q_4}) + \frac{\delta_{qQ}}{N}\left(\mathcal{A}_2^n(Q_1;\overline{Q_4}) + \mathcal{A}_2^n(Q_3;\overline{Q_2})\right)\right) \\ &- \delta_{c_1\,c_2}\delta_{c_3\,c_4}\left(\frac{1}{N}\left(\mathcal{A}_2^n(Q_1,\overline{Q_2}) + \mathcal{A}_2^n(Q_3,\overline{Q_4})\right) + \delta_{qQ}\left(\mathcal{A}_1^n(Q_1,\overline{Q_4}) + \mathcal{A}_1^n(Q_3,\overline{Q_2})\right)\right)\end{aligned} \qquad (4.2.7)$$

where $c_1..c_4$ are the quark colours and the arguments of $\mathcal{A}_i^n$ indicate the location of the $Z/\gamma$ vertex and thus the relevant charge associated with the matrix element e.g. $\mathcal{A}_1^0(Q_1,\overline{Q_2})$ refers to the diagram where the gauge boson couples to the quark/antiquark pair with momenta $p_1$ and $p_2$ respectively. See Figure 4.5. The delta function $\delta_{qQ}$ is only non-zero for identical quark flavours (which allows the primary quark/antiquark pair to be $q\bar{q}, Q\overline{Q}, q\overline{Q}$ and $Q\bar{q}$ whereas non-identical quarks only form the first two combinations). For tree level $n = 0$ we find

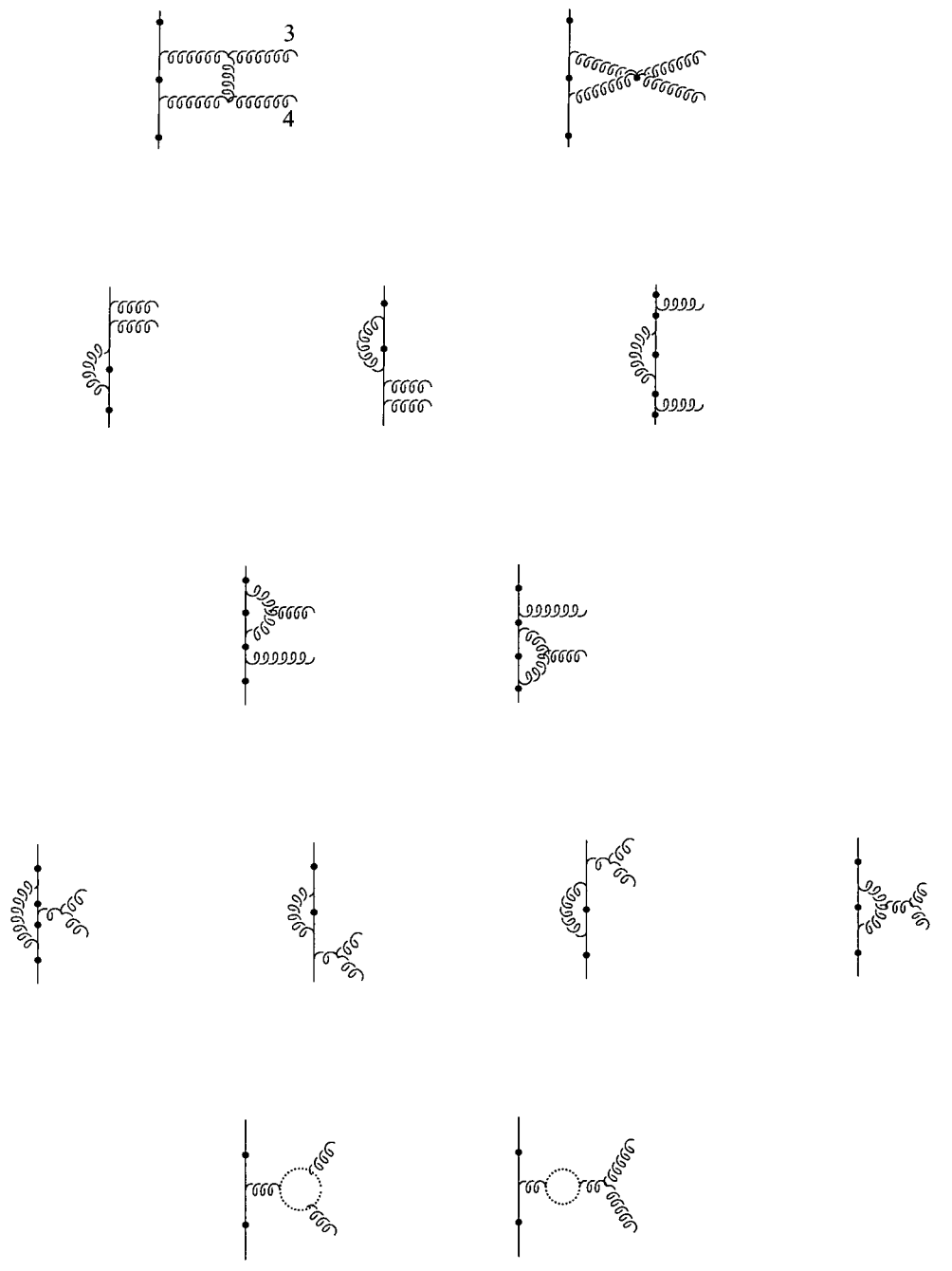


Figure 4.2: The set of Feynman diagrams responsible for the subamplitude function $\mathcal{M}_A^1(3,4)$ where we define the permutation of the gluons : from the top of the quark line, gluon 3 is the first encountered when reading around the diagram clockwise. As these diagrams represent the final state of the process, the virtual $Z/\gamma$ boson that is created in the electron positron collision attachs to these diagrams at the solid circle indicated (except in the second diagram where the solid circle along the gluon indicates a quartic gluon coupling). The dashed lines correspond to ghost loops. The top seven diagrams along with their $3 \leftrightarrow 4$ permutations contribute to $\mathcal{L}_A$ whereas all the diagrams contribute to $\mathcal{L}_A(3,4)$. In dimensional regularisation diagrams with external leg corrections are identically zero and therefore are not included here or in any of the other loop diagrams.

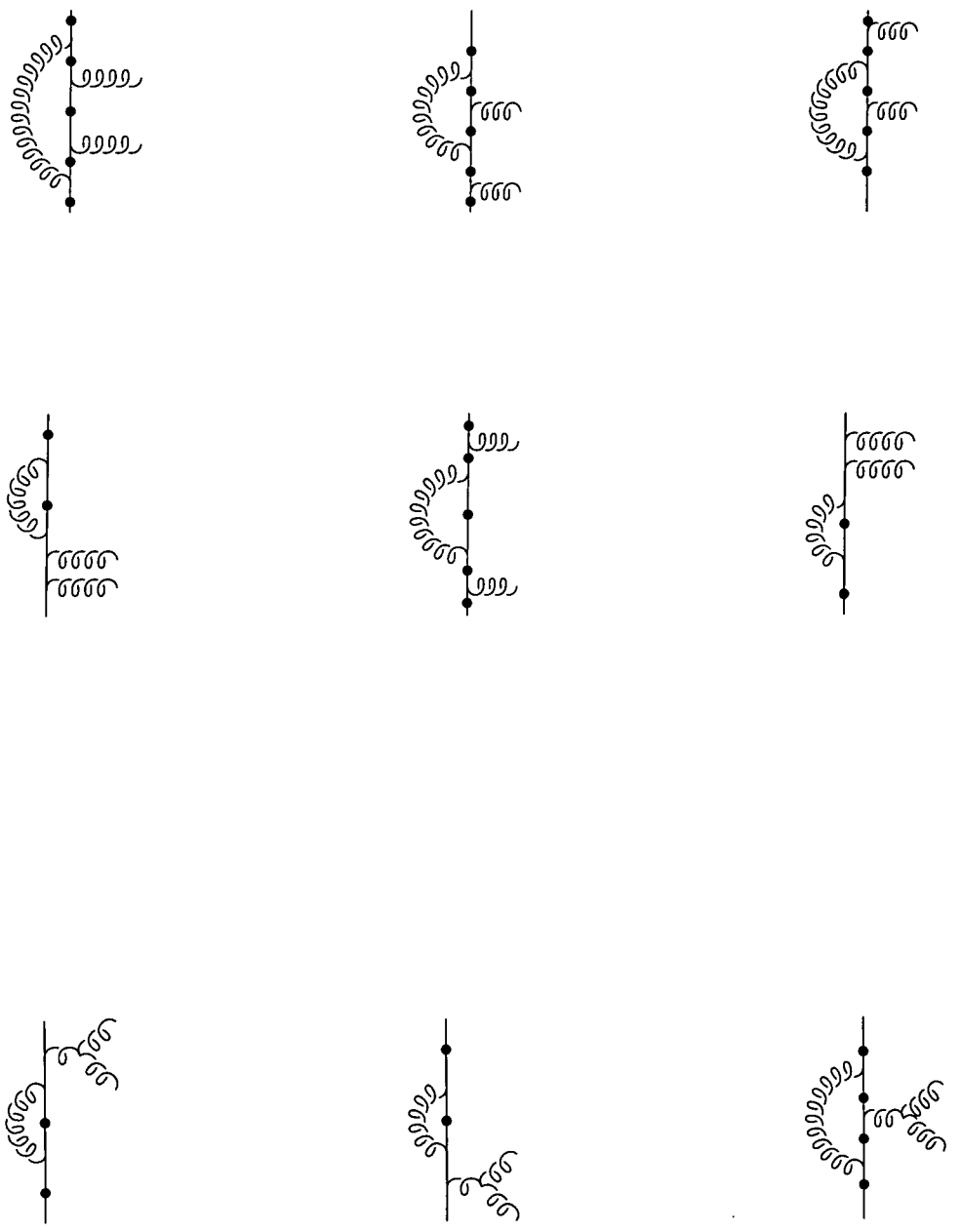

Figure 4.3: The set of Feynman diagrams responsible for the subamplitude function $\mathcal{M}_B^1(3,4)$ where we define the permutation of the gluons as such : from the top of the quark line, gluon 3 is the first encountered when reading around the diagram clockwise. As these diagrams represent the final state of the process, the virtual $Z/\gamma$ boson that is created in the electron positron collision attachs to these diagrams at the solid circle indicated. The top six diagrams alone contribute to $\mathcal{L}_B$ whereas all the diagrams contribute to $\mathcal{L}_B(3,4)$.

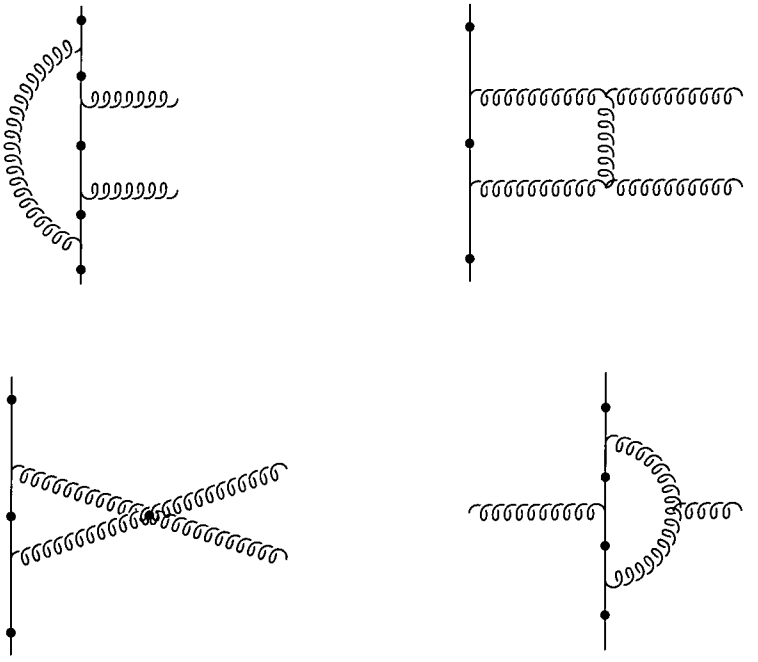

Figure 4.4: The set of Feynman diagrams responsible for the subamplitude function $\mathcal{M}_C^1(3,4)$ where we define the permutation of the gluons as such : from the top of the quark line, gluon 3 is the first encountered when reading around the diagram clockwise. As these diagrams represent the final state of the process, the virtual $Z/\gamma$ boson that is created in the electron positron collision attachs to these diagrams at the solid circle indicated. All the diagrams contribute to $\mathcal{L}_C$.

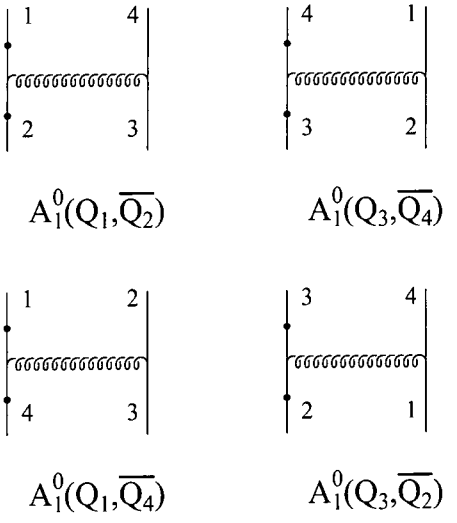


Figure 4.5: The relevant Feynman diagrams for the tree level process $Z/\gamma^\star \to q\bar{q}Q\overline{Q}$ where the flavour of the quarks can be identical or different. The first diagram has the $Z/\gamma^\star$ vertex attached to the quark line consisting of a quark with momentum $p_1$ and an antiquark with momentum $p_2$. This we denote with the symbol $\mathcal{A}_1^0(1,2)$. Similarly, the second diagram has the gauge boson vertex attached to the quark line consisting of a quark with momentum $p_3$ and an antiquark with momentum $p_4$. This is denoted with the symbol $\mathcal{A}_1^0(3,4)$. The third and fourth diagrams are only valid for processes with identically flavoured quark/antiquark pairs where we exchange $p_2 \leftrightarrow p_4$ for the third diagram (compared to the first diagram) and $p_1 \leftrightarrow p_3$ for the fourth diagram.

$$\mathcal{A}_1^0(i,j) = \mathcal{A}_2^0(i,j) \tag{4.2.8}$$

whereas at the one loop level $n = 1$, we can further colour decompose the $\mathcal{A}_i$ functions such that

$$\begin{aligned}
\mathcal{A}_1^1(i,j) &= N\mathcal{A}_C^1(i,j) - \frac{1}{N}(2\mathcal{A}_A^1(i,j) + \mathcal{A}_B^1(i,j)) \\
\mathcal{A}_2^1(i,j) &= N(\mathcal{A}_C^1(i,j) - \mathcal{A}_A^1(i,j)) - \frac{1}{N}(\mathcal{A}_A^1(i,j) + \mathcal{A}_B^1(i,j))
\end{aligned} \tag{4.2.9}$$

As before we form three groups of diagrams, $\mathcal{A}_A^1(i,j), \mathcal{A}_B^1(i,j)$ and $\mathcal{A}_C^1(i,j)$ which have the same colour structure and these are shown in Figure 4.6. One set of diagrams which we may have naively expected to be contributing are the closed fermion triangles, but according to Furry's theorem (a consequence of charge conjugation) these are identically zero i.e. QCD is charge conjugation invariant and the contributions for fermions circulating clockwise and anticlockwise cancel. Now let us consider the squared matrix elements. At tree level these are given by [68],

$$\begin{aligned}
\sum_{\text{spins}} \; |\mathcal{M}^0|^2 &= \frac{e^2 g^4}{4}(N^2-1) \\
&\times \left[\mathcal{T}(Q_1,\overline{Q_2};Q_1,\overline{Q_2}) + \mathcal{T}(Q_1,\overline{Q_2};Q_3,\overline{Q_4}) + \frac{\delta_{qQ}}{N}\left(\mathcal{T}(Q_1,\overline{Q_2};Q_1,\overline{Q_4}) + \mathcal{T}(Q_1,\overline{Q_2};Q_3,\overline{Q_2})\right)\right. \\
&+ \left.(Q_1 \leftrightarrow Q_3, \overline{Q_2} \leftrightarrow \overline{Q_4}) + \delta_{qQ}(\overline{Q_2} \leftrightarrow \overline{Q_4}) + \delta_{qQ}(Q_1 \leftrightarrow Q_3)\right]
\end{aligned} \tag{4.2.10}$$

where the arguments of the functions indicate the position of the $Z/\gamma$ vertex i.e. $\mathcal{T}(Q_1,\overline{Q_2};Q_1,\overline{Q_2})$ indicates the $Z/\gamma$ is attacted to the $q\bar{q}$ quark line (as opposed to the $Q\overline{Q}$ quark line) for both the matrix element and its conjugate whereas $\mathcal{T}(Q_1,\overline{Q_2};Q_3,\overline{Q_4})$ has the $Z/\gamma$ linking a $q\bar{q}$ line in the matrix element to a $Q\overline{Q}$ line in the conjugate.

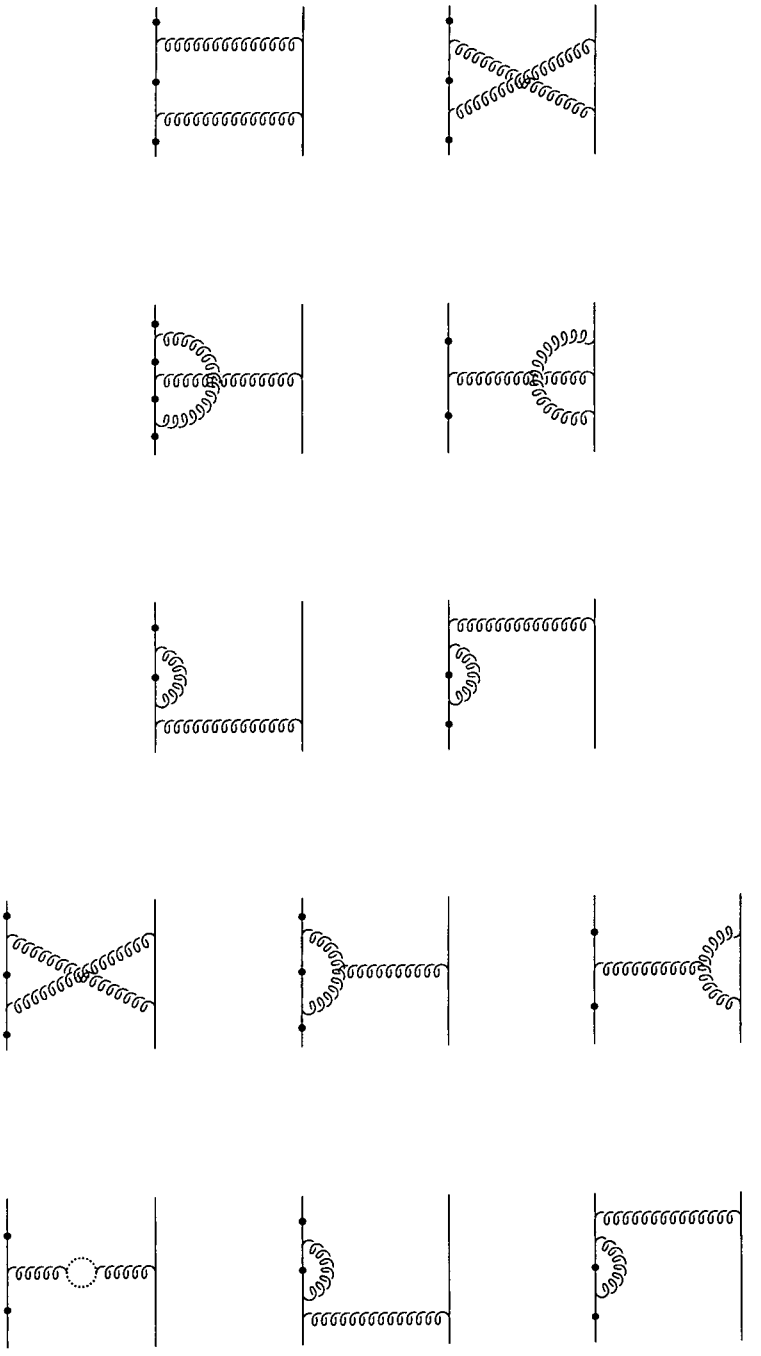

Figure 4.6: The set of Feynman diagrams responsible for the subamplitude functions $\mathcal{A}_A(i,j), \mathcal{A}_B(i,j)$ and $\mathcal{A}_C(i,j)$ where the top two diagrams are represented by $\mathcal{A}_A(i,j)$, the middle four are represented by $\mathcal{A}_B(i,j)$ and the last six are represented by $\mathcal{A}_C(i,j)$. The solid circle indicates the position of the initial $Z/\gamma$ boson.

For the one-loop squared matrix elements we write

$$\begin{aligned}
\sum_{\text{spins}} 2\,|\mathcal{M}^{(0)\dagger}M^1| = \frac{e^2g^4}{4}\left(\frac{\alpha_s N}{2\pi}\right)(N^2-1) \\
\Big(\Big[(\mathcal{L}_C(1,2;1,2)+\mathcal{L}_C(1,2;3,4)) \\
- \frac{1}{N^2}(2\mathcal{L}_A(1,2;1,2)+2\mathcal{L}_A(1,2;3,4)+\mathcal{L}_B(1,2;1,2)+\mathcal{L}_B(1,2;3,4))\Big] \\
+ \delta_{qQ}\Big[\frac{1}{N}(\mathcal{L}_C(1,2;1,4)+\mathcal{L}_C(1,2;3,2)-\mathcal{L}_A(1,2;1,4)-\mathcal{L}_A(1,2;3,2)) \\
- \frac{1}{N^3}(\mathcal{L}_A(1,2;1,4)+\mathcal{L}_A(1,2;3,2)+\mathcal{L}_B(1,2;1,4)+\mathcal{L}_B(1,2;3,2))\Big] \\
+ (Q_1 \leftrightarrow Q_3, \overline{Q_2} \leftrightarrow \overline{Q_4}) + \delta_{qQ}(\overline{Q_2} \leftrightarrow \overline{Q_4}) + \delta_{qQ}(Q_1 \leftrightarrow Q_3)\Big)
\end{aligned} \tag{4.2.11}$$

where

$$\mathcal{L}_\alpha(i,j;k,l) = \sum_{\text{spins}} |\mathcal{A}_\alpha^{(1)\dagger}(Q_i,\overline{Q_j})\mathcal{A}^0(Q_k,\overline{Q_l})| \tag{4.2.12}$$

Making use of crossing symmetry we find that $\mathcal{L}_\alpha(1,2;3,2)$ and $\mathcal{L}_\alpha(1,2;1,4)$ are related and thus the squared matrix element at the one loop level for the process $e^+e^- \to q\bar{q}Q\overline{Q}$ is given by 9 independent functions.

To calculate the virtual corrections to the 4 jet process, two separate techniques have been developed. For this thesis, we have used the squared matrix elements of [66] and [67] which utilise the usual prescription of conventional Feynman diagrams and the reduction of tensor integrals in $d$ dimensions. The virtual contribution was also calculated separately by the group of Bern, Dixon, Kosower and Weinzierl (BDKW) [63],[64] and [65]. The BDKW calculation differed in approach in that it was performed directly in the helicity amplitude approach using dimensional reduction, appealing to the analytic structure of the amplitudes and unitarity. This allowed the amplitudes to be fully described from specific collinear limits. The two results have been shown to be consistent with each other (see [47]).

## 4.3 The unresolved parton matrix elements

### 4.3.1 $e^+e^- \to q\bar{q}ggg$

As we have seen before, the matrix elements of multi-gluon emissions can be simply colour decomposed into a colour factor that is related to the permutations and colour connections of the gluons and a colourless subamplitude which contains the kinematical information about the diagram. For the NLO calculation of the process $e^+e^- \to 4$jets we write the hadronic current of the extra, unresolved contribution as

$$\hat{\mathcal{S}}_\mu(Q_1;1,2,3;\overline{Q_2}) = ieg^3 \sum_{P(1,2,3)} (t^{a1}t^{a2}t^{a3})_{c1\,c2}\mathcal{S}_\mu(Q_1;1,2,3;\overline{Q_2}) \tag{4.3.13}$$

where $a_1, a_2$ and $a_3$ are the colours of the three gluons and $c_1$ and $c_2$ are the quark/antiquark colours. As we have seen before, the permutations of colour matrices create the colour factor and $\mathcal{S}_\mu(Q_1;1,2,3;\overline{Q_2})$ describes the kinematical, gluon ordered subamplitude where a gluon with momentum $p_1$ is emitted first followed by a gluon with momentum $p_2$ and finally a gluon with momentum $p_3$ is emitted. The Feynman diagrams relevant to this subamplitude are shown in Figure 4.7. This then gives, when squared

$$\begin{aligned} |\hat{\mathcal{S}}_\mu V^\mu|^2 &= e^2\left(\frac{g^2N}{2}\right)^3\left(\frac{N^2-1}{N}\right) \\ &\quad\left[\sum_{P(1,2,3)}\left(|\mathcal{S}_\mu(Q_1;1,2,3;\overline{Q_2})V^\mu|^2 - \frac{1}{N^2}|\mathcal{S}_\mu(Q_1;1,2,\tilde{3};\overline{Q_2})V^\mu|^2\right)\right. \\ &+ \left.\left(\frac{N^2+1}{N^4}\right)|\mathcal{S}_\mu(Q_1;\tilde{1},\tilde{2},\tilde{3};\overline{Q_2})V^\mu|^2\right] \end{aligned} \tag{4.3.14}$$

where $V^\mu$ is the well-known QED electron current. As usual, the tilde on the gluon indicates its colour detachment from the rest of the gluons and as such it can be placed anywhere along the quark line e.g

$$\mathcal{S}_\mu(Q_1;1,2,\tilde{3};\overline{Q_2}) = \mathcal{S}_\mu(Q_1;1,2,3;\overline{Q_2}) + \mathcal{S}_\mu(Q_1;1,3,2;\overline{Q_2}) + \mathcal{S}_\mu(Q_1;3,1,2;\overline{Q_2}) \tag{4.3.15}$$

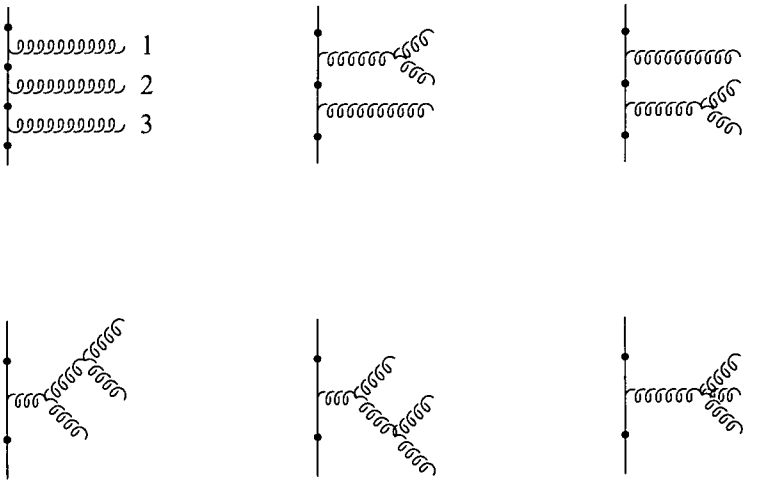


Figure 4.7: The Feynman diagrams contributing to the colourless subamplitude $\mathcal{S}_\mu(Q_1;1,2,3;\overline{Q_2})$. As indicated the ordering is such that a gluon with momentum $p_1$ is at the extreme top of the diagram, a gluon with momentum $p_2$ is next followed by a gluon with momentum $p_3$. The off-shell $\gamma/Z$ from the $e^+e^-$ annihilation attacts at the sites indicated by the solid circle. By combining different permutations of gluons, these diagrams can lead to cancellations such as for $\mathcal{S}_\mu(Q_1;1,2,\tilde{3};\overline{Q_2})$ where all the diagrams in which gluon $p_3$ couples to another gluon cancel and $\mathcal{S}_\mu(Q_1;\tilde{1},\tilde{2},\tilde{3};\overline{Q_2})$ where all triple gluon couplings cancel. This is analogous to the example we saw for $q\bar{q}\to gg$ where the two triple gluon diagrams cancelled for $\mathcal{S}_\mu(Q_1;\tilde{g},\tilde{g};\overline{Q_2})$.

### 4.3.2 $e^+e^- \to q\bar{q}Q\overline{Q}g$

The final contribution to the NLO calculation is that of the unresolved parton to the tree level process $e^+e^- \to q\bar{q}Q\overline{Q}$. This again may be colour decomposed to give colourless subamplitudes. Here we use a slightly different notation compared to the process $e^+e^- \to q\bar{q}Q\overline{Q}$ in order to clarify the various subamplitudes that combine to give the same colour structure. The form of the matrix element is given by

$$\begin{aligned}\widehat{\mathcal{T}}(Q_1,\overline{Q_2};Q_3,\overline{Q_4};1) &= i\frac{eg^3}{2}\left[t^{a1}_{c_1\,c_4}\delta_{c_3\,c_2}\mathcal{R}(Q_1,\overline{Q_2};Q_3,\overline{Q_4};1)+(Q_1\leftrightarrow Q_3;\overline{Q_3}\leftrightarrow\overline{Q_4})\right.\\ &- \left.(Q_1\leftrightarrow Q_3)-(\overline{Q_2}\leftrightarrow\overline{Q_4})\right] \qquad (4.3.16)\end{aligned}$$

where $c_1..c_4$ are the colours of the quarks (these are also affected by the symmetries) and $a_1$ is the gluon colour. Here as with the loop correction we label the two quarks, $q$ and $Q$ with momenta $p_1$ and $p_3$ respectively and the two antiquarks $\bar{q}$ and $\overline{Q}$ with momenta $p_2$ and $p_4$ respectively. This current can be further broken down into different diagrams and colour factors such that

$$\begin{aligned}\mathcal{R}(Q_1,\overline{Q_2};Q_3,\overline{Q_4};1) &= \delta_{Q_1Q_2}\delta_{Q_3Q_4}R^A(Q_1,\overline{Q_2};Q_3,\overline{Q_4};1)\\ &+ \frac{1}{N}\delta_{Q_3Q_2}\delta_{Q_1Q_4}R^B(Q_1,\overline{Q_2};Q_3,\overline{Q_4};1) \qquad (4.3.17)\end{aligned}$$

where the delta functions indicate whether the quarks are the same flavour or not. Also

$$\begin{aligned}R^A(Q_1,\overline{Q_2};Q_3,\overline{Q_4};1) &= \mathcal{A}^{Q_1Q_2}(Q_1;1;\overline{Q_4}|Q_3;\overline{Q_2})+\mathcal{A}^{Q_3Q_4}(Q_3;\overline{Q_2}|Q_1;1;\overline{Q_4})\\ R^B(Q_1,\overline{Q_2};Q_3,\overline{Q_4};1) &= \mathcal{B}^{Q_1Q_4}(Q_1;1;\overline{Q_4}|Q_3;\overline{Q_2})+\mathcal{B}^{Q_3Q_2}(Q_3;\overline{Q_2}|Q_1;1;\overline{Q_4})\end{aligned} \qquad (4.3.18)$$

The difference between these two functions is the direction of colour flow and where the vector boson is attached. This in turn dictates which partons can form colour antennae, the

electric charge of the quark coupling to the photon and the colour factor for the singular contribution where the antennae partons become collinear with the gluon. The superscripts on $\mathcal{A}$ and $\mathcal{B}$ give the quark line to which the photon couples such that $\mathcal{A}_\mu^{Q_1Q_2}$ has the photon attached somewhere along the quark line between quark 1 and antiquark 2. However, the colour antenna for $\mathcal{A}_\mu^{Q_1Q_2}$ is formed between quark 1 and antiquark 4 such that colour is transmitted through the gluon propagator whereas the colour antenna for $\mathcal{B}_\mu^{Q_1Q_4}$ lies between quark 1 and antiquark 4 with no colour being carried by the gluon. The relevant diagrams for each of these functions are shown in Figure 4.8.

The squared matrix element is given by

$$\begin{aligned}
|\widehat{\mathcal{T}}|^2 &= e^2\left(\frac{g^2N}{2}\right)^3\left(\frac{N^2-1}{N^2}\right) \\
&\times \Big[|\mathcal{R}(Q_1,\overline{Q_2};Q_3,\overline{Q_4};1)|^2+|\mathcal{R}(Q_1,\overline{Q_4};Q_3,\overline{Q_2};1)|^2 \\
&- \frac{2}{N}\mathrm{Re}(\mathcal{R}(\mathrm{Q_1},\overline{\mathrm{Q_2}};\mathrm{Q_3},\overline{\mathrm{Q_4}};1)+\mathcal{R}(\mathrm{Q_3},\overline{\mathrm{Q_4}};\mathrm{Q_1},\overline{\mathrm{Q_2}};1))(\mathcal{R}(\mathrm{Q_1},\overline{\mathrm{Q_4}};\mathrm{Q_3},\overline{\mathrm{Q_2}};1))^\dagger\Big] \\
&+ (Q_1\leftrightarrow Q_3,\overline{Q_2}\leftrightarrow\overline{Q_4})
\end{aligned} \tag{4.3.19}$$

where terms of the form $\mathcal{R}(Q_1,\overline{Q_2};Q_3,\overline{Q_4};1)(\mathcal{R}(Q_3,\overline{Q_4};Q_1,\overline{Q_2};1))^\dagger$ are zero due to the traceless nature of the colour matrices. We can rewrite to display all the colour factors as

$$\begin{aligned}
|\widehat{\mathcal{R}}|^2 &= e^2\left(\frac{g^2N}{2}\right)^3\left(\frac{N^2-1}{N^2}\right) \\
&\times \Big[|\mathcal{R}^A(Q_1,\overline{Q_2};Q_3,\overline{Q_4};1)|^2 \\
&+ \frac{1}{N^2}(|\mathcal{R}^B(Q_1,\overline{Q_4};Q_3,\overline{Q_2};1)|^2-|\overline{\mathcal{R}}(Q_1,\overline{Q_2};Q_3,\overline{Q_4};1)|^2) \\
&+ \frac{2\delta_{Q_1Q_3}}{N}\mathrm{Re}(\mathcal{R}^{\mathrm{A}}(\mathrm{Q_1},\overline{\mathrm{Q_2}};\mathrm{Q_3},\overline{\mathrm{Q_4}};1))(\mathcal{R}^{\mathrm{B}}(\mathrm{Q_1},\overline{\mathrm{Q_2}};\mathrm{Q_3},\overline{\mathrm{Q_4}};1))^\dagger \\
&- \frac{N^2+1}{2N^3}\delta_{Q_2Q_4}\mathrm{Re}(\overline{\mathcal{R}}(\mathrm{Q_1},\overline{\mathrm{Q_2}};\mathrm{Q_3},\overline{\mathrm{Q_4}};1))(\overline{\mathcal{R}}(\mathrm{Q_1},\overline{\mathrm{Q_4}};\mathrm{Q_3},\overline{\mathrm{Q_2}};1))^\dagger \\
&+ (Q_1\leftrightarrow Q_3,\overline{Q_2}\leftrightarrow\overline{Q_4})+\delta_{Q_1Q_3}(Q_1\leftrightarrow Q_3)+\delta_{Q_2Q_4}(\overline{Q_2}\leftrightarrow\overline{Q_4})\Big]
\end{aligned} \tag{4.3.20}$$

where

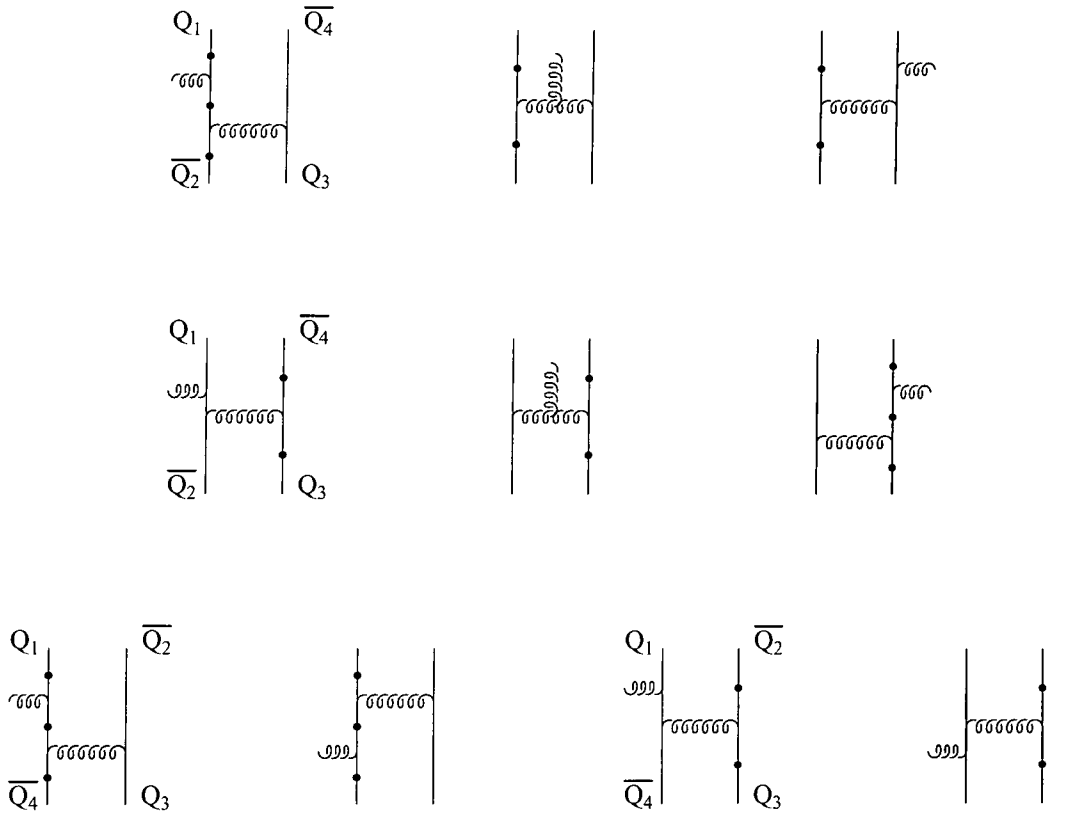


Figure 4.8: The Feynman diagrams contributing to the process $e^+e^- \to q\bar{q}Q\overline{Q}g$. The top three diagrams form the colourless subcurrent $\mathcal{A}_\mu^{Q_1Q_2}(Q_1;1;\overline{Q_4}|Q_3;\overline{Q_2})$, the next three form $\mathcal{A}_\mu^{Q_3Q_4}(Q_3;\overline{Q_2}|Q_1;1;\overline{Q_4})$, the first two diagrams on the bottom line form $\mathcal{B}_\mu^{Q_1Q_4}(Q_1;1;\overline{Q_4}|Q_3;\overline{Q_2})$ and the last two form $\mathcal{B}_\mu^{Q_3Q_2}(Q_3;\overline{Q_2}|Q_1;1;\overline{Q_4})$. The photon propagator couples to this final state current at the solid circles.

$$\begin{aligned}\overline{\mathcal{R}}(Q_1,\overline{Q_2};Q_3,\overline{Q_4};1) &= \mathcal{R}^A(Q_1,\overline{Q_2};Q_3,\overline{Q_4};1)+\mathcal{R}^A(Q_3,\overline{Q_4};Q_1,\overline{Q_2};1)\\ &= \mathcal{R}^B(Q_1,\overline{Q_4};Q_3,\overline{Q_2};1)+\mathcal{R}^B(Q_3,\overline{Q_2};Q_1,\overline{Q_4};1)\end{aligned} \quad (4.3.21)$$

## 4.4 Symmetries and negligible contributions

Although we have outlined all the possible sources which contribute to the cross section of the NLO calculation of $e^+e^- \to 4$ jets, we can make the numerical evaluation simpler by counting the symmetries inherent in the matrix elements. This reduces the number of

functions it is necessary to evaluate. Also, after phase space integration it can be shown that some contributions partially cancel and can thus be thought of as negligible for the rest of the calculation.

### 4.4.1 Negligible contributions

We begin by considering the four quark virtual terms. At tree level the $q\bar{q}Q\overline{Q}$ process has four diagrams that contribute to the squared matrix element term $\mathcal{T}(1,2;3,4)$. It can be seen that two of the contributing diagrams are related by the reversal of the $Q_3\overline{Q_4}$ quark line. (See Figure 4.9). If the cut between the matrix element and the conjugate was not present we would set this contribution to zero by Furry's theorem. However, as the quarks are indistinguishable, we find after phase space integration this leads to a cancellation between the diagrams because for each contribution from the first diagram's squared matrix element, an equal and opposite contribution can be found for the second diagram at a different phase space point. A similiar argument is used for the 1-loop level corrections. The cancellation for the 1-loop correction is not perfect and the resultant contribution is not zero, but is small enough to be thought of as negligible[48]. Therefore we treat terms of the form $\mathcal{L}(1,2;3,4)$ as negligible.

The only other contribution that we treat as negligible is part of the contribution to the subprocess $q\bar{q}Q\overline{Q}g$. In the same way as for the virtual term we shall not calculate those terms for which different quark pairs couple to the photon in the matrix element and the conjugate i.e. we treat terms of the form $\mathcal{A}^{Q_1Q_2}(Q_1;1;\overline{Q_4}|Q_3;\overline{Q_2})\mathcal{A}^{Q_3Q_4}(Q_3;\overline{Q_2}|Q_1;1;\overline{Q_4})^\dagger$ as equal to zero.

### 4.4.2 Symmetry factors

Making use of symmetry factors we can simplify the calculation greatly by evaluating one function and then multiplying it by a factor dependent on the degree of symmetry. We already are familiar with summing over the $n_F$ active quark flavours and we also note that for $n$ identical particles in the final state we attribute a factor $1/n!$ to the function.

We begin with the symmetries for the tree level process $Z/\gamma^\star \to q\bar{q}Q\overline{Q}$. For identical



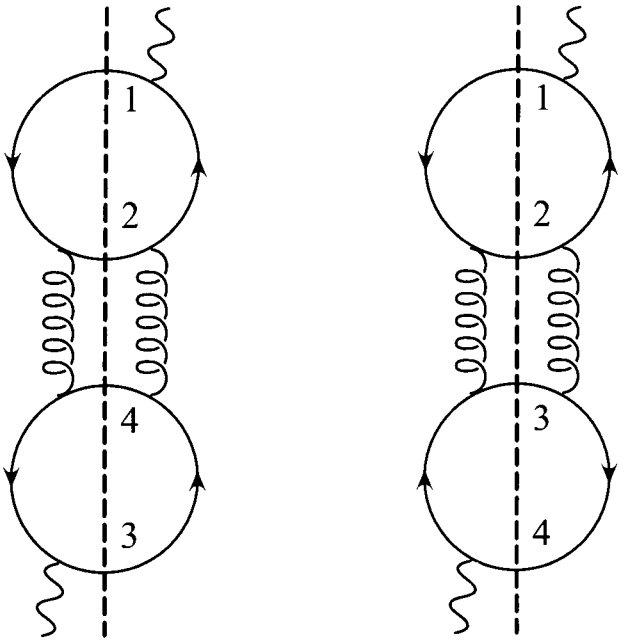


Figure 4.9: Two of the four diagrams that make up the four quark term $\mathcal{T}(1,2;3,4)$. The dotted line separates the matrix element from its conjugate.

final state quark pairs we must include a factor 1/4. This gives a symmetry factor of $n_F/4$ for matrix elements with identical quark flavours in the final state. Similarly there are $n_F(n_F-1)/2$ ways of choosing a pair of non-identical quarks in the final state. Collecting these all together we have

$$\mathcal{T}(1,2;1,2) \to 2 \times n_F(n_F-1)/2 + 4 \times n_F/4 = n_F^2 \tag{4.4.22}$$

where we have included the $1 \leftrightarrow 3$, $2 \leftrightarrow 4$ symmetry for the non-identical pairs and the $1 \leftrightarrow 3$, $2 \leftrightarrow 4$, the $1 \leftrightarrow 3$ and the $2 \leftrightarrow 4$ symmetries for the identical pair.

For the terms of the form $\mathcal{T}(1,2;1,4)$ (which only identical quark pairs contribute to) we have

$$\begin{aligned} \mathcal{T}(1,2;1,4) &\rightarrow 4 \times n_F/4 \\ \mathcal{T}(1,2;3,2) &\rightarrow 4 \times n_F/4 \end{aligned} \tag{4.4.23}$$

Note however that the term $\mathcal{T}(1,2;3,2)$ is generated by the symmetry $p_1 \leftrightarrow p_2, p_3 \leftrightarrow p_4$ from the term $\mathcal{T}(1,2;1,4)$. Therefore we put these together to form the single function, $\mathcal{T}(1,2;1,4)$ with symmetry factor $2n_F$.

For the one-loop correction to the process $Z/\gamma^\star \rightarrow q\overline{q}Q\overline{Q}$ the symmetries are identical giving

$$\begin{aligned} \mathcal{L}_i(1,2;1,2) + (1 \leftrightarrow 3, 2 \leftrightarrow 4 \text{ symmetry}) &\rightarrow n_F^2 \\ \mathcal{L}_i(1,2;1,4) + (1 \leftrightarrow 3, 2 \leftrightarrow 4 \text{ symmetry}) + (1 \leftrightarrow 3 \text{ symmetry}) &\rightarrow 2 \times n_F \\ +(2 \leftrightarrow 4 \text{ symmetry}) + (1 \leftrightarrow 2, 3 \leftrightarrow 4 \text{ symmetry}) & \end{aligned} \tag{4.4.24}$$

We now consider the symmetries of the other virtual term, that of the subprocess $q\overline{q}gg$. The tree level process can be written as two terms, $\mathcal{T}(3,4)$ and $\mathcal{T}$ which describe all possible terms when combined with their respective symmetry factors. The one loop factor is identical to the tree level term such that the ordered gluon term has an obvious symmetry under interchange of the gluons whereas the photon-like term has no such symmetry. Also a factor $1/2$ arises due to the identical nature of the gluons. Therefore we find

$$\begin{aligned} \mathcal{T}(3,4) + (3 \leftrightarrow 4 \text{ symmetry}) &\rightarrow 2 \times n_F/2 = n_F \\ \mathcal{T} &\rightarrow n_F/2 \end{aligned} \tag{4.4.25}$$

Extending this to the 1-loop correction gives

$$\begin{aligned} \mathcal{L}_i(3,4) + (3 \leftrightarrow 4 \text{ symmetry}) &\rightarrow 2 \times n_F/2 = n_F \\ \mathcal{L}_i &\rightarrow n_F/2 \end{aligned} \tag{4.4.26}$$

The extra unresolved contributions to the NLO calculation also contain symmetries with which we can use to multiply a single term by a symmetry factor to account for all possible terms. The simplest case is that of the subprocess $q\bar{q}ggg$ where we have a single quark pair in the matrix element and a $1/3!$ factor due to the identical nature of the three gluons. For the leading order colour term there are six symmetric terms under the permutation of the ordered gluons but there is also the identical particle factor of $1/3!$. For the sub-leading colour term with only one colour detached gluon there are two symmetric terms under the permutation of the ordered gluons and also three symmetric terms due to the indistinguish nature of the colour detached gluon. This again gives 6 terms. Finally we have the most subleading colour term where all the gluons are colour detached. Here the single term already includes all the permutations and thus we only need consider the identical particle factor. More concisely this gives

$$\begin{aligned}
|\mathcal{S}_\mu(Q_1;1,2,3;\overline{Q_2})V^\mu|^2 &\to 6\times n_F/3! = n_F \\
|\mathcal{S}_\mu(Q_1;1,2,\tilde{3};\overline{Q_2})V^\mu|^2 &\to 6\times n_F/3! = n_F \\
|\mathcal{S}_\mu(Q_1;\tilde{1},\tilde{2},\tilde{3};\overline{Q_2})V^\mu|^2 &\to n_F/3! = n_F/6
\end{aligned} \tag{4.4.27}$$

Finally we consider the subprocess $Z/\gamma^\star \to q\bar{q}Q\overline{Q}g$. The symmetry factors associated with this process follow the same rules as for the tree level process without the gluon, with the same division of terms into those that are relevant for all flavoured pairs and those that are only relevant for non-identical flavoured quark pairs. Thus we find

$$\begin{aligned}
|\mathcal{A}_\mu^{Q_1Q_2}(Q_1;1;\overline{Q_4}|Q_3;\overline{Q_2})|^2 &\to 2\times n_F^2/2 = n_F^2 \\
|\mathcal{A}_\mu^{Q_1Q_2}(Q_1;\overline{Q_4}|Q_3;1;\overline{Q_2})|^2 &\to 2\times n_F^2/2 = n_F^2 \\
|\mathcal{B}_\mu^{Q_1Q_2}(Q_1;1;\overline{Q_2}|Q_3;\overline{Q_4})|^2 &\to 2\times n_F^2/2 = n_F^2 \\
|\mathcal{B}_\mu^{Q_1Q_2}(Q_1;\overline{Q_2}|Q_3;1;\overline{Q_4})|^2 &\to 2\times n_F^2/2 = n_F^2 \\
|\mathcal{A}_\mu^{Q_1Q_2}(Q_1;1;\overline{Q_4}|Q_3;\overline{Q_2}) + \mathcal{A}_\mu^{Q_1Q_2}(Q_1;\overline{Q_4}|Q_3;1;\overline{Q_2})|^2 &\to 4\times n_F^2/2 = 2n_F^2 \\
\mathrm{Re}(\mathcal{A}_\mu^{Q_1Q_2}(Q_1;1;\overline{Q_4}|Q_3;\overline{Q_2})(\mathcal{B}_\nu^{Q_1Q_4}(Q_1;1;\overline{Q_4}|Q_3;\overline{Q_2}))^\dagger &\to 4\times n_F/4 = n_F \\
\mathrm{Re}(\mathcal{A}_\mu^{Q_1Q_2}(Q_1;1;\overline{Q_4}|Q_3;\overline{Q_2}) + \mathcal{A}_\mu^{Q_1Q_2}(Q_1;\overline{Q_4}|Q_3;1;\overline{Q_2})) \times & \\
(\mathcal{A}_\mu^{Q_1Q_2}(Q_1;1;\overline{Q_2}|Q_3;\overline{Q_4}) + \mathcal{A}_\mu^{Q_1Q_2}(Q_1;\overline{Q_2}|Q_3;1;\overline{Q_4}))^\dagger &\to 16\times n_F/4 = 4n_F
\end{aligned} \tag{4.4.28}$$

where the factor two on the first four terms is due to the $(1 \leftrightarrow 3, 2 \leftrightarrow 4)$ symmetry. The factor in the fifth term is due to the symmetric nature nature of $\overline{\mathcal{T}}$ (which contributes a factor 2) and the $(1 \leftrightarrow 3, 2 \leftrightarrow 4)$ symmetry. These first five factors are all due to non-identical and identical quark pair contributions together. The sixth and seventh terms now introduce all the symmetries possible for identical quark pairs only i.e.$(1 \leftrightarrow 3, 2 \leftrightarrow 4)$, $(2 \leftrightarrow 4)$ and $(1 \leftrightarrow 3)$. All four of these make up the factor in the sixth term whereas in the seventh term a factor 4 comes from the symmetries and another factor 4 is due to the factor 2 symmetry from each $\overline{\mathcal{T}}$ term in the $\overline{\mathcal{T}}(Q_1, \overline{Q_2}; Q_3, \overline{Q_4})\overline{\mathcal{T}}(Q_1, \overline{Q_4}; Q_3, \overline{Q_3})^\dagger$ term.

## 4.5 Using hybrid subtraction for the NLO calculation of $e^+e^- \to 4$ jets

Now we are in a position to evaluate the relevant antennae functions necessary for the numerical NLO calculation of $e^+e^- \to 4$ jets and see how these can be implemented alongside the terms produced by the slicing technique after the removal of the singular regions of phase space. To begin with we shall consider the dominant leading colour contribution and then extend this to produce the full colour result. As we have seen before, the hybrid subtraction technique will be bounded by theoretical cut-offs which we call $\delta$ for the phase space slicing and both $\delta$ and $\Delta$ for the subtraction. All dependence on $\delta$ will cancel exactly and we can justify driving the cut-off, $\delta$ small such that the approximations made by the slicing technique are valid whilst not producing large logarithms. The logarithms will now be of the form $\log(\Delta)$ and thus we keep this cut-off large to keep the numerical cancellation of these logarithms stable.

Before we begin with the NLO contribution, we consider the LO form. This will multiply both the divergent factors from the virtual and extra parton contributions later. For leading colour, this is given by

$$\frac{d\sigma_4^{\mathrm{LO}}}{\sigma_0} = \frac{(2\pi)^5}{s}\left(\frac{N^2-1}{N^2}\right)\left(\frac{\alpha_s N}{2\pi}\right)^2 |\mathcal{S}_\mu(Q_1; G_1, G_2; \overline{Q_2})V^\mu|^2 dPS_4\Theta_4 \tag{4.5.29}$$

where only the final state $qgg\bar{q}$ contributes at leading order in colour. Here $\Theta_4$ is the phase space cuts defining the physical quantity e.g. $D$ parameter.

For the slicing contribution we consider the extra unresolved parton. Its squared matrix element is given in a very similar form as the above equation.

$$\frac{d\sigma_5}{\sigma_0} = \frac{(2\pi)^7}{s}\left(\frac{N^2-1}{N^2}\right)\left(\frac{\alpha_s N}{2\pi}\right)^3 |\mathcal{S}_\mu(q_1;g_1,g_2,g_3;\overline{q_2})V^\mu|^2 dPS_5\Theta_5 \tag{4.5.30}$$

We write the labels for the quarks and gluons differently to demonstrate how the three parton antennae collapse to form two hard partons later. We also note that for any infra-red safe observable in the four resolved parton limit $\Theta_4 = \Theta_5$. At this level of colour we note that all the triple and quartic gluon vertices are present, so that the three available antennae consist of the partons, $(q_1, g_1, g_2)$, $(g_1, g_2, g_3)$ and $(g_2, g_3, \overline{q_2})$ where $g_1$ is unresolved in the first, $g_2$ in the second and $g_3$ in the third. The invariant masses of the unresolved partons run over the range $0 < \min(s_{q_1 g_1}, s_{g_1 g_2}) < \delta$ for the first antenna and so on.

The slicing term (at leading order) is simply a divergent factor multiplied by the tree level contributions (with different phase space mappings relating them). The general form of this factor for final states $q\overline{q} + ng$ (where $n$ is the number of resolved gluons) is given in [36]. For our case ($n = 2$) we find the divergent factor is given by

$$\begin{aligned} R(Q_1;G_1,G_2;\overline{Q_2}) &= \left(\frac{\alpha_s N}{2\pi}\right)\frac{1}{\Gamma(1-\varepsilon)}\left[\sum_{i,j}\left(\frac{1}{\varepsilon^2}\left(\frac{4\pi\mu^2}{s_{ij}}\right)^\varepsilon - \log^2\left(\frac{s_{ij}}{\delta}\right)\right)\right. \\ &+ \left.\frac{3}{2\varepsilon}\left(\frac{4\pi\mu^2}{\delta}\right)^\varepsilon + \frac{197}{18} - \pi^2\right] \\ &+ \left(\frac{\alpha_s}{2\pi}\right)\frac{2b_0}{\varepsilon}\frac{1}{\Gamma(1-\varepsilon)}\left(\frac{4\pi\mu^2}{\delta}\right)^\varepsilon \end{aligned} \tag{4.5.31}$$

By summing over the colour connected pairs $i, j$ we retrieve all the divergent terms. Note that some terms are common to two antennae, e.g the poles and logarithms containing $s_{g_1 g_2}$ are found in both the first and second antennae.

Now we consider the subtraction terms that need to be added and subtracted from the two divergent terms. We have already seen that at leading colour there exist three separate antennae which leads to three separate subtraction terms, each with its own phase space

mapping from three partons to two using Equation 3.3.10. For instance in the first antenna, $a = q_1, b = g_2, u = g_1$, giving $A = Q_1$ and $B = G_1$. Kinematical cuts to model jet variables, $\Theta_4$ are made after this mapping. We find for the 5 parton subtraction term

$$\begin{aligned}\frac{d\sigma_5^{\text{sub}}}{\sigma_0} &= \frac{(2\pi)^7}{s}\left(\frac{N^2-1}{N}\right)\left(\frac{\alpha_s N}{2\pi}\right)^3 dPS_5\Theta_4 \\ &+ \Big(A_{q_1g_1g_2}|\mathcal{S}_\mu(Q_1;G_1,g_2;\overline{q_2})V^\mu|^2 \\ &+ A_{g_1g_2g_3}|\mathcal{S}_\mu(q_1;G_1,G_2;\overline{q_2})V^\mu|^2 \\ &+ A_{g_2g_3\overline{q_2}}|\mathcal{S}_\mu(q_1;g_1,G_2;\overline{Q_2})V^\mu|^2\Big)\end{aligned} \tag{4.5.32}$$

and for the 4 parton subtraction term we have

$$\frac{d\sigma_4^{\text{sub}}}{\sigma_0} = (F_{Q_1G_1} + F_{G_1G_2} + F_{G_2\overline{Q_2}})d\sigma_4^{\text{LO}} \tag{4.5.33}$$

where the antennae functions $F_{ij}$ are those of Equations 3.3.24, 3.3.27 and 3.3.30 and where the four parton momenta used are the antenna momenta after mapping i.e. $Q_1$ and $G_1$ for the first antenna and the remaining resolved parton's original momenta i.e $g_3 \to G_2$ and $\overline{q_2} \to Q_2$ for the first antenna.

Finally we need to consider the virtual term necessary for this leading colour calculation. Again, we need only consider the sub-process $e^+e^- \to qgg\overline{q}$. This gives a term that is proportional to tree level (with a divergent multiplying factor) and a finite correction. Using Equation 4.2.5 and a re-written form for $\mathcal{L}_A(i,j)$ [66] such that

$$\begin{aligned}\mathcal{L}_A(G_1,G_2) &= \hat{\mathcal{L}}_A(G_1,G_2) + \frac{\Gamma^2(1-\varepsilon)\Gamma(1+\varepsilon)}{\Gamma(1-2\varepsilon)}|\mathcal{S}_\mu(Q_1;G_1,G_2;\overline{Q_2})V^\mu|^2 \\ &\times \left(-\frac{1}{\varepsilon^2}\left(\frac{4\pi\mu^2}{-s_{Q_1G_1}}\right)^\varepsilon - \frac{1}{\varepsilon^2}\left(\frac{4\pi\mu^2}{-s_{G_1G_2}}\right)^\varepsilon - \frac{1}{\varepsilon^2}\left(\frac{4\pi\mu^2}{-s_{G_2\overline{Q_2}}}\right)^\varepsilon - \frac{3}{2\varepsilon}\left(\frac{4\pi\mu^2}{-Q^2}\right)^\varepsilon\right)\end{aligned} \tag{4.5.34}$$

we can write the virtual, leading colour contribution as

$$\frac{d\sigma_4^{\rm virt}}{\sigma_0} = V(Q_1;G_1,G_2;\overline{Q_2})d\sigma_4^{\rm LO} + d\sigma_4^{\rm finite} \tag{4.5.35}$$

where

$$d\sigma_4^{\rm finite} = \frac{(2\pi)^5}{s}\left(\frac{N^2-1}{N}\right)\left(\frac{\alpha_s N}{2\pi}\right)^3 \hat{\mathcal{L}}_A(G_1,G_2)\Theta_4 dPS_4 \tag{4.5.36}$$

and the divergent factor is written as

$$V(Q_1;G_1,\,G_2;\overline{Q_2}) = \left(\frac{\alpha_s N}{2\pi}\right)\left(-\frac{1}{\varepsilon^2}\left(\frac{4\pi\mu^2}{-s_{Q_1G_1}}\right)^{\varepsilon} - \frac{1}{\varepsilon^2}\left(\frac{4\pi\mu^2}{-s_{G_1G_2}}\right)^{\varepsilon} - \frac{1}{\varepsilon^2}\left(\frac{4\pi\mu^2}{-s_{G_2\overline{Q_2}}}\right)^{\varepsilon} - \frac{3}{2\varepsilon}\left(\frac{4\pi\mu^2}{-Q^2}\right)^{\varepsilon}\right) \tag{4.5.37}$$

Now we can compile all of the separate pieces and thus form the analytic terms that will need to be integrated over in the Monte Carlo routine. These will be separately calculated using a four parton momentum generation and later combined with the numerical routines that integrate over five parton phase space. Collecting the slicing term, the analytic subtraction functions and the virtual terms and removing all ultra-violet divergences with the one loop renormalisation of $\alpha_s$ such that

$$\left(\frac{\alpha_s}{2\pi}\right) \to \left(\frac{\alpha_s(\mu^2)}{2\pi}\right)\left(1 - \frac{b_0}{\varepsilon}\left(\frac{\alpha_s(\mu^2)}{2\pi}\right)\frac{(4\pi)^{\varepsilon}}{\Gamma(1-\varepsilon)}\right) \tag{4.5.38}$$

we find the final form of the analytic function is given by

$$d\sigma_4^{\rm NLO} = K(Q_1;G_1,G_2;\overline{Q_2})d\sigma_4^{\rm LO} + d\sigma_4^{\rm finite} \tag{4.5.39}$$

where the tree level and finite contributions are the same as in Equations 4.5.29 and 4.5.36 with the replacement $\alpha_s \to \alpha_s(\mu^2)$. The factor multiplying tree level is now finite and is given in terms of

$$\begin{aligned} K(Q_1;G_1,G_2;\overline{Q_2}) &= \left(\frac{\alpha_s(\mu^2)N}{2\pi}\right)\left[\frac{197}{18}+\frac{\pi^2}{2}+F^{\Delta}_{Q_1G_1}\left(\frac{\Delta}{s_{Q_1G_1}}\right)+F^{\Delta}_{G_1G_2}\left(\frac{\Delta}{s_{G_1G_2}}\right)\right. \\ &+ \left. F^{\Delta}_{G_2\overline{Q_2}}\left(\frac{\Delta}{s_{G_2\overline{Q_2}}}\right)-\frac{10}{6}\log\left(\frac{s_{Q_1G_1}}{Q^2}\right)-\frac{11}{6}\log\left(\frac{s_{G_1G_2}}{Q^2}\right)-\frac{10}{6}\log\left(\frac{s_{G_2\overline{Q_2}}}{Q^2}\right)\right] \\ &+ \left(\frac{\alpha_s(\mu^2)}{2\pi}\right)2b_0\log\left(\frac{\mu^2}{Q^2}\right) \end{aligned} \tag{4.5.40}$$

We note that all dependence on the slicing phase space cut-off $\delta$ has been removed and now that the poles have been analytically cancelled, the four dimensional limit can be taken, removing all terms of order $\varepsilon$ or higher. The analytic term still depends on the remaining phase space cut-off $\Delta$. However when this is combined with the numerical routine calculating the five parton contribution, this dependence will be removed. By setting $\Delta$ large, the numerical stabilty of this cancellation improves and the final answer becomes independent of both phase space cut-offs.

Now we have seen how we can apply hybrid subtraction to the leading colour part of the NLO $e^+e^- \to 4$jets calculation, we shall quickly review the remaining terms of a full colour calculation. The techniques used for the leading colour calculation are exactly those which we shall use for the rest of the calculation and thus we shall detail a set of all (colour) order $K$ factors which will multiply various terms of the tree level. Firstly, we must identify the relevant antennae so as to be able to select the necessary antennae functions and factors. This will also make clear which partons become unresolvable at which order in colour, making the four parton contribution less confusing.

The simplest way to collate all the information is to consider the tree level result. We write it as

$$d\sigma_4^{\mathrm{LO}} = d\sigma_a^{\mathrm{LO}} - \frac{1}{2N^2}d\sigma_b^{\mathrm{LO}} + \frac{n_F}{N}d\sigma_c^{\mathrm{LO}} + \frac{2}{N^2}d\sigma_d^{\mathrm{LO}} \tag{4.5.41}$$

where each of the four terms, $d\sigma_i^{\rm LO}$, is the matrix element multiplied by the four parton phase space factor. Decomposing the matrix elements into colour subamplitudes gives

$$\frac{d\sigma_i^{\rm LO}}{\sigma_0} = \frac{(2\pi)^5}{Q^2}\left(\frac{N^2-1}{N^2}\right)\left(\frac{\alpha_s N}{2\pi}\right)^2 \mathcal{M}_i dPS_4 \tag{4.5.42}$$

where $\sigma_0$ is a normalisation factor given by the leading order result for the process $\gamma^\star \to q\bar{q}$ and the colourless amplitudes are given by

$$\begin{aligned}
\mathcal{M}_a &= |\mathcal{S}_\mu(Q_1; G_1, G_2; \overline{Q_2})V^\mu|^2 \\
\mathcal{M}_b &= |\mathcal{S}_\mu(Q_1; \tilde{G}_1, \tilde{G}_2; \overline{Q_2})V^\mu|^2 \\
\mathcal{M}_c &= \mathcal{T}(1,2;1,2) \\
\mathcal{M}_d &= \mathcal{T}(1,2;1,4)
\end{aligned} \tag{4.5.43}$$

The first term we have seen before and recognise as the leading colour contribution to the subprocess $qggq\bar{q}$. The second term is the sub leading contribution to the same process. The third and fourth terms make up the leading and sub-leading pieces of the four quark subprocess. Each antenna factor $A_{ijk}$ will multiply one of these four tree level colourless subamplitudes.

The form of each antenna can now be simply collected together such that the 5 parton subtraction contribution is given by

$$\frac{d\sigma_5^{\rm sub}}{\sigma_0} = \frac{(2\pi)^7}{s}\left(\frac{N^2-1}{N^2}\right)\left(\frac{\alpha_s N}{2\pi}\right)^3 dPS_5\Theta_4(\mathcal{A}^I - \frac{\mathcal{A}^{II}}{2N^2} + \frac{n_F\mathcal{A}^{III}}{N} + \frac{2\mathcal{A}^{IV}}{N^2}) \tag{4.5.44}$$

where

$$
\begin{aligned}
\mathcal{A}^I &= A_{q_1 g_1 g_2} |\mathcal{S}_\mu(Q_1; G_1, g_2; \overline{q_2}) V^\mu|^2 + A_{g_1 g_2 g_3} |\mathcal{S}_\mu(q_1; G_1, G_2; \overline{q_2}) V^\mu|^2 \\
&+ A_{g_2 g_3 \overline{q_2}} |\mathcal{S}_\mu(q_1; g_1, G_2; \overline{Q_2}) V^\mu|^2 \\
&+ \frac{n_F}{N} \Big( A_{q_1 \overline{q_4} q_3} |\mathcal{S}_\mu(Q_1; G_1, g_2; \overline{q_2}) V^\mu|^2 + A_{\overline{q_4} q_3 g} |\mathcal{S}_\mu(q_1; G_1, G_2; \overline{q_2}) V^\mu|^2 \\
&+ A_{q_3 \overline{q_4 q_2}} |\mathcal{S}_\mu(q_1; g_1, G_2; \overline{Q_2}) V^\mu|^2 + A_{g \overline{q_4} q_3} |\mathcal{S}_\mu(q_1; G_1, G_2; \overline{q_2}) V^\mu|^2 \Big) \\
&- \frac{1}{N^2} A_{q_1 g_3 \overline{q_2}} |\mathcal{S}_\mu(Q_1; g_1, g_2; \overline{Q_2}) V^\mu|^2
\end{aligned}
\tag{4.5.45}
$$

The first three terms for $\mathcal{A}^I$ come from the three antennae making up the leading colour contribution to $qggg\overline{q}$, namely $q_1 - g_1 - g_2$, $g_1 - g_2 - g_3$ and $g_2 - g_3 - \overline{q_2}$. We see for each that the mapping takes the three antenna partons and maps them to two which are entered into the colourless subamplitudes. (These are expressed as upper case letters whereas those partons not in the antenna have their original momenta in lower case.) The next four terms in $\mathcal{A}^I$ are due to the collinear limit of a quark and antiquark forming a gluon. When one of the colour lines pinches together, we are left with the four parton subamplitudes $|\mathcal{S}_\mu(Q_1; G_1, G_2; \overline{Q_2}) V^\mu|^2$ or $|\mathcal{S}_\mu(Q_1; \tilde{G}_1, \tilde{G}_2; \overline{Q_2}) V^\mu|^2$ depending on whether the remaining colour line runs through the virtual gluon or not. For $\mathcal{A}^I$ we consider the former case. The only antennae that can form must have the partons $q_3$ and $\overline{q_4}$ in them. These can be colour connected either to the gluon (on either side), the remaining quark or the remining antiquark. Finally, the sub-leading colour term for the three gluon process contributes the last term of $\mathcal{A}^I$, but only when the unresolved gluon is the colour detached one, leaving the other two gluons ordered. With unresolved colour detached gluons we can only form antennae $q_1 - \tilde{g}_3 - \overline{q_2}$.

$$
\begin{aligned}
\mathcal{A}^{II} &= A_{q_1 g_1 g_2} |\mathcal{S}_\mu(Q_1; \tilde{G}_1, \tilde{g}_3; \overline{q_2}) V^\mu|^2 + A_{q_1 g_1 g_2} |\mathcal{S}_\mu(Q_1; \tilde{g}_3, \tilde{G}_1; \overline{q_2}) V^\mu|^2 \\
&+ A_{g_1 g_2 \overline{q_2}} |\mathcal{S}_\mu(q_1; \tilde{G}_1, \tilde{g}_3; \overline{Q_2}) V^\mu|^2 + A_{g_1 g_2 \overline{q_2}} |\mathcal{S}_\mu(q_1; \tilde{g}_3, \tilde{G}_1; \overline{Q_2}) V^\mu|^2 \\
&+ \frac{2 n_F}{N} \Big( A_{q_1 q_3 \overline{q_4}} |\mathcal{S}_\mu(Q_1; \tilde{g}_1, \tilde{G}_2; \overline{q_2}) V^\mu|^2 + A_{q_3 \overline{q_4 q_2}} |\mathcal{S}_\mu(q_1; \tilde{g}_1, \tilde{G}_2; \overline{Q_2}) V^\mu|^2 \Big) \\
&+ \frac{1}{3} \left(1 + \frac{1}{N^2}\right) \Big( A_{q_1 g_1 \overline{q_2}} |\mathcal{S}_\mu(Q_1; \tilde{g}_2, \tilde{g}_3; \overline{Q_2}) V^\mu|^2 + A_{q_1 g_2 \overline{q_2}} |\mathcal{S}_\mu(Q_1; \tilde{g}_1, \tilde{g}_3; \overline{Q_2}) V^\mu|^2 \\
&+ A_{q_1 g_3 \overline{q_2}} |\mathcal{S}_\mu(Q_1; \tilde{g}_1, \tilde{g}_2; \overline{Q_2}) V^\mu|^2 \Big)
\end{aligned}
\tag{4.5.46}
$$

Here the first four terms of $\mathcal{A}^{II}$ are formed from the three gluon process. They are from the single colour detacted gluon digrams, but here, as opposed to $\mathcal{A}^{I}$, one of the ordered gluons is unresolved. This gives antennae of the form $q_1 - g_1 - g_2$ and $g_1 - g_2 - \overline{q_2}$, but now the remaining gluons (after mapping) are colour detached and we must write out all their permutations explicitly. Therefore we can have both the $|\mathcal{S}_\mu(Q_1; \tilde{G}_1, \tilde{g}_3; \overline{q_2})V^\mu|^2$ colourless subamplitude and the $|\mathcal{S}_\mu(Q_1; \tilde{g}_3, \tilde{G}_1; \overline{q_2})V^\mu|^2$ colourless subamplitude multiplying the $q_1 - g_1 - g_2$ antenna factor. Simialrly for the $g_1 - g_2 - \overline{q_2}$ antenna. The next two terms are again from the 4 quark process as described for $\mathcal{A}^{I}$, but now the external gluon attachs to a colour line that runs through the primary quark line only, thus making the collinear quark/antiquark pair (and therefore itself) colour detached. Here the antenna factors consist solely of quarks and antiquarks. The final three terms of $\mathcal{A}^{II}$ are due to the antennae of the 3 gluon process where all three gluons are colour detached. Here all the antennae are of the form $q_1 - \tilde{g}_i - \overline{q_2}$. It is not necessary to swap the order of the gluons in the colourless subamplitudes here as the mapping leaves them unaffected and therefore all permutations are already accounted for.

$$\begin{aligned}
\mathcal{A}^{III} &= (A_{q_1 g \overline{q_4}} + A_{q_3 g \overline{q_2}} - \frac{1}{N^2}(2A_{q_1 g \overline{q_4}} + 2A_{q_3 g \overline{q_2}} \\
&- 2A_{q_1 g q_3} - 2A_{\overline{q_2} g \overline{q_4}} + A_{q_1 g \overline{q_2}} + A_{q_3 g \overline{q_4}}))\mathcal{T}(1,2;1,2) \\
\mathcal{A}^{IV} &= (A_{q_1 g q_3} + A_{\overline{q_2} g \overline{q_4}} - \frac{1}{N^2}(A_{q_1 g \overline{q_2}} + A_{q_3 g \overline{q_4}} + A_{q_1 g \overline{q_4}} + A_{q_3 g \overline{q_2}} \\
&- A_{q_1 g q_3} - A_{\overline{q_2} g \overline{q_4}}))\mathcal{T}(1,2;1,4)
\end{aligned} \tag{4.5.47}$$

The remaining terms for $\mathcal{A}^{III}$ and $\mathcal{A}^{IV}$ are formed from the remaining four quark-one gluon terms. The presence of antennae of the form $\mathcal{A}_{q_1 g q_3}$ and $\mathcal{A}_{\overline{q_2} g \overline{q_4}}$ is due to the interference between antennae such as $\mathcal{A}_{q_1 g \overline{q_4}}$ and $\mathcal{A}_{q_3 g \overline{q_4}}$. They have the same form as the quark-antiquark antennae. $\mathcal{A}^{III}$ gives the functions for identical and non-identical quark pairs whereas $\mathcal{A}^{IV}$ is the antenna function for the identical quark pairs only.

Following the same technique as above for the four partonic contribution we write the slicing terms, the virtual terms and the subtraction terms all together in terms of $\mathcal{K}$ factors and logarithms that multiply the four tree level terms.

$$
\begin{aligned}
d\sigma_4^{\mathrm{NLO}} &= \left[\mathcal{K}(Q_1;G_1,G_2;\overline{Q_2}) - \frac{1}{N^2}\mathcal{K}(Q_1;\overline{Q_2})\right] d\sigma_4^I \\
&- \frac{1}{2N^2}\left[\mathcal{K}(Q_1;G_1;\overline{Q_2}) + \mathcal{K}(Q_1;G_2;\overline{Q_2}) - \left(1+\frac{1}{N^2}\right)\mathcal{K}(Q_1;\overline{Q_2})\right] d\sigma_4^{II} \\
&+ \frac{n_F}{N}\left[\mathcal{K}(Q_1;\overline{Q_4}) + \mathcal{K}(Q_3;\overline{Q_2}) - \frac{2}{3}\log\left(\frac{s_{Q_3\overline{Q_4}}}{Q^2}\right) + \frac{31}{9}\right. \\
&- \frac{1}{N^2}(2\mathcal{K}(Q_1;\overline{Q_4}) + 2\mathcal{K}(Q_3;\overline{Q_2}) - 2\mathcal{K}(Q_1;Q_3) - 2\mathcal{K}(\overline{Q_2};\overline{Q_4}) + \mathcal{K}(Q_1;\overline{Q_2}) \\
&+ \left.\mathcal{K}(Q_3;\overline{Q_4}) + 3\log\left(\frac{s_{Q_3\overline{Q_4}}}{Q^2}\right)) + \frac{n_F}{N}\left(\frac{-10}{9} + \frac{2}{3}\log\left(\frac{s_{Q_3\overline{Q_4}}}{Q^2}\right)\right)\right] d\sigma_4^{III} \\
&+ \frac{2}{N^2}\left[\mathcal{K}(Q_1;Q_3) + \mathcal{K}(\overline{Q_2};\overline{Q_4}) - \frac{2}{3}\log\left(\frac{s_{Q_3Q_4}}{Q^2}\right) + \frac{31}{9}\right. \\
&- \frac{1}{N^2}(\mathcal{K}(Q_1;\overline{Q_2}) + \mathcal{K}(Q_3;\overline{Q_4}) + \mathcal{K}(Q_1;\overline{Q_4}) + \mathcal{K}(Q_3;\overline{Q_2}) - \mathcal{K}(Q_1;Q_3) \\
&- \left.\mathcal{K}(\overline{Q_2};\overline{Q_4}) + 3\log\left(\frac{s_{Q_3\overline{Q_4}}}{Q^2}\right)) + \frac{n_F}{N}\left(\frac{-10}{9} + \frac{2}{3}\log\left(\frac{s_{Q_3\overline{Q_4}}}{Q^2}\right)\right)\right] d\sigma_4^{IV} + d\sigma_4^{\mathrm{finite}}
\end{aligned}
\tag{4.5.48}
$$

where $d\sigma_4^{\mathrm{finite}}$ now constitutes all the finite terms from the virtual contribution e.g. $\hat{\mathcal{L}_A}, \hat{\mathcal{L}_B}, \hat{\mathcal{L}_C}$ with relevant colour factors. The extra logarithms come from the virtual terms and are due to single poles of the form $\frac{1}{\varepsilon}(x)^{\varepsilon}$ being expanded in terms of $\varepsilon$. The factors $\frac{31}{9} - \frac{10n_F}{9N}$ are due to the self-energy corrections to the 4 quark virtual terms. The form of the $\mathcal{K}$ factors is given by taking the relevant slicing factor ($n = 1$ or $n = 0$) and combining it with the analytic antennae functions $F$ and the one loop coupling constant renormalisation such that.

$$
\begin{aligned}
\mathcal{K}(Q;G;\overline{Q}) &= \left(\frac{\alpha_s(\mu)N}{2\pi}\right)\left[\frac{130}{18} + \frac{\pi^2}{3} + F^{\Delta}_{QG}\left(\frac{\Delta}{s_{QG}}\right) + F^{\Delta}_{G\overline{Q}}\left(\frac{\Delta}{s_{g\overline{Q}}}\right)\right. \\
&- \left.\frac{10}{6}\log\left(\frac{s_{QG}}{\Delta}\right) - \frac{10}{6}\log\left(\frac{s_{G\overline{Q}}}{\Delta}\right)\right] + \left(\frac{\alpha_s(\mu)}{2\pi}\right) b_0 \log\left(\frac{\mu^2}{Q^2}\right) \\
\mathcal{K}(Q;\overline{Q}) &= \left(\frac{\alpha_s(\mu)N}{2\pi}\right)\left[\frac{63}{18} + \frac{\pi^2}{6} + F^{\Delta}_{Q\overline{Q}}\left(\frac{\Delta}{s_{Q\overline{Q}}}\right) - \frac{3}{2}\log\left(\frac{s_{Q\overline{Q}}}{\Delta}\right)\right] \\
\mathcal{K}(Q_i;Q_j) &= \mathcal{K}(\overline{Q_i};\overline{Q_j}) = \mathcal{K}(Q_i;\overline{Q_j})
\end{aligned}
\tag{4.5.49}
$$

## 4.6 Summary

In this chapter we have outlined all the contributions to the NLO calculation of the process $e^+e^- \to 4$ jets at all orders in colour. We have shown how the virtual diagrams for the final states $q\bar{q}gg$ and $q\bar{q}Q\overline{Q}$ can be grouped together at similiar orders of colour such that the entire expression can be written in terms of five and nine independent functions respectively. We have also seen the same process repeated for the extra, unresolved partonic contributions $q\bar{q}ggg$ and $q\bar{q}Q\overline{Q}g$.

Finally we have derived the analytic functions (for both a leading colour calculation and an all orders in colour calculation) in which the poles have been cancelled. These are to be integrated over four parton phase space and combined with the numerically calculated five partonic contribution which has been rendered finite by use of the subtraction terms.

In the next chapter we shall outline the results from these integrations which were calculated using a Monte Carlo program written specifically for this approach called `EERAD2` which calculates a number of 4 jet-like event shape variables .

# Chapter 5

# Data results for NLO 4 jet observables

## 5.1 Introduction

We now turn to the comparision of the theoretical calculations outlined in the previous chapters with experimental findings. There are many 4 jet observables that can be measured at modern particle detectors. All of these give some indication of the shape of the event, for instance how spherical the event is or how collimated the jets are. The topology of an event also can be used to indirectly measure other theoretical parameters such as $\alpha_s$ by comparing theoretical and experimental distributions for each observable. 4 jet observables are also useful for testing the Casimir factors of QCD and testing for the presence of light gluinos. Electron-positron annihilations are particularly useful as the results are clean and free from the uncertainty of parton distribution functions within hadrons which are necessary for proton-antiproton or electron-proton collisions.

Definitions of some 4 jet observables are given in Section 5.2. In Section 5.3 we compare the results of `EERAD2` with two other NLO 4 jet programs, namely `MENLO PARC`[55] and `DEBRECEN`[54] for the 4 jet rate, the $D$ parameter and Thrust minor, $T_{\text{minor}}$. The quantitative differences between these programs shall be briefly discussed. Section 5.4 presents the theoretical predictions for previously uncalculated 4 jet variables such as the narrow jet broadening, the light hemisphere mass and the jet transition variables for the Geneva and JADE algorithms. All of these are compared with experimental results in Section 5.5 gathered by the DELPHI collaboration and the variation with renormalisation scale is studied, at the physical and FAC scales.

## 5.2 Four jet event shapes

The sorts of variables we are interested in are four jet-like, since they can only be non-zero for final states in which there are four or more particles. They usually rely on the hadronic final state having some volume and, when the event is coplanar, some observables like the $D$ parameter are identically zero.

### 5.2.1 Definition of Variables

In the following definitions, the sums run over all $N$ final state particles, $k = 1, ..., N$. $\vec{p}_k$ is the three-momentum of particle $k$ in the c.m. frame, with components $p_k^i$, $i = 1, 2, 3$.

- $C$ and $D$ parameters [49]. We first construct the linear momentum tensor,

$$\Theta^{ij} = \frac{\sum_k \frac{p_k^i p_k^j}{|\vec{p}_k|}}{\sum_k |\vec{p}_k|}, \tag{5.2.1}$$

with eigenvalues $\lambda_i$ for $i = 1, 2, 3$. The normalisation is such that $\sum_i \lambda_i = 1$. For planar events one of the eigenvalues is zero. The $C$ and $D$ parameters are defined by,

$$\begin{aligned} C &= 3(\lambda_1\lambda_2 + \lambda_2\lambda_3 + \lambda_3\lambda_1) \\ D &= 27\lambda_1\lambda_2\lambda_3 \end{aligned} \tag{5.2.2}$$

$D$ can only be non-zero for non-planar four (or more) parton events, while three parton events may produce $0 < C < 0.75$. Only the region $C > 0.75$ should be considered four jet-like.

- Thrust minor, $T_{\text{minor}}$ [50]. We first define the thrust, major and minor axes $(\vec{n}_1, \vec{n}_2, \vec{n}_3)$ by,

$$T_i = \max_{\vec{n}_i} \frac{\sum_k |\vec{p}_k \cdot \vec{n}_k|}{\sum_k |\vec{p}_k|}, \tag{5.2.3}$$

where $\vec{n}_2$ is constrained by $\vec{n}_1 \cdot \vec{n}_2 = 0$. and $\vec{n}_3 = \vec{n}_1 \times \vec{n}_2$.

- Light hemisphere mass, $M_L^2/s$. The event is separated into two hemispheres $H_1$, $H_2$ divided by the plane normal to the thrust axis $\vec{n}_1$, as defined above. Particles that satisfy $\vec{p}_i \cdot \vec{n}_1 > 0$ are assigned to hemisphere $H_1$, while all other particles are in $H_2$. Then,

$$\frac{M_L^2}{s} = \frac{1}{s} \cdot \min_{i=1,2} \left( \sum_{\vec{p}_k \in H_i} p_k \right)^2 . \tag{5.2.4}$$

  Note that this is the common modification of the original definition suggested by Clavelli [51].

- Narrow jet broadening, $B_{\min}$ [52]. Using the same division into hemispheres as above, we define,

$$B_{\min} = \min_{i=1,2} \frac{\sum_{\vec{p}_k \in H_i} |\vec{p}_k \times \vec{n}|}{2 \sum_k |\vec{p}_k|}. \tag{5.2.5}$$

- Jet transition variable $y_4^S$. The $y_4^S$ variable denotes the value of the jet resolution parameter $y_{\text{cut}}$ at which an event changes from a four jet event to a three jet event where the jets are defined according to algorithm $S$. We consider three algorithms, the JADE algorithm ($S = J$) [18], the Durham algorithm ($S = D$) [21] and the Geneva algorithm ($S = G$) [22]. The jet-finding measures for each of these three algorithms can be found in Equations 2.2.3, 2.2.4 and 2.2.5. Recall that when particles combine, there is some ambiguity as to how to add the energies and momenta (see Section 2.2.2). In all three schemes, we use the E scheme i.e. we merely add four momenta,

$$p_{ij}^\mu = p_i^\mu + p_j^\mu. \tag{5.2.6}$$

  Other choices such as the E0 or P schemes where the cluster is made massless by rescaling the momentum or energy give similar results.

Of these variables, the $D$, $C$, $T_{\text{minor}}$ and $y_4^D$ distributions have been studied in [54].

### 5.2.2 Structure of Perturbative Prediction

The differential cross-section at centre-of-mass energy $\sqrt{s}$ for one of these four-jet variables ($O_4$) at next-to-leading order is described by two coefficients, $B_{O_4}$ and $C_{O_4}$ which represent the leading and next-to-leading order perturbative contributions,

$$\frac{1}{\sigma_0} O_4 \frac{d\sigma}{dO_4} = \left(\frac{\alpha_s(\mu)}{2\pi}\right)^2 B_{O_4} + \left(\frac{\alpha_s(\mu)}{2\pi}\right)^3 \left(2\beta_0 \log\left(\frac{\mu^2}{s}\right) B_{O_4} + C_{O_4}\right). \tag{5.2.7}$$

Both $B_{O_4}$ and $C_{O_4}$ are scale independent and do not depend on the beam energy. However, the running coupling $\alpha_s$ is calculated at renormalization scale $\mu$ which is commonly chosen to be the physical scale, $\mu = \sqrt{s}$. Compared to the leading order prediction, which decays monotonically with increasing $\mu$, the next-to-leading order term reduces the scale dependence somewhat through the first coefficient of the beta-function, $\beta_0 = (33 - 2N_f)/6$. For five active quark flavours, $\beta_0 = 3.833$.

### 5.2.3 Scale choice, theoretical uncertainty and resummations

As mentioned above, for hadronic observables in electron-positron annihilation it is common to choose the renormalisation scale to be the physical scale $\mu = \sqrt{s}$. This choice is motivated by naturalness arguments and the fact that choosing a scale far from $\sqrt{s}$ introduces large logarithms of the form $\log(\mu/\sqrt{s})$ in eq. (5.2.7). However, as we have seen in section 1.4, there are a number of choices of scale that attempt to model the rest of the perturbative series such as the FAC scale[13] and the PMS scale[12]. While even higher order corrections remain uncalculated, varying the renormalisation scale can only give a crude indication of the theoretical uncertainty. Therefore, in an attempt to make a fair estimate of the theoretical uncertainty on the NLO prediction we will show both the physical scale and FAC scale predictions.

Four jet event shapes typically depend on the event having some volume and not lying entirely in a plane. Typical hadronic events contain more than 20 hadrons and it is extremely unlikely that the value of any event shape is precisely zero for any experimental event. However, in a LO or NLO fixed order parton calculation, there only four or five partons

present in the final state and, when one or more are soft, the calculated $O_4$ may approach zero. In such circumstances, soft gluon singularities cause the fixed order prediction to become wildly unstable and grow logarithmically. In the small $O_4$ limits, the perturbative coefficients have the following form,

$$\begin{aligned} B_{O_4} &\to A_{32}L^3 + A_{22}L^2 + A_{12}L + A_{02}, \\ C_{O_4} &\to A_{53}L^5 + A_{43}L^4 + A_{33}L^3 + A_{23}L^2 + A_{13}L + A_{03}, \end{aligned} \tag{5.2.8}$$

where $L = \log(1/O_4)$, $A_{nm}$ are undetermined coefficients and thus whenever $L$ is sufficiently large, resummation effects will become important.[1] For the 4 jet rate the calculation of these coefficients has been performed and resummed in [57]. In comparing with data, we choose to make a cut on the size of $O_4$ which is typically in the range 0.001-0.01, since for such small values of $O_4$ we do not trust the NLO prediction. Equating this with the DELPHI data, the cut will usually be the lower edge of the second data bin.

## 5.3 Comparison with existing results

### 5.3.1 Four jet rates

As a check of the numerical results, Table 5.1 shows the predictions for each of the three Monte Carlo programs of the four jet rate for three jet clustering algorithms; the Jade-E0[18], Durham-E [21], and Geneva-E [22] algorithms. We show results with $\alpha_s(M_Z) = 0.118$ for three values of the jet resolution parameter $y_{cut}$. There is good agreement with the results from the other two calculations.

### 5.3.2 Shape variables

As mentioned earlier, Nagy and Trócsányi [54] have computed $C_D$ with their Monte Carlo DEBRECEN. In Table 5.2 we show the leading and next-to-leading order coefficients $B_D$ and $C_D$

[1] Whether the coefficients exponentiate and can be resummed will depend on the observable.

| Algorithm | $y_{\text{cut}}$ | MENLO PARC | DEBRECEN | EERAD2 |
|---|---|---|---|---|
| Durham | 0.005 | $(1.04 \pm 0.02) \cdot 10^{-1}$ | $(1.05 \pm 0.01) \cdot 10^{-1}$ | $(1.05 \pm 0.01) \cdot 10^{-1}$ |
| | 0.01 | $(4.70 \pm 0.06) \cdot 10^{-2}$ | $(4.66 \pm 0.02) \cdot 10^{-2}$ | $(4.65 \pm 0.02) \cdot 10^{-2}$ |
| | 0.03 | $(6.82 \pm 0.08) \cdot 10^{-3}$ | $(6.87 \pm 0.04) \cdot 10^{-3}$ | $(6.86 \pm 0.03) \cdot 10^{-3}$ |
| Geneva | 0.02 | $(2.56 \pm 0.06) \cdot 10^{-1}$ | $(2.63 \pm 0.06) \cdot 10^{-1}$ | $(2.61 \pm 0.05) \cdot 10^{-1}$ |
| | 0.03 | $(1.71 \pm 0.03) \cdot 10^{-1}$ | $(1.75 \pm 0.03) \cdot 10^{-1}$ | $(1.72 \pm 0.03) \cdot 10^{-1}$ |
| | 0.05 | $(8.58 \pm 0.15) \cdot 10^{-2}$ | $(8.37 \pm 0.12) \cdot 10^{-2}$ | $(8.50 \pm 0.06) \cdot 10^{-2}$ |
| JADE-E0 | 0.005 | $(3.79 \pm 0.08) \cdot 10^{-1}$ | $(3.88 \pm 0.07) \cdot 10^{-1}$ | $(3.87 \pm 0.03) \cdot 10^{-1}$ |
| | 0.01 | $(1.88 \pm 0.03) \cdot 10^{-1}$ | $(1.92 \pm 0.01) \cdot 10^{-1}$ | $(1.93 \pm 0.01) \cdot 10^{-1}$ |
| | 0.03 | $(3.46 \pm 0.05) \cdot 10^{-2}$ | $(3.37 \pm 0.01) \cdot 10^{-2}$ | $(3.35 \pm 0.01) \cdot 10^{-2}$ |

Table 5.1: The four-jet fraction as calculated by MENLO PARC, DEBRECEN and EERAD2, for the different jet recombination schemes and varying $y_{\text{cut}}$. The rate is normalized by the $\mathcal{O}(\alpha_s)$ total hadronic cross-section, $\sigma_{\text{had}} = \sigma_0 \left(1 + \alpha_s/\pi\right)$.

calculated by EERAD2, together with the DEBRECEN result. The two calculations are clearly consistent with one another, with the quoted errors overlapping in almost all cases. The errors from EERAD2 are of the order of 2% in each bin, except in the tail of the distribution where the errors rise as high as 10%. The infrared enhancement of the distribution described in section 5.2.3 means that the Monte Carlo procedure favours the phase space region corresponding to small values of the $D$ parameter, so that the large $D$ tail suffers larger errors. In fact $C_D$ drops by four orders of magnitude over the kinematic range of the observable so it is necessary to use importance sampling with respect to the observable distribution to ensure sufficient Monte Carlo points are produced in the high $D$ region. This is also true for all of the other shape variables.

In addition, Nagy and Trócsányi have also presented results for the next-to-leading order coefficents for thrust minor $T_{\text{minor}}$ and the jet transition variable in the Durham scheme $y_4^D$ [54]. Although we do not present a detailed comparison here, we note that the agreement is qualitatively the same as discussed for the $D$ parameter above. We find that the distributions extend beyond the range of coefficents presented in [54], with non-zero coefficients for bins in the ranges $0.5 < T_{\text{minor}} < 0.58$ and $0.125 < y_4^D < 0.17$.

| $D$ | $B_D$ | $C_D$ | DEBRECEN |
|---|---|---|---|
| 0.0200 | $(3.79 \pm 0.01) \cdot 10^2$ | $(1.47 \pm 0.00) \cdot 10^4$ | $(1.08 \pm 0.06) \cdot 10^4$ |
| 0.0600 | $(2.32 \pm 0.01) \cdot 10^2$ | $(1.25 \pm 0.01) \cdot 10^4$ | $(1.24 \pm 0.02) \cdot 10^4$ |
| 0.1000 | $(1.45 \pm 0.01) \cdot 10^2$ | $(8.69 \pm 0.04) \cdot 10^3$ | $(8.59 \pm 0.12) \cdot 10^3$ |
| 0.1400 | $(1.04 \pm 0.01) \cdot 10^2$ | $(6.39 \pm 0.03) \cdot 10^3$ | $(6.24 \pm 0.12) \cdot 10^3$ |
| 0.1800 | $(7.68 \pm 0.04) \cdot 10^1$ | $(4.89 \pm 0.03) \cdot 10^3$ | $(4.99 \pm 0.11) \cdot 10^3$ |
| 0.2200 | $(5.87 \pm 0.03) \cdot 10^1$ | $(3.88 \pm 0.03) \cdot 10^3$ | $(3.85 \pm 0.06) \cdot 10^3$ |
| 0.2600 | $(4.66 \pm 0.07) \cdot 10^1$ | $(3.04 \pm 0.03) \cdot 10^3$ | $(2.98 \pm 0.05) \cdot 10^3$ |
| 0.3000 | $(3.75 \pm 0.07) \cdot 10^1$ | $(2.51 \pm 0.04) \cdot 10^3$ | $(2.52 \pm 0.05) \cdot 10^3$ |
| 0.3400 | $(3.07 \pm 0.05) \cdot 10^1$ | $(2.02 \pm 0.03) \cdot 10^3$ | $(1.94 \pm 0.05) \cdot 10^3$ |
| 0.3800 | $(2.41 \pm 0.03) \cdot 10^1$ | $(1.61 \pm 0.03) \cdot 10^3$ | $(1.59 \pm 0.04) \cdot 10^3$ |
| 0.4200 | $(1.97 \pm 0.04) \cdot 10^1$ | $(1.37 \pm 0.02) \cdot 10^3$ | $(1.37 \pm 0.03) \cdot 10^3$ |
| 0.4600 | $(1.56 \pm 0.03) \cdot 10^1$ | $(1.09 \pm 0.01) \cdot 10^3$ | $(1.06 \pm 0.03) \cdot 10^3$ |
| 0.5000 | $(1.32 \pm 0.01) \cdot 10^1$ | $(8.97 \pm 0.14) \cdot 10^2$ | $(8.72 \pm 0.19) \cdot 10^2$ |
| 0.5400 | $(1.05 \pm 0.02) \cdot 10^1$ | $(7.12 \pm 0.15) \cdot 10^2$ | $(7.11 \pm 0.16) \cdot 10^2$ |
| 0.5800 | $(8.46 \pm 0.16) \cdot 10^0$ | $(5.79 \pm 0.12) \cdot 10^2$ | $(5.68 \pm 0.14) \cdot 10^2$ |
| 0.6200 | $(6.60 \pm 0.16) \cdot 10^0$ | $(4.55 \pm 0.09) \cdot 10^2$ | $(4.46 \pm 0.21) \cdot 10^2$ |
| 0.6600 | $(5.32 \pm 0.13) \cdot 10^0$ | $(3.58 \pm 0.07) \cdot 10^2$ | $(3.52 \pm 0.11) \cdot 10^2$ |
| 0.7000 | $(3.99 \pm 0.09) \cdot 10^0$ | $(2.80 \pm 0.09) \cdot 10^2$ | $(2.74 \pm 0.09) \cdot 10^2$ |
| 0.7400 | $(3.06 \pm 0.05) \cdot 10^0$ | $(2.05 \pm 0.08) \cdot 10^2$ | $(2.08 \pm 0.08) \cdot 10^2$ |
| 0.7800 | $(2.26 \pm 0.04) \cdot 10^0$ | $(1.58 \pm 0.04) \cdot 10^2$ | $(1.54 \pm 0.06) \cdot 10^2$ |
| 0.8200 | $(1.54 \pm 0.04) \cdot 10^0$ | $(1.05 \pm 0.03) \cdot 10^2$ | $(1.03 \pm 0.04) \cdot 10^2$ |
| 0.8600 | $(9.72 \pm 0.21) \cdot 10^{-1}$ | $(6.72 \pm 0.29) \cdot 10^1$ | $(6.66 \pm 0.31) \cdot 10^1$ |
| 0.9000 | $(5.63 \pm 0.16) \cdot 10^{-1}$ | $(3.85 \pm 0.17) \cdot 10^1$ | $(3.89 \pm 0.20) \cdot 10^1$ |
| 0.9400 | $(2.62 \pm 0.07) \cdot 10^{-1}$ | $(1.71 \pm 0.10) \cdot 10^1$ | $(1.71 \pm 0.19) \cdot 10^1$ |
| 0.9800 | $(5.34 \pm 0.11) \cdot 10^{-2}$ | $(3.15 \pm 0.27) \cdot 10^0$ | $(2.60 \pm 1.30) \cdot 10^0$ |

Table 5.2: The leading and next-to-leading order coefficients for the $D$ parameter. The NLO coefficient predicted by Nagy and Trócsányi Monte Carlo DEBRECEN [54] is also shown.

## 5.4 New results

In this section we extend the analysis of 4 jet-like event shape observables already found in the literature by reporting the leading and next-to-leading order coefficients for the light hemisphere mass, the narrow hemisphere broadening and the jet transition variable in both the JADE and Geneva schemes, $y_4^J$ and $y_4^G$. In particular, we examine the relative sizes of the two terms by inspecting the K factor (at the physical scale) for each variable across the allowed kinematic range of the distributions.

For all the variables presented in this section, we must be careful to differentiate between

the true behaviour of the distribution as the observable tends to zero and the behaviour in fixed order perturbation theory. Each of the observables should have a smooth behaviour as $O_4 \to 0$ rather than the divergent behaviour exhibited by the coefficients according to equation 5.2.8. To recover a smooth result in this limit it is necessary to resum powers of $\log(1/O_4)$ where possible, a procedure which has been performed already for many 3 jet-like variables [58, 52]

### 5.4.1 Light Hemisphere Mass

| $M_L^2/s$ | $B_{M_L^2/s}$ | $C_{M_L^2/s}$ |
|---|---|---|
| 0.0150 | $(3.23 \pm 0.08) \cdot 10^2$ | $(1.41 \pm 0.01) \cdot 10^4$ |
| 0.0250 | $(1.88 \pm 0.02) \cdot 10^2$ | $(8.85 \pm 0.10) \cdot 10^3$ |
| 0.0350 | $(1.25 \pm 0.02) \cdot 10^2$ | $(5.97 \pm 0.11) \cdot 10^3$ |
| 0.0450 | $(8.52 \pm 0.10) \cdot 10^1$ | $(4.14 \pm 0.08) \cdot 10^3$ |
| 0.0550 | $(5.97 \pm 0.06) \cdot 10^1$ | $(3.04 \pm 0.04) \cdot 10^3$ |
| 0.0650 | $(4.20 \pm 0.09) \cdot 10^1$ | $(2.15 \pm 0.05) \cdot 10^3$ |
| 0.0750 | $(3.02 \pm 0.07) \cdot 10^1$ | $(1.58 \pm 0.05) \cdot 10^3$ |
| 0.0850 | $(2.13 \pm 0.03) \cdot 10^1$ | $(1.11 \pm 0.02) \cdot 10^3$ |
| 0.0950 | $(1.39 \pm 0.04) \cdot 10^1$ | $(7.66 \pm 0.23) \cdot 10^2$ |
| 0.1050 | $(8.75 \pm 0.20) \cdot 10^0$ | $(4.97 \pm 0.17) \cdot 10^2$ |
| 0.1150 | $(5.18 \pm 0.13) \cdot 10^0$ | $(3.27 \pm 0.07) \cdot 10^2$ |
| 0.1250 | $(2.59 \pm 0.12) \cdot 10^0$ | $(1.66 \pm 0.07) \cdot 10^2$ |
| 0.1350 | $(8.97 \pm 0.35) \cdot 10^{-1}$ | $(6.61 \pm 0.41) \cdot 10^1$ |
| 0.1450 | $(2.49 \pm 0.13) \cdot 10^{-1}$ | $(1.79 \pm 0.09) \cdot 10^1$ |
| 0.1550 | $(5.00 \pm 0.27) \cdot 10^{-2}$ | $(3.75 \pm 0.26) \cdot 10^0$ |
| 0.1650 | $(1.46 \pm 0.21) \cdot 10^{-3}$ | $(2.30 \pm 0.37) \cdot 10^{-1}$ |

Table 5.3: The leading and next-to-leading order coefficients for the light jet mass $M_L^2/s$.

As defined before, the light hemisphere mass is the smaller invariant mass of the two hemispheres formed by separating the event by a plane normal to the thrust axis. The NLO coefficient $C_{M_L^2/s}$ evaluted at the physical scale $\mu = \sqrt{s}$ together with the LO term is given in Table 5.3. The errors are estimates from the numerical program and are typically 2-3% for each entry. As with the previously known results on four jet event shapes, the NLO terms are significantly larger than the LO term. Here, we see that $C_{M_L^2/s}$ is typically 50 times larger than $B_{M_L^2/s}$ so that even when the additional factor of $\alpha_s/2\pi$ is restored, the

NLO correction is large. This is illustrated by considering the K factor defined by,

$$K_{O_4} = 1 + \left(\frac{\alpha_s(\sqrt{s})}{2\pi}\right)\frac{C_{O_4}}{B_{O_4}}, \tag{5.4.1}$$

It is found that the K factor increases with the value of the observable, rising from 1.8 at small $M_L^2/s$ up to 2.4. This behaviour is similar to that observed for other four jet event shapes [54].

### 5.4.2 Narrow Hemisphere Broadening

Narrow hemisphere broadening, $B_{\min}$, is defined in a similiar manner to the light hemisphere mass. The event is again divided into two hemispheres by the plane normal to the thrust axis, but now the momenta transverse to the thrust axis is summed (normalised by the sum of absolute momenta) in each hemisphere. The narrow hemisphere is that with the least transverse momentum with respect to the thrust axis. Numerical results for this variable as calculated by EERAD2 can be found in Table 5.4. As with the light hemisphere mass, the NLO contribution is significant yielding a K factor of roughly 1.7 over most of the kinematic range of the variable

### 5.4.3 Jet transition variables

As previously stated the jet transition variable $y_4^S$ describes the scale where two jets merge, thereby changing a four jet event into a three jet event. This is essentially the same as the derivative of the four jet rate with respect to the jet resolution parameter $y_{\text{cut}}$. However, the number of jets in an event is dependent on the jet finding algorithm used to define the 'closeness' of particles which is compared with $y_{\text{cut}}$. In [54] the transition rate for the Durham jet finding algorithm [21] is given and we have checked that our results are consistent with these predictions. Here, we provide results for two other jet algorithms, the JADE and Geneva [22] schemes for which the jet finding measures are given in Equations 2.2.3, 2.2.4 and 2.2.5. We note that the Geneva algorithm enjoys the same benefits as the Durham algorithm in that it is also supposed to exponentiate, enabling infrared logarithms to be safely resummed. It also ensures that softly radiated gluons are clustered with hard partons unless the angle of separation between two soft gluons is much smaller than the angular separation between them and a hard parton.

| $B_{\min}$ | $B_{B_{\min}}$ | $C_{B_{\min}}$ |
|---|---|---|
| 0.0150 | $(1.19 \pm 0.01) \cdot 10^3$ | $(3.41 \pm 0.07) \cdot 10^4$ |
| 0.0250 | $(7.04 \pm 0.06) \cdot 10^2$ | $(2.56 \pm 0.02) \cdot 10^4$ |
| 0.0350 | $(4.80 \pm 0.02) \cdot 10^2$ | $(1.92 \pm 0.04) \cdot 10^4$ |
| 0.0450 | $(3.39 \pm 0.02) \cdot 10^2$ | $(1.41 \pm 0.02) \cdot 10^4$ |
| 0.0550 | $(2.49 \pm 0.02) \cdot 10^2$ | $(1.07 \pm 0.02) \cdot 10^4$ |
| 0.0650 | $(1.89 \pm 0.02) \cdot 10^2$ | $(8.04 \pm 0.12) \cdot 10^3$ |
| 0.0750 | $(1.43 \pm 0.02) \cdot 10^2$ | $(6.29 \pm 0.12) \cdot 10^3$ |
| 0.0850 | $(1.08 \pm 0.01) \cdot 10^2$ | $(4.81 \pm 0.08) \cdot 10^3$ |
| 0.0950 | $(8.19 \pm 0.04) \cdot 10^1$ | $(3.65 \pm 0.08) \cdot 10^3$ |
| 0.1050 | $(6.23 \pm 0.08) \cdot 10^1$ | $(2.77 \pm 0.09) \cdot 10^3$ |
| 0.1150 | $(4.69 \pm 0.06) \cdot 10^1$ | $(2.10 \pm 0.04) \cdot 10^3$ |
| 0.1250 | $(3.37 \pm 0.04) \cdot 10^1$ | $(1.45 \pm 0.04) \cdot 10^3$ |
| 0.1350 | $(2.36 \pm 0.04) \cdot 10^1$ | $(1.09 \pm 0.03) \cdot 10^3$ |
| 0.1450 | $(1.64 \pm 0.03) \cdot 10^1$ | $(7.07 \pm 0.25) \cdot 10^2$ |
| 0.1550 | $(9.82 \pm 0.12) \cdot 10^0$ | $(4.48 \pm 0.15) \cdot 10^2$ |
| 0.1650 | $(5.08 \pm 0.12) \cdot 10^0$ | $(2.18 \pm 0.10) \cdot 10^2$ |
| 0.1750 | $(1.71 \pm 0.04) \cdot 10^0$ | $(7.53 \pm 0.33) \cdot 10^1$ |
| 0.1850 | $(4.32 \pm 0.11) \cdot 10^{-1}$ | $(1.59 \pm 0.12) \cdot 10^1$ |
| 0.1950 | $(5.47 \pm 0.11) \cdot 10^{-2}$ | $(1.34 \pm 0.24) \cdot 10^0$ |

Table 5.4: The leading and next-to-leading order coefficients for the narrow jet broadening $B_{\min}$.

Our results for the two schemes are given in Tables 5.5 and 5.6. As can be seen from the tables the NLO coefficients are again large. The K factor for the JADE scheme is roughly 1.8-1.9, but is slightly smaller for the Geneva algorithm, typically in the region 1.4-1.6.

## 5.5 Comparison with experimental data

Four jet event shape observables have been studied extensively by the four LEP experiments. However, the most complete analysis of event shape variables has been carried out by the DELPHI collaboration [56]. Here we compare their study of the event shape variables discussed in section 5.2 with the results from EERAD2. Distributions based on charged particles alone as well as charged and neutral particles are presented. In this section, we wish to examine whether or not these event shapes can be described by fixed order perturbation theory. As discussed earlier, to avoid numerical instabilities in the infrared region where

fixed order perturbation theory is no longer valid we impose a cut on the smallness of the variable that is generally equal to the lower edge of the second bin. More precisely, that is,

$$\begin{aligned} D &> 0.008, \\ T_{\text{minor}} &> 0.02, \\ M_L^2/s &> 0.01, \\ B_{\text{min}} &> 0.01, \\ y_4^D &> 0.002, \\ y_4^J &> 0.002. \end{aligned} \tag{5.5.2}$$

The experimental distributions are normalised to the hadronic cross section (rather than the Born cross section) and are also not weighted by the observable, but are rather,

$$\frac{1}{\sigma_{\text{had}}} \cdot \frac{d\sigma}{dO_4} = \left(\frac{\alpha_s(\mu)}{2\pi}\right)^2 \frac{B_{O_4}}{O_4} + \left(\frac{\alpha_s(\mu)}{2\pi}\right)^3 \left(2\beta_0 \log\left(\frac{\mu^2}{s}\right) \frac{B_{O_4}}{O_4} + \frac{C_{O_4} - 2B_{O_4}}{O_4}\right). \tag{5.5.3}$$

Throughout, we choose $\alpha_s(M_Z) = 0.118$ which was consistent with the current world average [60] at the time of writing the program. In each case, the theoretical predictions have been evaluated using bins of the same size as in the experiment and therefore appear as histograms in the plots. The data is corrected for detector effects, but not for hadronisation effects.

Figures. 5.1 and 5.2 show the comparison between the leading order and next-to-leading order predictions evaluated at the physical scale $\mu = \sqrt{s} = M_Z$ for narrow jet broadening and light hemisphere mass with the published DELPHI data [56]. We see that in both cases, the LO prediction undershoots the data by a significant factor (about a factor of four), and that including the NLO correction improves the situation but still gives a rate that is much lower than the data. However, the NLO prediction still contains a large renormalisation scale uncertainty. Usually, one varies the choice of scale about the physical scale by a factor of two or so, but as discussed earlier, the FAC (or PMS) scale defined in Equation 1.4.36 are attractive alternative choices in that the known ultraviolet logarithms are resummed [59]. For both of these variables, the FAC scale is significantly less than the physical scale, for example, for $B_{\text{min}}$ , $\mu^{FAC} \sim 0.06\sqrt{s}$. This has the effect of increasing $\alpha_s$, thereby increasing

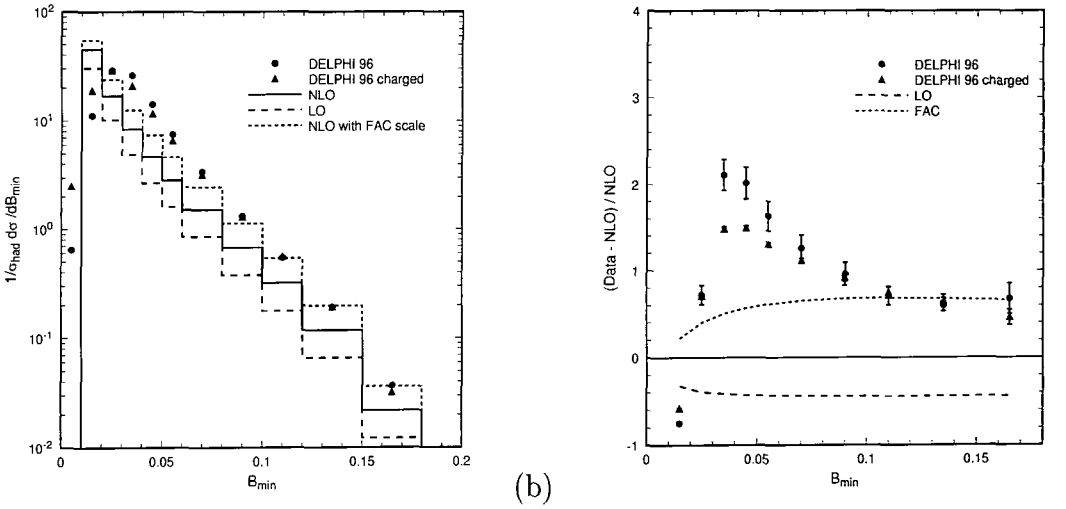


Figure 5.1: The leading order (dashed) and next-to-leading order (solid) predictions evaluated at the physical scale $\mu = \sqrt{s} = M_Z$ for (a) $1/\sigma_{\rm had} \cdot d\sigma/dB_{\rm min}$ compared to the published DELPHI data [56] and (b) the difference between data and NLO theory (normalised to NLO). The short-dashed line shows the next-to-leading order prediction using the FAC scale which is very nearly the same as the PMS scale (see Equation. 1.4.36).

the NLO prediction and in both cases, we see much improved agreement at larger values of the observable. At smaller values, and particularly in the region where the data turns over the agreement is still poor. This, of course, is where the infrared logarithms are large and need to be resummed. Furthermore, we also expect non-perturbative hadronisation effects or power corrections to influence the perturbative shape of the distribution [61, 62]. These contributions (together with resummation of the infrared logarithms) have played an important role in extracting useful information from analyses of three jet shape variables, and are likely to be important in analysing four jet event shapes.

A similar comparison of the perturbative predictions for the jet transition rates with the DELPHI measurements[2] is made in Figures 5.3 and 5.4. Once again, the LO distribution lies well below the data. This time, the NLO prediction lies much closer to the data for most of the available kinematic range. The FAC scale rate usually lies above the NLO prediction so that the data lies within the range of uncertainty engendered by the renormalisation group.

[2]The DELPHI data gives the differential jet rate rather than the jet transition variable. Up to a small ($\sim$ few %) correction from five (and more) jet events falling into a four jet configuration, the two quantities coincide at fixed order.

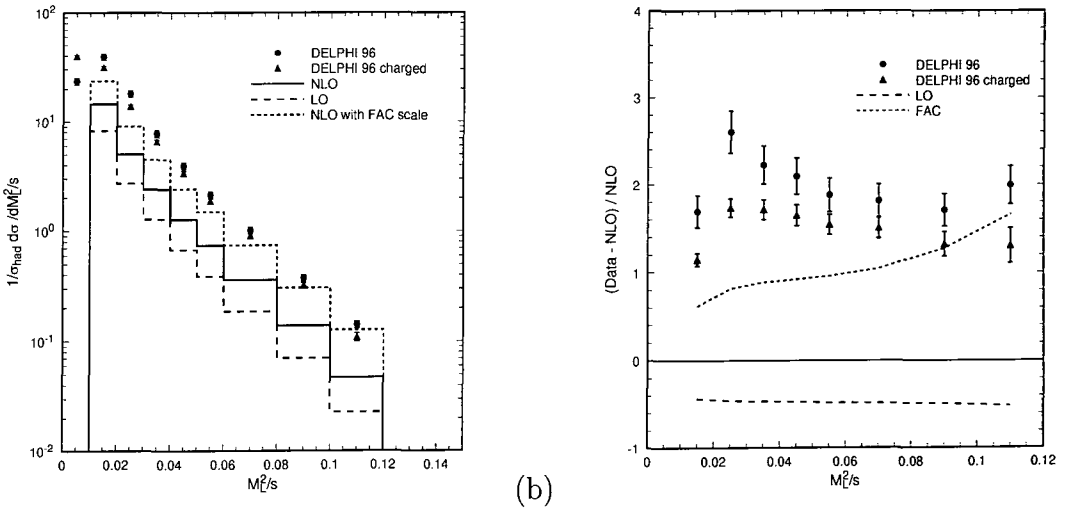


Figure 5.2: The leading order (dashed) and next-to-leading order (solid) predictions evaluated at the physical scale $\mu = \sqrt{s} = M_Z$ for (a) $1/\sigma_{\rm had} \cdot d\sigma/d(M_L^2/s)$ compared to the published DELPHI data [56] and (b) the difference between data and NLO theory (normalised to NLO). The short-dashed line shows the next-to-leading order prediction using the FAC scale which is very nearly the same as the PMS scale (see Equation 1.4.36).

For completeness, Figures 5.5 and 5.6 show the DELPHI data and perturbative predictions for the $D$ parameter and $T_{\rm minor}$ repectively. As expected from the analysis of Nagy and Trócsányi [54], the LO prediction for $D$ is too low by a factor of about four, while at the physical scale $\mu = \sqrt{s} = M_Z$ the NLO distribution is roughly twice as large but still lies a factor of two below the data. However, for the FAC scale (which for the $D$ parameter is approximately $0.035\sqrt{s}$) the prediction overshoots by 50% or so for $D > 0.1$ where the fixed order prediction is least affected by large infrared logs.

The importance of resumming these logs is clearly shown in Figure 5.6 where the $T_{\rm minor}$ distribution is shown. For $T_{\rm minor} > 0.1$ the data again lies between the next-to-leading order predictions at the physical and FAC scales (which encompass an uncertainty of about a factor three for $T_{\rm minor} \sim 0.2$). However, the turn-over at $T_{\rm minor} = 0.1$ cannot be modelled without resumming the large logs which cause the perturbative prediction to grow rapidly. The same is true at small values of the light hemisphere mass and narrow jet broadening although there the effects are less pronounced because of the choice of bin sizes.

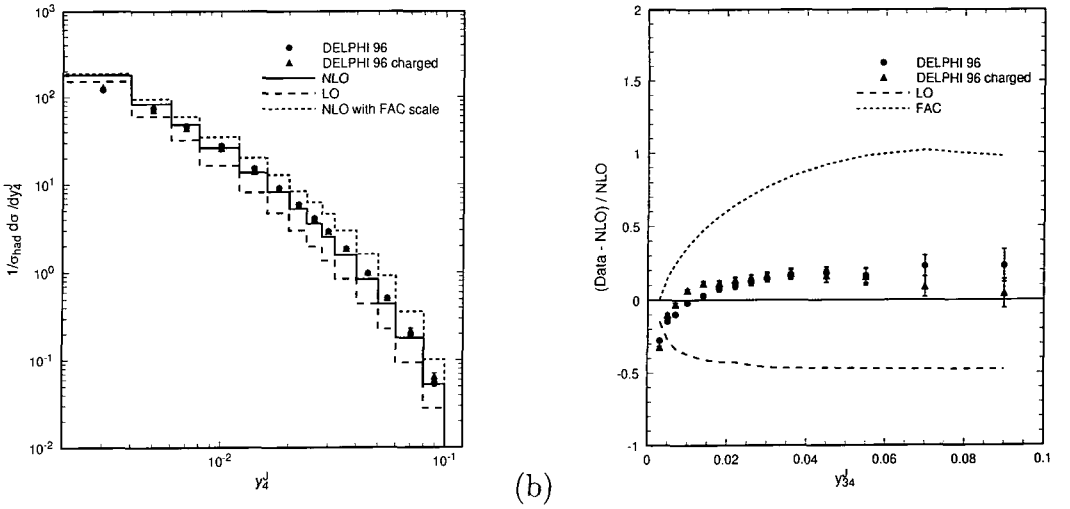


Figure 5.3: The leading order (dashed) and next-to-leading order (solid) predictions evaluated at the physical scale $\mu = \sqrt{s} = M_Z$ for (a) $1/\sigma_{\text{had}} \cdot d\sigma/dy_4^J$ compared to the published DELPHI data [56] and (b) the difference between data and NLO theory (normalised to NLO). The short-dashed line shows the next-to-leading order prediction using the FAC scale (see Equation 1.4.36).

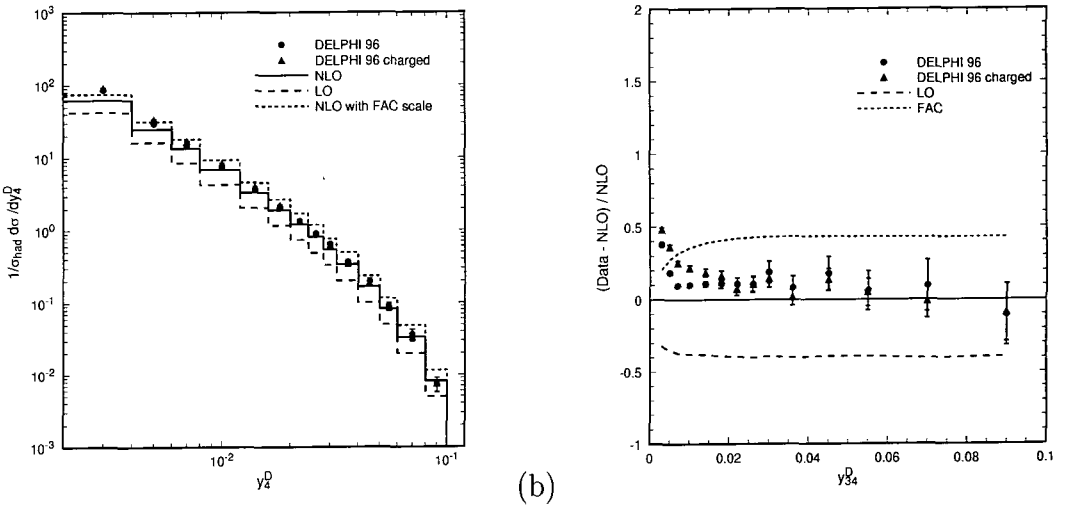


Figure 5.4: The leading order (dashed) and next-to-leading order (solid) predictions evaluated at the physical scale $\mu = \sqrt{s} = M_Z$ for (a) $1/\sigma_{\text{had}} \cdot d\sigma/dy_4^D$ compared to the published DELPHI data [56] and (b) the difference between data and NLO theory (normalised to NLO). The short-dashed line shows the next-to-leading order prediction using the FAC scale (see Equation 1.4.36).

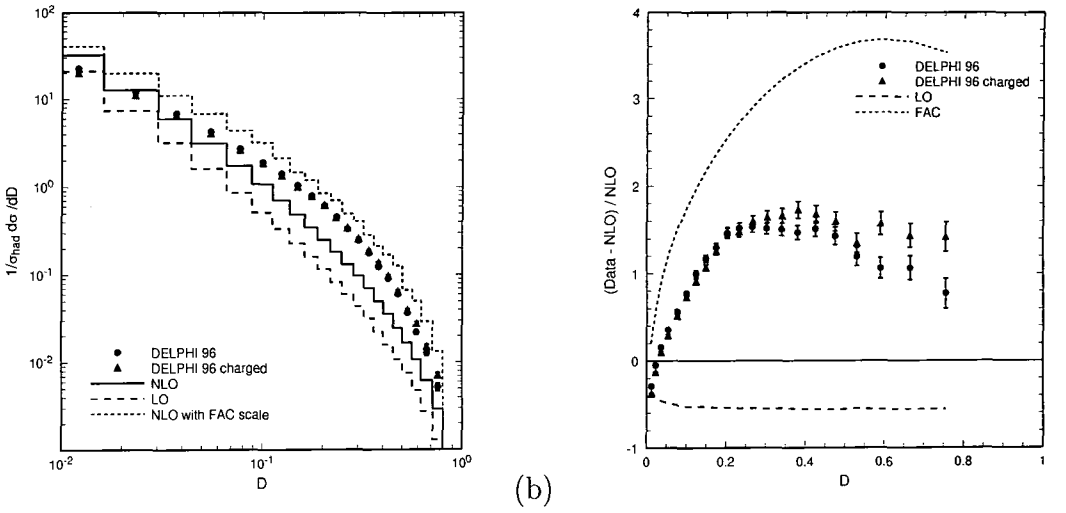


Figure 5.5: The leading order (dashed) and next-to-leading order (solid) predictions evaluated at the physical scale $\mu = \sqrt{s} = M_Z$ for (a) $1/\sigma_{\rm had} \cdot d\sigma/dD$ compared to the published DELPHI data [56] and (b) the difference between data and NLO theory (normalised to NLO). The short-dashed line shows the next-to-leading order prediction using the FAC scale (see Equation 1.4.36).

## 5.6 Summary

In this chapter we have introduced a number of 4 jet-like event shape variables which have been encoded into the NLO Monte Carlo program, `EERAD2`. This routine has been based on the prescriptions described in the earlier chapters of this thesis. We have compared these results with the experimental data as collected by the DELPHI collaboration at CERN and with two other Monte Carlo routines, `MENLO PARC` and `DEBRECEN`. For those variables that have been calculated by the other groups (the 4 jet rate, the $D$ parameter and Thrust minor) the agreement is good. For those variables that have not been calculated we present the scale independent coefficients for both LO and NLO. From these a prediction for $\alpha_s$ can be made, either by fitting directly to the experimental data or by using the renormalisation group equations and the property of asymptotic scaling [69].

It is found that the NLO corrections for all variables is large, but that the total is still short of the data. This maybe due to uncertainty in the scale, higher order corrections, power corrections and at small values of some of the variables, resummation effects need to

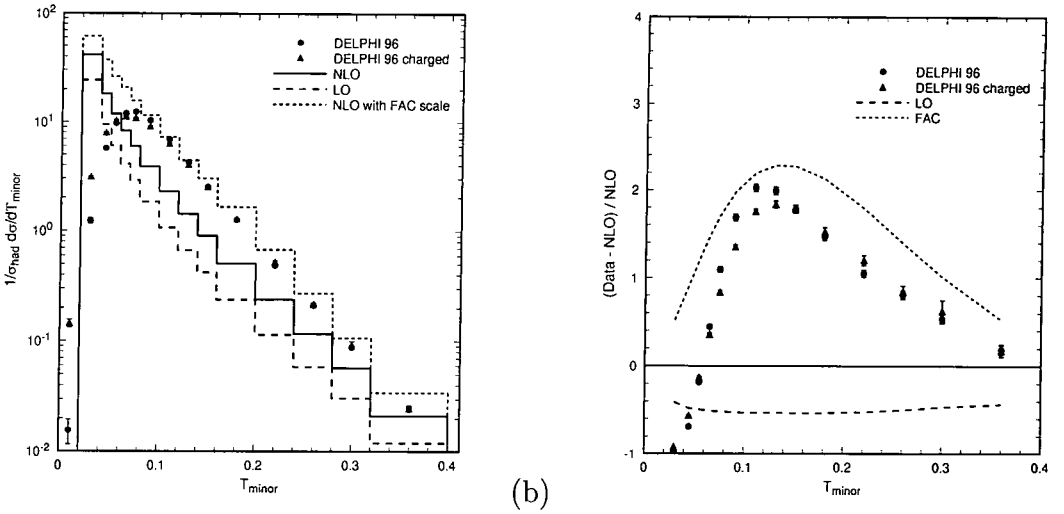


Figure 5.6: The leading order (dashed) and next-to-leading order (solid) predictions evaluated at the physical scale $\mu = \sqrt{s} = M_Z$ for (a) $1/\sigma_{\text{had}} \cdot d\sigma/dT_{\text{minor}}$ compared to the published DELPHI data [56] and (b) the difference between data and NLO theory (normalised to NLO). The short-dashed line shows the next-to-leading order prediction using the FAC scale (see Equation 1.4.36).

be taken into consideration.

| $y_4^G$ | $B_{y_4^G}$ | $C_{y_4^G}$ |
|---|---|---|
| 0.0250 | $(8.00 \pm 0.04) \cdot 10^2$ | $(9.93 \pm 0.34) \cdot 10^3$ |
| 0.0350 | $(5.59 \pm 0.04) \cdot 10^2$ | $(9.91 \pm 0.30) \cdot 10^3$ |
| 0.0450 | $(4.15 \pm 0.03) \cdot 10^2$ | $(8.57 \pm 0.13) \cdot 10^3$ |
| 0.0550 | $(3.15 \pm 0.03) \cdot 10^2$ | $(7.31 \pm 0.18) \cdot 10^3$ |
| 0.0650 | $(2.47 \pm 0.02) \cdot 10^2$ | $(5.96 \pm 0.12) \cdot 10^3$ |
| 0.0750 | $(1.93 \pm 0.02) \cdot 10^2$ | $(4.99 \pm 0.14) \cdot 10^3$ |
| 0.0850 | $(1.50 \pm 0.02) \cdot 10^2$ | $(3.96 \pm 0.11) \cdot 10^3$ |
| 0.0950 | $(1.23 \pm 0.01) \cdot 10^2$ | $(3.36 \pm 0.13) \cdot 10^3$ |
| 0.1050 | $(9.88 \pm 0.12) \cdot 10^1$ | $(2.84 \pm 0.06) \cdot 10^3$ |
| 0.1150 | $(7.90 \pm 0.09) \cdot 10^1$ | $(2.19 \pm 0.09) \cdot 10^3$ |
| 0.1250 | $(6.07 \pm 0.08) \cdot 10^1$ | $(1.69 \pm 0.11) \cdot 10^3$ |
| 0.1350 | $(4.79 \pm 0.07) \cdot 10^1$ | $(1.53 \pm 0.08) \cdot 10^3$ |
| 0.1450 | $(3.84 \pm 0.06) \cdot 10^1$ | $(1.15 \pm 0.04) \cdot 10^3$ |
| 0.1550 | $(3.00 \pm 0.05) \cdot 10^1$ | $(8.41 \pm 0.53) \cdot 10^2$ |
| 0.1650 | $(2.26 \pm 0.04) \cdot 10^1$ | $(6.52 \pm 0.36) \cdot 10^2$ |
| 0.1750 | $(1.61 \pm 0.02) \cdot 10^1$ | $(4.99 \pm 0.33) \cdot 10^2$ |
| 0.1850 | $(1.21 \pm 0.02) \cdot 10^1$ | $(3.60 \pm 0.23) \cdot 10^2$ |
| 0.1950 | $(8.71 \pm 0.27) \cdot 10^0$ | $(2.53 \pm 0.20) \cdot 10^2$ |
| 0.2050 | $(5.70 \pm 0.16) \cdot 10^0$ | $(1.78 \pm 0.17) \cdot 10^2$ |
| 0.2150 | $(3.89 \pm 0.09) \cdot 10^0$ | $(1.20 \pm 0.11) \cdot 10^2$ |
| 0.2250 | $(2.41 \pm 0.06) \cdot 10^0$ | $(6.83 \pm 0.87) \cdot 10^1$ |
| 0.2350 | $(1.43 \pm 0.05) \cdot 10^0$ | $(4.87 \pm 0.36) \cdot 10^1$ |
| 0.2450 | $(7.69 \pm 0.30) \cdot 10^{-1}$ | $(2.57 \pm 0.25) \cdot 10^1$ |
| 0.2550 | $(3.78 \pm 0.09) \cdot 10^{-1}$ | $(1.18 \pm 0.13) \cdot 10^1$ |
| 0.2650 | $(1.50 \pm 0.04) \cdot 10^{-1}$ | $(4.57 \pm 0.79) \cdot 10^0$ |
| 0.2750 | $(4.20 \pm 0.17) \cdot 10^{-2}$ | $(1.15 \pm 0.35) \cdot 10^0$ |
| 0.2850 | $(4.59 \pm 0.39) \cdot 10^{-3}$ | $(1.16 \pm 0.65) \cdot 10^{-1}$ |
| 0.2950 | $(5.37 \pm 0.91) \cdot 10^{-5}$ | $(2.15 \pm 1.11) \cdot 10^{-3}$ |

Table 5.5: The leading and next-to-leading order coefficients for the jet transition variable in the Geneva-E algorithm $y_4^G$.

| $y_4^J$ | $B_{y_4^J}$ | $C_{y_4^J}$ |
|---|---|---|
| 0.0075 | $(6.02 \pm 0.01) \cdot 10^2$ | $(1.75 \pm 0.01) \cdot 10^4$ |
| 0.0125 | $(3.60 \pm 0.01) \cdot 10^2$ | $(1.33 \pm 0.02) \cdot 10^4$ |
| 0.0175 | $(2.47 \pm 0.01) \cdot 10^2$ | $(1.02 \pm 0.04) \cdot 10^4$ |
| 0.0225 | $(1.78 \pm 0.01) \cdot 10^2$ | $(7.63 \pm 0.32) \cdot 10^3$ |
| 0.0275 | $(1.34 \pm 0.01) \cdot 10^2$ | $(6.19 \pm 0.16) \cdot 10^3$ |
| 0.0325 | $(1.01 \pm 0.01) \cdot 10^2$ | $(4.76 \pm 0.12) \cdot 10^3$ |
| 0.0375 | $(7.88 \pm 0.08) \cdot 10^1$ | $(3.86 \pm 0.11) \cdot 10^3$ |
| 0.0425 | $(6.19 \pm 0.05) \cdot 10^1$ | $(3.07 \pm 0.16) \cdot 10^3$ |
| 0.0475 | $(4.99 \pm 0.05) \cdot 10^1$ | $(2.38 \pm 0.12) \cdot 10^3$ |
| 0.0525 | $(3.89 \pm 0.05) \cdot 10^1$ | $(2.08 \pm 0.11) \cdot 10^3$ |
| 0.0575 | $(3.13 \pm 0.05) \cdot 10^1$ | $(1.54 \pm 0.05) \cdot 10^3$ |
| 0.0625 | $(2.43 \pm 0.04) \cdot 10^1$ | $(1.26 \pm 0.03) \cdot 10^3$ |
| 0.0675 | $(1.90 \pm 0.03) \cdot 10^1$ | $(9.68 \pm 0.58) \cdot 10^2$ |
| 0.0725 | $(1.49 \pm 0.04) \cdot 10^1$ | $(7.70 \pm 0.35) \cdot 10^2$ |
| 0.0775 | $(1.21 \pm 0.02) \cdot 10^1$ | $(5.89 \pm 0.41) \cdot 10^2$ |
| 0.0825 | $(9.38 \pm 0.18) \cdot 10^0$ | $(4.83 \pm 0.35) \cdot 10^2$ |
| 0.0875 | $(6.94 \pm 0.09) \cdot 10^0$ | $(3.50 \pm 0.19) \cdot 10^2$ |
| 0.0925 | $(5.36 \pm 0.11) \cdot 10^0$ | $(2.48 \pm 0.27) \cdot 10^2$ |
| 0.0975 | $(3.85 \pm 0.06) \cdot 10^0$ | $(1.93 \pm 0.19) \cdot 10^2$ |
| 0.1025 | $(2.84 \pm 0.07) \cdot 10^0$ | $(1.26 \pm 0.11) \cdot 10^2$ |
| 0.1075 | $(1.97 \pm 0.07) \cdot 10^0$ | $(9.99 \pm 1.22) \cdot 10^1$ |
| 0.1125 | $(1.30 \pm 0.06) \cdot 10^0$ | $(6.69 \pm 0.94) \cdot 10^1$ |
| 0.1175 | $(8.32 \pm 0.37) \cdot 10^{-1}$ | $(3.57 \pm 0.52) \cdot 10^1$ |
| 0.1225 | $(4.94 \pm 0.07) \cdot 10^{-1}$ | $(2.36 \pm 0.44) \cdot 10^1$ |
| 0.1275 | $(3.05 \pm 0.10) \cdot 10^{-1}$ | $(1.85 \pm 0.38) \cdot 10^1$ |
| 0.1325 | $(1.70 \pm 0.03) \cdot 10^{-1}$ | $(8.38 \pm 3.15) \cdot 10^0$ |
| 0.1375 | $(8.94 \pm 0.29) \cdot 10^{-2}$ | $(4.99 \pm 1.15) \cdot 10^0$ |
| 0.1425 | $(4.20 \pm 0.12) \cdot 10^{-2}$ | $(2.01 \pm 0.38) \cdot 10^0$ |
| 0.1475 | $(1.67 \pm 0.07) \cdot 10^{-2}$ | $(1.08 \pm 0.73) \cdot 10^0$ |
| 0.1525 | $(5.51 \pm 0.44) \cdot 10^{-3}$ | $(3.94 \pm 2.32) \cdot 10^{-1}$ |
| 0.1575 | $(8.48 \pm 0.58) \cdot 10^{-4}$ | $(4.37 \pm 2.44) \cdot 10^{-2}$ |

Table 5.6: The leading and next-to-leading order coefficients for the jet transition variable in the JADE-E0 algorithm $y_4^J$.

# Chapter 6

# A new calculation: $p\overline{p} \rightarrow \gamma +$ jets at $O(\alpha\alpha_s^2)$

## 6.1 Introduction

We now turn our attention to another important calculation in pQCD, that of prompt photon production in hadronic collisions. Specifically, this part of the thesis will concentrate on the emission of a resolved photon from the collision/annihilation of protons and antiprotons. There are many papers in the literature that have studied prompt photon production from hadronic collisions [72] and related processes in electron-proton collisions[70] and electron-positron annihilations [71]. However for this calculation we apply the fragmentation power counting of Morgan and Glover [71] which was introduced for the electron-positron initial state.

Photon production is considered to be a good probe into the underlying dynamics of both the short range interactions of partons and the composition of the proton itself (where for certain phase space configurations this process can determine the gluon distribution in the poorly understood regime of moderate values of $x$, the longitudinal momentum fraction carried by the parton inside the hadron). This is due to the simple nature of the photon coupling and the clean signal seen in the detectors. A high energy photon is identified by a shower in the electromagnetic calorimeter, accompanied by no charged tracks pointing to the energy deposit. Not only is this subject important for testing existing theories, but it is vital in order to reduce backgrounds in the search for the Higgs boson.

The production of photons has two sources; firstly in the hard partonic process where the photon is well separated from the other partons and secondly at smaller scales where the photon can either be emitted collinear to its parent quark or where a parton can fragment into a photon. The hard partonic mechanism is well understood and can be calculated using pQCD whereas the smaller scale process contains a universal, non-perturbative effect and uncancelled infra red poles. However, as we shall see later, the non-perturbative term can be constrained by a well-determined evolution and the poles absorbed into the definition of the fragmentation.

This chapter will concentrate on introducing the theoretical tools necessary to calculate the photon distribution. Section 6.2 will outline the isolated and non-isolated photon events as described above and Section 6.3 introduces the concept of the fragmentation function making use of the process $e^+e^- \to \gamma + 1$ jet for which the non perturbative fragmentation function has been experimentally measured. Section 6.4 will detail a necessary tool in dealing with hadronic colliders, that of initial state radiation and how this leads to $C_a^H(x)$ functions. Section 6.5 will incorporate these two functions into the calculation and outline the Monte Carlo, DPRAD.

## 6.2 Photon emission and fragmentation functions

Let us look at the two cases of photon emission more closely. Isolated photon emission is an attractive area to study many aspects of both pQCD and new physics as the non-perturbative fragmentation contributions are neglected due to their collinear nature. Isolated photons are emitted at a scale where perturbation theory is reliable and as such tend to be well separated from the remaining partons. This is due to the uncertainty principle where over a short time scale, an off-shell internal quark line propagates a small distance before returning on shell by emitting a photon. The photon-quark pair have a large invariant mass and the angle between them is large leading to the isolation of the photon.

Experimentally (and theoretically), isolation of a photon is determined by applying a cone algorithm. There are a number of different techniques [72, 73] for doing this and here we outline the most common found in the literature [72].

A cone of specified half angle $\delta$ is centred on the photon direction. For hadron colliders this cone is usually taken to be a region in pseudorapidity-azimuthal angle space determined by the equation

$$R < \sqrt{(\Delta\eta)^2 + (\Delta\phi)^2} \tag{6.2.1}$$

where for small values of $\eta$, $R \approx \delta$. Inside the cone, the total hadronic energy is calculated. If it is less than a certain cut (usually a fraction of the photon's energy), the event is retained. Note that the amount of hadronic energy cannot be exactly zero (and the isolation complete) as this is infrared unsafe because the phase space of potential soft gluon radiation is limited. Therefore isolated photon calculations cannot completely neglect fragmentation contributions although they are suppressed.

In $e^+e^-$ colliders a different procedure is used. Typically the photon is removed from the event and normal clustering algorithms (as described in Section 2.2.1) are applied to the remaining partons/jets. The photon is returned and the event retained if the photon remains resolvable from the clustered partons/jets. (See Figure 6.1 for the phase space division using the cone algorithm in the process $e^+e^- \to \gamma + 1$ jet.) Note that this technique combines any partons originally inside the cone into jets outside the cone. It also treats gluons and quarks differently, allowing soft gluons inside the cone, but quarks are kept out. In experimental calculations the exact nature of the hadronic energy is not classified and it was seen that using this algorithm the NLO predicted rate for the process $e^+e^- \to \gamma + 1$ jet was too large. It was suggested (Stirling and Glover in[72]) that the two step nature of this prescription was responsible for this discrepancy.

An alternative approach to photon calculations is to attempt to experimentally measure the non-perturbative fragmentation component of the fragmentation function and use this universal quantity in other theoretical calculations. The cone algorithm can be used for this type of analysis, although a better algorithm would be more susceptible to the fraction of the parent quark's momentum carried off by the photon. Also by allowing electromagnetic and hadronic clustering a closer representation of experimental techniques can be found. One method proposed (see Morgan and Glover in [71]) is to treat the photon in a democratic manner, retaining it in the event whilst the clustering algorithm is applied. The jet with the

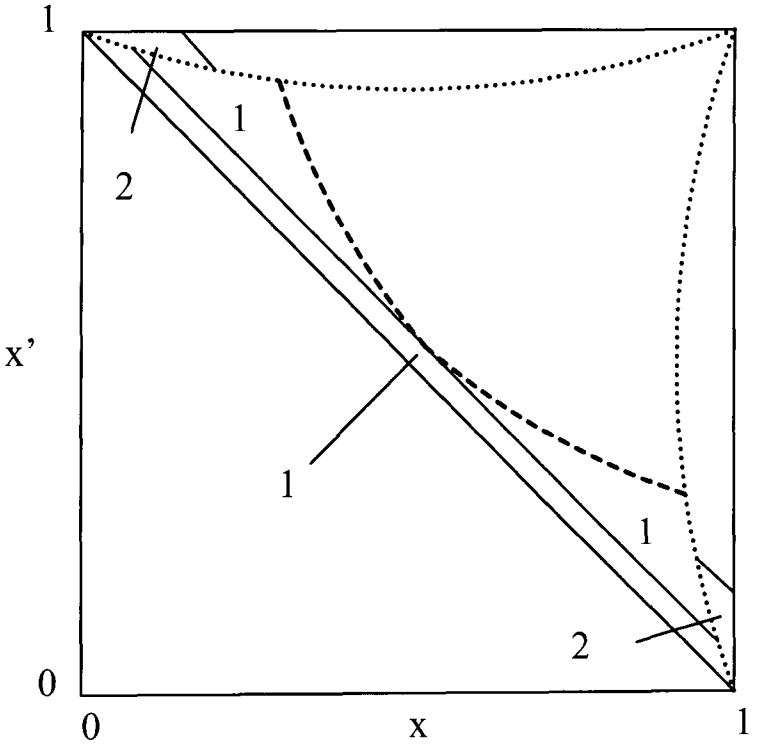


Figure 6.1: The Dalitz plot for the process $e^+e^- \to q\bar{q}\gamma$ where $x' = 1 - s_{q\gamma}/s$ and $x = 1 - s_{\bar{q}\gamma}/s$ using the cone algorithm. Plotted are the two regions that contribute to the process $e^+e^- \to \gamma + 1$ jet, for two different clustering algorithms, JADE and Durham. Regions 2 are common to both algorithms and are the regions in which the photon is emitted collinear to the quark/antiquark (along the $x/x' = 1$ line) and where the hadronic energy inside the cone is less than $\varepsilon E_\gamma$. Regions 1 are where the quark and antiquark merge to form a single jet and are different for the two clustering algorithms.

photon in it is declared the photon candidate and the event is rejected if the hadronic energy in it makes up more than a certain fraction of the total energy. i.e we define a parameter

$$z = \frac{E_\gamma}{(E_\gamma + E_{\text{had}})} \tag{6.2.2}$$

such that $z$ must be higher than a certain cut for the event to be retained. This better models the democracy of the experimental measurement. Also the algorithm no longer suppresses the second source of photon emission and the photon is allowed to be emitted collinear to the quark, thus making the calulation sensitive to long range, non-perturbative physics. This can then be used to measure the photon fragmentation function and once this universal function is known it can be applied to different processes.

Let us consider the inclusive NLO calculation for the process $e^+e^- \to \gamma + 1$ jet. This process is particularly sensitive to the fragmentation of final state partons, as it has no LO diagram. Therefore, the lowest order terms that constitute this process are $e^+e^- \to q\bar{q}\gamma$ where the quark and antiquark become collinear and form a single jet and the fragmentation process $e^+e^- \to q\bar{q}$ where the quark or the antiquark fragment (see Figure 6.2). We shall use this process to demonstrate how the collinear quark-photon poles can be absorbed into the non-perturbative fragmentation function. This then leads to a well-defined evolution equation for the fragmentation function with respect to the fragmentation scale which is similar to the renormalisation scale of Section 1.3. From this evolution equation and other considerations a parametric form for the fragmentation function can be proposed, the parameters of which must be experimentally measured. It is these parameters that the ALPEH collaboration have measured in[74].

## 6.3 Construction of the $q \to \gamma$ fragmentation function

Photon-quark collinear divergences are defined as in the previous chapters (i.e. $s_{q\gamma} < s_{\text{min}}$ where $s_{\text{min}}$ is similiar to $\delta$ in the 4 jet calculation. We make the change to avoid confusion between the cut and the cone size) using the slicing technique to divide the phase space into resolved and unresolved regions. They are absorbed into the definition of the fragmentation

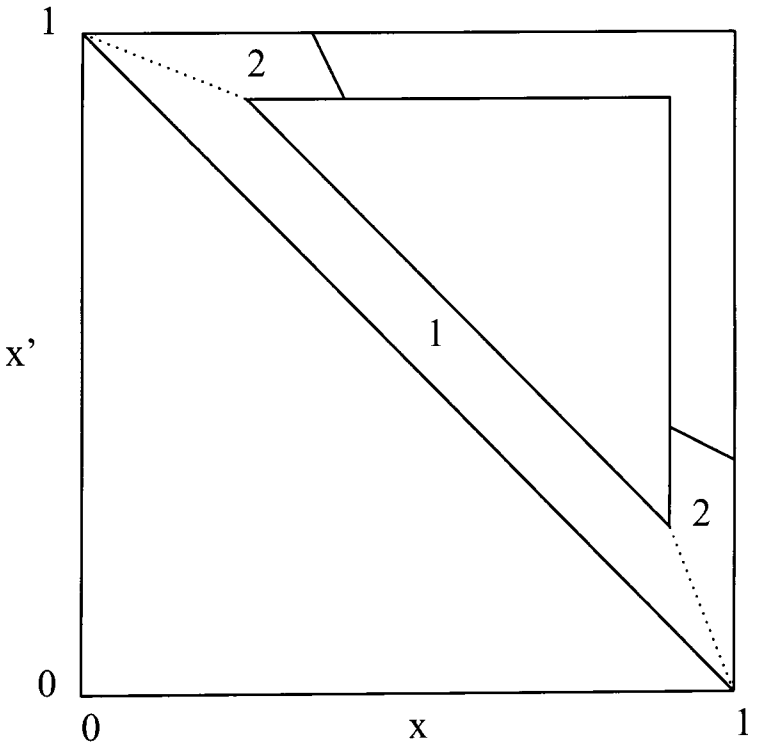


Figure 6.2: The Dalitz plot for the process $e^+e^- \to q\bar{q}\gamma$ where $x' = 1 - s_{q\gamma}/s$ and $x = 1 - s_{\bar{q}\gamma}/s$ using the democratic algorithm. Plotted are the two regions that contribute to the process $e^+e^- \to \gamma + 1$ jet, for the JADE clustering algorithms. Regions 2 are the regions in which the photon is emitted collinear to the quark/antiquark (along the $x/x' = 1$ line) and where the energy fraction of the electromagnetic energy over the total jet energy is greater than $z_{\text{cut}}$. Region 1 is where the quark and antiquark form a single jet.These two regions are divided by the dotted line.

function, $D_{a\to\gamma}(z)$ in much the same way as the loop corrections to the quark-gluon vertex were absorbed into the definition of the coupling constant $\alpha_s$ (see Section 1.3). Therefore the infinite bare $D_{a\to\gamma}(z)$ is replaced by the finite $\mathcal{D}_{a\to\gamma}(z)$. The two functions are related by the expression.

$$\mathcal{D}_{a\to\gamma}(z) = D_{a\to\gamma}(z) - \frac{1}{\varepsilon}\left(\frac{4\pi\mu_R^2}{s_{\min}}\right)^{\varepsilon}\frac{1}{\Gamma(1-\varepsilon)}\left(\frac{\alpha\, e_q^2}{2\pi}\right)[z(1-z)]^{-\varepsilon}P^{(0)}_{q\gamma\to q}(z) \tag{6.3.3}$$

where the LO photon splitting function, $P^{(0)}_{q\to\gamma}(z)$ has the same $z$ dependence as the gluon one (see Equation 2.3.54). The second term is the explicit form of the divergence (after slicing) as the photon becomes collinear with the quark. This includes $\mu_R$ as the usual renormalisation scale (from here on we refer to the renormalisation scale as $\mu_R$ to avoid confusion between other scales).

As with coupling constant renormalisation (in the $\overline{\text{MS}}$ scheme) this factorisation of singularities introduces a scale to the new finite quantity. Making this explicit we write the bare fragmentation function as a counter term to the collinear pole with some degree of non-perturbative input so that

$$D_{q\to\gamma}(z) = D_{q\to\gamma}(z,\mu_{\text{frag}}) + \frac{1}{\varepsilon}\left(\frac{4\pi\mu_R^2}{\mu_{\text{frag}}^2}\right)\frac{1}{\Gamma(1-\varepsilon)}\left(\frac{\alpha\, e_q^2}{2\pi}\right)P^{(0)}_{q\to\gamma}(z) \tag{6.3.4}$$

This gives the full result of the finite, dressed fragmentation function at LO as

$$\mathcal{D}_{q\to\gamma}(z) = D_{q\to\gamma}(z,\mu_{\text{frag}}) + \left(\frac{\alpha\, e_q^2}{2\pi}\right)\left(P^{(0)}_{q\to\gamma}(z)\log\left(\frac{s_{\min}\, z(1-z)}{\mu_{\text{frag}}^2}\right) + z\right) \tag{6.3.5}$$

As well as deriving the perturbative part of the fragmentation function, we note that $\mathcal{D}$ must be independent of the unphysical fragmentation scale $\mu_{\text{frag}}$ at each order. Therefore, at this order we can write an evolution equation which the perturbative part of the function forces on the non-perturbative part such that

$$\frac{\partial D_{q\to\gamma}(z,\mu_{\rm frag})}{\partial \log(\mu^2_{\rm frag})} = \left(\frac{\alpha\, e_q^2}{2\pi}\right) P^{(0)}_{q\to\gamma}(z) \tag{6.3.6}$$

This is similar to the evolution equation of the running coupling constant and just as $\alpha_s$ can be run to different scales once known at one, so can the non-perturbative part of the fragmentation function. The evolution equation is only of this form at this order i.e. $\mathcal{O}(\alpha)$ and at higher orders we must include additional terms where, for example the quark emits an unresolved gluon before fragmenting. Similarly we will have a contribution from gluons decaying into a collinear $q\bar{q}$ pair where one of the pair later fragments into a photon. This can be thought of as the gluon fragmenting and is thus the leading order term for the function $D_{g\to\gamma}(z,\mu_{\rm frag})$. However we do not include this for our calculation as in the Glover/Morgan power counting scheme it is $\mathcal{O}(\alpha\alpha_s)$.

Another consequence of renormalising the fragmentation function is that a pseudo pole has been introduced into the perturbative term. In the process $e^+e^- \to \gamma + 1$ jet this was explicitly demonstrated by Morgan and Glover in[71]. (Note that the appearance of this pole is dependent on the renormalisation scheme used. For schemes such as $\mathrm{DIS}_\gamma$[75] the pole is absorbed into the non-perturbative term already.) We find that the perturbative part of the fragmentation function has a term of the form $\log(1-z)^2$ (where one factor comes from the renormalisation as seen above and the other from the boundary between the quark-photon collinear phase space region and the quark-antiquark collinear phase region) which blows up as $z \to 1$. Therefore we place a further constraint on $D_{q\to\gamma}(z,\mu_{\rm frag})$ that it must cancel this pseudo-pole ensuring the $e^+e^- \to \gamma + 1$ jet rate is well-behaved as $z \to 1$.

Also, as $s_{\rm min}$ is an artifical construct, physical observables cannot depend on it. It is seen that when recombined with the resolved photon contributions that all dependence disappears (assuming $s_{\rm min}$ is taken small enough for the approximations to hold true).

A possible form for the non-perturbative part of the fragmentation function calculated at the order $O(\alpha)$ has the structure

$$D^{\rm LO}_{q\to\gamma}(z,\mu_{\rm frag}) = \left(\frac{\alpha\, e_q^2}{2\pi}\right) P^{(0)}_{q\to\gamma}(z) \log\left(\frac{\mu^2_{\rm frag}}{\mu_0^2}\right) + D^{\rm LO}_{q\to\gamma}(z,\mu_0) \tag{6.3.7}$$

where $\mu_0$ and $D^{\rm LO}_{q\to\gamma}(z,\mu_0)$ are constants of integration or more physical, $\mu_0$ can be thought of as the scale at which the physics becomes non-perturbative and as such can only be determined from experimental measurement which will give $D^{\rm LO}_{q\to\gamma}(z,\mu_0)$. As can be seen, this function has the correct form to satisfy both the cancellation of the pseudo-pole and the evolution equation.

The values of $\mu_0$ and $D^{\rm LO}_{q\to\gamma}(z,\mu_0)$ have been extracted from data gathered by the ALEPH collaboration using a democratic algorithm and the Durham clustering in the region $0.7 < z < 0.95$. It was found that

$$D^{\rm LO}_{q\to\gamma}(z,\mu_0) = \left(\frac{\alpha\, e_q^2}{2\pi}\right)\left(-P^{(0)}_{q\to\gamma}(z)\log(1-z)^2 - 1 - \ln\left(\frac{M_Z^2}{2\mu_0^2}\right)\right) \tag{6.3.8}$$

This then leads to a one parameter fit the result of which is given by

$$\mu_0 = 0.14^{+0.21+0.22}_{-0.08-0.04}\ \text{GeV} \tag{6.3.9}$$

However, if the calculation of $e^+e^- \to 1$ jet is extended to $\mathcal{O}(\alpha\alpha_s)$ [79] and the form of the fragmentation function recalculated we find that

$$\begin{aligned} D^{\rm NLO}_{q\to\gamma}(z,\mu_{\rm frag}) &= D^{\rm NLO}_{q\to\gamma}(z,\mu_0) + \left(\frac{\alpha e_q^2}{2\pi}\right)\log\left(\frac{\mu^2_{\rm frag}}{\mu_0^2}\right)P^{(0)}_{q\to\gamma}(z) \\ &+ \left(\frac{\alpha e_q^2}{2\pi}\right)\left(\frac{\alpha_s}{2\pi}\right)\log\left(\frac{\mu^2_{\rm frag}}{\mu_0^2}\right)P^{(1)}_{q\to\gamma}(z) \\ &+ \frac{1}{2}\left(\frac{\alpha\, e_q^2}{2\pi}\right)\left(\frac{\alpha_s}{2\pi}\right)\log^2\left(\frac{\mu^2_{\rm frag}}{\mu_0^2}\right)P^{(0)}_{q\to q}(z)\otimes P^{(0)}_{q\to\gamma}(z) \\ &+ \left(\frac{\alpha_s}{2\pi}\right)\log\left(\frac{\mu^2_{\rm frag}}{\mu_0^2}\right)P^{(0)}_{q\to q}(z)\otimes D^{\rm NLO}_{q\to\gamma}(z,\mu_0) \end{aligned} \tag{6.3.10}$$

where $P^{(1)}_{q\to\gamma}(z)$ is the next to leading order quark to photon universal splitting function and $P^{(0)}_{q\to q}(z)$ is the leading order quark to quark universal splitting function [38]. The non-perturbative input $D^{\rm NLO}_{q\to\gamma}(z,\mu_0)$ can then be extracted by performing a similar fit to the ALEPH data [74] (except now we also have to fit for $\alpha_s(M_Z)$ as well) giving

$$D^{\mathrm{NLO}}_{q\to\gamma}(z,\mu_0) = \left(\frac{\alpha e_q^2}{2\pi}\right)\left(-P^{(0)}_{q\to\gamma}(z)\log(1-z)^2 + 20.8(1-z) - 11.07\right) \tag{6.3.11}$$

with $\mu_0 = 0.64$ GeV and $\alpha_s(M_Z) = 0.124$.

Another form for the fragmentation function can be derived by considering the evolution equations and resumming all the leading logarithms (LL) and next to leading logarithms (NLL) respectively. For this thesis we shall present a basic overview of this technique. For more details the reader is referred to [78]. Let us for the moment assume that the perturbative part of the fragmentation function is proportional to $\alpha/\alpha_s$ instead of the fixed approach where it is proportional to $\alpha$. This adapts the LO evolution equation such that the convolution between the fragmentation function and the quark to quark splitting is as important as the quark to photon splitting function. Therefore the new LO and NLO evolution equations are given by

$$\begin{aligned}
\frac{\partial D^{\mathrm{LO}}_{q\to\gamma}(z,\mu^2_{\mathrm{frag}})}{\partial\log(\mu^2_{\mathrm{frag}})} &= \left(\frac{\alpha e_q^2}{2\pi}\right)P^0_{q\to\gamma}(z) + \left(\frac{\alpha_s}{2\pi}\right)P^{(0)}_{q\to q}(z)\otimes D_{q\to\gamma}(z,\mu^2_{\mathrm{frag}}) \\
\frac{\partial D^{\mathrm{NLO}}_{q\to\gamma}(z,\mu^2_{\mathrm{frag}})}{\partial\log(\mu^2_{\mathrm{frag}})} &= \left(\frac{\alpha e_q^2}{2\pi}\right)\left(P^0_{q\to\gamma}(z) + \frac{\alpha_s}{2\pi}P^{(1)}_{q\to\gamma}(z)\right) \\
&+ \left(\frac{\alpha_s}{2\pi}\right)\left(P^{(0)}_{q\to q}(z) + \frac{\alpha_s}{2\pi}P^{(1)}_{q\to q}\right)\otimes D_{q\to\gamma}(z,\mu^2_{\mathrm{frag}}) +
\end{aligned} \tag{6.3.12}$$

As with the fixed order technique the solutions to Equations 6.3.12 have two contributions, a perturbative, pointlike term and a non-perturbative hadronic term. The perturbative part of the resummed solution of Equation 6.3.12 is found by the following prescription

- The leading logarithmic (LL) or beyond leading logarithmic (BLL) approximation is performed by Mellin transforming the respective evolution equation. A Mellin transform is defined as

$$D_{q\to\gamma}(n,\mu^2_{\mathrm{frag}}) = \int_0^1 dz\; z^{n-1}D_{q\to\gamma}(z,\mu^2_{\mathrm{frag}}) \tag{6.3.13}$$

The transform has the effect of separating any convoluted functions and thus making the necessary integration over $\log(\mu^2_{\text{frag}})$ possible. Therefore after Mellin transformation an analytic solution can be found.

- The solution is then Mellin inverted numerically such that the fragmentation function is returned to $z$ space. For LL, only terms of the order $\alpha_s^n \log^{n+1}(\mu^2_{\text{frag}})$ are kept whereas for BLL both leading logarithms and logarithms of the form $\alpha_s^n \log^n(\mu^2_{\text{frag}})$ are retained. The coupling constant is expanded according to the beta function up to the order required. Approximations of these numerical resummed solutions can be obtained analytically by expanding the solution as a series in $\alpha_s$ in moment space and then analytically inverting the truncated expression.

From the asymptotic limit of the Mellin transform where the solution is independent of any experimental input

$$D^{\text{asymptot}}_{q\to\gamma}(n, \mu^2_{\text{frag}}) = \left(\frac{\alpha e_q^2}{2\pi}\right) \frac{2\pi}{\alpha_s(\mu^2_{\text{frag}})} a(n) \tag{6.3.14}$$

we see justification for our choice that the fragmentation function is of the order $\mathcal{O}(\alpha/\alpha_s)$ unlike in the fixed order approach where it is simply $\mathcal{O}(\alpha)$. This makes the fragmentation contribution as important as the LO perturbative contribution in $p\overline{p} \to \gamma+$ jets.

The hadronic part of the fragmentation function is given by the solution of the homogenous evolution equation i.e $P^0_{q\to\gamma} = P^1_{q\to\gamma} = 0$. Again we perform a Mellin transformation to make the integral over the convolution possible and return the solution to $z$ space afterwards. However, an additional input must be included in the hadronic solution similar to the $D_{q\to\gamma}(z, \mu_0)$ term in the fixed order solution. This input can either be taken from experimental data or from a set of VMD (Vector Meson Dominance) model assumptions and whichever approach used is proportional to $\alpha$ only.

Even when both the perturbative and non-perturbative parts of the resummed solution have been calculated, there exists some ambiguity in how to combine them. One method is to combine the relevant terms together such as the LL pointlike solution with the LL hadronic solution. This approach was adopted by Glück, Reya and Vogt (GRV) [80]. However this

prescription has a tendency to include terms beyond the order being considered which can lead to significant contributions and must be systematically omitted.

Another approach performed by Bourhis, Fontannaz and Guillet (BFG) [81] links the BLL perturbative solution with the LL hadronic solution. We shall see later how this resummed approximation compares with the fixed order calculation.

For resummation techniques to work, the resummed logarithms must be the only large logarithms present in the calculation as all other logarithms are neglected including terms of the order $\ln(1-z)$ which we saw are important in the large $z$ limit for the process $e^+e^- \rightarrow \gamma + 1$ jet. When resummed analytic expressions for $D_{q\rightarrow\gamma}$ are implemented into a Monte Carlo routine for electron-positron annihilation, the $\ln(1-z)$ contribution from the perturbative counter term is not cancelled and the differential cross-section becomes negative for $0.9 < z < 1$. This was pointed out by B.R.Webber in [76] where he stated that the leading logarithmic approximation would be expected to yield accurate predictions for intermediate values of $z$ only. The ALEPH collaboration also made a fit to data for this form of the fragmentation function, but in order to approach the data, large values of $\Lambda$ were required (of the order 1 GeV). Scales of this size no longer allow for the dismissing of non-logarithmic terms in the fragmentation function and as such suggests that the LLA approach should be ruled out at values of $z$ between 0.7 and 0.9.

`DPRAD` makes use of the fragmentation function as defined in Equation 6.3.7 with the measured parameters of Equations 6.3.8 and 6.3.9 for the process $p\overline{p} \rightarrow \gamma+$ jets. We also study the effects of using the BFG resummed fragmentaion function. Before we can detail the structure of `DPRAD`, we need to consider another theoretical tool used in hadron colliders, that of calculating initial state radiation.

## 6.4 Initial state radiation and crossing functions

In our previous calculations we have only treated final state radiation because the initial state of $e^+e^-$ cannot radiate gluons. However in the collision of a proton and an antiproton, we allow ourselves the possibility of producing initial state hadronic radiation that is unresolved in the detector. This radiation (and the poles that are produced) is absorbed into the

structure functions of the participating hadrons in much the same way as the quark-photon collinear poles were absorbed into the fragmentation function of the previous section.

We again make use of the ordered subamplitudes which exhibit the universal soft and collinear limits after colour decomposition. (See Section 2.3.8). For a full derivation of the crossing functions the reader is referred to [77, 36]. What we present here is an overview of that proof.

The differential cross section at leading order for the hadronic process $a + b \to \gamma + n$ partons where each parton is identified as a jet and $a$ and $b$ are the hadrons involved is given by

$$d\sigma_{H_1H_2} = \sum_{ij} f_a^{H_1}(x_1) f_b^{H_2}(x_2) d\sigma_{ab}^{\mathrm{LO}}(x_1, x_2) dx_1 dx_2 \tag{6.4.15}$$

where $f_a^{H_1}$ is the probability of finding parton $a$ in hadron $H_1$ with momentum fraction $x_1$ and $d\sigma_{ab}(x_1, x_2)$ is the squared matrix element of the partonic process with initial state partons $a$ and $b$ with incoming kinematics $x_1$ and $x_2$. This also contains the relevant phase space factors and initial averaging factors. In order to retain the crossing properties of LO at NLO we define the differential cross section at NLO as

$$d\sigma_{H_1H_2} = \sum_{ab} \mathcal{F}_a^{H_1}(x_1 \mathcal{F}_b^{H_2}(x_2) d\sigma_{ab}^{\mathrm{NLO}}(x_1, x_2) dx_1 dx_2 \tag{6.4.16}$$

where $\mathcal{F}_a^{H_1}$ is the effective NLO structure function and $d\sigma_{ab}^{\mathrm{NLO}}$ is the finite NLO partonic cross section which can be calculated by crossing from the NLO calculation of the process vacuum $\to a+b+\gamma+ng$. This can be expressed as usual in terms of a perturbative expansion in the coupling such that

$$d\sigma_{ab}^{\mathrm{NLO}} = d\sigma_{ab}^{\mathrm{LO}} + \alpha_s d\, \delta\sigma_{ab}^{\mathrm{NLO}} \tag{6.4.17}$$

where the coupling is evaluated at the renormalisation scale, $\mu_R$. A similar form can be written for the effective NLO structure functions after mass factorisation, the renormalisation procedure that absorbs all the divergences from the initial state poles. This can be written as

$$\mathcal{F}_a^{H_1}(x_1) = f_a^{H_1}(x_1, \mu_F) + \alpha_s C_a^{H_1}(x_1, \mu_F) \tag{6.4.18}$$

where the function $C_a^{H_1}(x_1, \mu_F)$ is known as a crossing function. Here $\alpha_s$ is calculated at the renormalisation scale. It can also be calculated using the factorisation scale although the difference is negligible (assuming $\alpha_s \ln(\mu_R^2/\mu_F^2) \ll 1$). This gives the full NLO result as

$$\begin{aligned} d\sigma_{H_1H_2} &= \sum_{ab} \Big[ f_a^{H_1}(x_1) f_b^{H_2}(x_2) (d\sigma_{ab}^{\mathrm{LO}}(x_1, x_2) + \alpha_s d\delta\sigma_{ab}^{\mathrm{NLO}}) \\ &+ \alpha_s (C_a^{H_1}(x_1) f_b^{H_2}(x_2) + f_a^{H_1} C_b^{H_2}(x_2)) d\sigma_{ab}^{\mathrm{LO}}(x_1, x_2) \Big] \end{aligned} \tag{6.4.19}$$

The crossing functions receive two contributions, which are due to the inability of differentiating between a single incoming parton and two collinear partons where the collinear partons either exist a) in the initial state and the final state or b) both in the initial state. The first of these leads to a convolution between the structure function and the Altarelli-Parisi splitting functions. The second contribution is necessary to cancel the unphysical initial-initial state collinear pairs which come from crossing two collinear partons from the final state to the initial state. Schematically this gives

$$C_a^{H_1} \approx \sum_c \left[ \int_x^1 \frac{dz}{z} f_c^{H_1}\left(\frac{x}{z}\right) P_{c\to a}(z) - f_a^{H_1}(x) \int_0^1 dz\, P_{a\to c} \right] \frac{y_{\min}^{-\varepsilon}}{\varepsilon} \tag{6.4.20}$$

where $y_{\min} = s_{\min}/Q$ and where the first term is due to the emission of radiation into the final state and the second is the crossed final state unresolved radiation. (The minus sign of this term is due to the crossing prescription.)

The derivation of the crossing functions makes use of the factorisation of phase space and the matrix elements as seen in Section 2.3.8, but with some slight modifications due to the initial state. We begin by concentrating on the initial-final state collinear pairs. We write the phase space of the $2 \to 2$ process with parton $Q$ off-shell as

$$dQ^2 d^d P(a+b \to u+Q) = dQ^2 \frac{d^{d-1}p_u}{2E_u}(2\pi)^{2-d}\delta(s_{ab} - |s_{au}| - |s_{bu}| - Q^2) \tag{6.4.21}$$

where the absolute values of the mass invariants are used to ensure positive values for those invariants between initial and final partons. We then write the $d-1$ integral as a 1 dimensional radial term multiplied by a $d-2$ dimensional angular term. This gives

$$\frac{d^{d-1}p_u}{2E_u} = \frac{d\Omega_{d-2}}{2}(E_u \sin\theta)^{d-3} dE_u d\theta \tag{6.4.22}$$

where $\theta$ is the angle between $u$ and $b$. Substituting the integration variables for invariants using the Jacobian we find

$$E_u^2 \sin^2\theta = \frac{s_{au}s_{ub}}{s_{ab}}; \quad ds_{au}ds_{ub} = 2E_u \sin\theta s_{ab} dE_u d\theta \tag{6.4.23}$$

which leads to

$$\frac{1}{2s_{ab}} dQ^2 d^d P(a+p \to u+Q) = dQ^2 \frac{d\Omega_{d-2}}{8}\left[\frac{|s_{au}||s_{bu}|}{s_{ab}}\right]^{\frac{d-4}{2}} \frac{d|s_{au}|d|s_{ub}|}{s_{ab}^2}(2\pi)^{2-d}\delta(s_{ab}-|s_{au}|-|s_{ub}|-Q^2) \tag{6.4.24}$$

As there is no dependence on the virtuality of $Q$ we can integrate over this without changing the rest of the factor. Now we consider the configuration where $u$ is collinear to $b$ such that $|s_{ub}| < s_{\min}$ and we introduce parton $h$ which participates in the hard scattering process. It carries a fraction $z$ of the parent quark's momentum such that

$$\begin{aligned} p_h &= z p_b; \quad s_{ah} = z s_{ab} \\ p_u &= (1-z) p_b; \quad |s_{au}| = (1-z) s_{ab} \end{aligned} \tag{6.4.25}$$

In this limit we find that the $2 \to 2$ body phase space factorises to a collinear term multiplied by the $2 \to 1$ phase space.

$$\frac{1}{s_{ab}} d^d P(a+b \to u+Q) \to d^d P_{\rm col}(b \to u+h) \frac{1}{2 s_{ah}} d^d P(a+h \to Q) \tag{6.4.26}$$

where

$$d^d P_{\rm col}(b \to u+h) = dz ds_{ub} z[(1-z)s_{ub}]^{\frac{4-d}{2}} \frac{d\Omega_{d-2}}{4} (2\pi)^{2-d} \frac{1}{2\pi} \tag{6.4.27}$$

This is the form for the collinear phase space factor that we shall use later. Now we shall briefly consider the behaviour of collinear initial state matrix elements.

The matrix elements, as in the collinear final state configurations, factorises when an initial state parton is collinear to a final state parton such that for $b$ and $u$ collinear we find

$$|\mathcal{M}(.., b, u, ...)|^2 \to c_F^{b \to u\, h} |\mathcal{M}(.., h, ...)|^2 \tag{6.4.28}$$

where

$$c_F^{i \to j\, k} = \left( \frac{g^2 N}{2} \right) \frac{1}{|s_{ij}|} \frac{P_{j\, k \to i}(z)}{z} \tag{6.4.29}$$

As we can see this is very similar to the final-final collinear factor. The extra factor $1/z$ is due to the identity of the partons becoming collinear. In the initial-final example we can see that the invariant mass is a factor $z$ smaller as we allow the parton with momentum fraction $(1-z)$ to take part in the hard scattering whereas before the hard scattering parton had a momentum fraction equal to 1. As before we shall use the conventional Altarelli-Parisi splitting functions which are defined in Equation 2.3.54. The major difference between the initial-final splitting and the final-final splitting is that the parton that participates in the hard scattering can not be soft. This places a lower bound on the value of $z$ unlike the final-final collinearity where the parent parton participates in the hard scattering and $z$ can be equal to 0. The upper bound of $z$ is also set by demanding that the final state parton in the initial-final collinear pair must not be soft (to avoid the double counting of final state soft gluons).

Incorporating Equation 6.4.26 and 6.4.28 into the cross section for the collinear pairing $s_{ub} < s_{\min}$ gives

$$d\sigma_{\text{initial}} = \sum_{a\,h\,b} f_a^{H_1}(x_1)[f_b^{H_2} c_F^{b\to uh} dP^d_{\text{col}}(b \to u+h)\delta(x_2 - zx')dx']d\sigma^{\text{LO}}_{ah}(x_1,x_2)dx_1dx_2 \quad (6.4.30)$$

where momentum fraction $x_2$ carried by parton $h$ is given by the momentum fraction $x'$ carried by parton $b$ multiplied by the fraction left after the emission of parton $u$ which carries off a fraction $(1-z)$ of the incoming momentum. Comparing this equation with Equation 6.4.19 we see the form of the crossing function is given by

$$\alpha_s C^{H_2}_{h,\text{initial}}(x_2) = \sum_b f_b^{H_2}(x') c_F^{b\to uh} dP^d_{\text{col}}(b \to u+h)\delta(x_2 - zx') \quad (6.4.31)$$

Making this explicit we substitute in Equations 6.4.29 and 6.4.27 giving

$$C^{H_2}_{h,\text{initial}}(x_2) = -\left(\frac{N}{2\pi}\right)\frac{1}{\Gamma(1-\varepsilon)}\left(\frac{4\pi\mu_R^2}{s_{\min}}\right)\frac{1}{\varepsilon}\sum_b \frac{1}{4}\int_{x'}^{1-z_2}\frac{dz}{z}(1-z)^{-\varepsilon}P_{hu\to b}(z)f_b^{H_2}\left(\frac{x'}{z}\right) \quad (6.4.32)$$

where we have integrated the delta function over the $y$ momentum fraction, giving the extra factor $1/z$, and also over the invariant mass $s_{ub}$ between the limits $0 < s_{ub} < s_{\min}$ assuming $0^{-\epsilon} = 0$. The scale $\mu_R$ is introduced to keep $\alpha_s$ dimensionless and the limits on the $z$ integral ensure that $u$ is not soft. (Here $z_2 = s_{\min}/|s_{bn}|$ where $n$ is the colour connected neighbour of $b$ and $|s_{un}| = (1-z)|s_{bn}|$.) The lower bound is fixed by assuming that parton $b$ is carrying all of the proton's momentum ($x' = 1$) and then the fraction needed to ensure $x_2$ enters the hard process is $z = x_2$.

As the splitting functions $P_{q\bar{q}\to g}$ and $P_{gq\to q}$ are not sensitive to the upper bound of the $z$ integral due to the non-singular nature of soft quarks (the quark-antiquark splitting does not depend on any of the limits and the quark-gluon splitting is only dependent on the lower bound whereas the gluon-quark splitting is only dependent on the upper bound) we allow their upper bounds to equal 1. We can also set the upper bound to 1 for the other two splittings by using the $(\ )_+$ prescription such that

$$\begin{aligned}
\int_x^{1-z_2} dz \frac{g(z)}{(1-z)^{1+\varepsilon}} &= \left(\frac{z_2^{-\varepsilon}-1}{\varepsilon}\right) g(1) + \int_x^1 dz \frac{g(z)}{[(1-z)^{1+\varepsilon}]_+} \\
\int_x^1 dz \frac{g(z)}{[(1-z)^{1+\varepsilon}]_+} &= \int_x^1 dz \frac{g(z)}{(1-z)_+} - \varepsilon \int_x^1 dz\, g(z) \left(\frac{\log(1-z)}{1-z}\right)_+ \\
\int_x^1 dz \frac{g(z)}{(1-z)_+} &= \int_x^1 dz \frac{g(z)-g(1)}{1-z} + g(1)\log(1-x) \\
\int_x^1 dz\, g(z) \left(\frac{\log(1-z)}{1-z}\right)_+ &= \int_x^1 dz \frac{g(z)-g(1)}{1-z}\log(1-z) + \frac{g(1)}{2}\log^2(1-x)
\end{aligned} \tag{6.4.33}$$

provided that $g(1)$ is well behaved. Therefore we can write the crossing functions all in terms of

$$C_{h,\text{initial}}^{H_2} = -\left(\frac{N}{2\pi}\right) \frac{1}{\Gamma(1-\varepsilon)} \left(\frac{4\pi\mu_R^2}{s_{\min}}\right)^{\varepsilon} \frac{1}{\varepsilon} \sum_b \int_{x_2}^1 \frac{dz}{z} f_b^{H_2}\left(\frac{x_2}{z}\right) J_{b\to h}(z, z_2) \tag{6.4.34}$$

where

$$
\begin{aligned}
J_{g\to g}(z,z_2) &= \left(\frac{z_2^{-\varepsilon}-1}{\varepsilon}\right)\delta(1-z)+\frac{z}{[(1-z)^{1+\varepsilon}]_+}+\frac{(1-z)^{1-\varepsilon}}{z}+z(1-z)^{1-\varepsilon} \\
J_{q\to q}(z,z_2) &= \left(1-\frac{1}{N^2}\right)\left[\left(\frac{z_2^{-\varepsilon}-1}{\varepsilon}\right)\delta(1-z)+\frac{1}{2}\left(\frac{1+z^2}{[(1-z)^{1+\varepsilon}]_+}-\varepsilon(1-z)^{1-\varepsilon}\right)\right] \\
J_{q\to g}(z,z_2) &= \frac{1}{4}P_{gq\to q}(z)(1-z)^{-\varepsilon} \\
J_{g\to q}(z,z_2) &= \frac{1}{4}P_{q\bar{q}\to g}(z)(1-z)^{-\varepsilon}
\end{aligned}
\tag{6.4.35}
$$

Now we must form the contribution from the crossed final state collinear pair. This is given by the final-final splitting seen in the previous chapters recalling now that $h \to ub$ rather than $b \to uh$

$$
d\sigma_{\text{final}} = \sum_{abh} f_a^{H_1}(x_1)[f_h^{H_2}(x_2)c_F^{bu\to h}d^dP_{\text{col,final}}]d\sigma_{ah}^{\text{LO}}(x_1,x_2)dx_1dx_2 \tag{6.4.36}
$$

where the equations for $c_F^{ij\to k}$ and $d^dP_{\text{col,final}}$ are given in Equations 2.3.54 and 2.4.67 respectively. This gives the form of the crossing function as

$$
\alpha_s C_{h,\text{final}}^{H_2}(x_2) = -\left(\frac{\alpha_s N}{2\pi}\right)\frac{1}{\Gamma(1-\varepsilon)}\left(\frac{4\pi\mu_R^2}{s_{\min}}\right)^{\varepsilon} f_h^{H_2}(x_2)\frac{1}{\varepsilon}\sum_b I_{bu\to h}(z_1,z_2) \tag{6.4.37}
$$

The function $I_{bu\to h}(z_1,z_2)$ is an integral over the momentum fraction $z$ and the integration limits $z_1$ and $z_2$ are again due to the requirement that $u$ cannot be soft where $z_1$ is defined as $s_{\min}/|s_{hn}|$ ($n$ is a colour connected neighbour). Therefore the integral is given by exactly the same form as for a final-final collinear pair

$$
I_{bu\to h}(z_1,z_2) = \frac{1}{4}\int_{z_1}^{1-z_2} dz[z(1-z)]^{-\varepsilon}P_{bu\to h}(z) \tag{6.4.38}
$$

which leads to

$$
\begin{aligned}
I_{gg\to g}(z_1,z_2) &= \left(\frac{z_1^{-\varepsilon}+z_2^{-\varepsilon}-2}{\varepsilon}\right)-\frac{11}{6}+\left(\frac{\pi^2}{3}-\frac{67}{18}\right)\varepsilon \\
I_{qg\to q}(z_1,z_2) &= \left(1-\frac{1}{N^2}\right)\left[\left(\frac{z_2^{-\varepsilon}-1}{\varepsilon}\right)-\frac{3}{4}+\left(\frac{\pi^2}{6}-\frac{7}{4}\right)\varepsilon\right] \\
I_{q\bar{q}\to g} &= \frac{1}{N}\left[\frac{1}{3}+\frac{5\varepsilon}{9}\right]
\end{aligned}
\tag{6.4.39}
$$

Combining these two functions into a single crossing kernel which is convoluted with the structure functions we find for the crossing function

$$
\begin{aligned}
C_h^{H_2} &= C_{h,\text{initial}}^H(x)-C_{h,\text{final}}^H(x) \\
&= \sum_b \int_x^1 \frac{dz}{z} f_b^H\left(\frac{x}{z}\right) X_{b\to h}(z)
\end{aligned}
\tag{6.4.40}
$$

where

$$
\begin{aligned}
X_{g\to g}(z) = &- \left(\frac{N}{2\pi}\right)\frac{1}{\Gamma(1-\varepsilon)}\left(\frac{4\pi\mu_R^2}{s_{\min}}\right)^{\varepsilon}\frac{1}{\varepsilon}\Big(J_{g\to g}(z,z_1)+J_{g\to g}(z,z_2)-\big[I_{gg\to g}(z_1,z_2) \\
&+ \frac{n_F}{N}I_{q\bar{q}\to g}(0,0)\big]\delta(1-z)\Big) \\
X_{q\to q}(z) = &- \left(\frac{N}{2\pi}\right)\frac{1}{\Gamma(1-\varepsilon)}\left(\frac{4\pi\mu_R^2}{s_{\min}}\right)^{\varepsilon}\frac{1}{\varepsilon}(J_{q\to q}(z,z_2)-I_{qg\to q}(0,z_2)\delta(1-z)) \\
X_{g\to q}(z) = &- \left(\frac{N}{2\pi}\right)\frac{1}{\Gamma(1-\varepsilon)}\left(\frac{4\pi\mu_R^2}{s_{\min}}\right)^{\varepsilon}\frac{1}{\varepsilon}J_{g\to q}(z,0) \\
X_{q\to g}(z) = &- \left(\frac{N}{2\pi}\right)\frac{1}{\Gamma(1-\varepsilon)}\left(\frac{4\pi\mu_R^2}{s_{\min}}\right)^{\varepsilon}\frac{1}{\varepsilon}J_{q\to g}(z,0)
\end{aligned}
\tag{6.4.41}
$$

where all dependence on the bounds of the integrals exactly cancels, leaving the kernel independent of the hard process. Note that for the gluon-gluon splitting we include two terms $J(z,z_2)$ and $J(z,z_1)$. This is due to the different ordering that the gluons can achieve in the splitting. The delta functions are used for calculated integrals at an arbitrary point along the $z$ integral with $z=1$ choosen for simplicity. The last two kernels $X_{g\to q}$ and $X_{q\to g}$ have no contribution from the crossed collinear pair as these would lead to soft initial quark states (as we let the upper bound equal 1) which are not allowed.

However, we still have explicit $1/\varepsilon$ poles that need to be absorbed. This is done by renormalising the bare LO structure functions $f_h^H(x)$ in the equation

$$\mathcal{F}_h^H(x) = f_h^H(x) + \alpha_s C_h^H(x) \tag{6.4.42}$$

The bare structure function is renormalised to give a finite LO structure function which is scale dependent and an infinite counter term that will cancel with the intial state collinear pairs. This can be written as

$$f_h^H(x) = f_h^H(x, \mu_F) - \alpha_s \sum_b \int_x^1 \frac{dz}{z} f_b^H\left(\frac{x}{z}, \mu_F\right) R_{b\to h}(z, \mu_F) \tag{6.4.43}$$

Therefore the finite crossing functions are given by

$$C_h^H(x, \mu_F) = \sum_b \int_x^1 \frac{dz}{z} f_b^H\left(\frac{x}{z}, \mu_F\right) \left(X_{b\to h}(z) + R_{b\to h}(z, \mu_F)\right) \tag{6.4.44}$$

These $R_{b\to h}(z, \mu_F)$ counter terms exactly cancel all the collinear poles leaving the effective structure functions independent of the factorisation scale although the fixed order cross section is dependent on $\mu_F$ as we neglect terms of the form $\alpha_s^2 C_a^{H_1}(x_1, \mu_F) C_b^{H_2}(x_2, \mu_F)$. For the exact forms of the counter terms the reader is referred to the previous reference of [77]. It is assumed for this overview that the scheme used is the $\overline{\text{MS}}$ scheme. After cancellation and integration, the finite form of the crossing functions is given by

$$C_h^{H,\overline{\text{MS}}}(x, \mu_F) = \left(\frac{N}{2\pi}\right) \left[A_h^H(x, \mu_F) \log\left(\frac{s_{\min}}{\mu_F^2}\right) + B_h^{H,\overline{\text{MS}}}(x, \mu_F)\right] \tag{6.4.45}$$

where we have summed over all partons $b$. The full form of the functions $A$ and $B$ can be found in [77]. Therefore, given a set of structure functions in a given scheme we can derive a set of process independent crossing functions which can be used in conjunction with the $\mathcal{O}(\alpha\alpha_s)$ $2 \to 2$ hard processes to calculate the $\mathcal{O}(\alpha\alpha_s^2)$ contribution from initial state radiation.

## 6.5 The full result and structure of DPRAD

We combine these two theoretical contributions to the standard NLO final state photon production calculations to find the resultant $\mathcal{O}(\alpha\alpha_s^2)$ form. In this section we shall outline the form of each contribution to the full prompt photon production process for this Monte Carlo.

### 6.5.1 LO contributions to 1 jet final states

The LO cross section for the production of a photon from hadron-hadron annihilation is relatively simple and the squared matrix elements can be calculated by hand or using a short FORM program. Without any quark flavour summation the LO contribution is given by

$$d\sigma^{\mathrm{LO}}_{\gamma+1\mathrm{jet}} = \int dx_1 dx_2 \sum_{ab} \frac{1}{2\hat{s}} f_a(x_1) f_b(x_2) |\mathcal{M}^{\mathrm{LO}}_{ab\to\gamma+1\ \mathrm{jet}}|^2 dPS_{2\to2} \tag{6.5.46}$$

where $x_1, x_2$ are the fractions of the hadron's momentum carried by the partons, $\hat{s} = x_1 x_2 s$ is the centre of mass energy of the partonic process, $f_a(x_1), f_b(x_2)$ are the LO parton distribution functions where parton $a$ is from the proton and parton $b$ is from the antiproton, $dPS_{2\to2}$ is the differential phase space factor for 2 to 2 body scattering and finally where the squared matrix elements are given by

$$|\mathcal{M}^{\mathrm{LO}}_{ab\to\gamma+1\ \mathrm{jet}}|^2 = 2\pi\alpha_s 4\pi\alpha\, e_q^2 (N^2-1) 8 \left( \frac{s_{qg}}{s_{q\gamma}} + \frac{s_{q\gamma}}{s_{qg}} \right) \tag{6.5.47}$$

However, we need to separately include the tree level processes $\overline{q}q \to g\gamma$, $q\overline{q} \to g\gamma$, $qg \to q\gamma$, $\overline{q}g \to \overline{q}\gamma$, $gq \to q\gamma$ and $g\overline{q} \to \overline{q}\gamma$ because the order and identity of the initial partons is important due to the different structure functions of the proton and the antiproton. We will assume for the rest of this thesis that the order of the initial partons is such that the first parton resides in the proton and the second in the antiproton. The relevant diagrams for this contribution are given in Figure 6.3

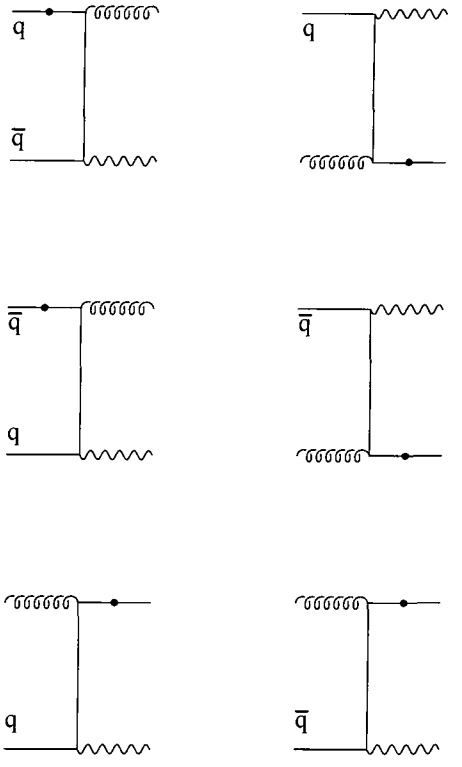


Figure 6.3: The tree level diagrams contributing to the process $p\bar{p} \to \gamma + 1$ jet. Diagrams are labelled such that the parton from the proton is in the top left hand corner of the diagram and the parton from the antiproton is in the bottom left hand corner of the diagram. Although many of the diagrams may appear the same, due to the different parton distribution functions of the proton and the antiproton we must calculate each individually i.e. no symmetry factor can be used to relate the cross section of the subprocess $q\bar{q} \to g\gamma$ to the cross section of $\bar{q}q \to g\gamma$ as the quark distribution is different in the proton compared to the antiproton. The dots on the quark lines indicate alternative locations for the photon which have been taken into account, but which do not affect the colour structure of the matrix elements.

### 6.5.2 LO contributions to 2 jet final states

Another source of tree level diagrams comes from the photon plus 2 jets final state diagrams. Again these can be calculated by FORM, but now we must consider three possible processes and their symmetries, $q\overline{q} \to gg\gamma$, $q\overline{q} \to Q\overline{Q}\gamma$ and $q\overline{q} \to q\overline{q}\gamma$. Therefore the cross section for this tree level process is given by

$$\begin{aligned} d\sigma^{\mathrm{LO}}_{\gamma+2\,\mathrm{jets}} &= \int dx_1 dx_2 \sum_{ab} \frac{1}{2\hat{s}} f_a(x_1) f_b(x_2) (|\mathcal{M}^{q\overline{q}\to gg\gamma}_{ab\to\gamma+2\,\mathrm{jets}}|^2 \\ &+ |\mathcal{M}^{q\overline{q}\to q\overline{q}\gamma}_{ab\to\gamma+2\,\mathrm{jets}}|^2 \\ &+ |\mathcal{M}^{q\overline{q}\to Q\overline{Q}\gamma}_{ab\to\gamma+2\,\mathrm{jets}}|^2) dPS_{2\to3} \end{aligned} \tag{6.5.48}$$

where the superscript refers to the subprocess and the subscript refers to the initial partons e.g. for the superscript $q\overline{q} \to gg\gamma$ we could have subscripts $q\overline{q} \to \gamma + 2$ jets, $qg \to \gamma + 2$ jets, $gq \to \gamma + 2$ jets plus all the charge conjugated initial states. $dPS_{2\to3}$ is the differential phase space factor for 2 to 3 body scattering. Firstly the squared matrix elements for the subprocess $q\overline{q} \to gg\gamma$ are given by

$$\begin{aligned} |\mathcal{M}^{q\overline{q}\to gg\gamma}_{ab\to\gamma+2\,\mathrm{jets}}|^2 &= (2\pi\alpha_s)^2 (4\pi\alpha e_q^2) N(N^2-1) 16 \Big[ |\mathcal{S}(Q;1,2;\overline{Q})|^2 + |\mathcal{S}(Q;2,1;\overline{Q})|^2 \\ &- \frac{1}{N^2} |\mathcal{S}(Q;\tilde{1},\tilde{2};\overline{Q})|^2 \Big] \end{aligned} \tag{6.5.49}$$

where

$$\begin{aligned} |\mathcal{S}(Q;1,2;\overline{Q})|^2 &= \frac{s^3_{qg_1} s_{g_1\overline{q}} + s^3_{qg_2} s_{g_2\overline{q}} + s^3_{q\gamma} s_{\gamma\overline{q}} + s_{qg_1} s^3_{g_1\overline{q}} + s_{qg_2} s^3_{g_2\overline{q}} + s_{q\gamma} s^3_{\gamma\overline{q}}}{s_{qg_1} s_{g_1g_2} s_{g_2\overline{q}} s_{q\gamma} s_{\gamma\overline{q}}} \\ |\mathcal{S}(Q;2,1;\overline{Q})|^2 &= \frac{s^3_{qg_1} s_{g_1\overline{q}} + s^3_{qg_2} s_{g_2\overline{q}} + s^3_{q\gamma} s_{\gamma\overline{q}} + s_{qg_1} s^3_{g_1\overline{q}} + s_{qg_2} s^3_{g_2\overline{q}} + s_{q\gamma} s^3_{\gamma\overline{q}}}{s_{qg_2} s_{g_2g_1} s_{g_1\overline{q}} s_{q\gamma} s_{\gamma\overline{q}}} \\ |\mathcal{S}(Q;\tilde{1},\tilde{2};\overline{Q})|^2 &= \frac{s_{q\overline{q}} (s^3_{qg_1} s_{g_1\overline{q}} + s^3_{qg_2} s_{g_2\overline{q}} + s^3_{q\gamma} s_{\gamma\overline{q}} + s_{qg_1} s^3_{g_1\overline{q}} + s_{qg_2} s^3_{g_2\overline{q}} + s_{q\gamma} s^3_{\gamma\overline{q}})}{s_{qg_1} s_{qg_2} s_{q\gamma} s_{g_1\overline{q}} s_{g_2\overline{q}} s_{\gamma\overline{q}}} \end{aligned} \tag{6.5.50}$$

We recover the related processes e.g. $qg \to qg\gamma$ by exchanging momenta in the invariants, but the form remains the same. All colour distinct diagrams are given in Figure 6.4

Secondly, the squared matrix elements for the subprocess $q\overline{q} \to Q\overline{Q}\gamma$ where the flavours of the quarks are distinct. We treat this separately to the process where the flavours of the quarks are identical. The form of the squared matrix elements before summation over the quark flavours is given by

$$\begin{aligned} |\mathcal{M}^{q\overline{q}\to Q\overline{Q}\gamma}_{ab\to\gamma+2\,\text{jets}}|^2 &= (2\pi\alpha_s)^2(4\pi\alpha)(N^2-1)16\left[e_q^2|\mathcal{T}(q,\overline{q};q,\overline{q})|^2 + e_Q^2|\mathcal{T}(Q,\overline{Q};Q,\overline{Q})|^2\right. \\ &+ \left. e_q e_Q|\mathcal{T}(q,\overline{q};Q,\overline{Q})|^2 + e_q e_Q|\mathcal{T}(Q,\overline{Q};q,\overline{q})|^2\right] \end{aligned} \tag{6.5.51}$$

where the arguments of the $\mathcal{T}$ functions indicate which quark line the photon couples to in the matrix element and the conjugate respectively. Note that the degree of colour is reduced by a factor $N$ for the four quark term compared to the 2 quark, 2 gluon term making this a sub-leading colour contribution. The $\mathcal{T}$ functions are given by

$$\begin{aligned} \mathcal{T}(q,\overline{q};q,\overline{q}) &= \frac{s_{qQ}^2 + s_{\overline{q}\overline{Q}}^2 + s_{q\overline{Q}}^2 + s_{Q\overline{q}}^2}{s_{q\gamma}s_{\gamma\overline{q}}s_{Q\overline{Q}}} \\ \mathcal{T}(Q,\overline{Q};Q,\overline{Q}) &= \frac{s_{qQ}^2 + s_{\overline{q}\overline{Q}}^2 + s_{q\overline{Q}}^2 + s_{Q\overline{q}}^2}{s_{q\overline{q}}s_{q\gamma}s_{\gamma\overline{q}}} \\ \mathcal{T}(q,\overline{q};Q,\overline{Q}) + \mathcal{T}(Q,\overline{Q};q,\overline{q}) &= (s_{qQ}^2 + s_{\overline{q}\overline{Q}}^2 + s_{q\overline{Q}}^2 + s_{Q\overline{q}}^2) \\ \times &\left(\frac{s_{q\overline{Q}}}{s_{q\gamma}s_{\gamma\overline{Q}}s_{q\overline{q}}s_{Q\overline{Q}}} + \frac{s_{Q\overline{q}}}{s_{Q\gamma}s_{\gamma\overline{q}}s_{q\overline{q}}s_{Q\overline{Q}}} - \frac{s_{qQ}}{s_{q\gamma}s_{Q\gamma}s_{q\overline{q}}s_{Q\overline{Q}}} - \frac{s_{\overline{q}\overline{Q}}}{s_{\gamma\overline{q}}s_{\gamma\overline{Q}}s_{q\overline{q}}s_{Q\overline{Q}}}\right) \end{aligned} \tag{6.5.52}$$

The final LO squared matrix elements to calculate are those for the subprocess $q\overline{q} \to q\overline{q}\gamma$ where the quark flavour is identical for the two fermion lines. Here we will refer to the quarks as pair 1 and pair 2 to identify which line the photon couples to. However, unlike the distinct quark flavour diagram there exist two LO matrix element diagrams, one in the $s$ channel and one in the $t$ channel. This leads to two squared terms and two interference terms in the squared matrix element which have different colour factors. We find

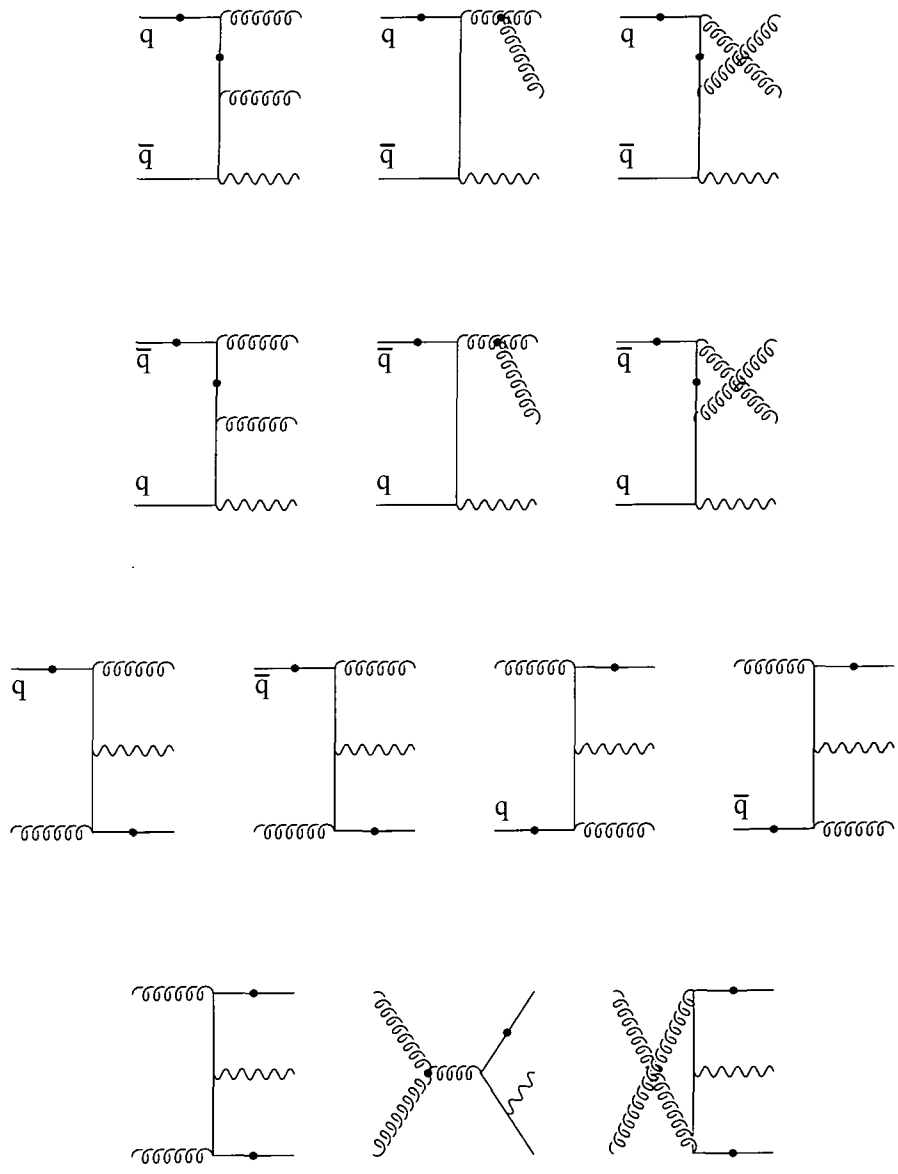


Figure 6.4: The tree level diagrams contributing to the process $p\bar{p} \to \gamma + 2$ jets through symmetries of the subprocess $q\bar{q} \to gg\gamma$. Diagrams are labelled such that the parton from the proton is in the top left hand corner of the diagram and the parton from the antiproton is in the bottom left hand corner of the diagram. Although many of the diagrams may appear the same, due to the different parton distribution functions of the proton and the antiproton we must calculate each individually i.e. no symmetry factor can be used to relate the cross section of the subprocess $q\bar{q} \to gg\gamma$ to the cross section of $\bar{q}q \to gg\gamma$ as the quark distribution is different in the proton compared to the antiproton. The dots on the quark lines indicate alternative locations for the photon which have been taken into account, but which do not affect the colour structure of the matrix elements. The dot on the gluon line indicates a triple gluon coupling.

$$|\mathcal{M}^{q\bar{q}\to q\bar{q}\gamma}_{ab\to\gamma+2\,\text{jets}}|^2 = (2\pi\alpha_s)^2(4\pi\alpha\, e_q^2)(N^2-1)16 \left(|\mathcal{T}_{\text{s channel}}|^2 + |\mathcal{T}_{\text{t channel}}|^2 + \frac{1}{N}(|\mathcal{T}_{\text{s channel}}\mathcal{T}^{\dagger}_{\text{t channel}}| + |\mathcal{T}_{\text{t channel}}\mathcal{T}^{\dagger}_{\text{s channel}}|)\right) \tag{6.5.53}$$

where

$$|\mathcal{T}_{\text{s channel}}|^2 = \left(\frac{s^2_{q_1q_2}+s^2_{\overline{q_1q_2}}+s^2_{q_1\overline{q_2}}+s^2_{q_2\overline{q_1}}}{s_{q_1\overline{q_1}}s_{q_2\overline{q_2}}}\right)\times \left[\frac{s_{q_1\overline{q_2}}}{s_{q_1\gamma}s_{\gamma\overline{q_2}}}+\frac{s_{q_2\overline{q_1}}}{s_{q_2\gamma}s_{\gamma\overline{q_1}}}+\frac{s_{q_1\overline{q_1}}}{s_{q_1\gamma}s_{\gamma\overline{q_1}}}+\frac{s_{q_2\overline{q_2}}}{s_{q_2\gamma}s_{\gamma\overline{q_2}}}-\frac{s_{q_1q_2}}{s_{q_1\gamma}s_{q_2\gamma}}-\frac{s_{\overline{q_1q_2}}}{s_{\gamma\overline{q_1}}s_{\gamma\overline{q_2}}}\right]$$

$$|\mathcal{T}_{\text{t channel}}|^2 = \left(\frac{s^2_{q_1q_2}+s^2_{\overline{q_1q_2}}+s^2_{q_1\overline{q_1}}+s^2_{q_2\overline{q_2}}}{s_{q_1\overline{q_2}}s_{q_2\overline{q_1}}}\right)\times \left[\frac{s_{q_1\overline{q_1}}}{s_{q_1\gamma}s_{\gamma\overline{q_1}}}+\frac{s_{q_2\overline{q_2}}}{s_{q_2\gamma}s_{\gamma\overline{q_2}}}+\frac{s_{q_1\overline{q_2}}}{s_{q_1\gamma}s_{\gamma\overline{q_2}}}+\frac{s_{q_2\overline{q_1}}}{s_{q_2\gamma}s_{\gamma\overline{q_1}}}-\frac{s_{q_1q_2}}{s_{q_1\gamma}s_{q_2\gamma}}-\frac{s_{\overline{q_1q_2}}}{s_{\gamma\overline{q_1}}s_{\gamma\overline{q_2}}}\right]$$

$$|\mathcal{T}_{\text{s channel}}\mathcal{T}^{\dagger}_{\text{t channel}}| + |\mathcal{T}_{\text{t channel}}\mathcal{T}^{\dagger}_{\text{s channel}}| = \left(\frac{(s^2_{q_1q_2}+s^2_{\overline{q_1q_2}})(s_{q_1\overline{q_1}}s_{q_2\overline{q_2}}+s_{q_1\overline{q_2}}s_{q_2\overline{q_1}}-s_{q_1q_2}s_{\overline{q_1q_2}})}{s_{q_1\overline{q_1}}s_{q_2\overline{q_2}}s_{q_1\overline{q_2}}s_{q_2\overline{q_1}}}\right)\times \left[\frac{s_{q_1\overline{q_1}}}{s_{q_1\gamma}s_{\gamma\overline{q_1}}}+\frac{s_{q_2\overline{q_2}}}{s_{q_2\gamma}s_{\gamma\overline{q_2}}}+\frac{s_{q_1\overline{q_2}}}{s_{q_1\gamma}s_{\gamma\overline{q_2}}}+\frac{s_{q_2\overline{q_1}}}{s_{q_2\gamma}s_{\gamma\overline{q_1}}}-\frac{s_{q_1q_2}}{s_{q_1\gamma}s_{q_2\gamma}}-\frac{s_{\overline{q_1q_2}}}{s_{\gamma\overline{q_1}}s_{\gamma\overline{q_2}}}\right] \tag{6.5.54}$$

which we note is another sub-leading colour contribution. The diagrams contributing to the 4 quark subprocess are given in Figure 6.5

### 6.5.3 Extra unresolved parton contribution to 1 jet final states

Having calculated the LO terms for the process $p\overline{p} \to \gamma+2$ jets we can easily find the $\mathcal{O}(\alpha\alpha_s^2)$ corrections to the process $p\overline{p} \to \gamma + 1$ jet due to an extra unresolved parton added to the tree level process $p\overline{p} \to \gamma + 1$ jet by using the singular limits of the two jet result. These are given in terms of $1/\varepsilon$ and $1/\varepsilon^2$ poles multiplied by the LO result for 1 jet final state. Therefore for the extra unresolved partons we have

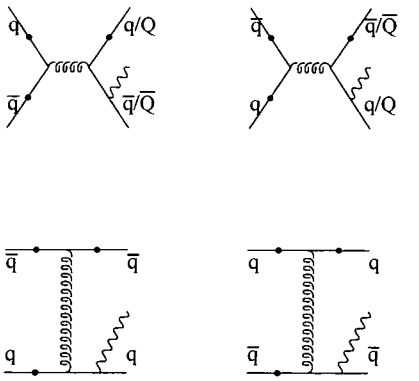


Figure 6.5: The tree level diagrams contributing to the process $p\overline{p} \to \gamma + 2$ jets through symmetries of the subprocesses $q\overline{q} \to q\overline{q}\gamma$ and $q\overline{q} \to Q\overline{Q}\gamma$ . Diagrams are labelled such that the parton from the proton is in the top left hand corner of the diagram and the parton from the antiproton is in the bottom left hand corner of the diagram. Although many of the diagrams may appear the same, due to the different parton distribution functions of the proton and the antiproton we must calculate each individually i.e. no symmetry factor can be used to relate the cross section of the subprocess $q\overline{q} \to Q\overline{Q}\gamma$ to the cross section of $\overline{q}q \to \overline{Q}Q\gamma$ as the quark distribution is different in the proton compared to the antiproton. The dots on the quark lines indicate alternative locations for the photon which have been taken into account, but which do not affect the colour structure of the matrix elements.

$$\begin{aligned}
\mathcal{R} \;=\; & \left[\left(\frac{\alpha_s N}{2\pi}\right)\left[\frac{1}{\varepsilon^2}\left(\frac{4\pi\mu_R^2}{|s_{qg}|}\right)^{\varepsilon} + \frac{1}{\varepsilon^2}\left(\frac{4\pi\mu_R^2}{|s_{g\overline{q}}|}\right)^{\varepsilon} - \log^2\left(\frac{|s_{qg}|}{s_{\min}}\right) - \log^2\left(\frac{|s_{g\overline{q}}|}{s_{\min}}\right)\right.\right. \\
& + \frac{3}{2\varepsilon}\left(\frac{4\pi\mu_R^2}{s_{\min}}\right)^{\varepsilon} + \frac{63+67-10n_f}{18} - \pi^2\left(\frac{2}{3} - \frac{\Theta(s_{qg})}{2} - \frac{\Theta(s_{g\overline{q}})}{2}\right) \\
& - \left.\left.\frac{1}{N^2}\left(\frac{1}{\varepsilon^2}\left(\frac{4\pi\mu_R^2}{|s_{q\overline{q}}|}\right) - \log^2\left(\frac{|s_{q\overline{q}}|}{s_{\min}}\right) + \frac{3}{2\varepsilon}\left(\frac{4\pi\mu_R^2}{s_{\min}}\right)^{\varepsilon} + \frac{63}{18} - \pi^2\left(\frac{1}{3} - \frac{\Theta(s_{q\overline{q}})}{2}\right)\right)\right] \right. \\
& + \left.\frac{\alpha_s b_0}{\varepsilon}\left(\frac{4\pi\mu_R^2}{s_{\min}}\right)^{\varepsilon}\right] |\mathcal{M}^{\mathrm{LO}}_{ab\to\gamma+1\,\mathrm{jet}}|^2
\end{aligned} \tag{6.5.55}$$

As usual, by renormalising $\alpha_s$ we eliminate the UV pole from the last term.

### 6.5.4 Virtual corrections

As we have seen before and according to the KLN theorem the singular terms present in the virtual contribution cancel the singularities from the extra unresolved parton contribution. The relevant diagrams for the virtual corrections can be seen in Figures 6.6 and 6.7. Here

we present the poles and finite terms as calculated.

$$\begin{aligned}\mathcal{V} &= \left[\left(\frac{\alpha_s N}{2\pi}\right)\left(-\frac{1}{\varepsilon^2}\left(\frac{|s_{qg}|}{s_{\min}}\right)^{\varepsilon}-\frac{1}{\varepsilon^2}\left(\frac{|s_{g\bar{q}}|}{s_{\min}}\right)^{\varepsilon}-\frac{3}{4\varepsilon}\left(\frac{|s_{qg}|}{4\pi\mu_R^2}\right)^{\varepsilon}-\frac{3}{4\varepsilon}\left(\frac{|s_{g\bar{q}}|}{4\pi\mu_R^2}\right)^{\varepsilon}-\frac{7}{2}\right)\right. \\ &+ \left.\frac{1}{N^2}\left(\frac{1}{\varepsilon^2}\left(\frac{|s_{q\bar{q}}|}{s_{\min}}\right)^{\varepsilon}+\frac{3}{2\varepsilon}\left(\frac{|s_{q\bar{q}}|}{4\pi\mu_R^2}\right)^{\varepsilon}+\frac{7}{2}\right)\right]|M^{\mathrm{LO}}_{ab\to\gamma+1\,\mathrm{jet}}|^2 \\ &+ \mathcal{F}(Q;g;\overline{Q}) \end{aligned} \tag{6.5.56}$$

where

$$\begin{aligned}\mathcal{F}(Q;g;\overline{Q}) &= 2\pi\alpha_s 4\pi\alpha(N^2-1)\left(\frac{\alpha_s N}{2\pi}\right)\left[3\left(\frac{s_{g\bar{q}}}{s_{qg}}-\frac{s_{qg}}{s_{g\bar{q}}}\right)\log\left(\frac{|s_{qg}|}{|s_{g\bar{q}}|}\right)+2\left(\frac{s_{g\bar{q}}}{s_{qg}}+\frac{s_{qg}}{s_{g\bar{q}}}\right)\log^2\left(\frac{|s_{qg}|}{|s_{g\bar{q}}|}\right)\right. \\ &+ \pi^2(1-\Theta(s_{qg})-\Theta(s_{g\bar{q}}))+\frac{1}{N^2}\left(\left(-4\frac{s_{g\bar{q}}}{s_{qg}}-2\frac{s_{qg}}{s_{g\bar{q}}}-4\right)\log^2\left(\frac{|s_{g\bar{q}}|}{|s_{q\bar{q}}|}\right)\right. \\ &+ \pi^2(1-\Theta(s_{g\bar{q}})-\Theta(s_{q\bar{q}}))+\left(-4\frac{s_{qg}}{s_{g\bar{q}}}-2\frac{s_{g\bar{q}}}{s_{qg}}-4\right)\log^2\left(\frac{|s_{qg}|}{|s_{q\bar{q}}|}\right) \\ &+ \pi^2(1-\Theta(s_{qg})-\Theta(s_{q\bar{q}}))+\left(\frac{6s_{g\bar{q}}}{s_{qg}}-4\right)\log\left(\frac{|s_{qg}|}{|s_{q\bar{q}}|}\right) \\ &+ \left.\left.\left(\frac{6s_{qg}}{s_{g\bar{q}}}-4\right)\log\left(\frac{|s_{g\bar{q}}|}{|s_{q\bar{q}}|}\right)\right)\right] \end{aligned} \tag{6.5.57}$$

In both the virtual and extra parton terms we have had to analytically continue $\log^2(x)$ such that invariant masses calculated between initial and final state partons will produce sensible results. Therefore we introduce $\Theta$ terms into the calculation. Combining the extra unresolved parton and virtual results and cancelling the IR poles we find

$$d\sigma^{\mathrm{NLO}}_{\gamma+1\,\mathrm{jet}} = \int dx_1 dx_2 \sum_{ab}\frac{1}{2\hat{s}} f_a(x_1) f_b(x_2) |\mathcal{M}^{NLO}_{ab\to\gamma+1\,\mathrm{jet}}|^2 dPS_{2\to 2} \tag{6.5.58}$$

where

$$\begin{aligned}|\mathcal{M}^{NLO}_{ab\to\gamma+1\,\mathrm{jet}}|^2 &= \mathcal{R}+\mathcal{V} \\ &= \left[\left(\mathcal{K}(Q;g;\overline{Q})-\frac{1}{N^2}\mathcal{K}(Q;\overline{Q})\right)|\mathcal{M}^{LO}_{\gamma+1\,\mathrm{jet}}|^2+\mathcal{F}(Q;g;\overline{Q})\right] \end{aligned} \tag{6.5.59}$$

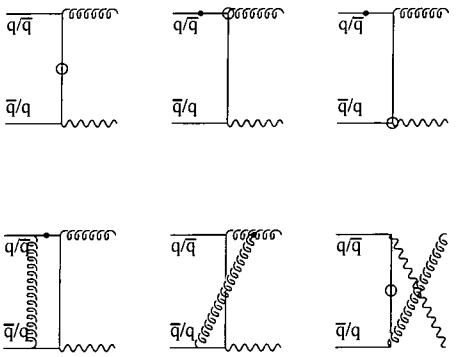


Figure 6.6: The virtual corrections to the subprocess $q\bar{q} \to g\gamma$ and $\bar{q}q \to g\gamma$. The circle indicates either a quark self energy i.e. a gluon emitted and reabsorbed or a vertex correction. The solid dots indicate alternative positions for the photon which have been taken into account in the calculation. As usual the proton's parton is in the top left hand corner of the diagram and the antiproton's parton is in the bottom left hand corner.

and where

$$\begin{aligned}
\mathcal{K}(Q;g;\overline{Q}) &= \left(\frac{\alpha_s(\mu_R^2)N}{2\pi}\right)\left[-\log^2\left(\frac{|s_{qg}|}{s_{\min}}\right)-\log^2\left(\frac{|s_{g\bar{q}}|}{s_{\min}}\right)+\frac{3}{4}\log\left(\frac{|s_{qg}|}{s_{\min}}\right)+\frac{3}{4}\log\left(\frac{|s_{g\bar{q}}|}{s_{\min}}\right)\right. \\
&+ \left.\frac{\pi^2}{2}\left(\Theta(s_{qg})+\Theta(s_{g\bar{q}})-\frac{4}{3}\right)+\frac{67}{18}-\frac{5n_F}{9N}\right]+\alpha_s(\mu^2)b_0\log\left(\frac{\mu^2}{s_{\min}}\right) \\
\mathcal{K}(Q;\overline{Q}) &= \left(\frac{\alpha_s(\mu_R^2)N}{2\pi}\right)\left[-\log^2\left(\frac{|s_{q\bar{q}}|}{s_{\min}}\right)+\frac{3}{2}\log\left(\frac{|s_{q\bar{q}}|}{s_{\min}}\right)+\frac{\pi^2}{2}\left(\Theta(s_{q\bar{q}})-\frac{2}{3}\right)\right]
\end{aligned} \tag{6.5.60}$$

Not shown here is the factorisation of the 3 body phase space into the 2 body phase space multiplied by regulating $x^\varepsilon$ terms. The reader is referred back to Chapter 2 for the details of this factorisation.

### 6.5.5 Crossing terms and fragmentation contributions

First we consider the crossing terms derived in Section 6.4. As stated before these simply replace the respective parton density functions and multiply the LO $\gamma+1$ jet matrix elements. Therefore we write

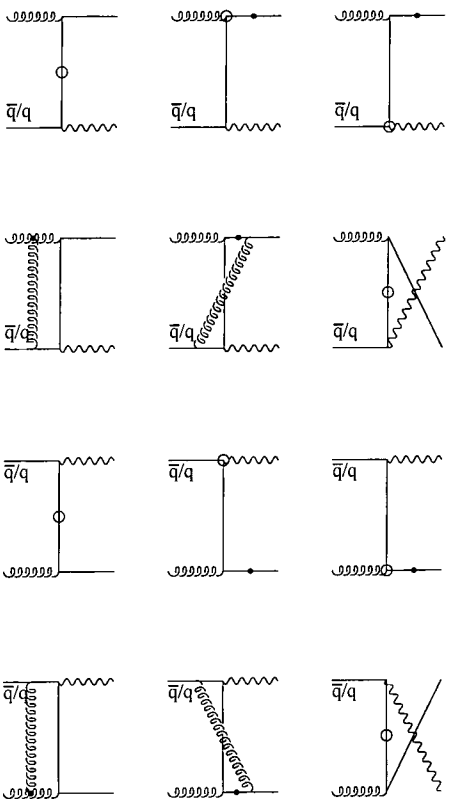


Figure 6.7: The virtual corrections to the subprocesses $qg \to q\gamma$, $gq \to q\gamma$, $\overline{q}g \to \overline{q}\gamma$ and $g\overline{q} \to \overline{q}\gamma$. The circle indicates either a quark self energy i.e. a gluon emitted and reabsorbed or a vertex correction. The solid dots indicate alternative positions for the photon which have been taken into account in the calculation. As usual the proton's parton is in the top left hand corner of the diagram and the antiproton's parton is in the bottom left hand corner.

$$d\sigma^{\text{cross}}_{\gamma+1\,\text{jet}} = \int dx_1 dx_2 \sum_{ab} \frac{1}{2\hat{s}} (C_a(x_1,\mu_F^2) f_b(x_2) + f_a(x_1) C_b(x_2,\mu_F^2)) |\mathcal{M}^{\text{LO}}_{ab\to\gamma+1\,\text{jet}}|^2 dPS_{2\to 2} \tag{6.5.61}$$

where the $C_a(x_1)$ functions are defined in Equation 6.4.45.

The final contribution we consider is due to the fragmentation of a final state parton into a photon. The matrix elements that are convoluted with the fragmentation function are those tree level diagrams of order $\mathcal{O}(\alpha\alpha_s^2)$ with quarks and/or antiquarks in the final state. See Figure 6.8 for the relevant LO diagrams. Therefore we need to consider all the symmetries of the diagrams $q\overline{q} \to gg$, $q\overline{q} \to Q\overline{Q}$ and $q\overline{q} \to q\overline{q}$ that have at least a single quark/antiquark in the final state. This gives the differential cross section as

$$\begin{aligned} d\sigma^{\text{frag}}_{\gamma+1\,\text{jet}} &= \int dx_1 dx_2 \sum_{ab} \frac{1}{2\hat{s}} f_a(x_1) f_b(x_2) (|\mathcal{M}^{\text{LO}}_{q\overline{q}\to gg}|^2 \\ &+ |\mathcal{M}^{\text{LO}}_{q\overline{q}\to q\overline{q}}|^2 \\ &+ |\mathcal{M}^{\text{LO}}_{q\overline{q}\to Q\overline{Q}}|^2) D_{q\to\gamma}(z,\mu^2_{\text{frag}}) dPS_{2\to 2} dz \end{aligned} \tag{6.5.62}$$

The squared matrix elements for these processes are well known and are reproduced in Equation 6.5.63.

$$\begin{aligned} |\mathcal{M}^{\text{LO}}_{q\overline{q}\to gg}|^2 &= 4\pi^2\alpha_s^2 N(N^2-1)8 \left( \frac{s_{qg_1} s_{qg_2}}{s_{g_1g_2}} + \frac{s^3_{qg_2}}{s_{qg_1} s_{g_1g_2}} + \frac{s_{qg_2} s_{qg_1}}{s_{g_1g_2}} + \frac{s^3_{qg_1}}{s_{qg_2} s_{g_1g_2}} \right. \\ &- \left. \frac{1}{N^2} \left( \frac{s_{qg_1}}{s_{qg_2}} + \frac{s_{qg_2}}{s_{qg_1}} \right) \right) \\ |\mathcal{M}^{\text{LO}}_{q_1\overline{q_1}\to q_2\overline{q_2}}|^2 &= 4\pi^2\alpha_s^2 (N^2-1)8 \left( \frac{s^2_{q_1q_2} + s^2_{q_1\overline{q_2}}}{s^2_{q_1\overline{q_1}}} + \frac{s^2_{q_1q_2} + s^2_{q_1\overline{q_1}}}{s^2_{q_1\overline{q_2}}} - \frac{2}{N} \frac{s^2_{q_1q_2}}{s_{q_1\overline{q_1}} s_{q_1\overline{q_2}}} \right) \\ |\mathcal{M}^{\text{LO}}_{q\overline{q}\to Q\overline{Q}}|^2 &= 4\pi^2\alpha_s^2 (N^2-1)8 \left( \frac{s^2_{qQ} + s^2_{q\overline{Q}}}{s^2_{q\overline{q}}} \right) \end{aligned} \tag{6.5.63}$$

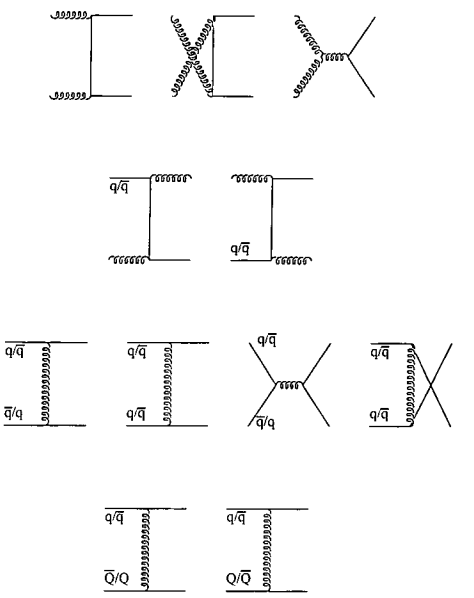


Figure 6.8: The tree level diagrams that are convoluted with the fragmentation function, $D_{q\to\gamma}(z,\mu_F^2)$ to produce the fragmentation contribution to the process $p\overline{p} \to \gamma + 1\,\text{jet}$. The only requirement is that one of the final state partons must be a quark or an antiquark. (At this order we neglect the contribution $D_{g\to\gamma}(z,\mu_F^2)$).

### 6.5.6 Final result

Bring all the separate contributions together we have

$$\begin{aligned} d\sigma_{p\overline{p}\to\gamma+X} &= d\sigma^{\text{LO}}_{\gamma+1\,\text{jet}} + d\sigma^{\text{NLO}}_{\gamma+1\,\text{jet}} + d\sigma^{\text{cross}}_{\gamma+1\,\text{jet}} \\ &+ d\sigma^{\text{LO}}_{\gamma+2\,\text{jet}} \\ &+ d\sigma^{\text{frag}}_{\gamma+1\,\text{jet}} \end{aligned} \tag{6.5.64}$$

We split up the equation in this manner to identify various groups. The top group can all be calculated using the 2 to 2 body differential phase space factor and therefore we only need to call this momentum generator once. The next term down is the only term that requires the 2 to 3 body differential phase space factor and therefore is set up on its own. Finally, the bottom term requires not only integration over 2 to 2 body scattering, but also contains an additional integral over the fraction, $z$ of the photon's momentum compared

to the photon cluster's momentum. All these calculations include integrals over the initial partons' momentum fractions $x_1$ and $x_2$. This is the basic structure of DPRAD. We have not included quark flavour summation here, but this is fully incorporated into the Monte Carlo. In the next chapter we analysis some of the results produced using both the fixed order and the BFG resummed fragmentation functions, comparing with data gathered at the Tevatron and studying some of the effects of cone algorithms and renormalisation/fragmentation scale dependence on the $z/p_T$ distributions.

### 6.5.7 $s_{\min}$ independence

Having collated all the separate pieces we outline the independence of the final calculation on the theoretical phase space division parameter, $s_{\min}$. This is the parameter we have used to define collinear and soft partons such that if $s_{ij} < s_{\min}$ and $s_{jk} < s_{\min}$ then parton $j$ is soft whereas if $s_{ij} < s_{\min}$ and $s_{jk} > s_{\min}$ then partons $i$ and $j$ are said to be collinear. When we calculate the sliced contribution to the process this introduces terms of the form $\log^2(s_{\min})$ and $\log(s_{\min})$. However, these are cancelled by the numerically calculated region of phase space where all the partons are resolved. In Figure 6.9 we demonstrate the $s_{\min}$ independence of DPRAD, an essential indication of whether the routine correctly calculates the cross section.

## 6.6 Summary

In this chapter we have introduced two theoretical tools necessary for the calculation of prompt photon production from hadron-hadron collisions. This is an important process to study as it facilitates our understanding of both the gluon distribution in the proton at moderate values of $x$ and the process of fragmenatation, a universal non-perturbative effect.

Firstly, we considered different techniques used in measuring and calculating prompt photons. Ideally, we would wish to eliminate the non-perturbative part of the calculation and this naively could be done by using isolated photons which are also relatively easy to measure. However, a perfectly isolated photon is an infra red unsafe object and therefore we must allow some degree of non-perturbation into the calculation to ensure a sensible answer.

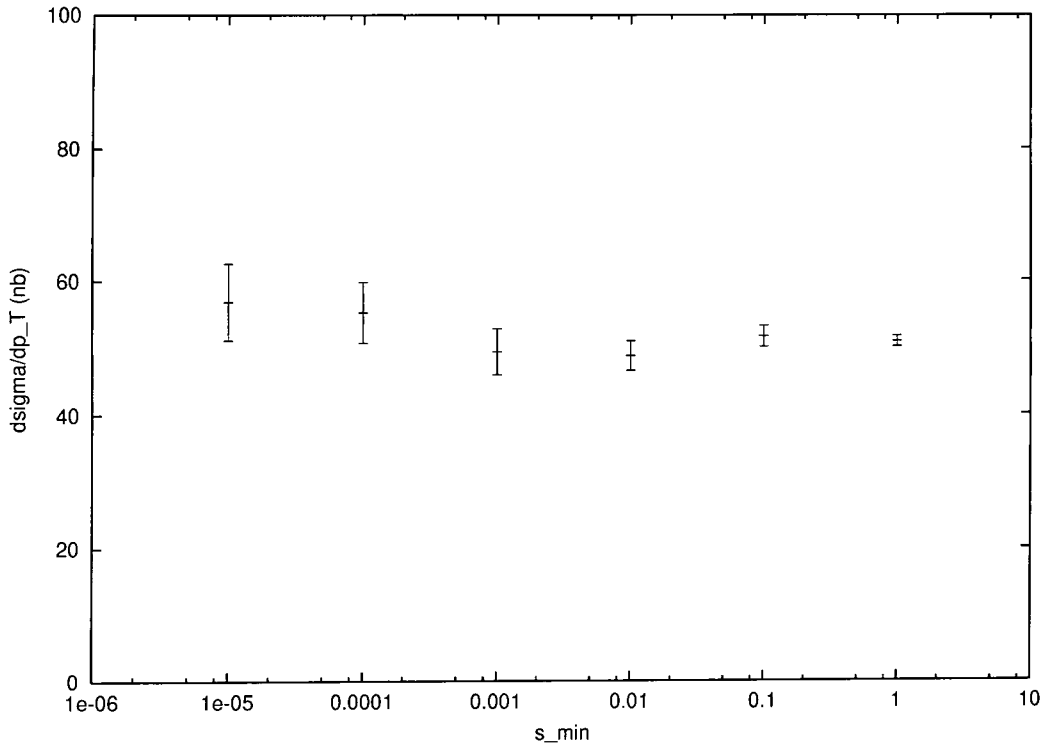


Figure 6.9: Plot demonstrating the independence of the calculated cross section on the theoretical parameter $s_{\min}$. The approximations made by the slicing routine are better at smaller values of $s_{\min}$, but as we can see, numerical instabilty is a problem in this region. Therefore we choose a value of $s_{\min} = 0.1$ for the rest of the calculation.

Alternatively we could embrace the entire calculation and attempt to measure the non-perturbative terms in other enviroments such as $e^+e^- \to \gamma + 1$ jet which we could use in our hadron-hadron collision due to its universal nature. We outlined this calculation, showing how potential infra red poles can be absorbed into the fragmentation function which in turn leads to an evolution equation for the fragmentation function. Another limitation placed on the fragmentation function is that it must be well-behaved in the limit $z \to 1$ where $z$ is the fraction of the parent parton's momenta which the photon carries away. We suggested a form for the $\mathcal{O}(\alpha)$ fragmentation function and also consider another form proportional to $\mathcal{O}(\alpha/\alpha_s)$ for which we outline a resummation technique to include all logarithms of the form $\alpha_s^n \log^{n+1}(\mu_{\rm frag})$ and $\alpha_s^n \log^n(\mu_{\rm frag})$. The technique we make use of for calculation is that of Bourhis, Fontannaz and Guillet (BFG).

Another contribution which needed to be addressed was that of initial state radiation which is not a concern for electron-positron calculations. Here, an initial state parton becomes indistinguishable from two collinear partons where parton $b$ splits into partons $u$ and $h$ and $s_{ub} \to 0$ leaving $h$ to take part in the hard scattering. These divergent contributions are absorbed into the structure function and the renormalisation leads to a crossing function which can be convoluted with hard processes to account for the finite terms remaining from these collinear states.

Finally we collated all the contributions to the process $p\bar{p} \to \gamma +$ jets at $\mathcal{O}(\alpha\alpha_s^2)$ and detailed their inclusion in the Monte Carlo, `DPRAD`. We present the results in the next chapter.

# Chapter 7

# Results and comparisons with prompt photon data

## 7.1 Introduction

In this chapter we study the photon transverse momentum distribution obtained using the parton level Monte Carlo DPRAD described in the preceding chapter. In particular, we investigate the effects of varying parameters inherent in the calculation of $p\overline{p} \to \gamma + X$ at $\mathcal{O}(\alpha\alpha_s^2)$. In Section 7.2 we present the results and analysis of varying certain theoretical parameters (such as the renormalisation scale) and of comparing the two different fragmentation functions outlined in the previous chapter; the fixed order, fragmentation function measured by ALEPH and the BFG resummed fragmentation function. We also make comparisons with experimental data gathered by the CDF and D0 collaborations [82, 83]. In Section 7.4 we briefly outline another technique used by other groups for this calculation, namely the $k_T$ broadening due to initial state soft gluon emission. Finally we summarise these findings in Section 7.5.

### 7.1.1 Initial parton contributions

In this section we briefly show how each of the leading order subprocesses contributes to the leading order calculation. As we have seen there are only two subprocesses, $q\overline{q} \to \gamma g$ and $qg \to q\gamma$ (with respective charge conjugation and swapped initial parton symmetries). In Figure 7.1 we show the percentage of each of the two contributions at different $p_T^\gamma$ values.

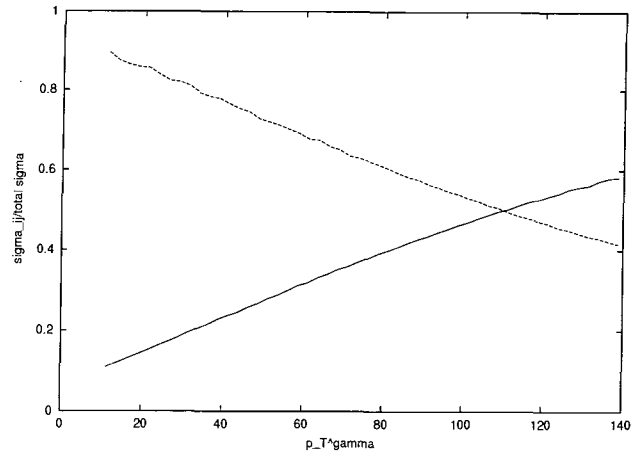


Figure 7.1: Ratio plot of the two subprocesess' contributions against the total leading order calculation. The solid line shows the percentage of the leading order result due to the subprocess $q\bar{q} \to g\gamma$ and its symmetries whereas the dashed line shows the contribution due to the subprocess $qg \to q\gamma$ and symmetries.

The solid line shows the $q\bar{q} \to \gamma g$ contribution and the dashed line shows the $qg \to q\gamma$ one. As we can see, at low values of the transverse photon momentum the quark-gluon initial state dominates over the quark-antiquark contribution. However, by 100 GeV, the two effects are roughly equal with the quark-gluon contribution falling off at higher $p_T^\gamma$ values, leaving the $q\bar{q} \to \gamma g$ contribution to dominate. Therefore, we see that to study the gluon distribution in the proton, we must concentrate on small values of the transverse photon momentum.

## 7.2 Uncertainty in the theoretical prediction

In this section we shall study the variations of the photon transverse momentum distribution with theoretical parameters such as the renormalisation and factorisation scales ($\mu_R, \mu_F$) and parton distribution functions (MRST98 upper, central and lower gluon) which are intrinsic to any observable in hadron-hadron collisions. We also study features specific to photon production such as isolation criteria (cone size, hadronic energy cut-off), as well as analysing the differences between the different fragmentation functions we have introduced (fixed order ALEPH and BFG resummation) and the inherent fragmentation scale ($\mu_{\text{frag}}$) dependence. We shall also look at distributions in $z$, the fraction of momentum carried by the photon in the photon cluster where it will become apparent that there is a problem. Finally we shall

compare the theoretical results of DPRAD with experimental measurements gathered by the CDF and D0 collaborations. These extend over the range 10-120 GeV for the transverse momentum of the photon and the rapidity ranges $|\eta_\gamma| < 0.9$ for CDF and both $|\eta_\gamma| < 0.9$ and $1.6 < |\eta_\gamma| < 2.5$ for D0.

### 7.2.1 Differences between the fragmentation functions

We begin by studying the differences between the two fragmentation functions we considered earlier. The fixed order ALEPH fragmentation function (FO) differs from the BFG resummed case in that it is totally $\mu_{\rm frag}$ independent at each order whereas we have some uncertainty due to scale choice in the fragmentation function of BFG. For this thesis we have taken two extreme cases, one that represents the hard scale in the process, $\mu_{\rm frag} = p_T^\gamma$, and one that reflects the fact that the fragmentation process is essentially a long distance process, $\mu_{\rm frag} = k_T$ where $k_T$ is the transverse momentum of the hadrons with respect to the photon direction. In practice this latter scale is $k_T = E_{\rm had}\sin(\delta)$ and where $\delta \approx R$, the cone size and $E_{\rm had}$ is the hadronic energy cut used in the definition of isolation. For the comparisons with experimental data presented here, $E_{\rm had}$ will be set at 2 GeV. Therefore the $\mu_{\rm frag} = k_T$ scale is fixed as opposed to the $\mu_{\rm frag} = p_T^\gamma$ scale (or physical scale) which varies with photon momentum. These two choices encompass the reasonable range of fragmentation scales (up to simple factors).

As a baseline choice, we choose the physical scale, $\mu_R = \mu_F = \mu_{\rm frag} = p_T^\gamma$ together with the ALEPH fragmentation function (FO) unless stipulated otherwise. Similarly, we select the MRST2 parton distributions which have been obtained using fits to the data assuming no intrinsic smearing due to transverse motion of the partons in the proton.

In Figure 7.2 we see the ratio plot of the differential cross sections, $d\sigma/dp_T^\gamma$ for the two extreme BFG scale choices compared against the baseline FO result. The lower scale (short dashed line) gives higher values of the cross section compared to FO, with values at high $p_T^\gamma$ being comparable with FO, but then rising to approximately 10% larger at low $p_T^\gamma$ values indicating the increasing importance of the fragmentation contribution at low $p_T^\gamma$. The higher, physical scale, choice (long dashed line) has smaller values of the cross sections compared to FO at large $p_T^\gamma$, but after dropping to a minimum at $p_T^\gamma \approx 30$ GeV the BGF

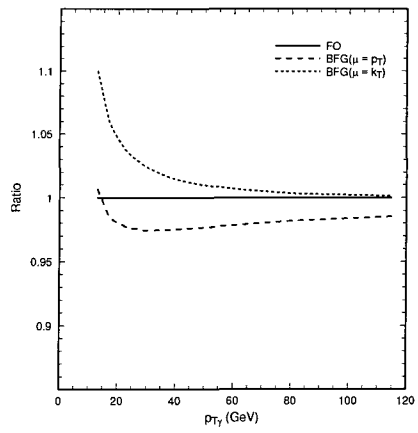


Figure 7.2: Ratio of the fixed order ALEPH fragmentation function calculation to the resummed BFG fragmentation function calculation. The two lines represent the two different scales BFG($\mu_{\rm frag} = p_T^\gamma$) and BFG($\mu_{\rm frag} = k_T$).

($\mu_{\rm frag} = p_T^\gamma$) result rises sharply so that for the lowest $p_T^\gamma$ bin it is approximately equal to the FO result.

We can understand these trends if we consider the $z$ distributions of the different non-perturbative fragmentation functions. To gauge the fragmentation function effect, we consider the combination of perturbative and non-perturbative parts,

$$\mathcal{D}_q(z,\mu^2_{\rm frag}) = D_q(z,\mu^2_{\rm frag}) + \frac{\alpha\, e_q^2}{2\pi}\log\left(\frac{s_{\rm min} z(1-z)}{\mu^2_{\rm frag}}\right)\frac{1+(1-z)^2}{z} \qquad (7.2.1)$$

for a given choice of $s_{\rm min}$ which we take to be 0.1 GeV$^2$. Changing $s_{\rm min}$ gives a weak dependence on $z$ due to the splitting function and affects all fragmentation functions equally. To be specific, we select the up quark fragmentation function and in Fig. 7.3 we show three lines representing the three approaches. The FO curve (solid line) rises as $z \to 1$ due to a factor $-\log((1-z)^2)$ in the non-perturbative part of the fragmentation function. This divergence is partially cancelled by the perturbative part of the fragmentation function and in the full calculation by the integration over the isolated photon region which both yield a factor $\log(1-z)$. In both of the BFG curves the fragmentation function dies away as $z \to 1$ due to the perturbative $\log(1-z)$ term. Note that to mimic the isolation criteria, which relates the minimum allowed $z$ value to the $p_T^\gamma$ via,

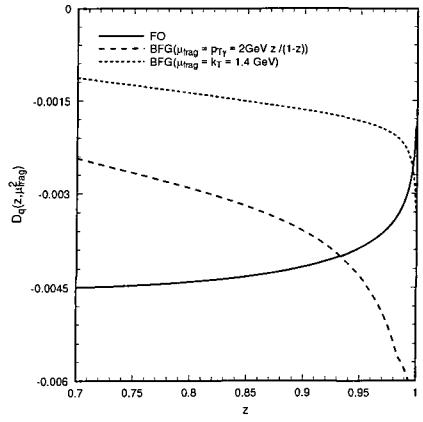


Figure 7.3: $z$ distributions of the three fragmentation functions considered, the fixed order (FO) ALEPH calculation (solid line), the BFG resummed function with $\mu_{\rm frag} = p_T^\gamma = 2z/(1-z)$ (dashed line) and the BFG resummed function with $\mu_{\rm frag} = k_T$ (dotted line). Note the difference in shape of the FO and BFG functions. This accounts for the rise at low $p_T^\gamma$ in Figure 7.2 in the BFG prediction as compared to FO.

$$z > \frac{p_T^\gamma}{E_{\rm had} + p_T^\gamma} \tag{7.2.2}$$

we have selected $\mu_{\rm frag} = p_T^\gamma = E_{\rm had} z/(1-z)$ for the hard scale BFG curve (dashed line). We now consider the $p_T^\gamma = 115 - 120$ GeV bin. If we have an allowed hadronic cone energy cut of $E_{\rm had} = 2$ GeV this corresponds to a $z_{\rm cut}$ value of 0.983 (115/117). This is the lowest value of $z$ that an event must exhibit to be retained and we numerically integrate up from $z_{\rm cut}$ to calculate the cross section (for that particular photon momentum). For the hard scale BFG result, the fragmentation contribution is clearly more negative than any of the other procedures, with the FO and soft scale BFG results being roughly equal, as seen in figure 7.2.

On the other hand, for the $p_T^\gamma = 10 - 15$ GeV bin, we integrate from values of $z_{\rm cut} = 0.833$ (10/12) upwards. Due to their shapes we see that the low scale BFG prescription integrated gives a smaller negative value than the FO approach which becomes increasingly more negative as $z_{\rm cut}$ decreases. The visible relative rise at small $p_T^\gamma$ is due to this effect. Similarly, the fragmentation contribution in the high scale BFG approach becomes closer to that for FO, giving the relative rise at small $p_T^\gamma$ seen in Figure 7.2.

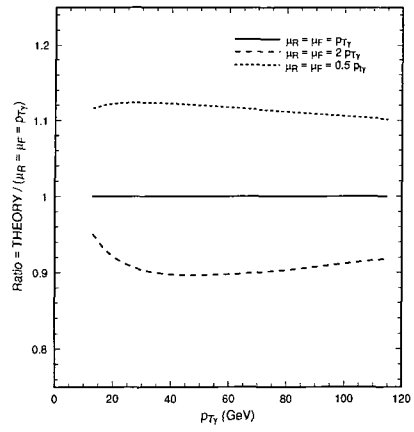


Figure 7.4: Ratio plot of the different predictions for $p\bar{p} \rightarrow \gamma+$ jets as a function of $p_T^\gamma$ obtained by varying the renormalisation scale and factorisation scales. This scale variation effects both FO and BFG results in the same way. We use the same value for both the factorisation scale and the fragmentation scale although this need not be the case. The dashed line demonstrates the effect of increasing the scale by a factor 2 while the dotted line corresponds to halving the scale.

### 7.2.2 Renormalisation and factorisation scale dependence

Two of the most important parameters that it is necessary to have some degree of control over in any perturbative calculation are the renormalisation scale $\mu_R$ and factorisation scale $\mu_F$. (See Section 1.4.) Figure 7.4 shows the effect obtained by varying $\mu_R = \mu_F$ by a factor of two around the physical scale $\mu_R = \mu_F = p_T^\gamma$. This gives some idea of the contribution of uncalculated higher order corrections.

We see that by varying the renormalisation (and factorisation) scale in DPRAD, for the lower scale choice there is an overall increase of about 10% in the cross section. The shape of the distribution has not been affected to any great degree. However, for $\mu_R = \mu_F = 2p_T^\gamma$, although we have an overall 10% decrease compared to the physical scale, we do see a slight relative increase of about 5% in the cross section at low $p_T^\gamma$ ($p_T^\gamma < 20$ GeV). This is precisely the region where data and theory disagree most strongly. However, an increase of 5% is not sufficient to explain the differences seen between theory and data and so we cannot attribute the data-theory disagreement to scale variation solely.

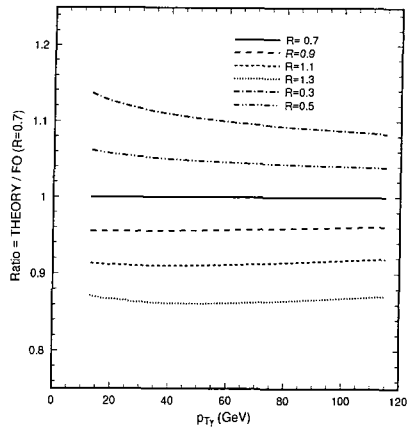


Figure 7.5: Ratio of the fixed order ALEPH fragmentation function calculation with cone size $R = 0.7$ to the same calculation with different values for $R$ as a function of $p_T^\gamma$. Again, this behaviour is similar for both of the fragmentation functions under consideration.

### 7.2.3 Dependence on the photon isolation criteria

Another important effect to examine is the dependence on the isolation criteria used i.e. on the parameters used to separate isolated photon events from fragmentation contributions and other events. In our predictions we have used a cone algorithm which places a cone around the photon of size $R = \sqrt{(\Delta\eta)^2 + (\Delta\phi)^2} = 0.7$. Any partons inside the cone are then checked against an allowed hadronic energy cut. If the amount of hadronic energy is greater than the cut then the photon is considered to be non-isolated and the event is removed from consideration. In comparisons with the experimental data, this cut is usually fixed at 2 GeV. On the other hand, in electron-positron collisions, the amount of hadronic energy must be less than a fixed percentage of the photon cluster energy. Clearly the contribution from very isolated photons - i.e. the lowest order contribution, is unaltered by changing the isolation requirements. However, by changing these cuts, together with the cone size, we can investigate the contribution from both real radiation and fragmentation.

By increasing the cone size we incorporate more hadronic energy into the cone and therefore the probability of the photon remaining isolated decreases. This is exactly what we see in Figure 7.5 where we have plotted the ratio of results using different sized cones against the standard $R = 0.7$ cone. Increasing the size of the cone from 0.7 decreases the differential cross section by a few per cent almost independently of $p_T^\gamma$. Similarly, smaller

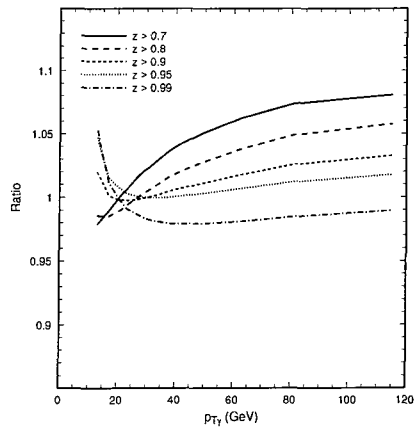


Figure 7.6: Ratio of the prediction using the fixed order ALEPH fragmentation function for different values of $z_{\rm cut}$ compared to the same calculation with $E_{\rm had} = 2$ GeV. Similar results are also obtained using the BFG fragmentation function.

cone sizes give a slight rise in the cross section.

In Figure 7.6 we show the variations induced by altering the hadronic energy cut off, $z_{\rm cut}$. As $z_{\rm cut}$ (or $1 - E_{\rm had}/E_{\rm cluster}$) increases, more events that previously made the cut are rejected. For example, when $z_{\rm cut} = 0.7$, a gluon with energy 2 GeV can exist in the cone with a photon of energy 10 GeV. However, if $z_{\rm cut}$ is increased to 0.9 this event fails the cut and is removed from consideration. Therefore as $z_{\rm cut} \to 1$, events that pass the cut become more and more isolated and the differential cross section should decrease accordingly. This is what we see for large values of $p_T^\gamma$ in Figure 7.6 where $z_{\rm cut} = 0.7$ is approximately 10% larger than $z_{\rm cut} = 0.99$ for the $p_T^\gamma = 115 - 120$ GeV bin. However, for small values of $p_T^\gamma$ e.g. $p_T^\gamma < 30$ GeV we see the reverse occuring i.e. the differential cross section increasing as $z_{\rm cut}$ increases. To study this effect we have calculated the $z$ distribution of the FO result for specific $p_T^\gamma$ bins. These can be seen in Figure 7.7.

In Figure 7.7 we show the distribution in $z$ for the fixed order calculation in the $p_T^\gamma$ bins 10-15 GeV, 15-20 GeV, 20-25 GeV and 25-30 GeV respectively with $z_{\rm cut} = 0.7$. At $z = 1$ the photon is completely isolated and here the differential cross section is largest. This corresponds to the parts of the calculation where quarks and gluons either become collinear with each other and distinct from the photon (i.e. not inside the cone) or that all the particles are distinct. Away from $z = 1$ we have the fragmentation contribution to the

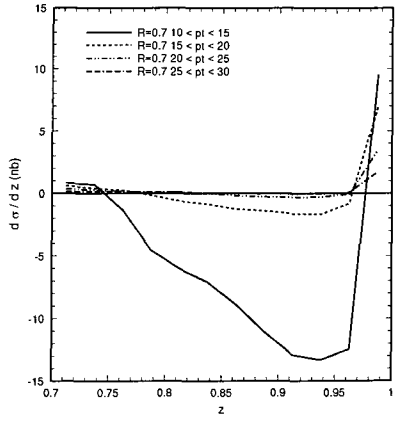


Figure 7.7: The differential cross section $d\sigma/dz$ as a function of the fraction $z = p_T^\gamma/p_{\text{cluster}}$ for the $p_T^\gamma$ bins 10-15 GeV, 15-20 GeV, 20-25 GeV and 25-30 GeV respectively.

calculation as well as the collinear quark-photon final states.

In this figure we immediately see the reason for the unexpected behaviour of Figure 7.6 where the cross section appears to increase as the isolation criteria is stiffened. The differential cross section is actually negative for certain values of $z$ and becomes increasingly more negative for smaller values of $p_T^\gamma$. Also, at small values of $p_T^\gamma$, the range over which the differential cross section is negative grows. This is reminiscent of a similar problem seen in [84] where, in the process $e^+e^- \to \gamma + 1$ jet a negative differential cross section was also observed.

Glover and Morgan, studying both the cone and the democratic algorithms, in electron-positron collisions considered the same differential cross section in $z$ and found a similar effect. Although in principle the cross section for photon + $X$ should be well behaved as a function of $z$, there is an effect to consider. There is a discontinuity across the boundary between the isolated region in which $z = 1$ and the region where the parton lies inside the photon's cone where $z \neq 1$ (the boundary between regions 1 and 2 of Figure 6.1). When hadronisation effects are taken into consideration (the process of extending the partonic picture to the hadronic one) sizeable shifts are seen in $z$. This will always be the case, however there is a dramatic effect when the matrix elements are large leading to big shifts in the cross section which makes parton level predictions of the accompanying hadronic energy particularly unreliable. ALEPH [85], using the democratic cone algorithm, saw this

effect in the shower Monte Carlo they used as a spilling over of parton level events from the 0.99-1 bin into the 0.95-0.99 bin at the hadron level. In other words, a previously isolated photon with $z$=1 may, during the hadronisation process, find that a soft gluon is now within the isolation cone such that $z$ is reduced to below 0.99. ALEPH therefore changed their definition of isolation and defined an isolated photon as one which has $z > z_{\rm iso} = 0.95$ (i.e. combined the bins) and compared this against the partonic picture with $z > z_{\rm iso}$. This makes sense because although hadronisation effects change the precise value of $z$, they tend not to move events from the isolated to non-isolated categories i.e. a isolated photon with $z = 1$ will not be moved further than 0.05 due to hadronisation and thus with the new definition of $z_{\rm iso}$ it will still remain isolated. This worked satisfactorily for the democratic algorithm where the cone size is effectively 90°. However, in cone algorithm the range of $z$ values for which the differential cross section is negative is larger and a smaller value of $z_{\rm iso}$ is required. In parton language, a smaller cone allows the quark-photon collinear singularity to be probed more closely. This is where the matrix elements are much larger and consequently the hadronisation effects are much more marked. This shows up as an enlargement of the region where the parton-level differential cross section is negative as the cone size decreases. In other words, with smaller cones the hadronisation effects are more pronounced due to the fact that we are trying to resolve the collinear region where perturbation theory breaks down. Thus the minimum allowed hadronic energy in the cone should rise to minimise the size of hadronisation effects that are not included in the theoretical calculation, but which are clearly present in the data.

We can also see the effect of increasing the cone size for the process $p\overline{p}+X$ in Figure 7.8. We see that as the cone size increases, the region of negative differential cross section becomes smaller. We are moving further away from the collinear region and hadronisation effects are becoming smaller. We note that for the CDF and D0 measurements, $R$ is taken to be 0.7. Although the largest cone seems to have the largest cross section (after integration) this is misleading as the $z = 1$ peak shrinks with increasing cone size as can be seen clearly in Figure 7.5.

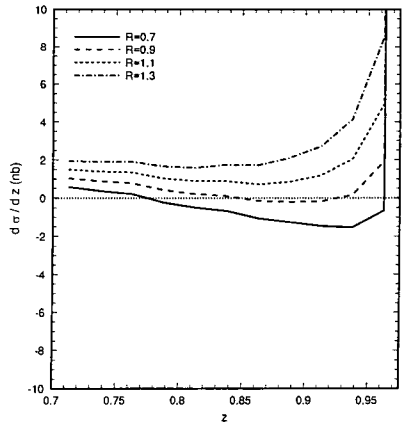


Figure 7.8: The differential cross section as a function of $z = p_\gamma / p_{\text{cluster}}$ for the $p_T^\gamma$ bin 15-20 GeV. The figure highlights the effects of different cone sizes on the fixed order ALEPH fragmentation function calculation.

### 7.2.4 Dependence on the parton density functions

We consider the variation of the results with different parton distribution function inputs. For brevity we only consider variations induced by the five different parton distributions developed by the MRST98 collaboration. Figure 7.9 shows a ratio plot of the different distributions with respect to the baseline MRST2 set as a function of $p_T^\gamma$. This distribution was choosen as a baseline because it contains no intrinsic $k_T$ smearing and therefore is closer to the perturbative approach we have adopted for this calculation. We see that all the results lie within a band of 14% at the small $p_T^\gamma$ end with the high $\alpha_s$ distribution giving the largest result and the low $\alpha_s$ distribution giving the lowest one. All the results decrease as we increase $p_T^\gamma$ so that at $p_{T\gamma} = 120$ GeV the band has thinned to about 10%. However, the low $\alpha_s$ distribution has the correct shape to account for some of the disagreement between theory and data.

### 7.2.5 Predictions using the resummed fragmentation function

In this section we compare the fixed order results with those using the BFG resummed fragmentation function. In the previous section we saw that the $z$ distribution of the smaller $p_T^\gamma$ bins for the FO result left us with a region where the differential cross section became

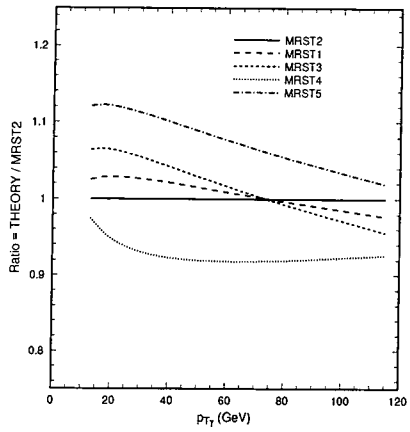


Figure 7.9: Ratio plot of the fixed order result with different parton distribution inputs. All ratios are compared against MRST2 which is the set of parton distribution functions with no intrinsic $k_T$ smearing. The lines are as follows MRST1 = central gluon ($\langle k_T \rangle = 0.4$ GeV,$\alpha_s = 0.1175$), MRST3 = lower gluon ($\langle k_T \rangle = 0.64$ GeV, $\alpha_s = 0.1175$), MRST4 = lower $\alpha_s$ ($\langle k_T \rangle = 0.4$ GeV,$\alpha_s = 0.1125$), MRST5 = higher $\alpha_s$ ($\langle k_T \rangle = 0.4$ GeV,$\alpha_s = 0.1225$).

negative. We consider those same distributions, but plot the results found using the BFG resummed fragmentation function. We consider the two extreme fragmentation scales, the physical scale where $\mu_{\text{frag}} = p_T^\gamma$ and a smaller scale set at $\mu_{\text{frag}} = k_T$ as defined in Section 7.2.1.

Figure 7.10 shows the $z$ distributions for different $p_T^\gamma$ bins for both fixed order and resummed fragmentation functions. We see that with the large fragmentation scale $\mu_{\text{frag}} = p_T^\gamma$, the resummed and fixed order predictions are qualitatively very similar; we have the same problem with the differential cross section becoming negative at large values of $z$. This problem is particularly apparent at small $p_T^\gamma$. Quantitatively, there are still slight differences and the high scale BFG predictions are slightly less negative than their FO counterparts and the range of $z$ for which it is negative is smaller. Neverthless, we again take this to be a warning sign that hadronisation effects are both sizeable and necessary to give a physical answer. However, when we consider the smaller scale $\mu_{\text{frag}} = k_T$, we find that the differential cross section is positive definite for all values of $z$ and for all the $p_T^\gamma$ bins. Based on this discussion, we suggest that the resummed fragmentation function with a small scale is the best theoretical model to directly compare with the experimental data.

We note in passing that the BFG resummed fragmentation function has the same be-

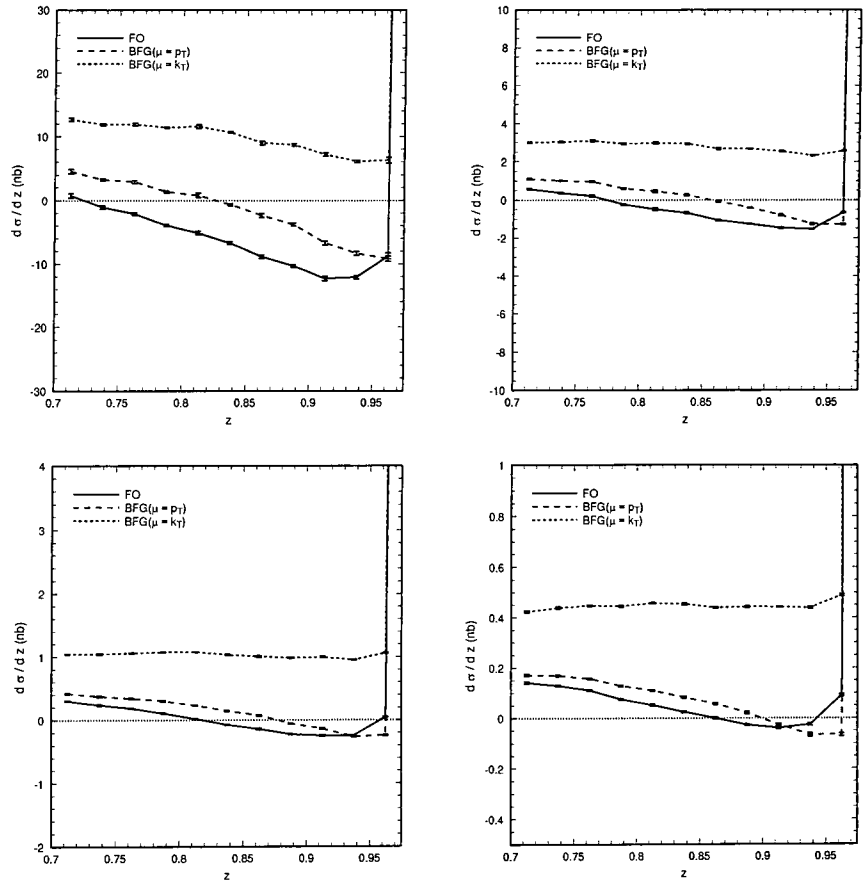


Figure 7.10: The differential cross section as a function of the fraction $z$ for different $p_T^\gamma$ bins, 10 GeV $< p_T^\gamma <$ 15 GeV, 15 GeV $< p_T^\gamma <$ 20 GeV, 20 GeV $< p_T^\gamma <$ 25 GeV, and 25 GeV $< p_T^\gamma <$ 30 GeV, respectively. The three lines shown are the fixed order ALEPH fragmentation function (solid), the BFG resummed fragmentation function with $\mu_{\rm frag} = p_T^\gamma$ (long-dashed) and the BFG resummed fragmentation function with $\mu_{\rm frag} = k_T$ (short-dashed).

haviour as the FO result with respect to the other perturbative parameters. For example, with increasing cone size the differential cross section grows for $z < 1$ and the $z = 1$ peak shrinks giving an overall decrease in differential cross section as $R$ increases.

## 7.3 Comparison with the data

The final figures of this result section (Figure 7.11) are the comparisons between the CDF and D0 data and theory. For the theory lines we have plotted the LO result, the BFG ($\mu_{\rm frag} = p_T^\gamma$)

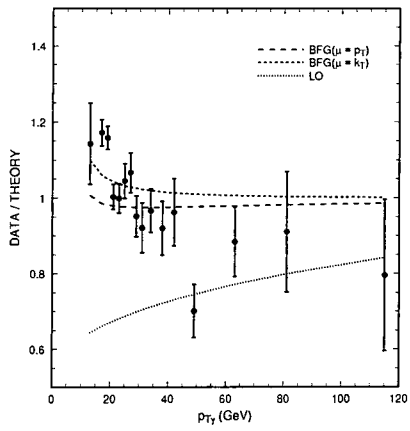


Figure 7.11: The ratio of experiment to the baseline NLO fixed order result for the CDF experiment with $|\eta_\gamma| < 0.9$. The dotted line shows the ratio of the lowest order prediction (LO) to NLO FO, while the large dashed (short dashed) lines show the ratio of the BFG $\mu_{\rm frag} = p_T^\gamma$ ($\mu_{\rm frag} = k_T$) predictions to the same baseline theory.

NLO result and the BFG ($\mu_{\rm frag} = k_T$) result using the isolation criteria appropriate to the CDF experiment ($R = 0.7$, $E_{\rm had} = 2$ GeV). Based on the previous discussion the best motivated theoretical prediction is the BFG ($\mu_{\rm frag} = k_T$) curve. However, we see that it is unable to produce a steep enough slope at low $p_T^\gamma$ to accurately describe the data. In the next section we outline one possible technique which has been used to improve the fit.

With the experience gained through examining the prompt photon transverse energy distribution for the CDF experiment, we now turn to the data gathered by D0. The D0 photon isolation cone is somewhat smaller $R = 0.4$ and the amount of hadronic energy is limited to be $E_{\rm had} < 2$ GeV.

## 7.4 Intrinsic $k_T$ broadening and initial state soft gluon resummation

It has been noted [86] that unexplained deviations between experimentally measured direct photon cross sections and NLO calculations exist. These discrepancies exist for essentially all direct photon data sets; fixed target, ISR, the S$p\bar{p}$S and the TEVATRON. This can be seen especially clearly in the E706 fixed target data [87]. One possible explanation for this

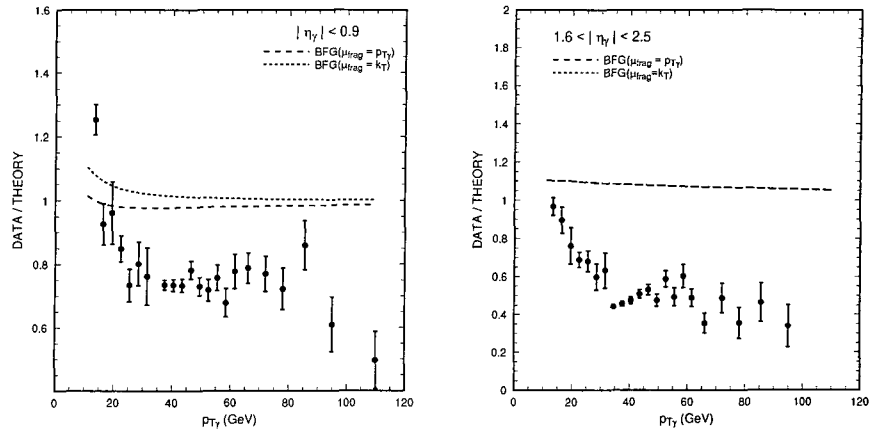


Figure 7.12: The ratio of experiment to the baseline NLO fixed order result for the D0 experiment with (a) $|\eta_\gamma| < 0.9$ and (b) $1.6 < |\eta_\gamma| < 2.5$. The large dashed (short dotted) lines show the ratio of the BFG $\mu_{\rm frag} = p_T^\gamma$ ($\mu_{\rm frag} = k_T$) predictions to the same baseline theory.

disagreement is initial state soft gluon radiation which gives a transverse boost to the hard scattering process itself. Of course, some degree of transverse momenta is expected due to the finite size of the proton which is labelled *intrinsic* $k_T$ broadening. However, we expect that this is a relatively small effect being of the order $\langle k_T \rangle = 0.3$ GeV per parton.

However, [88] claim that additional $k_T$ *smearing* has been observed in dimuon, diphoton and dijet pairs over a wide range of centre of mass energies. They claim that the average transverse momentum of the pair is firstly too large to be intrinsic (0.5-5 GeV) and secondly that it increases logarithmically with $\sqrt{s}$. They state that "similar soft gluon effects are expected to be present in all hard scattering processes, such as the inclusive production of jets or direct photons" [89]. In their paper they outline the necessary resummation calculation, noting that at collider energies most of the $k_T$ is attributed to the perturbative part of the resummation together with a non-perturbative input that specifies the contribution of gluon emission in the infrared. The non-perturbative function is then determined by convoluting with the LO perturbative prediction, integrating over $k_T$ fitting to the data. This procedure depends on the form of the non-perturbative function which is typically taken to be Gaussian. Using this method, Apanasevich *et al* found that a reasonable fit to the Tevatron data could be achieved with a Gaussian width $\langle k_T \rangle = 3.5$ GeV. The $k_T$ smearing generally moves events from low $p_T^\gamma$ where the cross section is largest out to larger $p_T^\gamma$. Because the cross section falls

off dramatically with increasing $p_T^\gamma$, even a slight smearing can have a noticeable effect. Of course, the effects die off with increasing $p_T^\gamma$ and generally they only affect the cross section in the region $p_T^\gamma < 40$ GeV.

Unfortunately, there is no value of $\langle k_T \rangle$ that can simultaneously explain all of the available data. In particular, the recent E706 data seems to require a $\langle k_T \rangle$ out of line with both the lower and higher energy experiments. In fact, according to [90] "including $k_T$ effects may help some data sets (E706) to agree with theoretical predictions, but it simultaneously destroys the agreement with other sets (WA70, ISR) with theory". Another concern over the inclusion of $k_T$ smearing voiced by Aurenche *et al* was that fitting the value of $\langle k_T \rangle$ depends on the perturbative cross section. At small values of $p_T^\gamma$ the perturbative predictions are not stable with respect to the renormalisation and factorisation scales and so the perturbative cross section and therefore the smearing $\langle k_T \rangle$ are dependent on these scales. Also, it has been shown that a reasonable fit to data can be achieved by essentially fine tuning the gluon distribution [91].

## 7.5 Summary

In this chapter we have used the Monte Carlo routine DPRAD to make predictions for the photon transverse momentum distribution and compared these predictions with data obtained by the CDF and D0 experiments at the TEVATRON. We have reproduced the well known effect that the theory undershoots the data at small $p_T^\gamma \sim 20$ GeV. We have investigated the different fragmentation functions outlined in the previous chapter, namely the fixed order, ALEPH measured fragmentation function and the BFG resummed fragmentation function. In particular we have investigated the effects of changing the theoretical inputs such as the renormalisation scale, the parton density functions and the way in which the photon isolation is applied. The most striking effect was that as the isolation condition is relaxed - the amount of hadronic energy accompanying the photon is increased, the cross section appeared to decrease. This is counterintuitive and can be traced back to the differential cross section in $z$ being negative for the FO and BFG ($\mu_{\rm frag} = p_T^\gamma$) predictions. One way of understanding this is that the isolation criterion is probing the region where hadronisation effects cause large shifts in the measured $z$ value. A parton level event with $z = 1$ is turned into an event with $z = z_{\rm had} < 1$ at the hadron level. Parton level theoretical predictions will

have great difficulty in describing this effect. One way round this is to lower the isolation cut $z_{\rm cut}$ so that the event is retained at both the parton and hadron level. In fact, in $e^+e^-$ annihilation, the ALEPH collaboration studied the $z$ distribution before deciding on the isolation criteria. This has not been done at the TEVATRON. An alternative approach is to lower the fragmentation scale $\mu_{\rm frag}$ which has the effect of increasing the fragmentation contribution at high $z$ (but still $z < 1$). Evolution to lower $z$ is then suppressed and the $z$ distribution rendered positive definite. This is rather less satisfactory, but in the absence of an experimental investigation of the $z$ distribution yields the best theoretical prediction for the photon transverse energy distribution. As we see from Figs. 7.11 and 7.12, this goes some way towards improving the agreement between theory and experiment, but still leaves room for improvement. One possible explanation may be the inclusion of $k_T$ broadening due to intrinsic transverse momenta considerations and initial state soft gluon resummation. However, the perturbative part of this calculation has not yet been performed and the current models that assume this part of the calculation can be approximated using a Gaussian smearing are still too different and dependent on the perturbative predictions to definitely state that this is the source of the necessary additional theory.

# Chapter 8

# Conclusions

## 8.1 Review

In this thesis we have utilised some of the modern techniques used in NLO QCD calculations for both electron-positron and proton-antiproton experiments. Specifically we have concentrated on the NLO calculations of the processes $e^+e^- \to 4$ jets and $p\bar{p} \to \gamma + X$ and have produced two Monte Carlo routines, `EERAD2` and `DPRAD`, that can be used in the evalution of any 4 jet variable and the transverse photon momentum distribution respectively.

In Chapter 1 we introduced the formation of the QCD Lagrangian using the quark model as a basic picture and outlined how this leads to the perturbative expansion of physical variables in terms of the coupling constant, $g$. We studied the necessary gauge invariance and the differences between the non-Abelian nature of QCD and Abelian QED. We also considered the prescription of renormalisation where the absorption of the ultra violet poles into the bare gluon and quark fields and the bare coupling leads to the concept of a running coupling constant. For QCD (unlike QED) we find that the strength of the coupling diminishes as energy increases making it an asymptotically free field theory. Renormalisation also introduces a scale, $\mu$, into NLO QCD calculations which all truncated observables depend on. This scale is arbitrary, but is usually taken to be the scale of the process ($\mu = \sqrt{s}$) known as the physical scale. However, we also considered other scales proposed by Stevenson and Grunberg.

Although the likelihood of a process occuring is controlled by the short distance per-

turbative QCD picture the formation of hadrons is governed by non-perturbative physics. Therefore at leading order only can we directly relate quarks and gluons to jets. At higher order we start to model the partonic showers that form jets and so a prescription for quantifying the number of jets in an event is required. These are known as jet finding algorithms and ideally they are insensitive to long range hadronisation. For this thesis we concentrated on three variants, the JADE, DURHAM and GENEVA algorithms. Looking at higher order techniques in Chapter 2 we saw how NLO QCD calculations introduce new divergences due to the integration over internal loop momenta. These are infra-red poles and these divergences cancel, order by order, with the poles present in processes with a single extra unresolved parton according to the KLN theorem. The formation of colour algebra also aids the evaluation of NLO quantities, deriving the colour factors that can be factorised into the calculation. After this colour division we are left with kinematical terms which we can group into ordered gluon emission; this is known as colour decomposition. These ordered subamplitudes then display factorisation properties in the soft and collinear regimes, allowing us to write the divergent extra unresolved contribution as a divergent factor multiplied by the hard remaining process.

Having identified the cancellation of infra red divergences it is then necessary to develop a routine which analytically removes these poles. In Chapter 3 we studied three contemporary techniques, but for the NLO calculation of the process $e^+e^- \to 4$ jets in this thesis we have used a new variant of the hybrid subtraction scheme (the hybrid subtraction scheme uses both the slicing and subtraction scheme to remain universal and independent of additional theoretical parameters). This particular prescription relies on the factorisation of the matrix elements and the phase space using an antenna of particles where the antenna consists of two colour connected partons from which a third unresolved parton is emitted. This then factorises the full matrix element and phase space term into a hard scattering term and a divergent antenna factor. We derive the necessary integrals for each of the four types of antennae, utilising the $N = 1$ supersymmetric identity which relates the NLO splitting functions to each other. It is these functions that are used in `EERAD2`.

In Chapter 4 we outlined the calculations necessary for the evalution of NLO observables from the process $e^+e^- \to 4$ jets. This includes the virtual diagrams from $e^+e^- \to q\bar{q}gg$ and $e^+e^- \to q\bar{q}Q\overline{Q}$ using the matrix elements of [66, 67] and the extra, unresolved parton diagrams from $e^+e^- \to q\bar{q}ggg$ and $e^+e^- \to q\bar{q}Q\overline{Q}g$. Making use of symmetries and neglecting

some contributions reduces the lengthy calculation to a more compact form.

Comparing EERAD2 to results obtained with the other Monte Carlo routines, MENLO PARC and DEBRECEN in Chapter 5 gives good agreement for the 4 jet fraction and in the case of DEBRECEN for the 4 jet variables, $D$ parameter and Thrust minor as well. We have also present the NLO coefficients for previously uncalculated variables such as the light hemisphere mass, the narrow hemisphere broadening and the jet transition variable for the GENEVA and JADE algorithms. For each distribution it was found that the NLO corrections were of the order of 100% of the LO result, although for all the observables calculated at the physical scale this was still a factor 2 below the experimental data as measured by the DELPHI collaboration. Using a smaller scale such as the FAC scale seems to model the experimental data better. For observable $O_4$ it is clearly seen that the resummation of leading and subleading logarithms of the type $\log(1/O_4)$ is necessary in the infra red region.

Chapter 6 looks at the NLO calculation for the process $p\bar{p} \to \gamma +$ jets. For this calculation we need to introduce two more ideas, that of fragmentation and initial state collinearities. Fragmentation is one of the processes by which a photon can enter the final state of a process. It is a universal, non-perturbative effect where a parton fragments into a photon which carries off a momentum fraction $z$ of the parent parton's momentum. This occurs during the hadronisation process and is described by the function $D_{i\to\gamma}(z)$. However, we can also produce photons perturbatively and in some configurations this gives a divergent result i.e. when the photon becomes collinear with its parent parton. These poles can be absorbed into the fragmentation function in much the same way as the 1 loop quark self energy corrections are absorbed into the defintion of the quark wavefunction. This renormalisation procedure introduces a scale to the process, $\mu_{\text{frag}}$ which the fragmentation must be independent of, placing a constraint on the non-perturbative part of the function. The coupling of this non-perturbative contribution is contested in the literature and for this calculation we have used a form with coupling proportional to $\mathcal{O}(\alpha)$ which we justify by using the experimental measurement of the $e^+e^- \to \gamma + 1$ jet rate. The other technique introduced in this chapter is a method of dealing with initial state radiation and the potential divergences present here. With a initial state hadronic current we can form initial-final state collinear states which are normalised into the definition of the structure functions. In this thesis the NLO calculation is performed with all of the particles in the final state, then we cross two into the initial state. This correctly contains all the final-final divergences and the newly introduced initial-final

divergences. However it introduces non-physical initial-initial state divergences which we subtract from the process. From this we form the necessary $\mathcal{K}$ factors for the calculation and divergent crossing terms which are renormalised, introducing another scale $\mu_F$. All these calculations are incorporated into the Monte Carlo routine DPRAD.

Finally in Chapter 7 we compared the results obtained using DPRAD with experimental measurements made by the CDF and D0 collaborations. We also studied differences induced in the results due to the variation of parameters such as the renormalisation and factorisation scales, the cone size and hadronic energy cut-off and the parton distribution function inputs. In studying the $z$ distribution at fixed $p_T^\gamma$ we found that for the lower values of $p_T^\gamma$ ($< 30$ GeV) the distribution becomes negative for large values of $z$. This was similar to a problem seen in the process $e^+e^- \to \gamma+1$ jet where the cause was related to the spilling over of isolated events into lower $z$ valued events due to hadronisation. To solve this, the ALEPH colaboration and Glover and Morgan combined the final bins in the definition of isolation. This effect was also seen to be cone size dependent. For the $p\overline{p} \to \gamma+$ jets case we have shown that another solution is to make use of a resummed fragmentation function at small $\mu_{\text{frag}}$ which gives a positive definite $z$ distribution for all $p_T^\gamma$. For this thesis we have used the fragmentation function of Bourhis, Fontannaz and Guillet (BFG) and considered its form at two extreme scales, $p_T^\gamma$ and $k_T = E_{\text{had}} \sin\delta$. Comparing theory and experiment still leaves a shortfall in theory at small $p_T^\gamma$ and one suggestion for resolving this is the inclusion of initial state gluon resummation which leads to $k_T$ smearing effects. However, the result of the dominant part of this effect remains uncalculated and models that attempt to approximate it are many and varied. Also in [91] it has been shown that the data can be fitted by fine tuning the gluon distribution. Finally, the inclusion of $k_T$ effects relies on a stable perturbative calculation in the low $p_T^\gamma$ regime, but here the variation with scale is too large for such a precise calculation. Therefore, we do not include any $k_T$ effect in this calculation except that inherent in the MRST98 functions.

Remaining work that needs to be considered in light of these calculations includes further phenomenology of four jet production. Having seen the large NLO corrections and the remaining theory-data discrepancy at the physical scale, this may suggest choosing a smaller scale (as we have done) or including non-perturbative power corrections. Also the debate remains over the theory-data disagreement in direct photon production. Whether fine-tuning of the perturbative parameters or initial state gluon emission resummation is the missing

piece of this puzzle requires much more work to resolve this discrepancy.

# Appendix A

## Local gauge invariance of the QCD Lagrangian

One of the most fundamental principles underpinning the formulation of QCD is that of local gauge invariance. This symmetry ensures that the Lagrangian (and thus any physical process) has no dependence on a spatial definition of the SU(3) colour charge. If we define our Lagrangian as in Equation 1.2.9 (using Equation 1.2.8 in our definition as well) and use the spatially dependent SU(3) transformation in Equation 1.2.11, then we see that the first term in the Lagrangian is only independent of $V$ if and only if the covariant derivative multiplied by the fundamental triplet transforms as the fundamental triplet i.e. $\mathcal{D}'\psi' = V(x)\mathcal{D}\psi$. This forces a transformation law on the gluon field which defines the covariant derivative. This transformation is given by (here we drop the colour indices for clarity)

$$t^a A_a^\mu \rightarrow V(x)t^a A_a^\mu V^\dagger(x) - \frac{i}{g}V(x)(\partial^\mu V^\dagger(x)) \tag{A.0.1}$$

where repeated indices are summed over. We will show that this transformation, along with the transformation of the quark field leads to the local invariance of the QCD Lagrangian. Consider the transformations of Equation 1.2.12. Then

$$\mathcal{D}^\mu\psi \rightarrow \partial^\mu(V(x)\psi) + ig\left[V(x)t^a A_a^\mu V^\dagger(x) - \frac{i}{g}V(x)(\partial^\mu V^\dagger(x))\right]V(x)\psi \tag{A.0.2}$$

Expanding this out and recalling that all SU(3) transformations obey the unitary relation $VV^\dagger = 1$ we find,

$$\mathcal{D}^\mu\psi \rightarrow \partial^\mu(V(x))\psi + V(x)\partial^\mu(\psi) + igV(x)t^a A_a^\mu\psi + V(x)(\partial^\mu V^\dagger(x))V(x)\psi \tag{A.0.3}$$

We then make use of the product rule, rewriting the last term such that

$$\mathcal{D}^\mu\psi \rightarrow \partial^\mu(V(x))\psi + V(x)\partial^\mu(\psi) + igV(x)t^a A_a^\mu\psi - (\partial^\mu V(x))V^\dagger(x)V(x)\psi \tag{A.0.4}$$

where $\partial^\mu(V(x)V^\dagger(x)) = \partial^\mu(1) = 0$, again employing the unitary condition. This leads to the cancellation of the first and last terms giving

$$\mathcal{D}^\mu\psi \rightarrow V(x)(\partial^\mu\psi) + igV(x)t^a A_a^\mu\psi \equiv V(x)\mathcal{D}^\mu\psi \tag{A.0.5}$$

and we have shown that using the SU(3) transformations that the first term of the proposed Lagrangian is local gauge invariant.

Now let us consider the kinetic term. The form of the field strength tensor we shall use here is that given by Equation 1.2.10 which generalises to the form

$$[\mathcal{D}^\mu, \mathcal{D}^\nu]\psi = igF^{\mu\nu}\psi \tag{A.0.6}$$

where $\sum_a F^{\mu\nu\ a}t^a = F^{\mu\nu}$. We know that under an SU(3) transformation the covariant derivative transforms as $\mathcal{D}^\mu \rightarrow V\mathcal{D}^\mu V^\dagger$. Therefore for gauge invariance we require

$$\begin{aligned}
[D^{\mu\prime}, D^{\nu\prime}]\psi' &= igF^{\mu\nu\prime}\psi' \\
VD_\mu V^\dagger VD_\nu V^\dagger V\psi - VD_\nu V^\dagger VD_\mu V^\dagger V\psi &= igF^{\mu\nu\prime}V\psi \\
VD_\mu D_\nu\psi - VD_\nu D_\mu\psi &= igF^{\mu\nu\prime}V\psi \\
V[D_\mu, D_{nu}]\psi &= igF^{\mu\nu\prime}V\psi \\
igVF_{\mu\nu}\psi &= igF^{\mu\nu\prime}V\psi \\
F^{\mu\nu\prime} &= VF^{\mu\nu}V^\dagger
\end{aligned} \tag{A.0.7}$$

With this transformation property we can now show that the kinetic term is locally gauge invariant. We first need to demonstrate that

$$-\frac{1}{4}F_a^{\mu\nu}F_{\mu\nu\ a} = \mathrm{Tr}\left[-\frac{1}{2}F_{\mu\nu}F^{\mu\nu}\right] \tag{A.0.8}$$

where

$$\begin{aligned}\mathrm{Tr}\left[-\frac{1}{2}F_{\mu\nu}F^{\mu\nu}\right] &= -\frac{1}{2}F_{\mu\nu\ a}F_b^{\mu\nu}\mathrm{Tr}[t^a,t^b] \\ &= -\frac{1}{4}F_{\mu\nu\ a}F_a^{\mu\nu}\end{aligned} \tag{A.0.9}$$

where $\mathrm{Tr}[t^a,t^b] = 1/2\delta^{ab}$. Therefore, by substituting in the gauge transformed quantities and using the cyclic properties of trace, we see that the kinetic term is locally gauge invariant. We have now shown that all the terms in the proposed Lagrangian are locally gauge invariant (as well as any quark mass terms as well). However, there can be no mass term for the gauge bosons as this is clearly not gauge invariant.

# Appendix B

## The 1 loop correction to the process $e^+e^- \rightarrow$ hadrons

In this appendix we shall look at the method developed by Feynman used to evaluate the difficult one-loop integrals found in all NLO calculations. For the purpose of demonstrating this technique we shall study the vertex loop correction of the NLO calculation of $e^+e^- \rightarrow$ hadrons (See Figure B). For this calculation we multiply the loop diagram with the tree level diagram to give a squared matrix element of the order $\mathcal{O}(\alpha_s)$. After performing all the traceology in $4-2\varepsilon$ dimensions we find

$$|\overline{\mathcal{M}}|^2 = 32N(\varepsilon-1)ie_q^2 g^2 C_F \mu^{2\varepsilon} \int_{-\infty}^{\infty} \frac{d^{4-2\varepsilon}k}{(2\pi)^{4-2\varepsilon}} \left[ \frac{\varepsilon(p'.k')(p.k) + \varepsilon(p.p')(k.k') - (\varepsilon+2)(p.k')(p'.k)}{(k^2+i\epsilon)(k'^2+i\epsilon)((k-p)^2+i\epsilon)} \right] \tag{B.0.1}$$

where $|\overline{\mathcal{M}}|^2$ represents the interference between the tree level process and the 1 loop process. We find that the factor $i$ later cancels with another $i$ coming from the integral over the loop momentum, leaving the squared matrix element positive definite. Note also the difference between $\epsilon$, the small distance moved in complex space used to define the time ordered product and $\varepsilon$, the small change in the number of dimensions. Finally we introduce the scale, $\mu^{2\varepsilon}$, in order to keep the coupling constant dimensionless in $d$ dimensions.

The basic idea of *Feynman parameterisation* is to squeeze the denominator factors of the squared matrix element into a single quadratic polynomial. This quadratic can then be

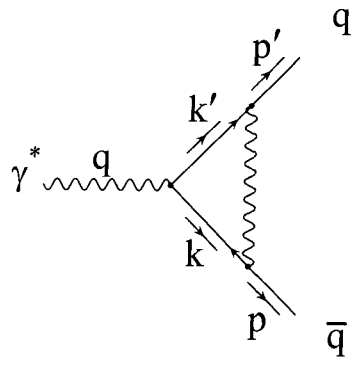


Figure B.1: 1-loop correction term in the NLO calculation of $e^+e^- \to$ hadrons

shifted such that the square can be completed and the remaining spherically symmetric integral can easily be performed. However, the cost of this procedure is to introduce additional parameters to the calculation which in turn will need to be integrated over. Let us consider an integral with just two factors in the denominator first.

$$\frac{1}{AB} = \int_0^1 dx \frac{1}{[xA + (1-x)B]^2} = \int_0^1 dxdy\delta(x+y-1)\frac{1}{[xA+yB]^2} \tag{B.0.2}$$

Putting this identity into a real example might give

$$\begin{aligned} \frac{1}{(k-p)^2(k^2)} &= \int_0^1 dxdy\delta(x+y-1)\frac{1}{[x(k-p)^2 + y(k^2)]^2} \\ &= \int_0^1 dxdy\delta(x+y-1)\frac{1}{[k^2 - 2xp.k + xp^2]^2} \end{aligned} \tag{B.0.3}$$

By letting $l = k - xp$ we can complete the square and the integral depends solely on $l^2$ and can easily be evaluated since $d^4k = d^4l$. For a general result we require the identity

$$\frac{1}{A_1A_2A_3...A_n} = \int_0^1 dx_1...dx_n\delta(\sum x_i - 1)\frac{(n-1)!}{[x_1A_1 + x_2A_2 + ... + x_nA_n]^n} \tag{B.0.4}$$

Now let us apply Equation B.0.4 to our matrix element example in Equation B.0.1. We write

$$\frac{1}{((k-p)^2+i\varepsilon)(k^2+i\varepsilon)(k'^2+i\varepsilon)} = \int_0^1 dzdydx \frac{2}{D^3}\delta(x+y+z-1) \tag{B.0.5}$$

where $D$ is given by

$$\begin{aligned} D &= x((k-p)^2+i\varepsilon) + y(k^2+i\varepsilon) + z(k'^2+i\varepsilon) \\ &= l^2 + Q^2zy + i\varepsilon \\ &= l^2 - \Delta \end{aligned} \tag{B.0.6}$$

The form of $D$ is given by using the identities $k' = q-k$, $p^2 = p'^2 = 0$, $q-p = p'$, $q^2 = Q^2$ and finally $l = k - zq - xp$. We write the numerator of the matrix element in term of $l, p, Q, \varepsilon$ and the Feynman parameters $x, y$ and $z$ and make use of the identities

$$\begin{aligned} &\int_{-\infty}^{\infty} \frac{d^{4-2\varepsilon}l}{(2\pi)^{4-2\varepsilon}} \frac{l^\mu}{D^3} = 0 \\ &\int_{-\infty}^{\infty} \frac{d^{4-2\varepsilon}l}{(2\pi)^{4-2\varepsilon}} \frac{l^\mu l^\nu}{D^3} = \int_0^{\infty} \frac{d^{4-2\varepsilon}l}{(2\pi)^{4-2\varepsilon}} \frac{g^{\mu\nu}l^2}{(4-2\varepsilon)D^3} \end{aligned} \tag{B.0.7}$$

The first of these identities follows from symmetry as $D$ depends only on $l^2$ thus making the integrand on odd function. The second identity can be evaluated by rewriting $l^\mu l^\nu$ as $Ag^{\mu\nu}$ which also will vanish by symmetry unless $\mu = \nu$. We have to evaluate $A$ and we do this by postmultiplying both sides by $g_{\mu\nu}$ which gives $l^2 = A(4-2\varepsilon)$. So using the identities of Equation B.0.7 we find the numerator reduces to

$$\frac{l^2Q^2(1-\varepsilon)^2}{2(2-\varepsilon)} + \frac{Q^4[zy(\varepsilon-1)-x]}{2} \tag{B.0.8}$$

Therefore the matrix element is now given by

$$\left|\overline{\mathcal{M}}\right|^2 = 32N(\varepsilon-1)ie_q^2g^2C_F\mu^{2\varepsilon}\int_{-\infty}^{\infty}\frac{d^{4-2\varepsilon}l}{(2\pi)^{4-2\varepsilon}}\int_0^1\frac{dxdydz\delta(x+y+z-1)}{D^3}$$
$$\left[\frac{l^2Q^2(1-\varepsilon)^2}{2(2-\varepsilon)}+\frac{Q^4[zy(\varepsilon-1)-x]}{2}\right] \tag{B.0.9}$$

At this point of the calculation we introduce another technique necessary to analytically integrate over the momentum variable $l$, namely *Wick rotation.* By rotating the coordinate system from the Minkowski metric to the Euclidean metric (where there is no relative minus sign between spacial and temporal diagonal elements) we can easily perform the integral. We define an Euclidean variable $l_E$ such that the temporal component is $l^0$ multiplied by $i$, but the spatial components of $l_E$ are the same as the spatial components of $l$ which implies the measure has been multiplied by $i$ as well. Therefore we have rotated the contour of integration throught 90° (anticlockwise to avoid the poles) in the $l^0$ plane. Now we can evaluate the integral as we can write the $d$ dimensional measure as a radial measure and the volume of a $d$ dimensional sphere. Therefore

$$\int_{-\infty}^{\infty}\frac{d^{4-2\varepsilon}l}{(2\pi)^{4-2\varepsilon}}\frac{1}{(l^2-\Delta)^3}=\frac{(-1)^3i}{(2\pi)^{4-2\varepsilon}}\int d\Omega_{4-2\varepsilon}\int_0^{\infty}\frac{l_E^3dl_E}{(l_E^2+\Delta)^3} \tag{B.0.10}$$

where the volume of a $d$ dimensional sphere is defined as in Equation 2.3.16. So we are left with integrals that we can reformulate with the change of variables $l_E^2 = w\Delta$ to give beta functions in $w$. Therefore we find the two momentum integrals reduce to

$$\begin{aligned}\int_{-\infty}^{\infty}\frac{d^{4-2\varepsilon}l}{(2\pi)^{4-2\varepsilon}}\frac{1}{[l^2-\Delta+i\varepsilon]^3} &= \frac{i(-1)^3\pi^{2-\varepsilon}\Gamma(1-\varepsilon)}{\Gamma(3)}\frac{1}{\Delta^{1-\varepsilon}}\\ \int_{-\infty}^{\infty}\frac{d^{4-2\varepsilon}l}{(2\pi)^{4-2\varepsilon}}\frac{l^2}{[l^2-\Delta+i\varepsilon]^3} &= \frac{i\pi^{2-\varepsilon}(-1)^4\Gamma(\varepsilon)}{2\Gamma(3)}\frac{4-2\varepsilon}{\Delta^{\varepsilon}}\end{aligned} \tag{B.0.11}$$

We are left with integrals over the two independent Feynman parameters having let $\varepsilon \to 0^-$ to regulate the poles present in the $\Gamma(\varepsilon)$ functions. Both of the remaining integrals are fairly

straightforward and give further $\Gamma$ functions. We expand the function to express the poles in terms of $1/\varepsilon$ and $1/\varepsilon^2$ poles making the poles explicit. Thus the final form of the divergent matrix element for the 1-loop correction to $e^+e^- \to$ hadrons is given by

$$\left|\overline{\mathcal{M}^2}\right|^2 = \frac{Ne_q^2 g^2 C_F Q^2}{\pi^2}\left(\frac{4\pi\mu^2}{Q^2}\right)^{\varepsilon}(-1)^{\varepsilon}\frac{\Gamma(1+\varepsilon)\Gamma^2(1-\varepsilon)}{\Gamma(1-2\varepsilon)}\left[\frac{-1}{\varepsilon^2}-\frac{1}{2\varepsilon}-\frac{5}{2}+O(\varepsilon)\right] \quad \text{(B.0.12)}$$

We then multiply by the phase space factor $(\Gamma(1-\varepsilon)(4\pi)^{\varepsilon}/8\pi(q^2)^{\varepsilon}\Gamma(2-2\varepsilon))$ and the initial flux $(1/2q)$. In Appendix C the form of phase space factors will be studied in more detail. This gives

$$\sigma^{1-\text{loop}} = \sigma^{\text{tree}}\frac{C_F\alpha_s}{2\pi}\left(\frac{4\pi\mu^2}{Q^2}\right)^{\varepsilon}\frac{1}{\Gamma(1-\varepsilon)}\left[\frac{-2}{\varepsilon^2}-\frac{3}{\varepsilon}-8+\pi^2\right] \quad \text{(B.0.13)}$$

where $\sigma^{\text{tree}}$ is equal to the cross section of the tree level diagram and is of the form

$$\sigma^{\text{tree}} = \alpha e_q^2\left(\frac{4\pi\mu^2}{Q^2}\right)^{\varepsilon}\frac{\Gamma(2-\varepsilon)}{\Gamma(2-2\varepsilon)} \quad \text{(B.0.14)}$$

We complete the NLO calculation for $e^+e^- \to$ hadrons by considering the extra unresolved parton contribution. Taking the squared matrix element for the extra parton process we have

$$\left|\overline{\mathcal{M}}\right|^2 = 8C_F e_q^2 g^2(1-\varepsilon)\left[\frac{y_{q\bar{q}}}{y_{qg}y_{\bar{q}g}}+\frac{y_{qg}}{y_{\bar{q}g}}+\frac{y_{\bar{q}g}}{y_{qg}}-\varepsilon\left(\frac{y_{qg}}{y_{\bar{q}g}}+\frac{y_{\bar{q}g}}{y_{qg}}\right)-2\varepsilon\right] \quad \text{(B.0.15)}$$

Rewriting the phase space factor in terms of the dimensionless invariant mass, $y_{ij}$ (where $y_{ij} = s_{ij}/Q^2$) we find (see Appendix C)

$$\frac{Q^2}{16(2\pi)^3}\left(\frac{4\pi\mu^2}{Q^2}\right)^{\varepsilon}\frac{1}{\Gamma(2-2\varepsilon)}\int dy_{qg}dy_{\bar{q}g}(y_{qg}y_{\bar{q}g}(1-y_{qg}-y_{\bar{q}g}))^{-\varepsilon} \quad \text{(B.0.16)}$$

Putting the squared matrix element and initial flux into this integral and redefining one of the variables such that both variables run from 0 to 1 we can perform the integrals to give a cross-section comprising of several beta functions. After much algebra we are left with

$$\sigma^{3\,\text{partons}} = C_F e_q^2 g^2 \frac{Q}{4(2\pi)^3} \left(\frac{4\pi\mu^2}{Q^2}\right)^{\varepsilon} \frac{\Gamma(2-\varepsilon)}{\Gamma(2-2\varepsilon)} \frac{\Gamma(1-\varepsilon)^2}{\Gamma(1-3\varepsilon)} \left[\frac{2}{\varepsilon^2} + \frac{3}{\varepsilon} + \frac{19}{2}\right] \tag{B.0.17}$$

which in terms of the tree level cross section is given by

$$\sigma^{3\,\text{partons}} = \sigma^{\text{tree}} \frac{C_F \alpha_s}{2\pi} \left(\frac{4\pi\mu^2}{Q^2}\right)^{\varepsilon} \frac{\Gamma(1-\varepsilon)^2}{\Gamma(1-3\varepsilon)} \left[\frac{2}{\varepsilon^2} + \frac{3}{\varepsilon} + \frac{19}{2}\right] \tag{B.0.18}$$

It can be shown that the Gamma function factors in front of the loop calculation (Equation B.0.12) and the 3 parton calculation are the same as the $\varepsilon \to 0$ limit is taken. Therefore we can clearly see that the coefficients of the double and single poles of the loop term are exact opposite to those of the 3 parton term and thus the sum of the two is a finite result. In the $\varepsilon \to 0$ limit

$$\sigma^{\text{total}} = \sigma^{\text{tree}} + \sigma^{3\,\text{partons}} + \sigma^{\text{loop}} = \sigma^{\text{tree}} \left[1 + \frac{\alpha_s}{\pi}\right] \tag{B.0.19}$$

Therefore we have shown that for the process $e^+e^- \to$ hadrons the Kinoshita-Lee-Nauenberg theorem is obeyed for the NLO calculation of the cross section.

# Appendix C

## Phase space factors for multi parton final states in $d$ dimensions.

### C.0.1 2 body final states

It can be shown [40] that the form of the phase space factor (or more physically the number of final states per particle per unit volume) is derived from consideration of the boundary conditions placed upon quantum particles bound in a finite region and the normalised density of particles in this region. For $n$ particles in the final state the expression is given by

$$\frac{d^{d-1}p_1}{2E_1(2\pi)^{d-1}}\frac{d^{d-1}p_2}{2E_2(2\pi)^{d-1}}\cdots\frac{d^{d-1}p_n}{2E_n(2\pi)^{d-1}}(2\pi)^d\delta^d(q-p_1-p_2-\ldots-p_n) \tag{C.0.1}$$

However in many cases it is more useful to convert this integral into one over other quantities such as mass invariants or the transverse momentum. Consider the simple case of a 2 body system. Let us redefine the integral firstly in terms of invariant masses and later in terms of transverse momentum. Both are necessary for the calculations considered in this thesis. One of the $d-1$ dimensional measures can be written in terms of a $d$ dimensional one and a delta function such that the original $d$ dimensional delta function is integrated away.

$$\frac{d^{d-1}p}{2E} = d^dp\delta(p^2)\theta(p^0) \tag{C.0.2}$$

Then the other measure is written in terms of its radial component and its solid angle such that

$$d^{d-1}p = p^{d-2}dpd\Omega_{d-1}\theta(p) = E^{d-2}dEd\Omega_{d-1}\theta(E) \tag{C.0.3}$$

since we are dealing with massless particles. This gives for the phase space factor the function,(assuming that the integral over momentum $p_1$ has been performed)

$$\frac{\delta((q-p_2)^2)\theta(E_1)\theta(E_2)E_2^{d-3}dE_2}{2(2\pi)^{d-2}} \tag{C.0.4}$$

The delta function can be rewritten so that it depends on the invariant $s_{12} = 2p_1.p_2$ since $q^\mu = p_1^\mu + p_2^\mu$. $E_2$ can also be rewritten in terms of this invariant such that $E_2 = s_{12}/2Q$ where $q^2 = Q^2$. Therefore the phase space factor in terms of invariants is given by

$$\frac{\delta(Q^2 - s_{12})\theta(E_1)\theta(E_2)s_{12}^{\frac{d-4}{2}}ds_{12}}{2^{d-1}(2\pi)^{d-2}} \tag{C.0.5}$$

and this is the final form that is used in all 2 body calculations contained in this thesis.

### C.0.2 3 body final states

For our NLO calculation of $e^+e^- \to$ hadrons we were required to calculate the three body phase space factor. For simplicity we shall use the mass invariants again. Removing one integration by making use of the delta function (assuming that the integrated momentum was $p_3$) leaves us with

$$\frac{d^{d-1}p_1}{2E_1}\frac{d^{d-1}p_2}{2E_2}\delta(p_3^2)(2\pi)^{3-2d} \tag{C.0.6}$$

Again we can write the remaining measures in terms of a radial part and a solid angle. However, another variable now needs to be considered, the angle between the two independent momenta. We divide the two measures into radial components and two solid angles, but not of the same dimension. One solid angle has a degree of freedom made explicit.

$$\frac{1}{4}dE_1dE_2d\theta_{12}d\Omega_{d-2}d\Omega_{d-3}(E_1E_2\sin(\theta_{12}))^{d-3}\delta(p_3^2)(2\pi)^{3-2d} \tag{C.0.7}$$

It is here that we introduce the Gram determinant that is related to the Jacobian used when switching from momenta to invariants in phase space integrals. In our three dimensional example it is given by

$$\Delta(q,p_1,p_2)=\Delta(p_1,p_2,p_3)=\frac{1}{4}s_{12}s_{13}s_{23}=Q^2E_1^2E_2^2\sin^2(\theta_{12}) \tag{C.0.8}$$

as it is defined to be determinant of the matrix

$$\Delta(p_1,p_2,\cdots,p_n)=\begin{vmatrix} p_1\cdot p_1 & p_1\cdot p_2 & \cdots & p_1\cdot p_n \\ p_2\cdot p_1 & p_2\cdot p_2 & \cdots & p_2\cdot p_n \\ \vdots & \vdots & & \vdots \\ p_n\cdot p_1 & p_2\cdot p_n & \cdots & p_n\cdot p_n \end{vmatrix} \tag{C.0.9}$$

Therefore using the Gram determinant and re-expressing the measures in terms of mass invariants such that

$$dE_1dE_2d\theta_{12}=(16Q^2s_{12}s_{13}s_{23})^{-1/2}ds_{12}ds_{13}ds_{23} \tag{C.0.10}$$

the final form of the three particle phase space, generated from the decay of a single massive particle is given by

$$\frac{1}{(2)^{d+1}}\int Q^{2-d}ds_{12}ds_{13}ds_{23}d\Omega_{d-2}d\Omega_{d-3}(s_{12}s_{13}s_{23})^{\frac{d-4}{2}}\delta(s_{12}+s_{13}+s_{23}-Q^2)(2\pi)^{3-2d} \quad \text{(C.0.11)}$$

Thus the Gram determinant defines the boundaries of available phase space such that if $\Delta_3 > 0$ we lie outside of the kinematical region.

### C.0.3 Two to two body scattering

Now let us consider the case where we wish to define a differential cross-section for a two to two body scattering $1 + 2 \to a + b$ such as the reaction $p\overline{p} \to q\overline{q}$ where not only do we include the 2 body phase space factor, but we also consider the momentum fractions of the incoming partons. In this thesis it has been necessary to calculate the cross-section with respect to the transverse momentum. This gives a phase space factor of the form

$$dx_1dx_2\frac{1}{4\pi^2}\frac{d^3p_a}{2E_a}\frac{d^3p_b}{2E_b}\delta^4(p_1+p_2-p_a-p_b) \quad \text{(C.0.12)}$$

where $x_1$ and $x_2$ are the momentum fractions of the incoming partons such that

$$\begin{aligned} p_1^\mu &= x_1P^\mu = \frac{x_1\sqrt{s}}{2}(1,0,0,1) \\ p_2^\mu &= x_2\overline{P^\mu} = \frac{x_2\sqrt{s}}{2}(1,0,0,-1) \end{aligned} \quad \text{(C.0.13)}$$

where $P$ and $\overline{P}$ are the momenta of the proton and antiproton respectively. We also define $\sqrt{s} = 2P.\overline{P}$ and $\sqrt{\hat{s}} = 2p_1.p_2$. We can rewrite the transverse components of the measure such that

$$dp_a^xdp_a^y = rdrd\theta = \pi d(r^2) = \pi d(p_T^2) \quad \text{(C.0.14)}$$

which, using the transverse part of the delta function determines the transverse component of parton $b$. This then gives

$$dp_T^2 \frac{dp_L^a}{2E_a} \frac{dp_L^b}{2E_b} dx_1 dx_2 \frac{1}{4\pi} \delta\left(\frac{\sqrt{s}}{2}(x_1+x_2) - E_a - E_b\right) \delta\left(\frac{\sqrt{s}}{2}(x_1-x_2) - p_L^a - p_L^b\right) \quad \text{(C.0.15)}$$

To remove the longitudinal momentum integrals we substitute these for integrals over rapidity $y$ where

$$y = \frac{1}{2}\log\left(\frac{E+p_L}{E-p_L}\right) = \log\left(\frac{E+p_L}{p_T}\right) \quad \text{(C.0.16)}$$

Therefore we substitute $y_a$ for $p_L^a$ and $y_b$ for $p_L^b$ to give

$$dp_T^2 dy_a dy_b dx_1 dx_2 \frac{1}{16\pi} \delta\left(\frac{\sqrt{s}}{2}(x_1+x_2) - E_a - E_b\right) \delta\left(\frac{\sqrt{s}}{2}(x_1-x_2) - p_L^a - p_L^b\right) \quad \text{(C.0.17)}$$

We can remove the final longitudinal momentum dependence from the delta functions by using the identities

$$E_a = p_T \cosh(y_a), \quad p_L^a = p_T \sinh(y_a) \quad \text{(C.0.18)}$$

and finally we are left with

$$\begin{aligned} dp_T^2 dy_a dy_b \frac{1}{16\pi} \delta\left(p_T(\cosh(y_a)+\cosh(y_b)) - \frac{\sqrt{s}}{2}(x_1-x_2)\right) \\ \times \quad \delta\left(p_T(\sinh(y_1)+\sinh(y_2)) - \frac{\sqrt{s}}{2}(x_1-x_2)\right) dx_1 dx_2 \end{aligned} \quad \text{(C.0.19)}$$

Now we perform the $x_1$ and $x_2$ integrals such that the measures become

$$dp_T^2 dy_a dy_b \frac{1}{8s\pi} \tag{C.0.20}$$

whilst the delta functions define the intial momenta fractions as

$$x_1 = \frac{p_T}{\sqrt{s}}(e^{-y_a} + e^{-y_b}), \quad x_2 = \frac{p_T}{\sqrt{s}}(e^{y_a} + e^{y_b}) \tag{C.0.21}$$

# Bibliography


[1] M.Gell-Mann, Phys.Rev. **92** (1953) 833

[2] K.Nishijima, Prog.Theor.Phys. **12** (1954) 107
K.Nishijima, Prog.Theor.Phys. **13** (1955) 285

[3] M.Gell-Mann, Phys.Lett.**8** (1964) 214

[4] G.Zweig, CERN preprints 8182/TH.401,8419/TH.412 (1964)

[5] For a review of these experiments see : J.I.Friedman, H.W.Kendall and R.E.Taylor, Rev. Mod. Phys. **63** (1991) 573

[6] L.H.Ryder, Quantum Field Theory, Cambridge University Press (1992)

[7] J.Outhwaite, private communication

[8] Arnd Brandenburg and Peter Uwer, Nucl.Phys **B515** (1998) 279

[9] R.K.Ellis, QCD at Tasi 1994, FERMILAB-Conf-94/410-T

[10] S.Bethke hep-ex/9812026

[11] Z.Kunszt and P.Nason 'Z Physics at LEP1', CERN 89-08 (1989)

[12] P.M.Stevenson, Phys Rev **D23** (1981) 2916

[13] G.Grunberg, Phys.Lett **B95** 70 (1980)
G.Grunberg, Phys.Rev **D29** 2315 (1984)

[14] C.J.Maxwell and J.A.Nicholls, Phys Lett **B213** (1988) 217

[15] T.Kinoshita, J.Math.Phys **3** (1962) 650

[16] T.D.Lee and M.Nauenberg, Phys.Rev **133** (1964) 1549

[17] G.Sterman and S.Weinberg, Phys.Rev.Lett **39** (1977) 1436

[18] JADE Collaboration: S.Bethke et al, Phys. Lett **B213** (1988) 235

[19] N.Brown and W.J.Stirling Phys.Lett **B252** (1990) 657

[20] R.K.Ellis, W.J.Stirling and B.R.Webber 'QCD and Collider Physics', Cambridge University Press (1996)

[21] S.Catani, Yu.L. Dokshitzer, M.Olsson, G.Turnock and B.R.Webber, Phys.Lett **B269** (1991) 432

[22] S.Bethke, Z.Kunszt, D.E.Soper and W.J.Stirling, Nucl Phys **B370** (1992) 310;Erratum,preprint hep-ph/9803267

[23] L.Dixon and A.Signer Phys.Rev **D56** (1997) 4031

[24] S.Moretti, L.Lönnblad, T.Sjöstrand hep-ph/9804296

[25] R.Akers et al, OPAL Collaboration, Z. Phys **C65** (1995) 367

[26] R.Barate et al, ALEPH Collaboration, Phys. Rep **294** (1998) 1

[27] G.R.Farrar 'Experimental and Cosmological Implications of Light Gauginos', RU-97-82,hep-ph/9710395

[28] Z.Nagy and Z.Trócsányi, hep-ph/9712385

[29] J.M.Campbell, E.W.N.Glover and C.J.Maxwell hep-ph/9803254

[30] W.Pauli and F.Villars, Rev Mod Phys **21** (1949) 434

[31] G.t'Hooft and M.Veltmann, Nucl Phys **B44** (1972a) 189
C.G.Bollini and J.J.Giambiagi, Phys Lett **40B** (1972) 566
G.M.Cicuta and E.Montaldi, Nuovo Cimento Lett **4** (1972) 329
J.F.Ashmore, Nuovo Cimento Lett **4** (1972) 289
E.R.Speer and M.J.Westwater Ann.Inst.Henri Poincaré **A14** (1971) 1

[32] J.Collins 'Renormalisation' Cambridge University Press (1984)

[33] W.T.Giele 'Properties and Calculations of Multi Parton Processes'

[34] F.A.Berends and W.T.Giele,Nucl. Phys **B306** (1988) 759

[35] F.A.Berends and W.T.Giele,Nucl. Phys **B313** (1989) 595

[36] W.T.Giele and E.W.N.Glover, Phys Rev **D46** (1992) 1980

[37] D.R.Yennie, S.C.Frautschi and H.Suura, Annals of Physics **13** (1961) 379

[38] G.Altarelli and G.Parisi, Nucl. Phys **B126** (1977) 298

[39] G.t'Hooft and M.Veltman, Nucl. Phys **B44** (1972) 189

[40] F.Halzen and A.D.Martin, 'Quarks and Leptons', John Wiley and Sons Inc (1984)

[41] Z.Kunszt and D.E.Soper, Phys Rev.**D 46** (1992) 1980

[42] K.Fabricius, I.Schmitt, G.Kramer and G.Schierholz, Z.Phys **C11** (1981) 315
W.T.Giele and E.W.N.Glover, Phys Rev **D46** (1992) 1980

[43] A.Gehrmann-De Ridder, PhD thesis, University of Durham, 1997

[44] R.K.Ellis, D.A.Ross and A.E.Terrano, Nucl Phys **B178** (1981) 421

[45] S.Catani and M.H.Seymour, Phys Lett **B378** (1996) 287; Nucl Phys **B485** (1997)

[46] D.Kosower, Phys Rev. **D57** (1998) 5410

[47] J.M.Campbell, PhD thesis, University of Durham, 1998

[48] L.Dixon and A.Signer, Phys.Rev.D **56** (1997) 4031

[49] G. Parisi, Phys. Lett. **B74** (1978) 65.

[50] S. Brand et al, Phys. Lett. **12** (1964) 57;
E. Farhi, Phys. Rev. Lett. **39** (1977) 1587.

[51] L. Clavelli, Phys. Lett. **B85** (1979) 111.

[52] S. Catani, G. Turnock, B.R. Webber, Phys. Lett. **B295** (1992) 269.

[53] J.D. Bjorken, S. Brodsky, Phys. Rev. **D51** (1970) 1416.

[54] Z. Nagy and Z. Trócsányi, Phys. Rev. Lett. **79** (1997) 3604 [hep-ph/9707309];
Nucl. Phys. B, Proc. Suppl. **64** (1998) 63 [hep-ph/9708344];
'Next-to-leading order calculation of four-jet observables in electron positron annihilation', hep-ph/9806317;
'Multijet rates in $e^+e^-$ annihilation: perturbation theory versus LEP data', hep-ph/9808364.

[55] A. Signer and L. Dixon, Phys. Rev. Lett. **78** (1997) 811 [hep-ph/9609460];
A. Signer and L. Dixon, Phys. Rev. **D56** (1997) 4031 [hep-ph/9706285];
A. Signer, Comput. Phys. Comm. **106** (1997) 125;
A. Signer, Proceedings of 32nd Rencontres de Moriond: QCD and High-Energy Hadronic Interactions, p 211 (1997) March 1997 [hep-ph/9705218].

[56] P. Abreu et al, DELPHI Collaboration, Z. Phys. **C73** (1996) 11.

[57] S.J.Burby Phys.Lett. **B453** (1999) 54

[58] S. Catani, G. Turnock, B.R. Webber, L. Trentadue, Phys. Lett. **B263** (1991) 461; Nucl. Phys. **B407** (1993) 3;
S. Catani, G. Turnock, B.R. Webber, Phys. Lett. **B272** (1991) 368; Phys. Lett. **B295** (1992) 269;
S. Catani and B.R. Webber, hep-ph/9801350.

[59] C.J. Maxwell, 'Complete renormalisation group improvement of QCD perturbation theory', hep-ph/9809270.

[60] R.M. Barnett et al, Phys. Rev. **D54** (1996) 1 and 1997 off-year partial update from http://pdg.lbl.gov.

[61] B.R. Webber, Phys. Lett. **B339** (1994) 148;
B.R. Webber, *Proc. Summer School on Hadronic Aspects of Collider Physics, Zuoz, Switzerland, 1994* [hep-ph/9411384];
G.P. Korchemsky and G. Sterman, Nucl. Phys. **B437** (1995) 415;
G.P. Korchemsky and G. Sterman, *Proc. 30th Rencontres de Moriond, Les Arcs, France, 1995* [hep-ph/9505391];

P. Nason and M.H. Seymour, Nucl. Phys. **B454** (1995) 291;
R. Akhoury and V.I. Zakharov, Phys. Lett. **B357** (1995) 646;
R. Akhoury and V.I. Zakharov, Nucl. Phys. **B465** (1996) 295.

[62] Yu.L. Dokshitser and B.R. Webber, Phys. Lett. **B352** (1995) 451 [hep-ph/9504219];
Phys. Lett. **B404** (1997) 321 [hep-ph/9704298];
Yu.L. Dokshitser, G. Marchesini and B.R. Webber, Nucl. Phys. **B469** (1996) 93 [hep-ph/9512336].

[63] Z.Bern, L.Dixon and D.A.Kosower, Nucl. Phys. Proc. Suppl. **51C** (1996) 243

[64] Z.Bern, L.Dixon and D.A.Kosower, Nucl. Phys. **B513** (1998) 3

[65] Z.Bern, L.Dixon, D.A.Kosower and S.Weinzerl, Nucl. Phys. **B489** (1997) 3

[66] J.M.Campbell, E.W.N.Glover and D.J.Miller, Phys.Lett **B409** (1997) 503

[67] E.W.N.Glover and D.J.Miller, Phys.Lett **B396** (1997) 257

[68] R.K.Ellis, D.A.Ross and A.E.Terrano, Nucl.Phys. **B178** (1981) 421

[69] C.J.Maxwell, Phys.Lett **B409** (1997) 450-454

[70] A.Gehrmann-De Ridder, G.Kramer and H.Speisberger, hep-ph/9903377
L.E.Gordon, Phys.Rev.**D57** (1998) 235
G.Kramer, D.Michelsen and H.Speisberger, Eur.Phys.J. **C5** (1998) 293

[71] E.W.N.Glover and A.G.Morgan, Z.Phys. **C62** (1994) 311
M.Glück, E.Reya and A.Vogt, Phys.Rev.**D48** (1993) 116
L.Bourhis, M.Fontannaz and J.Ph.Guillet, Eur.Phys.J.**C2** (1998) 529

[72] H.Baer,J.Ohnemus and J.F.Owens, Phys.Rev.**D42** (1990) 61
P.Aurenche, R.Baier and M.Fontannaz, Phys.Rev.**D42** (1990) 1440
P.Aurenche, P.Chiapetta, M.Fontannaz, J.P.Guillet and E.Pilon, Nucl.Phys. **B399** (1993) 34
E.L.Berger and J.Qiu, Phys.Rev.**D44** (1991) 2002
E.W.N.Glover and W.J.Stirling Phys.Lett.**B295** (1992) 128
Z.Kunszt and Z.Trocsanyi, Nucl.Phys.**B394** (1993) 139
L.E.Gordon and W.Vogelsang, Phys.Rev. **D50** (1993) 1901

[73] S.Frixione, Phys.Lett.**B429** (1998) 369

[74] ALEPH collaboration: D.Buskulic et al, Z.Phys **C62** (1994) 311

[75] M.Glück, E.Reya and A.Vogt, Phys.Rev. **D45** (1992) 3986
M.Glück, E.Reya and A.Vogt, Phys.Rev. **D46** (1993) 1973

[76] B.R.Webber, Contribution to the Durahm workshop on Jet Studies and HERA, J.Phys. **G17** (1991) 1441

[77] W.T.Giele, E.W.N.Glover and D.A.Kosower, FERMILAB-Pub-92/230-T

[78] A.Gehrmann-De Ridder, G.Kramer and H.Speisberger, [hep-ph 9907511]

[79] A.Gehrmann-De Ridder, T.Gehrmann and E.W.N.Glover, Phys.Lett. **B414** (1997) 354

[80] M.Glück, E.Reya and A.Vogt, Phys.Rev. **D48** (1993) 116

[81] L.Bourhis, M.Fontannaz and J.Ph.Guillet, Eur.Phys.J. **C2** (1998) 529

[82] Abe *et al*, Phys.Rev.Lett **73** (1994) 2662
Abe *et al*, Phys.Rev. **D48** (1993) 2998
Abe *et al*, Phys.Rev.Lett **68** (1992) 2734

[83] Abachi *et al*, Phys.Rev.Lett **77** (1996) 5011

[84] E.W.N.Glover and A.G.Morgan, Phys.Lett. **B334** (1994) 208

[85] ALEPH collaboration, presented by J.C.Thompson, 29th Rencontres de Moriond, Meribel, March 1994

[86] J.Huston *et al*, Phys.Rev. **D51** (1995) 6139

[87] L.Apanasevich *et al*, Phys.Rev.Lett **81** (1998) 2642

[88] L.Apanasevich *et al* Phys.Rev. **D59** (1999) 074007

[89] R.Feynman, R.Field, G.Fox, Phys.Rev. **D18** (1978) 3320
A.P.Contgouris *et al*, Nucl. Phys **B179** (1981) 461
A.P.Contgouris *et al*, Phys.Rev. **D32** (1985) 1134



[90] P.Aurenche, M.Fontannaz, J.Ph.Guillet, B.Kniehl, E.Pilon, M.Werlen, Eur.Phys.J. **C9** (1999) 107

[91] W.Vogelsang and A.Vogt, Nucl.Phys. **B453** (1995) 334